UNIVERSIDAD COMPLUTENSE DE MADRID
FACULTAD DE CIENCIAS QUÍMICAS

TESIS DOCTORAL

Nuevos materiales conmutables híbridos para aplicaciones como sensores a nivel molecular

Novel switchable hybrid materials for applications as sensors at the molecular level

MEMORIA PARA OPTAR AL GRADO DE DOCTOR

PRESENTADA POR

Estefanía Fernández Bartolomé

Director

José Sánchez Costa

Madrid

UNIVERSIDAD COMPLUTENSE DE MADRID
FACULTAD DE CIENCIAS QUÍMICAS

TESIS DOCTORAL

Nuevos materiales conmutables híbridos para aplicaciones como sensores a nivel molecular

Novel switchable hybrid materials for applications as sensors at the molecular level

Memoria para optar al grado de doctor presentada
por: ESTEFANÍA FERNÁNDEZ BARTOLOMÉ

Director:
JOSÉ SÁNCHEZ COSTA

AGRADECIMIENTOS

En primer lugar, me gustaría dar las gracias a todas las personas que han sido partícipes en esta tesis doctoral, ya que gracias a todos vosotros hoy he llegado hasta aquí.

Quiero agradecer de manera especial mi director de tesis José Sánchez Costa por haberme dado la oportunidad de pertenecer a su grupo de investigación y formarme como investigadora durante todo el periodo de mi tesis doctoral.

También dar las gracias, al Instituto IMDEA Nanociencia, a la Universidad Complutense de Madrid, a todos Servicios Interdepartamentales de Investigación, así como, a los Sincrotrones de ALBA y Lawrence Berkeley National Laboratory (Berkeley) que han hecho posible realizar esta Tesis doctoral.

Y me gustaría agradecer también al Ministerio de Economía, Industria y Competitividad y al Ministerio de Ciencia e Innovación por haber financiado esta Tesis doctoral a través de los proyectos RYC-2014-16866, CTQ2016-80635-P, SEV-2016-0686 y NANOMAGCOST-CM, S2018/NMT-4321.

INDEX

ABSTRACT

Novel switchable hybrid materials for applications as sensors at the molecular level

INTRODUCTION

Nowadays, as a result for a good knowledge of the principles of crystal engineering, it is possible to design reactive solids which are able to perform solid-state reactions with greater ease than ever before[1]. This kind of solid-state reactions has been the focus in many investigations in the last decade. And particularly interesting are, the so-called single-crystal-to-single-crystal (SCSC) reactions, in which a single reactive crystal produces a product in the form of a single crystal[2,3,4]. In these SCSC transformation, the crystal is exposed to external stimuli such as solvent vapors[5], heat[6], light[7] and pressure[8], producing changes in its physical and structural properties such as color[5,9], magnetism[10], porosity[11], luminescence[8], expansion and shrinkage of the crystal[6].

The SCSC transformations triggered by a gas-solid reaction have received great attention due to their potential applications in the development of functional materials. Specifically, these materials could be used as chemical sensors for the detection of toxic gases or volatile organic compounds (VOCs)[12,13]. Because the presence of VOCs in the atmosphere poses a threat to human health and the enviroment[14]. Apart from that, it is also well known that thermal SCSC transformations can causes phase transition in materials at molecular level[15,16,17], which are associated with big changes in the physical properties.

OBJECTIVES

The main aim of this doctoral thesis is to broaden the knowledge of solid-state intermolecular reactions by single-crystal-to-single-crystal (SCSC) transformation.

For this purpose, the design, synthesis, crystallization and characterization of new metallic coordination compounds and carbon-based dynamic organic compounds have been carried out. Additionally, the study of the physical-chemical responses of these materials under external stimuli such as the sorption of small harmful molecules or temperature, which can produce the change of color or the size of the crystal, has been done. In order to achieve this aim, different studies have been carried out, which will be presented in the following results.

RESULTS

The experimental results of this thesis have been divided into four chapters:

Chapter 2 describes the synthesis of an unprecedented MOF 3D non-porous architecture[18] formed by the reaction between a novel extended triazole-based ligand (PM-Tria), $Fe(BF_4)_2$ and FeF_2 salt. Furthermore, it is also explained its interesting crystalline structure, which is compared with an XIV century Islamic mosaic, found in the Alhambra Palace in Granada (Spain) showing a surprising and beautiful resemblance. Finally, the changes of the physical properties, such the change of color when the crystals are exposed to acetic acid are also studied

In chapter 3, the synthesis of a 2D iron (II) polymer, $\{FeCl_2(pyz)_2\}_n$, that presents an interesting reversible SCSC behavior in response to pyridine vapor, which is accompanied by a color change has been reported. It should also be noted that the ligand exchange process is completely reversible with persistence of crystallinity, obtaining a reusable sensor. This behavior has also been studied when $\{FeCl_2(pyz)_2\}_n$ has been embedded in two different polymers, PDMS and PMMA.

Chapter 4 is devoted to the development of a novel and very promising family of pure molecular dynamic crystalline frameworks held together by means of weak CH···HC Van der Waals interactions, that have been reported for the first time in this field[5]. This organic fullerene-based material exhibits a non-porous dynamic crystalline structure capable of undergoing SCSC reactions with a color change by VOCs exposition, hydrazine in particular, giving rise to a toposelective and controlled hydrogenation (in 24 positions) on the surface of the fullerene.

Finally, in the last experimental chapter, the synthesis of a new crystalline dynamic polymorph hexakis adduct fullerene has been reported. This new fullerene displays an irreversible thermal polymorphic phase transitions resulting in the formation of a new polymorph, which through an extensive characterization study was identified to be the non-hidrogenated [60]fullerene hexakis adduct described in the chapter 4. The change in color is due to the hydrogenation (dissimilar hydrogenation due to the disposition of the butyl malonate arms of the fullerene) of the new fullerene in 24 positions by the actions of hydrazine vapors and has also been studied. The creation of these novel and dynamics carbon-based advanced

absorbent materials can be applied in a variety of direct technological applications, as chemo sensor and environmental remediation devices.

CONCLUSIONS

In this thesis unprecedented crystalline non-porous materials of diverse nature, acting as porous materials, have been developed, including diverse coordination polymers and dynamic organic materials. These materials are very interesting, novel and they possess a great functional property and they can be applied in diverse fields as sensors and stores of harmful molecules and as actuators.

REFERENCES

1 G. R. Gautam R. Desiraju, J. J. Vittal and A. Ramanan, *Crystal engineering : a textbook*, World Scientific, 2011.

2 A. Chaudhary, A. Mohammad and S. M. Mobin, *Crystal Growth and Design*, 2017, **17**, 2893–2910.

3 G. K. Kole and J. J. Vittal, *Chemical Society Reviews*, 2013, **42**, 1755–1775.

4 J. J. Vittal, *Coordination Chemistry Reviews*, 2007, **251**, 1781–1795.

5 E. Fernandez-Bartolome, J. Santos, A. Gamonal, S. Khodabakhshi, L. J. McCormick, S. J. Teat, E. C. Sañudo, J. S. Costa and N. Martín, *Angewandte Chemie International Edition*, 2019, **58**, 2310-2315.

6 Z. S. Yao, M. Mito, T. Kamachi, Y. Shiota, K. Yoshizawa, N. Azuma, Y. Miyazaki, K. Takahashi, K. Zhang, T. Nakanishi, S. Kang, S. Kanegawa and O. Sato, *Nature Chemistry*, 2014, **6**, 1079–1083.

7 L. T. Ni, M. Nagarathinam and J. J. Vittal, *Angewandte Chemie International Edition*, 2005, **44**, 2237–2241.

8 H. Ito, M. Muromoto, S. Kurenuma, S. Ishizaka, N. Kitamura, H. Sato and T. Seki, *Nature Communications*, 2013, **4**, 1–5.

9 E. Resines-Urien, E. Burzurí, E. Fernandez-Bartolome, M. Á. García García-Tuñón, P. de la Presa, R. Poloni, S. J. Teat and J. S. Costa, *Chemical Science*, 2019, **10**, 6612-6616.

10 J. S. Costa, S. Rodríguez-Jiménez, G. A. Craig, B. Barth, C. M. Beavers, S. J. Teat and G. Aromí, *Journal of the American Chemical Society*, 2014, **136**, 3869–3874.

11 L. Wen, P. Cheng and W. Lin, *Chemical Communications*, 2012, **48**, 2846–2848.

12 S. Supriya and S. K. Das, *Journal of the American Chemical Society*, 2007,

129, 3464–3465.

13 G. van Koten, M. Albrecht, M. Lutz and A. L. Spek, *Nature*, 2000, **406**, 970–974.

14 *Indoor air quality : organic pollutants : report on a WHO meeting, Berlin, West, 23-27 August 1987.*, Copenhagen : World Health Organization, Regional Office for Europe, 1989.

15 Z. S. Yao, M. Mito, T. Kamachi, Y. Shiota, K. Yoshizawa, N. Azuma, Y. Miyazaki, K. Takahashi, K. Zhang, T. Nakanishi, S. Kang, S. Kanegawa and O. Sato, *Nature Chemistry*, 2014, **6**, 1079–1083.

16 S. Q. Su, T. Kamachi, Z. S. Yao, Y. G. Huang, Y. Shiota, K. Yoshizawa, N. Azuma, Y. Miyazaki, M. Nakano, G. Maruta, S. Takeda, S. Kang, S. Kanegawa and O. Sato, *Nature Communications*, 2015, **6**, 1–7.

17 D. Das, T. Jacobs and L. J. Barbour, *Nature Materials*, 2010, **9**, 36–39.

18 E. Fernandez-Bartolome, J. Santos, S. Khodabakhshi, L. J. Mcormick, S. J. Teat, C. S. De Pipaon, J. R. Galan-Mascarós, N. Martín and J. Sanchez Costa, *Chemical Communications*, 2018, **54**, 5526–5529.

RESUMEN

Nuevos materiales conmutables híbridos para aplicaciones como sensores a nivel molecular

INTRODUCCIÓN

Actualmente, gracias al desarrollo del conocimiento de los principios de la ingeniería de los cristales, es posible diseñar con mayor facilidad, sólidos reactivos que sean capaces de realizar reacciones en estado sólido[1]. En la última década, este tipo de reacciones ha sido el foco de muchas investigaciones, en particular, las reacciones conocidas como reacciones single-crystal-to-single-crystal (SCSC), en las que un monocristal reactivo produce un producto en forma monocristal[2,3,4]. En estas transformaciones SCSC, el cristal se expone a estímulos externos como: vapores de disolvente[5], temperatura[6], luz[7] y presión[7], produciendo cambios en sus propiedades físicas y estructurales como el color[5,9], magnetismo[10], porosidad[11], luminiscencia[8], expansión y contracción del cristal[8].

Las transformaciones SCSC desencadenadas por una reacción gas-sólido han recibido gran atención debido a sus potenciales aplicaciones en el desarrollo de materiales funcionales. Concretamente, estos materiales podrían utilizarse como sensores químicos para la detección de gases tóxicos o compuestos orgánicos volátiles (COVs)[12,13]. La presencia de COVs en la atmósfera, representa una gran amenaza para la salud humana y el medio ambiente[14]. Además, también se tiene el conocimiento, que las transformaciones SCSC térmicas pueden provocar una transición de fase en los materiales a nivel molecular[15,16,17], las cuales están asociadas a grandes cambios en las propiedades físicas.

OBJETIVOS

El objetivo principal de esta tesis doctoral es ampliar el conocimiento de las reacciones intermoleculares del estado sólido a través de las transformaciones SCSC. Para ello, se ha llevado a cabo el diseño, síntesis, cristalización y caracterización de nuevos compuestos de coordinación y compuestos orgánicos dinámicos basados en carbono. Además, también se ha realizado el estudio de las respuestas físico-químicas de estos materiales bajo estímulos externos como la absorción de pequeñas moléculas nocivas o la temperatura, que pueden producir el cambio en el color o en el tamaño del cristal. Para lograr este objetivo, se realizarán diferentes estudios que serán presentados en los siguientes resultados.

RESULTADOS

Los resultados experimentales de esta tesis se han dividido en cuatro capítulos:

En el capítulo 2 se describió la síntesis de una arquitectura de MOF en 3D no porosa sin precedentes[18] formada por la reacción entre un novedoso ligando extendido basado en triazoles (PM-Tria) y las sales de $Fe(BF_4)_2$ y FeF_2. Además, también se explica su interesante estructura cristalina, la cual se compara con la de un mosaico islámico del siglo XIV, encontrado en el Palacio de la Alhambra de Granada (España), con la que muestra un sorprendente y hermoso parecido. Por último, también se estudiaron los cambios de las propiedades físicas, el cambio de color, cuando los cristales se expusieron al ácido acético.

En el capítulo 3, se ha descrito la síntesis de un polímero 2D de hierro (II), $\{FeCl_2(pyz)_2\}_n$, que presenta interesantes cambios de color cuando los monocristales del polímero se exponen a vapores de piridina. También cabe destacar que el proceso de intercambio de ligandos es completamente reversible persistiendo de la cristalinidad de los materiales, obteniendo un sensor reutilizable. Este comportamiento también se ha estudiado cuando $\{FeCl_2(pyz)_2\}_n$ es embebido en dos polímeros diferentes, PDMS y PMMA.

El capítulo 4 está dedicado al desarrollo de una novedosa y muy prometedora familia de marcos cristalinos dinámicos, unidos por medio de interacciones débiles CH---HC de Van der Waals, los cuales han sido publicados por primera vez en este campo[5]. Este material orgánico basado en el fullereno exhibe una estructura cristalina dinámica no porosa capaz de sufrir reacciones SCSC mediante la exposición de COVs, hidrazina en particular, que genera un cambio de color en el material debido a que se produce una hidrogenación topo selectiva y controlada (en 24 posiciones) en la superficie del fullereno.

Finalmente, en el último capítulo experimental se ha estudiado la síntesis de un nuevo polimorfo dinámico cristalino de fullereno. Al aplicar temperatura, este novedoso fullereno presenta una transición de fase irreversible que da lugar a la

formación de un nuevo polimorfo. Mediante un exhaustivo estudio de caracterización se identificó que este nuevo polimorfo correspondía al fullereno hexaaducto no hidrogenado descrito en capítulo 4. Sobre este nuevo polimorfo, también se estudiaron los cambios de color asociados a la hidrogenación (en este caso se hidrogena de manera disimilar debido a la disposición de los brazos del malonato de butilo del fullereno) del nuevo fullereno en 24 posiciones por la acción de los vapores de hidrazina. La síntesis de estos materiales novedosos y dinámicos basados en el carbono pueden utilizarse en potenciales aplicaciones tecnológicas, como quimio sensores y dispositivos de recuperación ambiental.

CONCLUSIONES

En esta tesis se han desarrollado materiales cristalinos no porosos sin precedentes de diferente naturaleza, que actúan como materiales porosos, incluyendo diversos polímeros de coordinación y materiales orgánicos dinámicos. Estos materiales son muy interesantes, novedosos y poseen una gran funcionalidad, pudiendo ser aplicados en diversos campos como sensores y almacenes de moléculas nocivas.

REFERENCIAS

1 G. R. Gautam R. Desiraju, J. J. Vittal and A. Ramanan, *Crystal engineering : a textbook*, World Scientific, 2011.

2 A. Chaudhary, A. Mohammad and S. M. Mobin, *Crystal Growth and Design*, 2017, **17**, 2893–2910.

3 G. K. Kole and J. J. Vittal, *Chemical Society Reviews*, 2013, **42**, 1755–1775.

4 J. J. Vittal, *Coordination Chemistry Reviews*, 2007, **251**, 1781–1795.

5 E. Fernandez-Bartolome, J. Santos, A. Gamonal, S. Khodabakhshi, L. J. McCormick, S. J. Teat, E. C. Sañudo, J. S. Costa and N. Martín, *Angewandte Chemie International Edition*, 2019, **58**, 2310-2315.

6 Z. S. Yao, M. Mito, T. Kamachi, Y. Shiota, K. Yoshizawa, N. Azuma, Y. Miyazaki, K. Takahashi, K. Zhang, T. Nakanishi, S. Kang, S. Kanegawa and O. Sato, *Nature Chemistry*, 2014, **6**, 1079–1083.

7 L. T. Ni, M. Nagarathinam and J. J. Vittal, *Angewandte Chemie International Edition*, 2005, **44**, 2237–2241.

8 H. Ito, M. Muromoto, S. Kurenuma, S. Ishizaka, N. Kitamura, H. Sato and T. Seki, *Nature Communications*, 2013, **4**, 1–5.

9 E. Resines-Urien, E. Burzurí, E. Fernandez-Bartolome, M. Á. García García-Tuñón, P. de la Presa, R. Poloni, S. J. Teat and J. S. Costa, *Chemical Science*, 2019, **10**, 6612-6616.

10 J. S. Costa, S. Rodríguez-Jiménez, G. A. Craig, B. Barth, C. M. Beavers, S. J. Teat and G. Aromí, *Journal of the American Chemical Society*, 2014, **136**, 3869–3874.

11 L. Wen, P. Cheng and W. Lin, *Chemical Communications*, 2012, **48**, 2846–2848.

12 S. Supriya and S. K. Das, *Journal of the American Chemical Society*, 2007, **129**, 3464–3465.

13 G. van Koten, M. Albrecht, M. Lutz and A. L. Spek, *Nature*, 2000, **406**, 970–974.

14 *Indoor air quality : organic pollutants : report on a WHO meeting, Berlin, West, 23-27 August 1987.*, Copenhagen : World Health Organization, Regional Office for Europe, 1989.

15 Z. S. Yao, M. Mito, T. Kamachi, Y. Shiota, K. Yoshizawa, N. Azuma, Y. Miyazaki, K. Takahashi, K. Zhang, T. Nakanishi, S. Kang, S. Kanegawa and O. Sato, *Nature Chemistry*, 2014, **6**, 1079–1083.

16 S. Q. Su, T. Kamachi, Z. S. Yao, Y. G. Huang, Y. Shiota, K. Yoshizawa, N. Azuma, Y. Miyazaki, M. Nakano, G. Maruta, S. Takeda, S. Kang, S. Kanegawa and O. Sato, *Nature Communications*, 2015, **6**, 1–7.

17 D. Das, T. Jacobs and L. J. Barbour, *Nature Materials*, 2010, **9**, 36–39.

18 E. Fernandez-Bartolome, J. Santos, S. Khodabakhshi, L. J. Mcormick, S. J. Teat, C. S. De Pipaon, J. R. Galan-Mascarós, N. Martín and J. Sanchez Costa, *Chemical Communications*, 2018, **54**, 5526–5529.

1. INTRODUCTION

Reactivity is a fundamental chemical property of molecules[1]. It is known that matter exists in three states: solid, liquid, and gaseous and the molecules can undergo reactions in all the three states of matter and any combination of the three. Solid state reactions can be classified in the following categories: (i) solid → products, (ii) solid + gas → products, (iii) solid + solid → products, and (iv) solid + liquid→ products[2].

From the point of view of understanding the influence of governing factors and structure on solid-state reactions, new synthetic strategies[3,4,5] have recently been proposed that differ from the classical approaches both wet chemistry and conventional solid state reactions, solid + solid. Traditionally these latter conventional reactions have been carried out under harsh conditions, high temperature, high pressure and precise formulation control. In sharp contrast, nowadays chemists are taking advantage of the high structural diversity and tunable chemical and physical properties of solids materials, which offer a promising possibility to synthesize new materials and molecular compounds that are less available, or not available at all, with classical methodologies[6,7]. As important type of solid-state reactions are those based on single-crystal materials[8].

Since the first connection between the fields of solid-state reactions and crystal engineering provide by Schmidt et al. in 1971[9], many efforts have been developed in order to find the relationship between the structure and reactivity in solid-state reactions. Despite the development in this field, it is still a challenge for the scientist to control the reactivity in the solid state[10,11] due to the restrictions in the closed molecular packing. For this reason, the synthesis of new reactive crystalline materials with desirable physical and chemical properties remains a difficult task[7].

Over the last few years, both the fields of crystal engineering[12] and supramolecular chemical engineering[13] as well as single crystal X-ray diffraction techniques have improved greatly making it easier than ever to monitor single crystal reactions.

In this doctoral thesis, a type of solid state reactions from crystalline materials will be studied (as well as the changes that occur in these materials when an external stimulus is applied to them), among which are included coordination compounds and purely organic compounds to be used in many application as chemical sensors or the absorption and separation of novices molecules. Therefore, before starting to describe what the crystals are and the reactions in solid state based on them, we are going to define briefly, what the coordination and organic compounds are.

The IUPAC defined coordination compounds as: “a coordination compound is any compound that contains a coordination entity. A coordination entity is an ion or neutral molecule that is composed of a central atom, usually that of a metal, to which is attached a surrounding array of atoms or groups of atoms, each of which is called ligands”[14]. When coordination compounds with coordination entities are repeated and extended in 1, 2 or 3 dimensions, they are called “coordination polymers”. This infinite net is defined by coordination bonds, weaker interaction than typical covalent bonding. The coordination compounds that can be formed are very diverse, due to the extensive combinations of geometry and connectivity that can occur between the metal ion or cluster and the ligand.

Other sources like the Encyclopaedia Britannica has defined the organic compound: ”as a large class of chemical compounds in which one or more atoms of carbon are covalently linked to atoms of other elements, most commonly hydrogen, oxygen, or nitrogen”[15].

1.1. SINGLE CRYSTAL

As De Barr described, the word 'crystal' comes from a Greek word meaning clear ice which was also applied to rock crystal (clear, transparent quartz). It was not until about the 17th century that the word was extended to other naturally occurring, transparent minerals which showed a regularity of outward form[16]. In science, a **crystal** represents a regular arrangement of atoms, molecules, or ions in a specific repeating pattern, which can be generated by periodic translations of a basic motif or building block that extends out in three-dimensions (Figure 1 a). Therefore, the single crystal is essentially a single giant grain in which the arrangement of molecules exhibits strict order[17]. The simplest repeating structural portion of a crystal lattice is called the **unit cell**. The angles (α, β, γ) and lengths (a, b, c) utilized to define the size and type of a unit cell, relative to an origin, are the **unit cell parameters** (the ‘lattice parameters’). The angle between *a* and *b* is referred as γ, that between *b* and *c* is α, and that between *a* and *c* is β (Figure 1 b)[18].

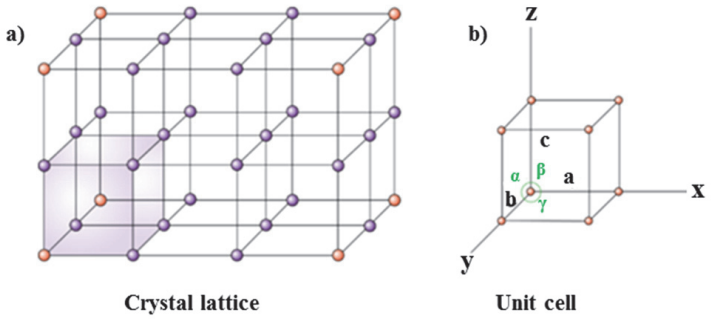

Figure 1. a) Crystal lattice representation. b) Unit cell representation[19].

The relationship between the unit cell parameters in three dimensions as a result of the symmetry of the structure gives rise to the seven **crystal systems**, some of which have more than one type of lattice[20]. There are six different lattices, primitive with only corner lattice points (P), base-centred (A, B, C, F) and body-centred (I) (Figure 2). By the combination of the seven crystal systems and the six numbers of different lattices, it would be possible to find 42 (6×7) different types of space lattices. But we actually only get 14 distinctly different lattices known as **Bravais lattices**, and not more, as for these are the only ways in which indistinguishable points can occur uniquely in three dimensions of space (Figure 2)[18].

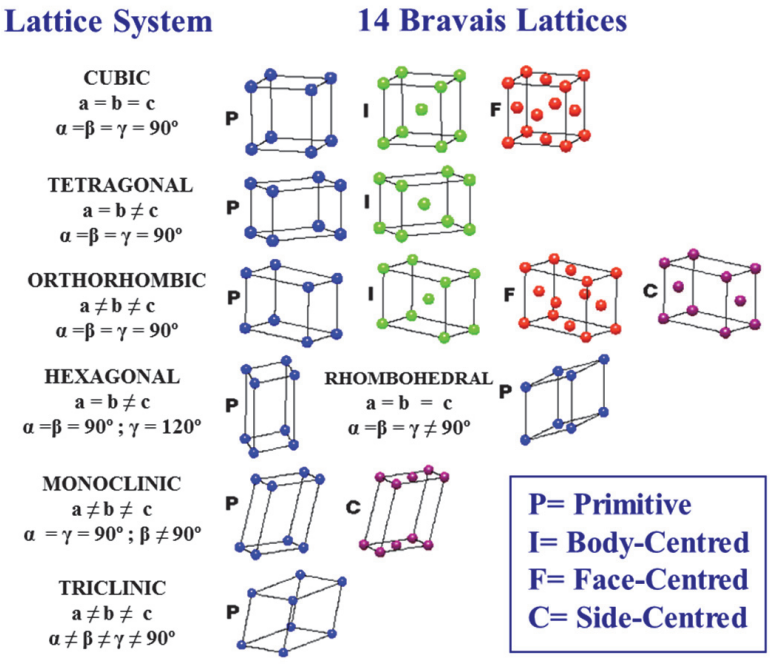

Figure 2. The lattice systems and the fourteen Bravais lattices representation.

To each crystal system there corresponds a certain minimum of symmetry elements, such as centre of symmetry, axes of symmetry and planes of symmetry[16]. The symmetry of a crystal is described by its space group. The space group is the set of geometrical symmetry operations that take a three-dimensional periodic

object (say a crystal) into itself[21]. In three dimensions there are 230 space groups, representing the different possible combinations of point group symmetry and translational symmetry[22].

Diffraction techniques, especially those using X-rays, are the most important methods available for the determination of the crystal structures. Used to locate the positions of atoms and ions forming a solid compound, these techniques provide a description of structures in terms of characteristics such as bond lengths, bond angles and positional atomic coordinates of ions and molecules in a unit cell. That is why it is important to obtain single crystals, since through the X-ray diffraction patterns obtained from them, it allows chemists to identify the structure of molecules and extended lattices and explain tendencies in many properties.

The lack of defects associated with grain boundaries can provide single crystals with unique properties, particularly mechanical, optical, (because light scattering is another common effect of grain boundaries and associated voids, and therefore single crystals are required in optical studies[23]) and electrical, which can also be anisotropic, depending on the type of crystallographic structure[24]. Various other physical properties such as piezoelectricity, pyroelectricity, ferroelectricity, and other optoelectronic properties were used for sensor and detector applications in single crystals[23]. Based on these properties, these single crystals can be used for important practical applications in technology. Some of these applications are shown in Table 1.

Table 1. Practical Applications of Single Crystals[23].

Material Class	Devices
Semiconductors	Electrical diodes, hall effect magnetometer, integrated circuits, infrared detectors, light-emitting diodes, photo diodes, photo conduction devices, radiation detectors, transistors, thyristors
Optical materials	Electro-optic devices, laser hosts, lenses, prisms, windows, x-Ray monochromators, magneto-optic devices, nonlinear optical devices, polarizers
Hard materials and materials for mechanical components	Abrasives and cutting tools, bearings, substrates for high Tc superconductors, strain gauges, cantilevers
Piezoelectric materials	Resonant bulk wave devices, surface wave devices, transducers
Magnetic materials	Microwave filters, tape heads
Pyroelectric materials	Pyroelectric devices
Gems	Jewelry

It is a fact that single crystals find important uses in research and development. Thus, crystal growth under controlled conditions has become a necessity. The growing knowledge and control of solid-state reactions as well as the synthesis of crystalline structures has allowed scientists to study, know and deepen their properties and atomic structure. In this thesis, a type of solid-state reactions called **single-crystal-to-single-crystal (SCSC)** has been studied, in order to produce changes in the physical properties of the crystal for the use of sensing devices and detectors, among others.

1.2. SINGLE-CRYSTAL-TO-SINGLE-CRYSTAL TRANSFORMATIONS (SCSC)

As mentioned above, with knowledge of the principles of crystal engineering[12], it is easier to design reactive solids and carry out solid-state reactions. Therefore, with the development of this crystal engineering, a special case of solid-state reactions, in which a single reactive crystal produces a product in the form of a single crystal, has attracted great attention. This type of conversion has been known for a long time as single-crystal-to-single-crystal reaction (SCSC)[25,26,27,28]. In the transformation process of the SCSC, the crystal is exposed to external stimuli such as solvent vapors, heat and light and pressure, producing structurally processed products (Figure 3)[8,29,30].

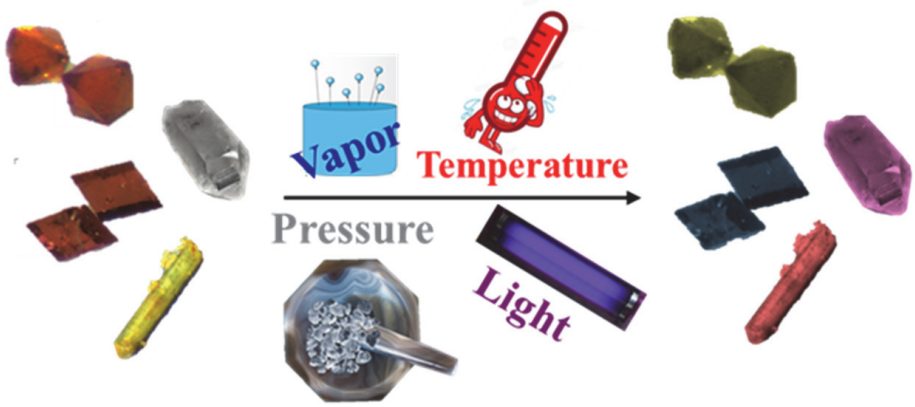

Figure 3. General schematic representation of SCSC transformation under different external stimuli.

In addition, the exposure of individual crystals to external forces generally results in the loss of crystallinity[31]. Due to damaged regions and imperfections produced by the crystal growth and post-synthetic treatment, the ideal crystal never exists[32]. Because of the shear forces and stress resulting from changes in components, the delicate single crystal has the tendency to increase mosaicist and

even break down into smaller fragments after the post-synthetic treatments (Figure 4)[33].

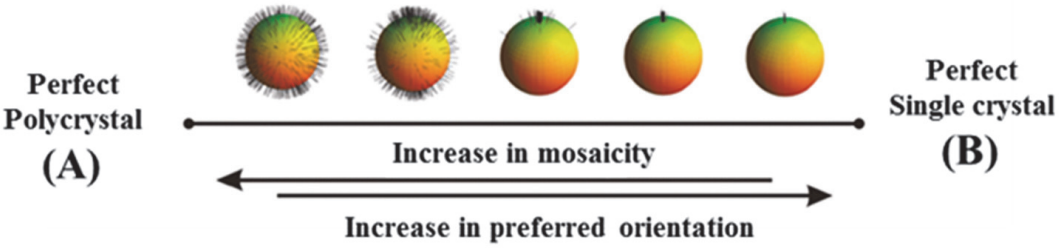

Figure 4. The distribution of orientations of coherently scattering domains could in principle determine the position of a sample between A (perfect polycrystal) and B (perfect single crystal). Each line coming out of the sphere represents a crystallographic axis (e.g. the c axis) of one coherently scattering domain. Lines originate in centers of respective spheres, which serve only to give an impression of three dimensionality. Reprinted with permission from ref 33. Copyright 2010 Crystal Growth & Design[33].

Therefore, a great difficulty to be taken into account in the SCSC transformation reactions in relation to the other solid-state reactions is the attempt to retain crystallinity after the reorganization of the atoms into solid-state. SCSC transformations can be obtained by X-ray diffraction analysis directly. Luckily, monocrystalline X-ray diffractometers are equipped with ever more sensitive detectors, so they are the principal method for determining structures unmistakably before and after these structural transformation and properties of these materials[34]. Hence, by means of single-crystal-to-single-crystal (SCSC) transformations, structural changes can be followed by X-ray diffraction more easily.

Such a direct insight furthers understanding of solid-state reaction mechanisms in a more visual and intuitive way. As well as directly visualizing the change in molecular structure during the transformation process, the SCSC transformation is fascinating because in some cases it leads to the formation of unusual products that otherwise could not be designed by routine synthetic routes[1,35]. Whereby it could be tried to achieve control of the molecular arrangement. When the crystal is exposed to external stimuli, SCSC transformations are accompanied by a change in physical properties such as magnetism, color, porosity, chirality, luminescence, as well as changes in, geometry, coordination number, dimensionality, etc[32,36,37,1,8]. These changes in the physical properties of the materials makes them a potential candidate for sensor technology[38,39].

It should also be taken into consideration that depending on the type of structural behaviour when applying the external stimuli, crystalline materials can be classified into three different groups: polymorphic compounds, dynamic materials and robust structures[40].

The first group of materials comprises compounds for which various transformable polymorphic forms are possible because of ordered transitions or moving atoms that break or modify the symmetry of crystals and network parameters. In dynamic materials, SCSC transitions include the division and/or formation of covalent or coordinated links, besides a reorganization of the network of intermolecular interactions which stabilize crystalline packaging, giving rise to notable changes in the general structural framework. Finally, the architecture of robust structures remains essentially intact throughout the entire transformation process of the SCSC, independent of any composition or functional variation that is driven, for example, by desorption/sorption of solvent molecules or by variations in the states of oxidation[40].

In this introduction, diverse examples of SCSC transformations reported in the literature will be described. These examples will be divided into the following sections based on the changes in properties and effects produced by different external stimuli. Thermally triggered SCSC transformations, light induced SCSC transformations, SCSC transformation induced by mechano-chemical forces and SCSC transformation induced by the inclusion of guest. Furthermore, examples discussed in this introduction all involve crystalline materials, which as mentioned in the previous paragraph, can be polymorphic compounds, dynamic materials and robust structures, within which including coordination compounds, porous and non-porous, and purely organic compounds.

1.3. THERMALLY TRIGGERED SCSC TRANSFORMATIONS

Temperature is one of the most common factors in determining the final topology of structures, and the removal of solvent molecules by heating represents one of the most straightforward methods for producing these various solid-state transformations[35]. When solvent host molecules are removed or exchanged with other solvents, the crystallinity are quite frequently retained. Some coordinating polymeric compounds often display such rigidity and robustness during solvent removal, behaving similarly to zeolites while retaining their monocrystalline nature[41,39,42]. An example is showed in the Figure 5, this material maintains unchanged the connectivity and geometry of the structure after dehydration, only very small structural changes are observed.

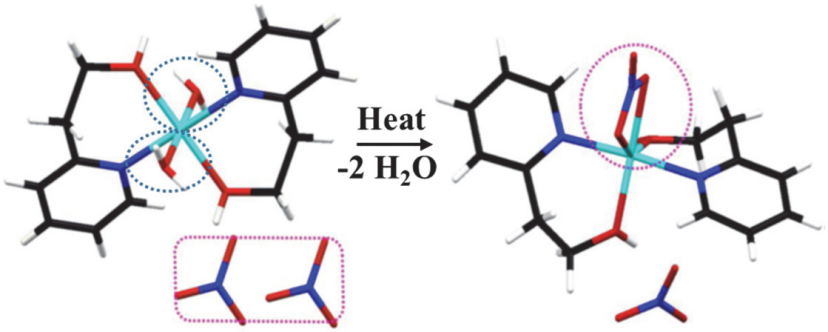

Figure 5. 0D to 0D structural thermal transformation. Reprinted with permission from ref 8. Copyright 2017 Crystal Growth & Design[8].

Conversely, in flexible and dynamic materials, the removal of coordinated solvents often drives structural reorganizations. Due to the evacuation effect that occurs during desolvation, parts of the molecule commence to move leading these structural rearrangements. This can happen in two ways. In the case of coordination compounds, if the coordination geometry surrounding the metal core changes but not the coordination number, structural transformation is triggered by the linking of the non-used donor atom(s) of the ligand or ligands already bonded closer to the metal core[43]. For example, the monodentate carboxylate ligands may use easily its unused oxygen atom for chelation, without changing the coordination number. In other situations, the empty coordination site generated by the loss of a coordinated solvent is occupied by the free or unused donor site(s) of another ligand or ligands of an adjacent polymer (such as halides may also bridge the metal for compensating this loss). These results give rise to a drastic movement of the molecular fragments that lead to structural transformation. This structural transformation is accompanied by a change of the entire structure, such as an increase or decrease in dimensionality, a distortion and sliding of network structures, change in conformation, breakage or generation of new bonds of the framework, in the coordination environment or space groups and polymerization[44,45,46,47,48,49].

However, a change in the whole structure can be produced sometimes without the participation of solvent vapor as a direct result of temperature variation[35]. The transformations of the SCSC that are occurring in this way are simply triggered by temperature increases or decreases. These changes can be in dimensionality, in polymerization and depolymerization involving the rupture and formation of new bonds and the lattice movement[50,51,52,53,54]. This is also characteristic of polymorphic compounds[55,56]. Figure 6 shows an example of polymorphic compound reported by Sheng-Qun Su et al[56], that exhibits thermally induced, abrupt crystal deformation through cooperative interaction in the crystal and reversible macroscopic shrinkage and expansion.

It has also been found in these materials described above, that solvent removal during SCSC conversion is accompanied by a change in their properties:

magnetism[57,50], thermal shrinkage or expansion[58], optical (change in color)[42,52] and luminescent properties[59], so these materials can be applied in many applications.

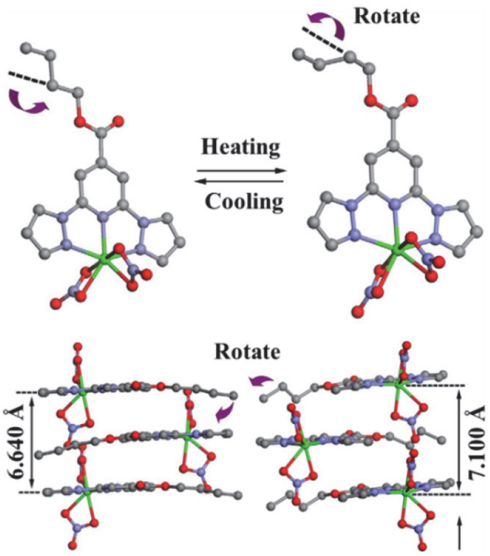

Figure 6. A reversible crystal deformation at a structural phase transition temperature. Reprinted with permission from ref 56. Copyright 2015 Nature Communication[56].

1.4. LIGHT-INDUCED SCSC TRANSFORMATIONS

When a single crystal is exposed to light, the observed solid-state structural changes are known as photoinduced SCSC transformation. Over the last decade, since the seminal work of Schmidt[9], UV irradiation-induced reactions have intrigued the attention of many chemists, because without the requirement for other environmental conditions, they provide an unparalleled approach to accomplish molecular reorganization or transformation. SCSC transformations and topochemical reactions have been widely investigated in organic chemistry[60,61]. Transformations from one coordination polymeric structure to another are relatively uncommon in solid-state supramolecular reactions, compared to solid-state photochemical reactions that involve two molecules, because breakage and bonding must occur in more than one direction simultaneously[35,62]. It provides a powerful way to synthesize novel materials that are impossible to obtain through conventional synthetic routes.

In the vast majority of cases, the SCSC photoinduced transformation is accompanied by [2 + 2] cycloaddition whereby two reactive centers are aligned parallel to each other and separated by less than 4.2 Å (Schmidt's alignment criterion for the solid-state reaction)[7,8]. 1,2-Bis(4′-pyridyl) ethylene, also known popularly as bpe, has been extensively used in this type of reactions[35,63], and in the last few years, other asymmetric ligands containing alkenyl groups have been

studied[64]. While the geometrical criteria for such topochemical dimerization are well established, it has been a challenge to organize the two double bonds in the solid state.

As previously mentioned, following Schmidt's topochemical criteria for cycloaddition photochemical transformations, the distance amid the two bonds must not surpass 4.2 Å. The transformations that take place in a coordination polymer must also respect this distance. Another critical factor is the correct orientation of the C=C bonds. In rigid crystal structures can be found reactive C=C bonds where the ligands pairs with are parallels aligned at fairly close distance, thus producing photochemical transformations without changes in dimensionality[62,65,66,67].

On the other side, in dynamic compounds, increased movement and rotation of ions and ligands always accompany this type of reaction. In addition, this rearrangement and shrinkage always leads to an increase in the dimensionality of the structure.

In some examples, the ligands are in parallel stacking mode[68,69,70] and in the case of higher dimensional structures, the ligand pairs are in orientation with various chains or layers, showing a head-to-tail fashion (Figure 7)[71,72,73,74]. The last two gives rise to an increase in the dimensionality. In all the case mentioned, the C=C are in the range of [3.5-3.9] Å.

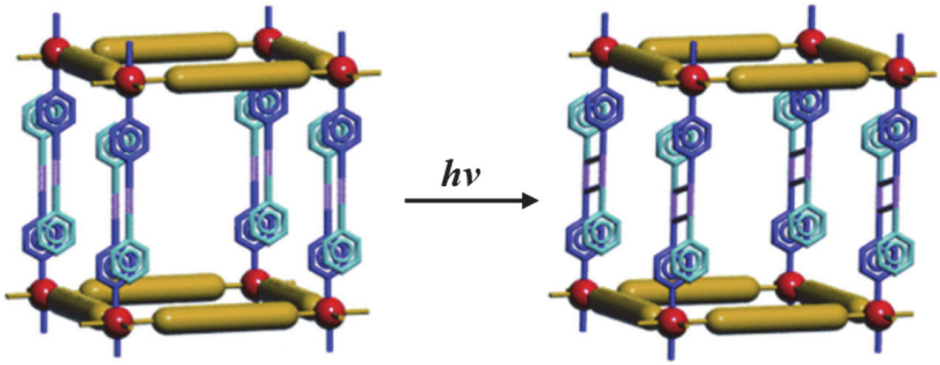

Figure 7. Schematically diagram of the transformation of 2D interdigitated layer to 3D structure by photodimerization [2+2]. Reprinted with permission from ref 35. Copyright 2018 Inorganic Chemistry Frontiers[35].

In addition, there are certain interactions, which can help to align these double bonds in parallel and satisfying the Schmidt geometric criteria for photo reactivity. For example, MacGillivray et al[75] achieved remarkable success in aligning double bonds across a number of small organic molecules as well as Jagadese J. Vittal et al[76] in a lead complex, by utilizing the directionality and strength of hydrogen bonds. In another work reported by Jagadese J. Vittal[77], the one dimensional chains of the cadmium complex are aligned parallel owing to hydrogen interactions but the water molecule coordinated with the acetate ions did not allow cooperative

molecular movements which did not result in a 100% photodimerization, only a 33%. In this case, 100% photodimerization was due to the thermal dehydration of the compound that caused a structural rearrangement between adjacent ligands arranged crosswise to form a staircase structure, which led to parallel orientation with appropriate distance satisfying Schmidt's criteria.

This example has unexpected photochemical behavior, but it could be a new strategy to produce these kinds of photochemical transformations.

Light induced SCSC transformations assisted by π···π contacts have also been reported[78,79], where the alignments of the ligands are reinforced due to a significant face-to-face π···π interactions.

In another example, MacGillivray et al[64] has utilized the argentophilic forces to stack the olefins double bonds of the complex. In this case the Ag···Ag interactions played a key role to produce the photo-dimerization (Figure 8).

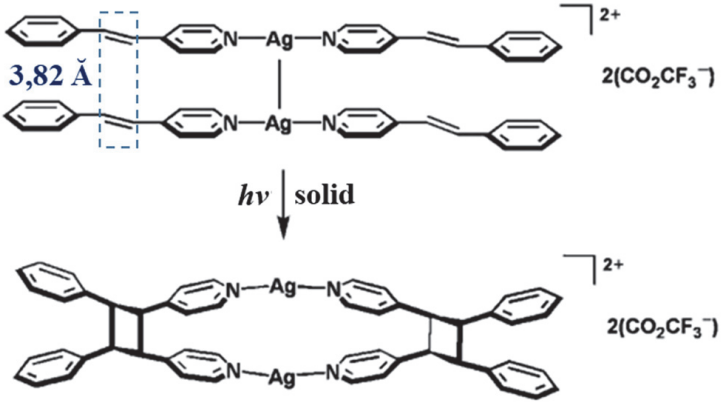

Figure 8. Photoinduced SCSC transformation where Ag···Ag interactions played a key role. Reprinted with permission from ref 64. Copyright 2005 Angewandte Chemie International Edition[64].

During the photochemical reactions, the structural changes in these materials are also similar to those observed in the thermal methods, which include change of coordination number and geometry around a metallic center, change in connectivity, dimensionality, and interpenetration. When there is no change in dimensionality, there is only the formation of new bonds. Metal complexes have been used successfully for polymerization and oligomerization of acetylenes and olefins[62,36,80]. These variations are accompanied by changes in physical and chemical properties such a change in color[81], conductivity[70], luminiscence[80,67,68], among others.

1.5. SCSC TRANSFORMATION INDUCED BY MECHANOCHEMICAL FORCES

Pressure is another external stimulus that can be applied in this type of transformation. Mechanical-chemical grinding is one of the most commonly used forms to apply mechanical force and is extensively employed in the synthesis of many organic, organometallic, inorganic, and metal-organic hybrid materials.

This section is divided into two points. Firstly, in examples where complete mechanical-chemical grinding is applied, and secondly, where only partial mechanical force is employed.

1.5.1. Mechano-chemical grinding

The transformations induced by complete mechanical-chemical milling cannot normally be directly investigated by single crystal X-ray diffraction. Nonetheless, the crystalline form is maintained at the microcrystalline scale, with larger crystals merely decomposing into smaller crystals. In such situations, the structures could be determined from PXRD diffraction data in most cases. For that purpose, the PXRD patterns of the bulk sample are matched with those simulated from the monocrystalline data obtained by other routes, and the directly acquired structural analysis using PXRD diffraction data is also widely carried out[35].

Applying mechanical forces generates several types of structural transformations as a result of the loss or absorption of solvents[82], where is produced a structural rearrangement and pedal-like motion of molecular fragments. In addition, milling can assist in the more efficient performance of solid-state reactions, including photodimerization reactions because milling increases the reaction activity by facilitating the movement of molecules to align in parallel mode, as required for photodimerization reactions. In fact, in the research work published by Vittal et al.[83] in 2008 about a Zinc coordination complex, it was observed that applying UV irradiation only produced a 46% photochemical conversion. Conversely, when a mechanical force was implemented, its yield increased up to 88%. This enhance is because grinding increases the surface area, which leads to a considerable improvement in reactivity when a higher surface area is exposed to UV radiation. Not only an increase of the surface is produced, but also milling speeds the motion-pedals of the olefin to a parallel alignment resulting in better interactions between active sites to reach a greater reaction velocity and conversion.

In addition, it has been observed that by applying these mechanical forces it is possible to produce the dimerization of compounds. The first dimerization of a metal complex through a mechanic-chemical reaction was reported by Sun el al.[84], which was accompanied by a color change (Figure 9).

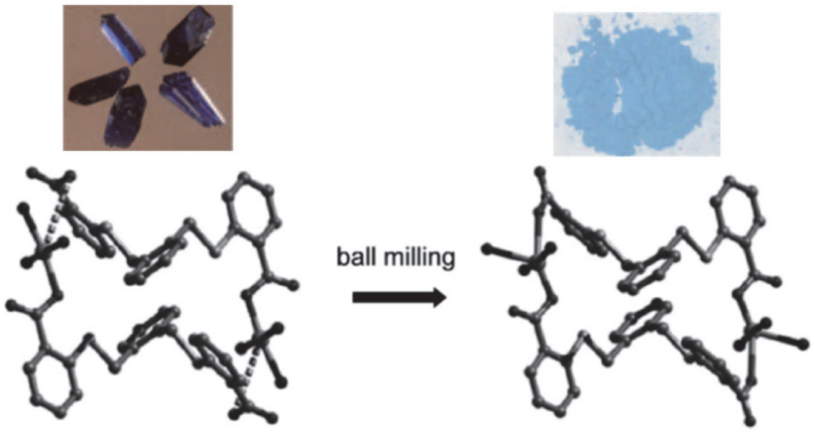

Figure 9. Solid-state transformation under grinding[84].

As several movements of atoms occur at the micro level, it can lead to drastic changes in the structure, such as when ligand replacement reactions are carried out. Some examples that perfectly illustrate these major structural changes are those published by Vittal et al.[62,85]. In these research works, the acetate and trifluoroacetate ligands in the two 1-D CPs can easily be replaced by bromide ions during mechanochemical grinding with KBr, producing, in one of them, the transformation of a 1-D ladder to 1-D zig zag chain and in the other one, the transformation from 1D to 2D sheet-like (Figure 10). This substitution results in major structural changes.

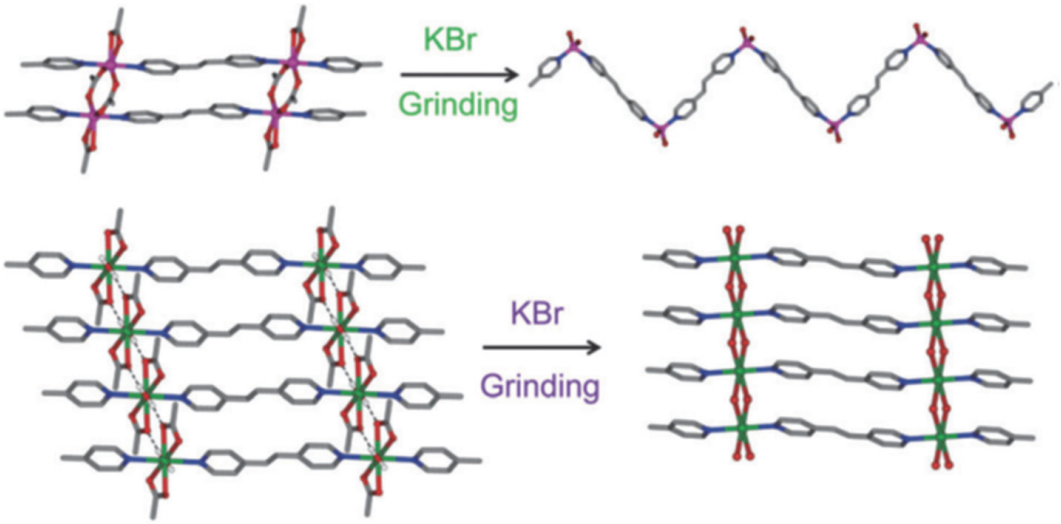

Figure 10. Structural transformation involving 1-D ladder CP to 1-D zig zag and 1-D linear to 2-D sheet-like upon grinding with KBr. Reprinted with permission from ref 1. Copyright 2013 Chemical Society Review[1].

Likewise, it has been proven that the reversible transformation by ion exchange of the thiocyanate bridge ligand by the bromide ion is responsible for the structural

transformation of a three-dimensional Pb(II) to another three-dimensional Pb(II), in this case with milder structural changes[86].

During the mechanic-chemical reactions, the structural transformations include change in dimensionality, in the coordination geometry of the metal, structural rearrangement and exchange of coordinated ions, these transformations lead to changes in the color [84,85] and texture[85] of the material upon grinding.

In all the above-mentioned cases, the structures have been determined by PXRD diffraction, since they have been contrasted with the simulated patterns spectra of the crystalline structures obtained by other routes.

1.5.2. Partial mechanical force

Anisotropic forces in bulk usually crack the integrity of a single crystal. For this reason, crystals resulting from mechanical solid-state transformations are still too small to be determined by single crystal X-ray diffraction. Nevertheless, if small pits on the surface of the crystal cause the structural transformation by needle prick, the integrity of the single crystal can be preserved completely. This phenomenon has been found in some supramolecular crystal coordination cases[35].

In 2003, the first partial mechanical induced SCSC transformation example in molecular crystals was reported by Ito el al.[87]. In this publication, they displayed that a small mechanical stimulus by milling or using a needle can lead to a SCSC transformation of an isolated polymorph of gold. In the second case, using a needle, the crystalline structure is maintained and the phase transition occurred first in the initial contact and then spontaneously progressed through the entire crystal, so this phase-change can be monitored by single crystal X-ray diffraction. Moreover, this change of phase was accompanied by structural changes including intermolecular interactions and a drastic photo luminescent color change caused by the switching of the intermolecular interactions (Figure 11). Ito and co-workers have also been published a similar SCSC phase transition in a gold complex induced by mechanical force in the same year[88].

One year later, another interesting example in which the needle pricking technique is applied was published by Tao el al.[89]. They reported a new polymorph of copper (II) which after being submitted to mechanical stimulation; it is transformed into another polymorph accompanied by remarkable crystal dimension changes, doubling its length and halving its thickness, without crystal breakage (Figure 12).

By observing the structural and property changes, these materials could be used in applications such as sensors or in molecular mechanical actuators.

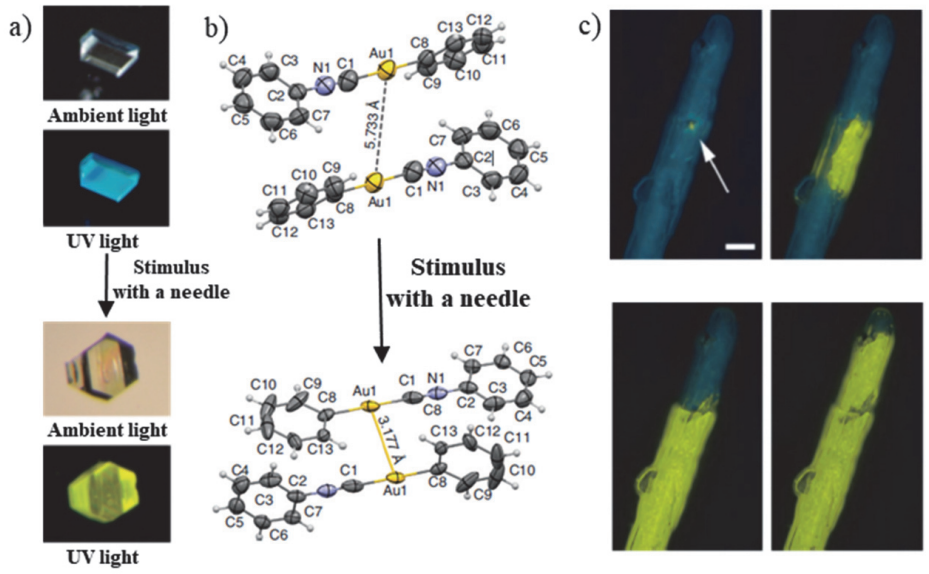

Figure 11. a) SCSC crystalline transformation of polymorphs under mechanical stimulus in ambient and ultraviolet (UV, 365 nm) light. b) SCSC transformation of polymorphs and formation of a new interaction. c) Mechanical stimulus-triggered phase transformation (scale bar, 200 mm). A small pit (left, white arrow) was first produced by pricking the fixed sample with a needle. The phase transformation gradually spread over the entire crystal after 9 h. Reprinted with permission from ref 87. Copyright 2013 Nature Communications[87].

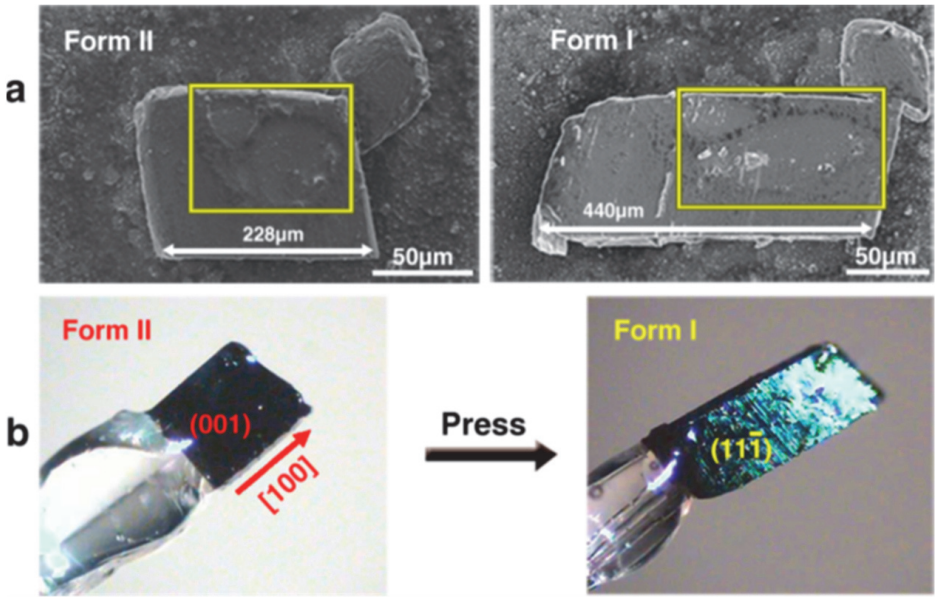

Figure 12. a) Scanning electron microscopy images of the crystal before and after phase transition. b) Face-indexing graphics of the same piece of crystal before and after the phase transition. Reprinted with permission from ref 35. Copyright 2018 Inorganic Chemistry Frontiers[35].

1.6. SCSC TRANSFORMATION INDUCED BY LOSS/UPTAKE OF SOLVENT VAPOR

SCSC transformations of coordination polymers are mainly caused by desorption, sorption or exchange of solvent molecules[90,91]. Generally, the solvent molecules employed in synthesis perform as a template in the crystals of as-synthesized materials to stabilize the structure. In porous materials, these molecules can be hosted in the cavities that contain these materials. On the other hand, in non-porous materials, a reorganization is produced in its internal network to be able to accommodate them.

There are three different processes involved when host molecules are evacuated from the as-synthetized crystal. One is that the coordination network may irreversibly collapse into a non-porous structure. The second process that can occur is that it may also persist unchanged. And the last one is that it can be transformed into a new structure that can reversibly desorption/sorption some types of host species[34].

Depending on the role of solvent molecule and the strength of the interaction, more drastic or partial changes in the structure can take place.

If the guest molecules are found in the channels, such as free solvent molecules, guest ligand molecules, guest metal ions, among others, these guest molecules have no strong coordination interaction with the framework. In contrast, some solvent molecules may even coordinate with metal ions or with a ligand group to form part of the host structure. In this case, the interactions are strong. The changes produced, particularly, by the elimination of lattice solvents and coordinated molecules of solvents; result in a significant structural transformation, such as polymerization, an increase or decrease in dimensionality or coordination number, among others. In fact, some processes of desolvation can trigger a part of the molecule to start moving, due to the evacuation effect, producing the breakage and formation of covalent bonds and therefore the rearrangement of the whole structure and the increase in dimensionality. The removal or exchange of these molecules can also be accomplished by heating, as discussed in the previous section 1.2.1, or via molecules exchange, in both cases. The following sections describe the principal changes resulting from desorption, sorption or exchange of solvent molecules that are coordinated in the structure or found in the crystal lattice in both porous and non-porous materials.

1.6.1. Transformation induced by coordinated solvent molecule in porous materials

Typically, the ligand donor atoms and metal ions contain a limited number of favored geometries and coordination numbers. In the majority of cases, the

maximum number of coordination and the appropriated geometry of a metal ion is steadier than the lower ones. However, there are some exceptions such as Cu (II) ions (octahedral and square planar). When a donor atom quits the metal ion, a donor from an external sphere will attempt to reach the vacant coordination site to preserve the initial coordination number and geometry, generating to a new connectivity of the structure[34].

Some of these changes results in an increase or decrease in the dimensionality and reorganization of the network. For example, Kitagawa al. reported a series of reversible topochemical transformations with dimensional changes (2D to 3D) caused by removal/addition of coordinated solvent molecules[92,93,94]. One of the three examples[92] presents a 2D compound in which by heating it at 80 degrees, all the coordinated water molecules in the complex are removed, giving a 3D framework. Two carboxylate oxygen atoms from another layer occupy these two vacant sites generated by removal of the coordinated water molecules, therefore some coordination bonds were broken and were reformed with these groups. The dehydrated compound can selectively adsorb H_2O vapor molecules to transform back the initial compound. Because lanthanides are coordinated in large quantities and ligands are so flexible, it is thought that this may provide structural freedom to facilitate such a significant structural transformation.

In addition, higher dimensional structures can be produced that lead to condensation by dehydration with temperature and also to a progressive increase in dimensionality by using the same mechanism applied in the above case, heating and dehydration/hydration[95] (Figure 13).

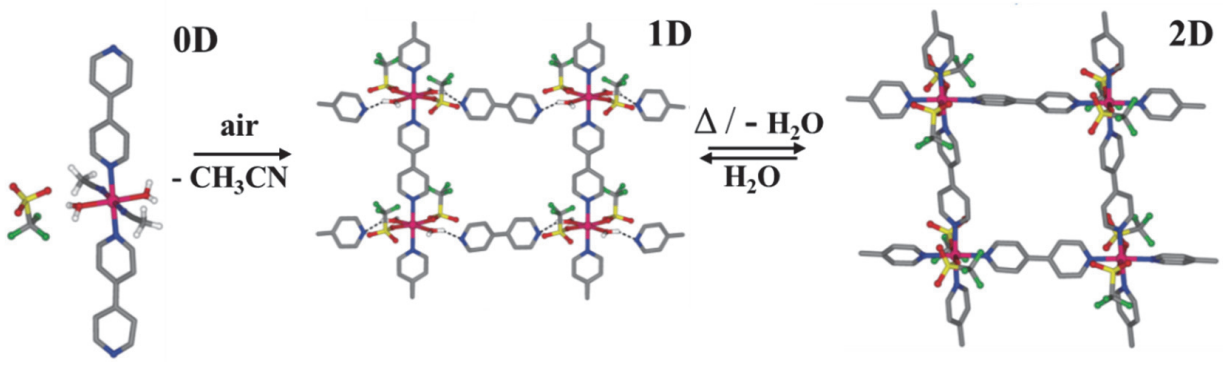

Figure 13. 0D to 1D to 2D structural transformation. Reprinted with permission from ref 1. Copyright 2013 Chemical Society Review[1].

Also, the chirality[96] and dimensionality of host structures can be disturbed by the exchange of solvents at the coordination sites[97]. This last example is distinctive by way of the 2D to 3D structural transformation increased the surface area, from 177 m^2g^{-1} to 1170 m^2g^{-1}, improving the porosity and sorption capacity.

The interpenetration number of the coordination polymers can be also changed when the removal/addition of coordinated solvent molecules occurs[38].

Apart from the distortion of the entire coordination framework, the change of coordinated solvent molecules can lead to highly important structural transformations around the coordination center[98] or both transformations take place (drastic transformation in the whole framework and changes around the coordination center)[99,100]. Moreover, in other examples, the host structure distortions and/or in the crystalline network may be negligible and even apparently ignorable[101]. Xiao-Ming Chen reported two examples[102,103] in which there was a change in its coordination geometry due to the removal of the solvent molecules, but without noticeable crystal lattice (Figure 14).

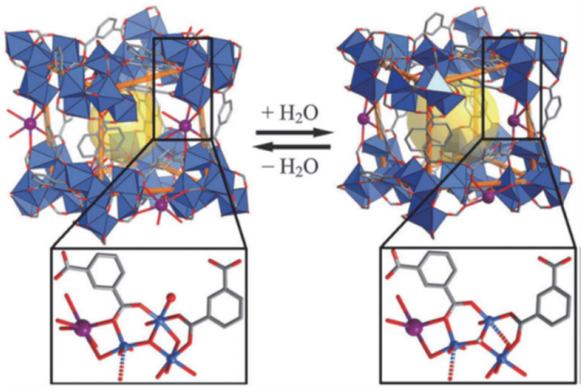

Figure 14. Interconversion between $[KCo_7(OH)_3(ipa)_6(H_2O)_4].12H_2O$ and $[KCo_7(OH)_3(ipa)_6]$ induced by removal and restoration of coordinated H_2O molecules. Hydrogen atoms are omitted for clarity. Reprinted with permission from ref 34. Copyright 2014 Chemical Society Reviews[34].

In addition, in these robust materials, it can be produced without a loss of structural integrity and change in its coordination geometry, guest solvent exchange by other coordination ligands and even the ability to modify the metal[104]. The robustness of a porous coordination network is an important factor because it can be applied in industry in separations and catalysis.

These are the principal transformation that can be generated by the remove/exchange of coordinated solvent molecule in porous materials. In the vast majority of this kind of transformations are involved in breaking and forming new bonds and the procedure of hydration or exchange of solvent can be produced by vapor diffusion (solvent vapor) or solvent immersion/soaking process (immerse the crystals in a solvent).

These transformations are accompanied by remarkable changes in their properties such as morphology[38], size[38], optical[93,95,38,97,98,102,103,99,100] and magnetic[93,94,102] properties.

1.6.2. Transformation induced by lattice solvent molecule in porous materials

In many porous structures, there is a wide variety of molecules in the channels. Solvent molecules of lattice interact with hostile structure via hydrogen bonding, π-π stacking and other weak interactions. The removal/adsorption of solvent molecules in the network barely undergoes change in the topology or connectivity of the coordination network[34].

As well as in the previous section, there have also been observed alterations in the interpenetration number[105,106]. Xiao-Ming Chen et al[44] reported an example in which revealed not only a drastic distortion and shrinkage of the network, but also a rearrangement from five- to six-fold interpenetration.

In some cases are observed that depending on the route used can lead to different types of SCSC transformations, by removing lattice solvent molecules[107]. The robust single crystals of as-synthesized $[Cu(iba)_2].2H_2O$ (Hiba = 4-(1H-imidazol-1-yl) benzoic acid)[108] showed a 3D network and contained waters molecules in its channels. This complex can be dehydrated in two ways, forming two isomeric coordination frameworks with cavities: in one of them is retained the original topology (the crystal was heated at 160 ºC for 12 h) and the other one is transformed in 2D network (the crystal is exposed in air at room temperature for two months (Figure 15). Therefore, kinetic or thermodynamic processes control the different routes. This example is very characteristic because depending on the route its behavior is both robust (maintain the structure) and very flexible (drastic changes in the structure as well as changes in dimensionality[109]). There are also examples where the structural integrity of a coordinating polymeric structure is also retained after complete desolvation and exchange the solvent molecules with other vapor solvents or sorption of the same solvent, confirming the analogy with the suggested zeolites[110,111].

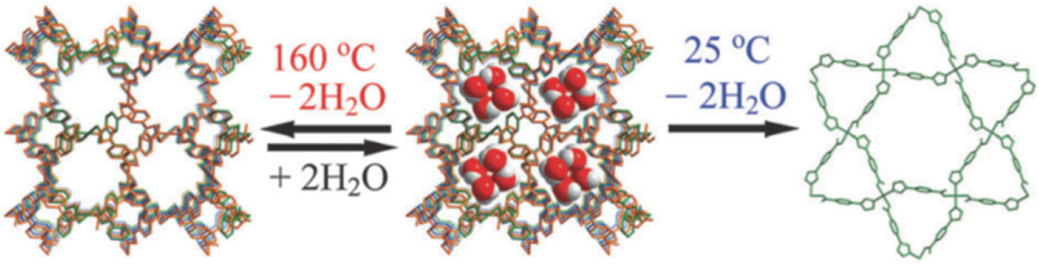

Figure 15. Conversion of 3D $[Cu(iba)_2].2H_2O$ to $[Cu(iba)_2]$ isomers either with the original topology or a 2D topology induced by removing lattice H_2O molecules at different temperatures. Reprinted with permission from ref 34. Copyright 2014 Chemical Society Reviews[34].

In other cases, important changes may be produced in the local connectivity of the building blocks and in the coordination geometry due to the alteration of the

solvent molecules in the crystalline network[112]. In this example, the coordination environment of the metal centers changed from square pyramidal to tetrahedral and the conventional paddle-wheel cluster converted to an open configuration, though the whole complex topology was unchanged, giving rise to the adsorption of a few gas molecules.

The adsorption/desorption of the network solvent in the majority of flexible porous materials just disrupts the host structure. Although there is no breakage/formation of new bonds, the structural transformation can still be very significant due to the flexibility of the network created not only by the multi-variable coordination geometries of metal ions, but also by the dynamic metal-ligand bonds and supramolecular packing. These materials can display diverse types of distortions depending on the topology of the coordination framework and the flexibility mode of the network[34].

A type of distortion that has been observed in this kind of compounds is the breathing behavior, structural transition from large pore to narrow pore or vice versa. Several groups have developed a highly breathable family of frameworks in which part of this process, framework distortion degree (flexibility/rigidity and breathing amplitude), can be controlled by lattice solvent molecules[113,114,115,116,117]. The Figure 16 showed two sequential SCSC transformations involving the shrinkage of the structure by releasing the solvent molecules in the network.

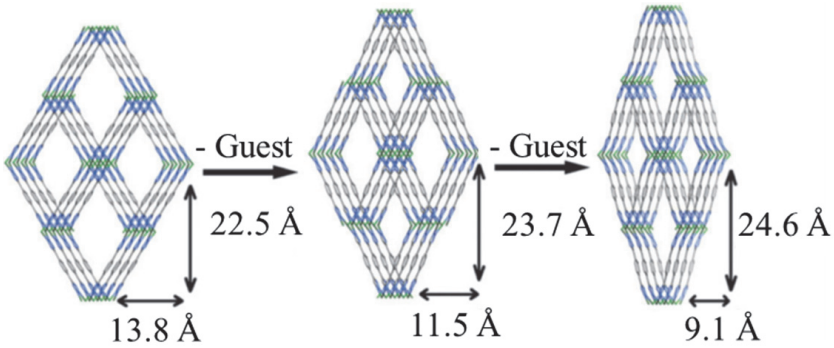

Figure 16. Multi-step SCSC distortion induced by removal of guest molecules. Coordinated and lattice solvent molecules, as well as framework hydrogen atoms are omitted for clarity Reprinted with permission from ref 34. Copyright 2014 Chemical Society Reviews[34].

Besides breathing behavior and distortion of the coordination framework, sliding between interpenetrated layers or packed coordination networks unleashed by guest exchange, dehydration and sorption, can likewise to disturb the porous material. In some examples it has been observed that this kind of distortions can produce the variation of the packing mode[118,119], expansion in the unit cell and channel size[120,91]. Moreover, cases that are even more special can involve an increase in volume (15 times regarding guest-free phase), a change in the spatial group and symmetry and

redistribution of the pores in the network (simultaneous shrinkage and expansion of pores in different degrees) during the adsorption/desorption of guests[121].

Numerous changes can take place in these materials due to the effect of the solvent molecules. But not only structural changes occur but also changes in chemical-physical properties such as conductivity[109], color[107,113,119], luminiscence[114,119], magnetic[115,111] that can be used in several application as gas adsorbents and separation[107,112,113,114,116], chemical sensors, among others.

1.6.3. Transformation induced by solvent molecule in non-porous materials

Fascinatingly, in non-porous solids, loss/uptake or exchange of guest is also possible, when it happens by diffusion through the crystal lattice, involving either breakage/formation of metal-ligand bonds or other rearrangement (e.g. conformational) to accommodate the guest. Achieving the diffusion of gaseous guest species in a reversible way without collapsing and preserving its crystallinity in a non-porous material, is a great challenge. The following are some examples of the two mechanisms involved (breakage/formation of metal-ligand bonds or other rearrangement) in the loss/uptake or exchange of guest process.

Reversible reactions in molecular crystals in which metal-ligand coordination bonds are broken or formed are uncommon, mainly in cases in which crystallinity is preserved. The uptake of guest molecules in the vapor phase into non-porous crystals is also unusual. The study published by Lee Brammer et al.[122] describes a silver coordinating polymer, $[Ag_4(tmp)_3\{O_2C(CF_2)_3CF_3\}_4(EtOH)_2]_n$, that notably displays these two unusual features. By heating the silver compound, the coordinated ethanol molecule is released, giving rise to the conversion of the $\{Ag_2(O_2CR)_2(EtOH)\}$ unit into the simple silver carboxylate dimer $\{Ag_2(O_2CR)_2\}$ which is accompanied with a color change. As a result of this SCSC transformation, the brakage of (Ag-O(H)Et) and ($EtOH\cdots O_{carboxylate}$) bonds and the formation of new covalent bonds ($Ag\text{-}O_{carboxylate}$) is produced (Figure 17).

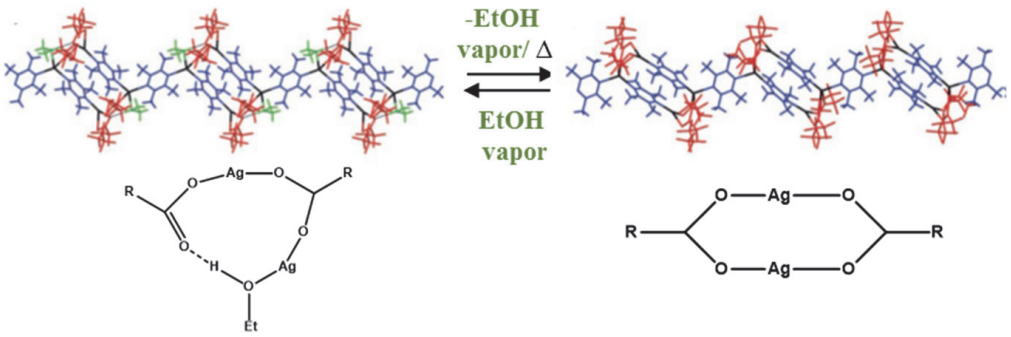

Figure 17. Reversible Single-crystal-to-single-crystal reaction involving loss and uptake of coordinated ethanol. Reprinted with permission from ref 122. Copyright 2008 Angewandte Chemie International Edition[122].

Other example was reported by Samar K. Das reported in 2007[123]. In which, a trinuclear iron compound is exposed to methanol vapors leading to the formation of new covalent bonds of Fe-O(H)Me and the rupture of the bonds of Fe-OH_2, in other words, the exchange of coordinated water molecule by methanol vapor at room temperature, with no loss of crystallinity (Figure 18) . This SCSC transformation is reversible when the new generate compound is exposed to water vapor molecules. The color of the crystals remained the same in this SCSC process.

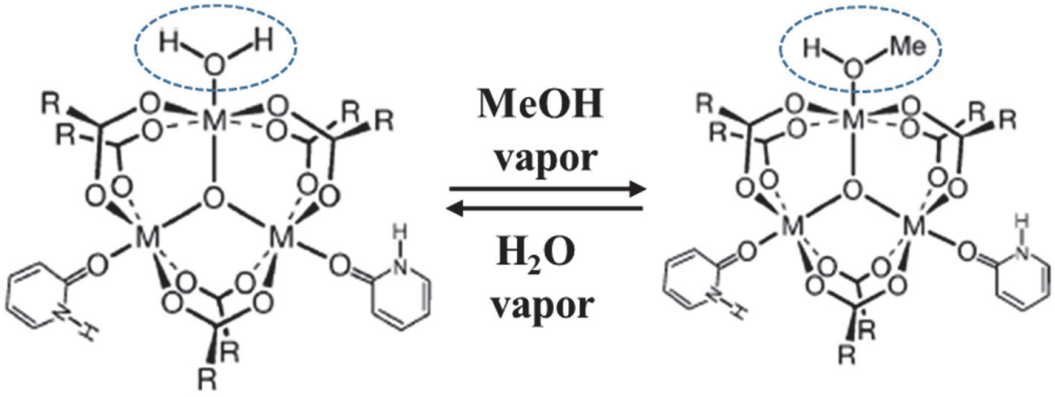

Figure 18. Reversible SCSC transformation through Fe-O(H)Me bond formation and Fe-OH_2 bond breaking (and vice versa) in a gas-solid reaction. Reprinted with permission from ref 123. Copyright 2007 Journal of the American Chemical Society[123].

Moreover, when the starting material were exposed to other alcohols, for example, ethanol, 1-propanol, 2-propanol, 1-butanol, etc., the crystals remained unreacted with them. Therefore, this material was selective for capturing methanol molecules.

In other cases, there are compounds that can be susceptible to different molecules and the guest exchange and structural transformations can be followed by the color change. Sally Brooker et al.[124] developed a new material in which not only new metal-ligand bonds were broken and formed, but also the compound was reorganized to accommodate the guest. In this material, it is possible to exchange coordinated acetonitrile molecules (breakage/formation of metal-ligand bonds) by ethanol (compound 2) and water (compound 3) vapor molecules, producing also ordered transient forms (1 TF3 and 2 THF3) (Figure 19). The transient forms contain solvents in the lattice, thus in order to exchange these molecules, there needs to be a reorganization in the structure. Non-porous materials capable of incorporating molecules through reorganization of the internal network are also extremely unusual, as their structural integrity does not usually withstand guest exchange reactions. In this case, this reorganization is achieved through the rotation of the ligands, thus facilitating the diffusion of the guest. In addition to the color changes, there are also shifts in magnetism and remarkably, a drastic transformation

between structure 1 and 3, which convert what was a discrete dinuclear complex into a polymer, respectively.

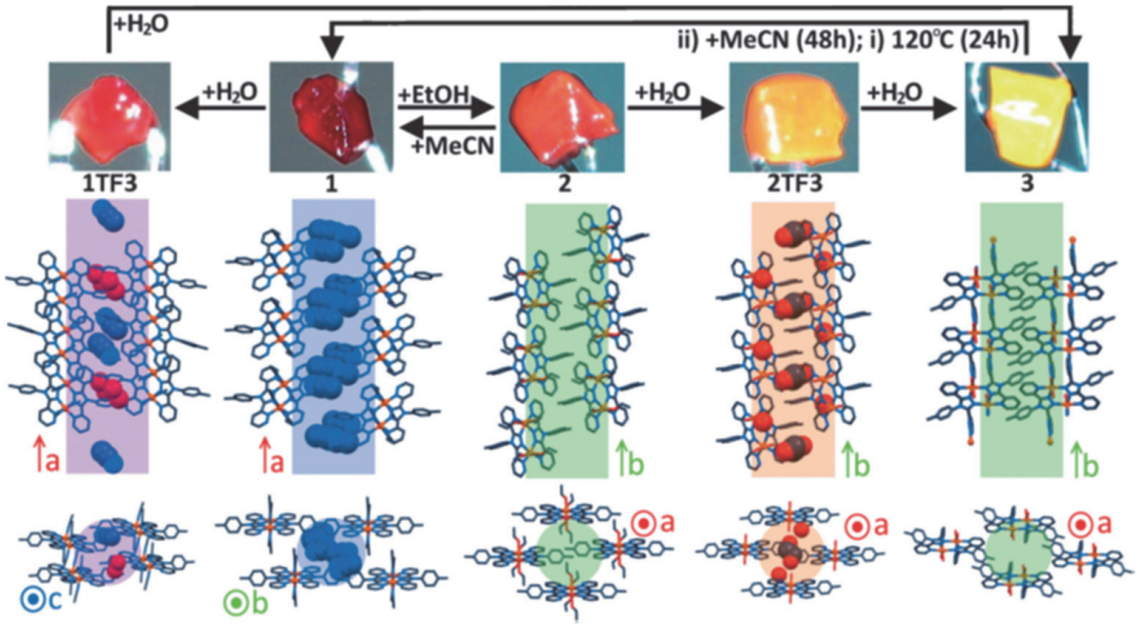

Figure 19. Summary of the observed cycle of transformations of 1. $[Fe_2(L)_2(MeCN)_4](BF_4)_4 \cdot 2MeCN$(1),$[Fe_2(L)_2(MeCN)_4](BF_4)_4 \cdot 0.5MeCN \cdot 0.5 H_2O$(1TF3),$[Fe_2(L)_2(EtOH)_4](BF_4)_4$(2),$[Fe_2(L)_2(H_2O)_4](BF_4)_4 \cdot 2H_2O \cdot 0.5EtOH$ (2TF3), and polymeric $\{[Fe(II)_2(L)_2(H_2O)_4](BF_4)_4\}_\infty$ (3). Reprinted with permission from ref 124. Copyright 2016 Angewandte Chemie[124].

Costa et al. also reported two clear example of internal lattice reorganization in order to incorporate or released[125,126] guest lattice molecules in non-porous complexes. In the first example, the iron complex, $[Fe(bpp)(H_2L)](ClO_4)_2 \cdot 1.5 C_3H_6O$, displayed two reversible SCSC transformation accompanied by drastic changes in color, magnetic and structural (symmetry, distances) properties. One of this transformation was desorption (by temperature) and absorption (by the exposure of the compound to acetone vapor) of a half molecule of acetone, and the other the exchange of small molecules, acetone by methanol and water and vice versa (Figure 20). As in the previous example, the second transformation was produced by the reorganization of the structure. Again, this reorganization is due to the flexibility of the ligands that, through their rotation, allow the incorporation of the molecules into the lattice.

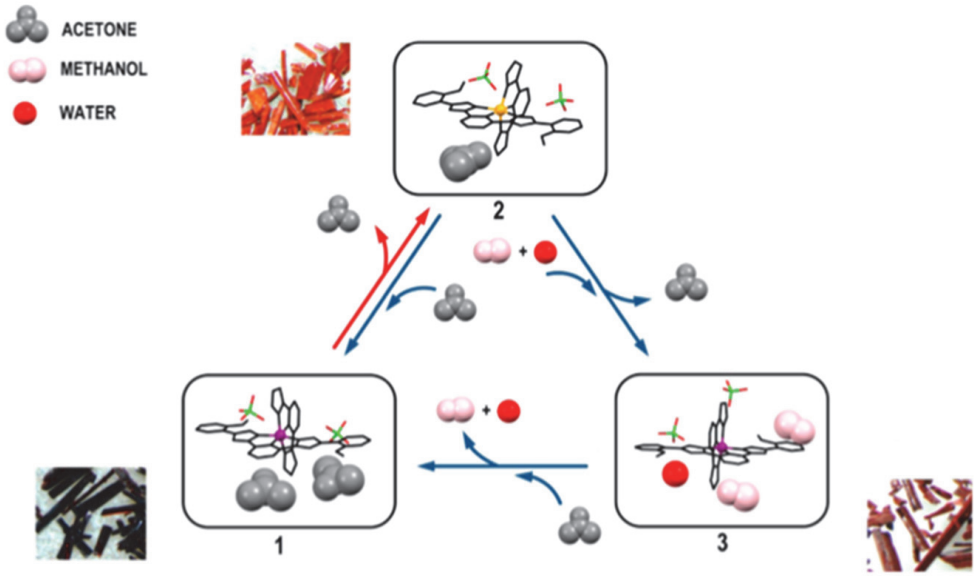

Figure 20. Reversible SCSC transformation through subsequent absorption, desorption, or exchange of small molecules. Reprinted with permission from ref 125. Copyright 2013 Journal of the American Chemical Society[125].

In the second example, the $\{[Fe(H_2O)_2(CH_3CN)_2(pyrazine)](BF_4)_2 \cdot (CH_3CN)_2\}_n$ complex[126], exhibited a reversible SCSC transformation due to the release (when the temperature increased) and sorption of lattice acetonitrile molecule from the crystal, resulting in drastic changes in color and a sharp magneto-structural transition (Figure 21).

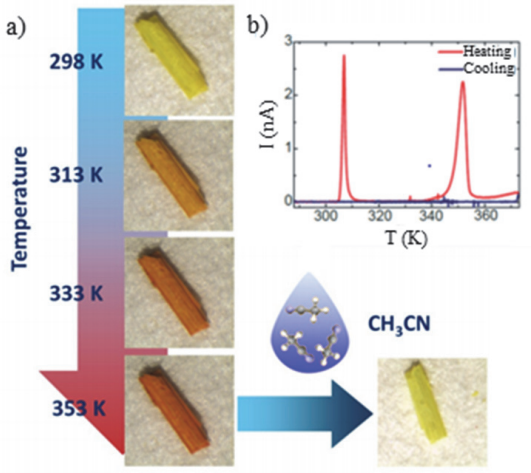

Figure 21. a) Color variation of the crystal under increasing temperature. The color is recovered after a drop of acetonitrile is added at room temperature. b) Electrical current I vs. temperature T measured for a single crystal. Reprinted with permission from ref 126. Copyright 2019 Chemical Science[126].

A purely organic structure without canals has also been reported, but which nevertheless facilitates the diffusion of guest species through its network due to its reorganitation[127].

As it has been observed, in non-porous compounds there are no structural changes as drastic as in porous compounds. Only changes in symmetry, bond distances, and polymerization, among others. It has also been shown that non-porous compounds by losing or exchanging small solvent molecules, exhibit remarkable variations in physical-chemical properties, such as optical, magnetic electronic[126], etc. Therefore, these materials are found to be excellent candidates for sensing, guest sequestration and separation, molecular electronics and opto-electronics applications.

1.7. VAPOCHROMISM PHENOMENON

In most of the examples mentioned in section 1.2.4 there is a common phenomenon called vapochromism. Vapochromic phenomenon occurs when "a substance changes color upon exposure to certain vapors, and consequently, the detection of these analytes can often occur even by the naked eye"[128] (Figure 20).

The color of a coordination complex may be predicted by using Crystal Field Theory. Crystal field theory was developed by Hans Bethe and John Hasbrouck van Vleck in which "describe the electronic structure of metal ions in crystals, where they are surrounded by anions (ligands) that create an electrostatic field with symmetry dependent on the crystal structure"[129]. In the free transition metal ion, the five d-orbitals are degenerated, in other words, they have the same energy. When the ligands approach the transition metal, there is a repulsion between their negative charge and the electronic metal cloud, which provokes the rupture of the degeneration of the d-orbitals. This breaking down of the degeneration causes the splitting of the d orbitals into high and low energy orbitals and the splitting is dependent on the geometry of the complex (Figure 22). The energy difference between the two levels is denominated Δ_0, crystal field splitting. In this splitting level, the electrons are filled from lower to higher energy orbitals. Two situations can arise when the lower energy levels are occupied by the highest number of unpaired electrons, that the following electron has the capability to fill an orbital with higher energy or pair with an electron residing in the lower energy orbital, this pairing of the electrons requires energy (spin pairing energy, P). If the crystal field splitting is greater than spin pairing energy, the electron moves to the orbital with higher energy, this situation is known as high spin (Figure 22). On the contrary, if the crystal field splitting is lower than the spin pairing energy, the electron go into orbitals as an unpaired electron (lower energy orbital), and this other situation is known as low spin (Figure 22).

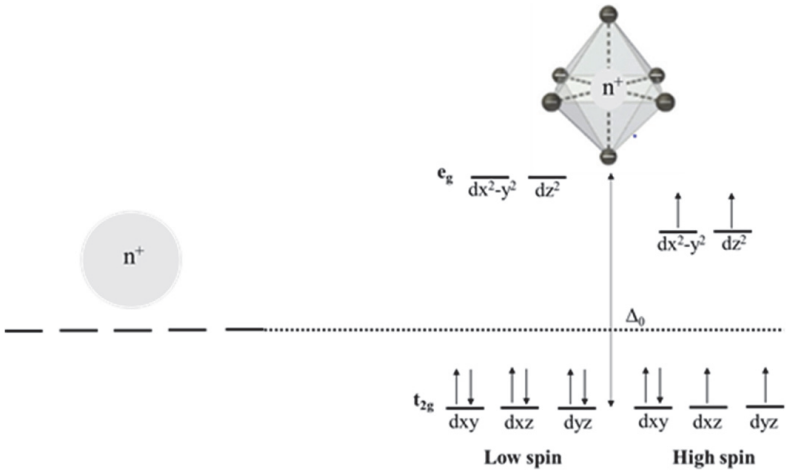

Figure 22. *d*-Orbitals Splitting in an octahedral ligand field and electrons filling in low and high spin.

Interestingly, the interchange in spin state between low spin (LS) and high spin (HS) configuration it can be produced when an external perturbation is applied, such as solvent molecules, producing macroscopic changes in optical properties. This phenomenon is called Spin Crossover (SCO) and is commonly observed with first row transition metal complexes with a d^4 through d^7electron configuration in an octahedral ligand geometry. This phenomenon has been illustrated in some examples in the section 1.6.3[124,125] (Figure 19 and Figure 20), and will be discussed in more detail in the introduction to chapter 2.

The crystal field splitting of the d orbitals is of the same order of magnitude as the energy of a photon of visible light. Therefore, it is possible that when a transition metal complex absorbs visible light at certain wavelengths, electrons may be excited from the lower to the higher energy states, when the d level is not completely filled. Consequently, the color is due to the electronic transitions between the energy levels whose energy difference falling within the visible area of the spectrum (700-400 nm) and this will depend on the energy and the color of the compound is always the complementary color to the one it absorbs because it is subtracted from the reflected or transmitted light.

Generally, a larger Δ_0 indicates that higher energy photons are absorbed (shorter wavelengths). This relationship is described in the equation $\Delta_0 = hc/\lambda$, where h and c are constants, and λ is the wavelength of absorbed light. Thus, the crystal field splitting, determines the color of the coordination complex and the color will depend on the factors that influence the value of the crystal field splitting.

The magnitude of the splitting of the d-orbitals in a transition metal complex depends on three things:

- The geometry of the complex: the splitting is greater in square plane, then in octahedral (Figure 22) and finally in tetrahedral complexes.

- The oxidation state and size of the metal: the higher state of oxidation and size, the greater the crystal field splitting.
- The nature of the ligands: they are classified as strong (large Δ_0/low spin) or weak (small Δ_0/high spin) based on the spectrochemical series: CO^-, NO^-, $CN^->NO_2^-$ >en>py≈NH_3>$EDTA^{4-}$>SCN^->H_2O>ONO^->ox^{2-}>OH^->F^->SCN^->Cl^->Br^->I^-.

Hence, depending on these factors the field will have a determined value that will result in one color or another. In summary, the higher the value of Δ_0, the shorter the wavelengths of light, the more energy colors are absorbed and complementary colors are observed.

If the solvent is located in the lattice, the loss or inclusion of such solvent leads to a rearrangement of the whole network affecting the metal's sphere of coordination. This fact triggers a change in its properties, including the optical properties[125,126].

Due to the uptake and desorption of volatile organic molecules, notable changes in color properties have been observed using a wide diversity of transition-metal (organic) assemblies. However, not many studies have been reported on the vapochromic field using pure organic crystals. This is probably due to their imagined low adsorption capacity compared to metal-organic structure systems, and the absence of orbital interactions "*d*" necessary for a versatile color change. Nevertheless, the synthesis of vapochromic organic crystals without a transition metal core is possible, in fact is a matter of interest, owing to their low cost and the huge variety of molecular designs. The first example was published in 2010 by Takeshi Naota et al.[130]. Subsequently, other examples of organic vapochromic molecules have also been reported[131,132].

The most of organic crystals reported in the literature are based on aromatic ligands assembled by non-covalent interactions, such as Van de Walls, π-π interactions and hydrogen-bonding, which provide flexibles and porous structures. Thus, the sorption and desorption of small guest molecules disturb the crystal packing and modify the interactions and thereby the charge transfer (CT) between organic ligands. The modification on the CT, due the perturbation of the transitions n→π* and π→π* of the chromophore ligands, by the intercalation or accommodation of small volatile molecule within the pores (porous materials) or cavities (due of the flexibility and reorganization of the non-porous materials) could give rise changes in color.

One of the aims of this thesis is to synthesize materials with this property (the change of color with the intercalation or accommodation of external molecule) to use them as chemical sensors.

1.8. OBJECTIVES

This Doctoral Thesis aims to expand the knowledge about the inter-molecular reactions in solid state by single-crystal-to-single-crystal (SCSC) transformation. Towards this aim, the design, synthesis, crystallization and characterization of new metal coordination compounds and carbon-based organic dynamic compounds have been done. Furthermore, the ability of these compounds to absorb small molecules as well as to change of crystal size with the temperature, will be studied, which is of great interest in different technological areas, especially for applications such as chemical sensors or storage of small molecules or gases.

The chapters of this thesis thus start by describing the synthesis and crystallization of these materials, followed by its characterization. Then, the SCSC transformations after undergoing external stimuli, such as temperature and small volatile molecules is described. Finally, in order to apply in technological areas, the complexes synthesized as chemical sensors or molecule storage, a complete study of the optical, thermal structural and magnetic properties of the materials after the SCSC have been carried out.

2. A Robust and Unique Iron(II) Mosaic-like MOF Architecture

The development of materials with specific constructions and properties is still one of the great challenges in modern chemistry. Nevertheless, through the knowledge acquired over the years and an appropriate combination of chemistry and crystallography, the ”design” of crystalline-based materials possessing predetermined structures and characteristics has evolved considerably. At the cutting-edge of these efforts emerged the field of extended 3-D crystalline polymers as a result of the spectacular development of porous crystalline materials[49,133].

The model of porous crystalline materials is zeolites. Gottardi and Galli described: “A natural zeolite is a framework alumina-silicate whose structure contains channels filled with water and exchangeable cations; ions exchange is possible at low temperature (100 ºC at the most) and water is lost at about 250 ºC and reversibly re-absorbed at room temperature”[134], Figure 23 illustrates zeolites in 3D with different pore sizes[135].

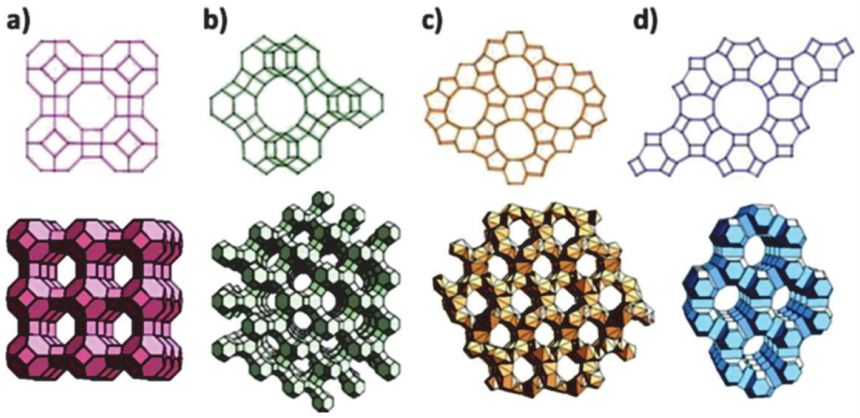

Figure 23. Representative zeolite frameworks, (with pore openings). (a) zeolite A (3D, 4.2 Å); (b) zeolite Y (3D, 7.4 Å); (c) Zeolite L (1D, 7.1 Å); (d) ZSM-5 (silicalite) (2D, 5.3 × 5.6 Å, 5.1 × 5.5 Å) dimensions of channel system. Reprinted with permission from ref 135. Copyright 2012 Semantic Scholar[135].

Although first laboratory reports of zeolite synthesis, by St Claire Deville, appeared as early as 1860s[136], it was not until 1954, a few years later[137], when Union Carbide Corporation started to commercialize synthetic zeolites as a new class of industrial material for purification and separation, based on the crucial work of Robert Milton and Donald Breck.

Historically, zeolites have been the backbone of the petrochemical industry for their application as heterogeneous catalysts and in separation in many petrochemical reactions and in refining processes[138]. Notwithstanding their industrial relevance, their chemistry and composition provide only limited control of the final product, due to incomplete understanding of the processes of zeolite formation[139]. This fact results in a methodology that is strongly based on trial and error, due to an intrinsic limitation of the traditional synthetic strategy to produce zeolites with a predictive structure. Thereby, in order to overcome the new technological challenges and society needs, chemists have approached rational design by using both organic and inorganic components in the elaboration of porous materials looking for an increase in the porosity degree, selectivity and flexibility[133,140]. In particular, since the 1990s, there has been an outpouring of research interest expanded in crystalline-based coordination polymers known as metal-organic frameworks (MOFs, Figure 24). This term "metal-organic framework" was presented by the group of Omar Yaghi for the first time in 1995[141].

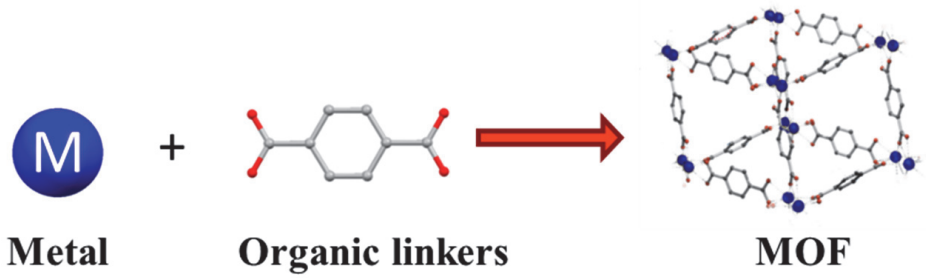

Figure 24. Generalized scheme for metal organic framework.

Over the past two decades, the scientific community has witnessed a great growth in the field of MOFs, reaching more than 61.000 MOF structures documented in the Cambridge Crystallographic data centre[142]. Each year, numerous papers continue to be published on new syntheses, structures and applications of these novel materials. This vast interest derives from the fact that MOFs show a wide variety of potential applications, which include gas uptake, sensing, catalysis, luminescence, electrical conductivity or biotechnology among many others, even surpassing those of zeolites. All these properties arise from their intrinsic porosity, higher specific surface area, lower densities and chemical versatility[143,144,145,146].

It is important to point out that for some years, a controversy has existed over the definition of this type of materials, giving rise to two possible descriptions. The first one describes the term MOF as “a class of crystalline materials formed by

coordination bonds between metal-based nodes (metal ions or clusters termed as SBUs) and organic linkers that have multiple coordination sites **that present exceptional porosities**. Both the metal component and the organic linker can be viewed as multitopic building blocks that self-assemble to form a rigid crystalline polymer"[147]. In contrast, the IUPAC defined this term as "is a coordination compound extending, through repeating coordination entities (ion or neutral molecule that is composed of a central atom, usually that of a metal, to which is attached a surrounding array of atoms or groups of atoms, each of which is called ligands), in 1, 2 or 3 dimensions, that **containing potential voids**"[14]. In this thesis, we have abided by the IUPAC definition.

Back to the chemical nature of the MOF, the coordination metal-ligand (M-L) bonds that connect metallic and organic components are generally weaker than most covalent bonds encountered in other porous materials (COFs, porous organic polymers)[133], but sufficiently strong to provide the necessary stability to evacuate pores and allow the wide range of applications that are at the focus of research involving MOFs. The variety of organic ligands, metal ions or clusters and structural motifs offer an infinite number of possible combinations[148]. Skilfully choosing the right molecular components allows control over the size, shape and functionality of these materials. Furthermore, this modularity in MOF synthesis also makes possible to design and synthetize size-tuneable structural voids for selective guest molecules absorption. These voids can act as highly specific molecular vessels with different absorption capabilities[149,150].

As mentioned above, some of the numerous applications of MOFs are in gas storage and sensors[151]. In fact, the MOF's exceptional tuning structures and properties are an important advantage for their use as potential chemo-sensors and as gas storage material candidates. Scientists have made many efforts to develop and improve MOFs capability of storing and/or selectively separating target gases such as CO_2, H_2, NH_3 and CH_4, among others, and small volatile organic molecules (VOCs)[152,153].

The great attention that these sensing materials have received is due to the great diversity of specific applications such as environmental monitoring, medical diagnostics catalysis, food quality control, defense and energy[154]. Thus, the development of **chemo-sensors** with high degree of selectivity and sensitivity has been for long a critical task for researchers. A principle for the design of these materials is that they must be able to detect substances and produce an easily measurable response such as a change of **color** (optical property), fluorescence or any other macroscopic property[155] (Figure 25). The magnitude of the transformations is normally highly depending on the analyte concentration, as well as physical and chemical properties of the analyte such as acidity or basicity.

Potential candidates for exploiting the subtle changes created by the insertion of small molecules into MOFs are the switchable materials called spin crossover compounds (SCO)[156] as mentioned in section 1.7.

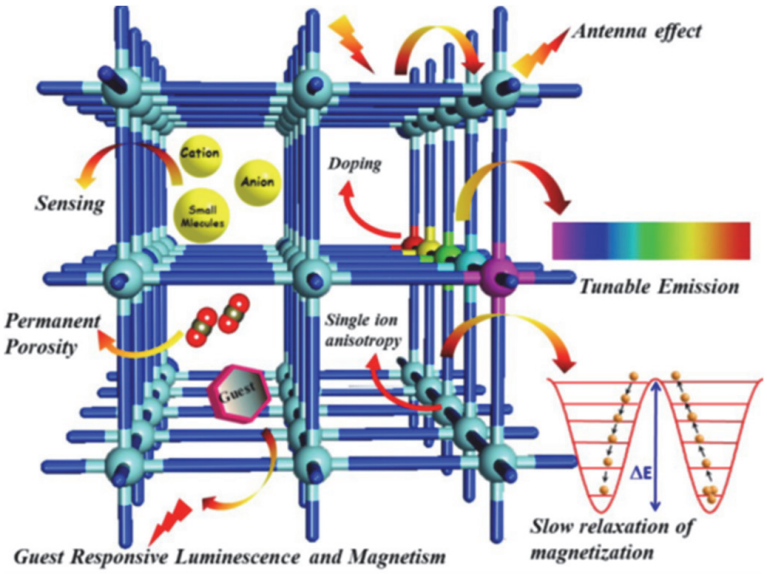

Figure 25. Schematic representation of the response of a MOF under external stimuli. Reprinted with permission from ref 157. Copyright 2014 Coordination Chemistry Reviews[157].

In fact, spin crossover could be considered the most spectacular example of molecular bistability. This phenomenon mainly occurs in iron (II) coordination compounds[158], whose electron configurations can move between high spin (HS) and low spin (LS) states under external perturbations (temperature, pressure, magnetic fields and light irradiation and even by guest uptake), producing macroscopic changes in magnetic, optical, dielectric, and structural properties (Figure 26).

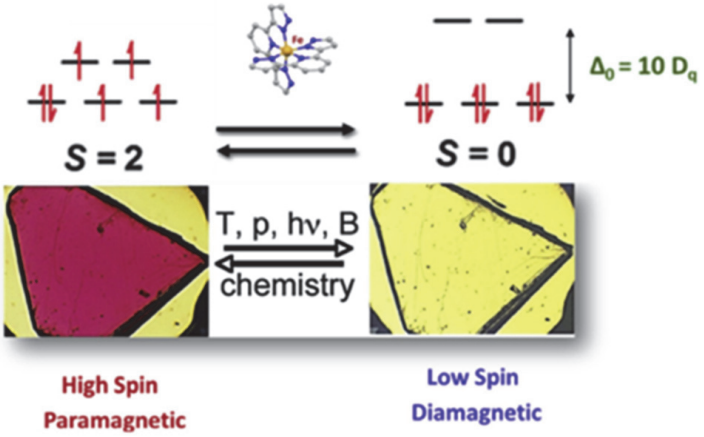

Figure 26. An illustration of the property's modification in an SCO sample. Reprinted with permission from ref 159. Copyright 2018 Comptes Rendus Chimie[159].

SCO is produced when the values of the crystal field splitting, Δ_0, and the spin pairing energy, P, are similar; when this happens the difference in energy between the HS and LS states is of the order of magnitude of the thermal energy (k_BT). For the purpose of achieving HS-LS energy differences of the order of k_BT [156], the most used pocked combination is [FeN_6] with N-coordinated ligands of variable denticity[160], although other less common sets of donor, have been also identified (e.g. N_4O_2, N_4S_2, P_4Cl_2 and P_4Br_2)[161].

It is clear that one of the most relevant SCO family is Fe (II) triazole-based complexes. Numerous studies have in fact been performed with these triazole ligands in order to develop these novel SCO complexes[162,163] and to perform a 'mix of reactive' of those for specific applications.

As far as we know, the SCO phenomenon for the Fe (II) triazole family of compounds has only been presented for 1D chains and shorter units such as oligomers[163], containing a specific coordination node between ligands and iron (Figure 27 c), whereas in 3D structures no examples have been reported yet. In contrast, iron 3D porous structures with this specific coordination node have been reported in the literature with two different azole family ligands: pyrazolates and tetrazoles.

The first example with pyrazolate ligands was described by Jeffrey R. Long group[164,165]. Specifically, the pyrazolate ligand used was: 1,4-benzenedipyrazole (H_2BDP). In first research work[164] a 3D porous iron (III) MOF with triangular channels is defined, where an effective separation of hexane isomers according to the degree of the branching is produced (Figure 27). In second research work [165], a 3D methane storage flexible iron (II) MOF with square channels that presented reversible phase transition during the sorption and desorption of methane was reported. Both compounds maintained the coordination node, but did not display SCO phenomenon.

To the best of our knowledge, only one iron (II) 3D porous example based on a tetrazole ligand, precisely the H_2bdt = 5,5′-(1,4-phenylene)bis(1H-tetrazole (see Figure 28), has been published[166,167]. In both publications the authors reported a porous material with the formula [$Fe_2(H_{0.67}bdt)_3$]·$13H_2O$. The triangular channels of the structure displayed a half-SCO behaviour as a function of temperature. This half-SCO behavior is due the asymmetric unit contains two crystallographically independent Fe (II) sites, one with HS Fe–N bond lengths whereas the other with low-spin (LS) ones. By decreasing the temperature, the material exhibits a significant contraction at the HS Fe^{II} sites, while no such effect exists for other Fe (II) sites. Therefore, this is the first example reported in the literature of iron (II) SCO 3D tetrazole based ligand (Figure 28).

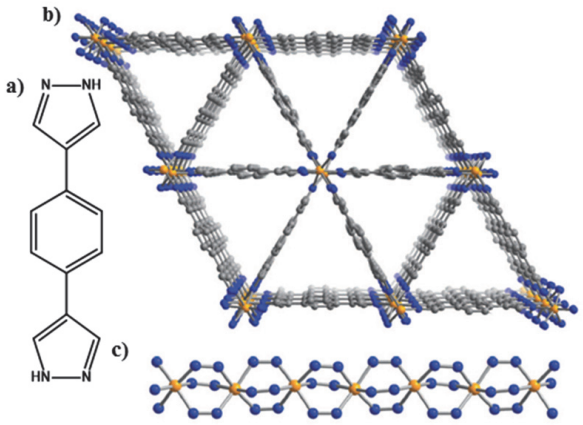

Figure 27. a) Depiction of the bridging ligand precursor, 1,4-benzenedipyrazole (H_2BDP). b) The view along the [001] direction in the orthorhombic crystal structure (space group Fddd). Orange, blue, and gray spheres represent Fe, N, and C atoms, respectively; H atoms are omitted for clarity. c) A perpendicular view of the one-dimensional chains of pyrazolate-bridged Fe (III) octahedral, excluding C and H atoms. Reprinted with permission from ref 164. Copyright 2013 Science[164].

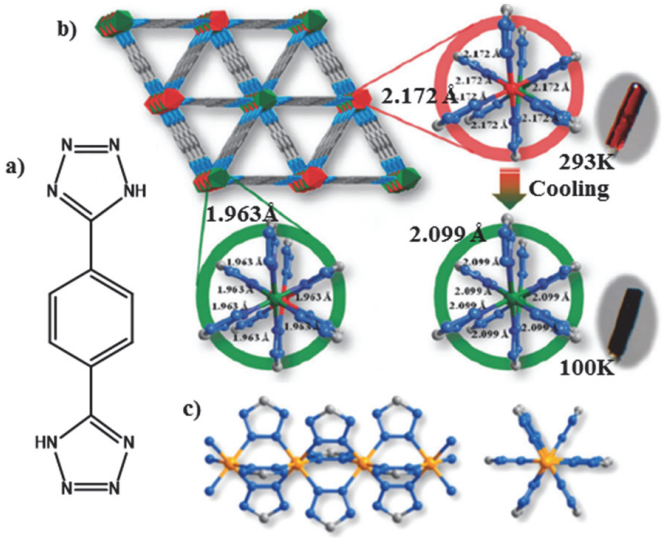

Figure 28. a) Depiction of the bridging ligand precursor, 5,5′-(1,4-phenylene) bis(1H-tetrazole) (H_2BDT). b) SCO transition accompanied with a clear crystal color change from red to black. c) Views of the Fe(II)-tetrazol triple bridge (left) and upper (right) 1D chain-shaped building block. Reprinted with permission from ref 167. Copyright 2012 Chemical Communication[167].

These previous examples lead us to try to synthesize a family of 3D SCO iron (II) compounds based on triazole ligands. Therefore, with the aim of obtaining large cavities coupled to iron (II) SCO metal centers, a novel bridging triazole-based ligand, namely [1,4-phenylene(methanylylidene)]-4H-1,2,4-triazol-4-amine (PM-Tria, Figure 29) has been synthesized. Consequently, in this chapter a synthetic,

structural and physico-chemical studies have been carried out. The best results were obtained through the reaction between the iron salts of $Fe(BF_4)_2$ and FeF_2 and PM-Tria, which resulted in the formation of an unprecedented 3D MOF architecture, but unfortunately without spin transition. This novel material will be described in detail in this chapter.

2.1. SYNTHESIS OF THE PM-TRIA AND COMPOUND 1

Chemicals and reagents were purchased from commercial suppliers and used as received.

2.1.1. Synthesis of the PM-Tria Ligand (N,N'E,N,N'E)-N,N'-(1,4-phenylenebis(methanylylidene))bis(4H-1,2,4-3)

Through a straightforward Schiff-base condensation reaction, a mixture of 4-amino-1,2,4-triazole (1.680 g, 20 mmol) and terephthalaldehyde (0.670 g, 5 mmol) in 30 mL of methanol was refluxed until completion was observed by TLC (hexane/EtOAc 2:1) after 24 h. Upon cooling to room temperature, the resulting off-white precipitate was filtered off and thoroughly washed with methanol. Further purification was achieved by recrystallization from DMSO, yielding a bright white solid (1.318 g, 95%) (Figure 29). This ligand was characterized by NMR and infrared spectroscopy. In the ^{1}H NMR (400 MHz, DMSO-d_6, δ) the principal signals were: 9.18 (s, 4H, benzyl ring), 9.17 (s, 2H, N=CH–Ar) and 8.03 (s, 4H, triazole ring) ppm (ANNEX A 1). FTIR (neat): 3126, 3081, 1683, 1608, 1514, 1493, 1463, 1316, 1287, 1213, 1165, 1053, 831, 721, 619, 536, 489 cm^{-1} (ANNEX A 2).

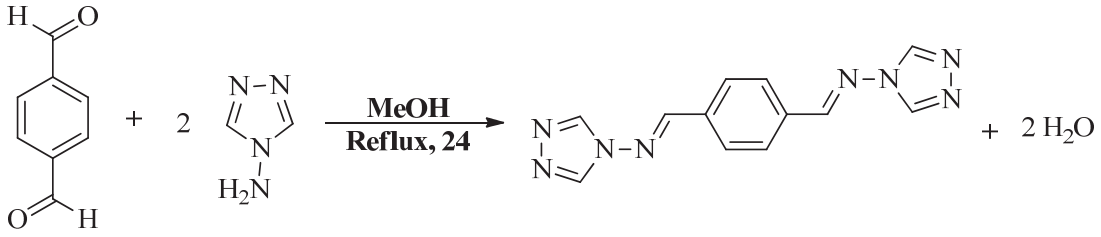

Figure 29. Synthesis of the PM-Tria Ligand.

2.1.2. Synthesis of $\{[Fe(L)_2(\mu\text{-}F)](BF_4)\}_n$ (1)

The synthesis of the compound **1** was carried out in two different ways:

a) A suspension of iron(II) tetrafluoroborate hexahydrate (19 mg, 0.056 mmol) and ascorbic acid (approx. 3 mg) in ethanol (4 mL) was added to a suspension of **PM-Tria**, (20 mg, 0.075 mmol) in ethanol (8 mL) and stirred for 10 minutes giving a cloudy solution. The mixture was transferred into a Parr reactor, sealed, and kept at

140 °C for 4 days in a furnace and cooled to room temperature. Small red crystals suitable for X-ray diffraction were formed after 4 days (20%, 3.9 mg) (Figure 30).

b) A suspension of iron(II) tetrafluoroborate hexahydrate (9.3 mg, 0.028 mmol), iron(II) fluoride (2.62 mg, 0.028 mmol) and ascorbic acid (approx. 3 mg) in ethanol (4 mL) was added to PM-Tria, (20 mg, 0.075 mmol) in ethanol (8 mL) and stirred for 10 minutes giving a cloudy solution. The mixture was transferred into a Parr reactor, sealed, and warmed at 140 °C for 4 days in a furnace and cooled to room temperature. Small red crystals suitable for X-ray diffraction were formed (38.60%, 7.5 mg) (Figure 30).

FTIR (near, cm^{-1}): 3565(w), 3118 (w), 1617 (w), 1506 (m), 1403 (w), 1325 (w), 1295 (w), 1212 (m), 1167 (m), 1061 (s), 969 (s), 872 (m), 833 (m), 733 (m), 719 (m), 675 (w), 625 (s), 538 (m), 536 (m), 493 (s), 454 (s), 443 (s), 430 (s) (Figure 31); elemental analysis calculated (%) for $C_{24}H_{20}N_{16}FeF_5B \cdot 0.5\ C_2H_6O \cdot 1.7\ H_2O$($\{[Fe(L)_2(\mu\text{-}F)](BF_4)\}_n \cdot 0.5.\ C_2H_6O.\ 1.7\ H_2O$): C 40.15, N 29.97, H 3.56; found C 40.15, N 29.99, H 3.54.

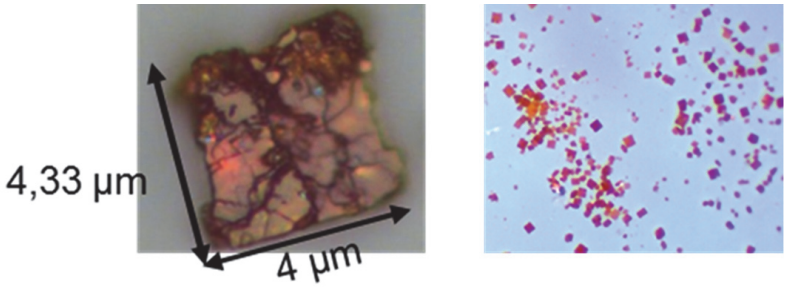

Figure 30. View of a single crystal obtained directly from the synthesis of **1** and a global view of crystalline sample **1** showing their size homogeneity[168].

2.2. RESULTS AND DISCUSSION

2.2.1. Synthesis optimization

The reaction of 1.33 ligand equivalents (**PM-Tria)** with one equivalent of $Fe(BF_4)_2$ in ethanol in a pressure container at 140 ˚C affords crystalline red cubic materials (Figure 30) with $\{[Fe(PM\text{-}Tria)_2(\mu_2\text{-}F)](BF_4)\}_n$ (**1**) formulation at moderate yield (20 %) after four days.

The fluoride ligand is *in situ* generated by decomposition of the BF_4^- counter ion of the starting Fe (II) salt due to the high temperature in a pressure tube (Figure 31, ANNEX A 3 and ANNEX A 4). Several reports have previously shown that the BF_4^- could be used as a fluoride source[169,170], so the reaction with the ligand and the metal ion can occur, which normally results in fluoride-containing coordination compounds[171]. After this observation, an alternative reaction has been performed by adding FeF_2 salt in combination with the $Fe(BF_4)_2$ and the **PM-Tria** in a 1:1:2.5

molar ratio. After four days, red crystalline cubic materials similar to those previously described are observed, but in a higher reaction yield 38% (Figure 30). It was also proven that the salt of $Fe(BF_4)_2$ was essential to obtain **1** and act as fluoride source, since the reaction between the salt of FeF_2 and PM-Tria was carried out in the same conditions as **1**. The compound obtained from that reaction was characterized by IR and X-ray powder diffraction (see in the ANNEX A 5) obtained in both techniques that the product was the ligand, so there was no reaction between the two reagents. Therefore, the $Fe(BF_4)_2 \cdot 6H_2O$ salt, ethanol and temperature play a very important role in the reaction. First, thanks to the decomposition of the BF_4^- counter ion the formation of Fe-F chains happens. Furthermore, the ethanol solubilizes the ligand enough (since the ligand the insoluble one) in order that the nucleation takes place slowly and of place to the formation of the compound in form of crystals. And finally, the temperature helps to BF_4^- decomposition and the solubility of the ligand.

2.2.2. Structural and physico-chemical study

Compound **1** has been characterized by different techniques. In the infrared spectrum of this compound is showed the characteristic vibrational modes of the three components, i.e. the PM-Tria ligand, the BF_4^- and the F^- counter ions. The bands observed in the (1600-1500) cm^{-1} range correspond to C=N stretching modes of the triazole ligand. 1061 cm^{-1} band is assigned to the B-F vibration (red line) of the BF_4^- counter ion and the bands observed in the (460-400) cm^{-1} range correspond to Fe-F (blue line) bond (Figure 31).

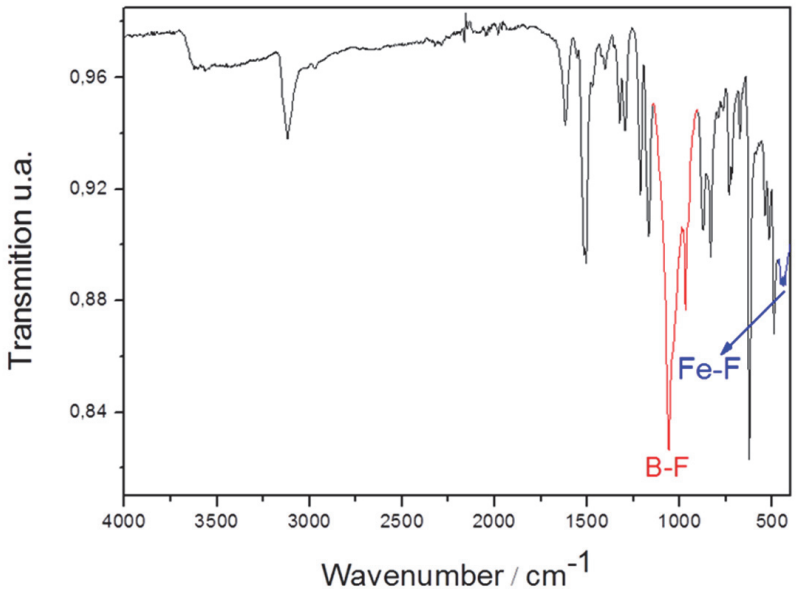

Figure 31. Infrared spectra of compound **1**[168].

Single-crystal X-ray diffraction on **1** was measured at 100 K in The Advanced Light Source (ALS) Synchrotron. **1** crystallizes in a tetragonal space group *P*4/*ncc*. The asymmetrical unit is composed of three PM-Tria ligands and three unequivalent crystallographic iron (II) metallic centers which are balanced by three BF_4^- and three F^- counter ions (Figure 32). Details for the structure solution and refinement are summarized in ANNEX A 6 and ANNEX A 7. As expected for an iron (II) cation, the metal center shows an octahedral environment[172,173]. The Fe(II) is coordinated by two fluoride ions acting as coordinating μ_2 ligands placed at the axial sites and four nitrogen atoms (belonging to four triazole-based **PM-Tria** ligand) at the equatorial positions (Figure 32).

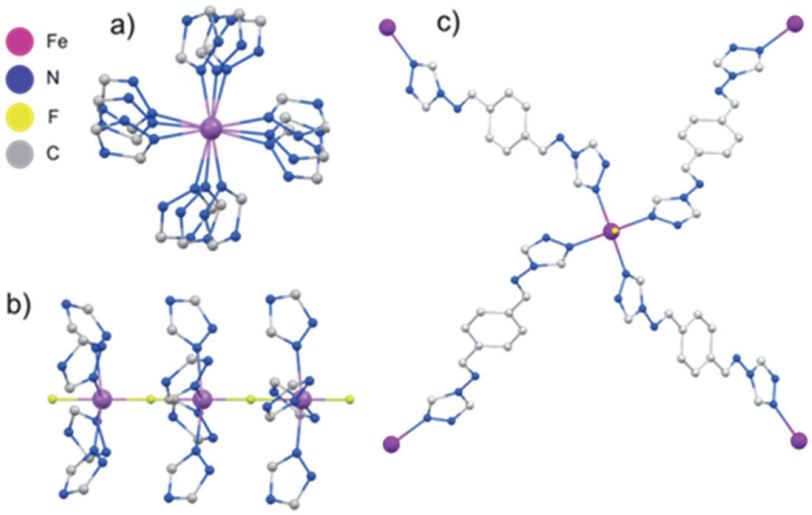

Figure 32. MERCURY view of **1** (hydrogen atoms have been removed for clarity). a) c view of a trimeric unit. b) b view of a the Fe(II)··F··Fe(II) trimeric unit. c) A segment of **1** illustrating the metallic connection along the c axis via **PM-Tria** ligands[168].

Every Fe (II) center is linked to four neighboring Fe(II) *via* four bridging **PM-Tria** ligands (Figure 32 c). The triazole surprisingly acts uniformly with a monodentate bridge character μ_1 instead of the well-known bidentate nature of this type of ligands with Fe(II) metal centers[163]. The three-dimensional structure expands along the one-dimensional nearly perfect polymer unit $\{Fe(II)\text{─}F\}_n$ (Figure 33 b and Figure 34) of 180°, this selected angle is given in the Table 2. The average Fe−X = 2.1 Å bond length, being X = N and F donor atoms, an effective indication that the metal core is in its high-spin (HS) electronic configuration at the given temperature[125] (Table 2). This observation is also confirmed by the magnetic measurements (see below in this chapter).

Table 2. Selected angles [°] and bond lengths [Å] for compound **1**.

Selected angles [°]	Selected bond lengths [Å]	
Fe(1)-F(1)-Fe(2) 180	**Fe(1)**	
Fe(2)-F(2)-Fe(3) 180	**Fe(1)-N(1) 2.164(3)**	**Fe(1)-F(3) 1.943(6)**
Fe(3)-F(3)-Fe(1) 180	**Fe(1)-F(3) 2.117(6)**	**Feav-X 2.119**
F(1)-Fe(1)-F(3) 180	**Fe(2)**	
N(1)-Fe(1)-N(1) 167.40	**Fe(2)-N(7) 2.166(3)**	**Fe(2)-F(1) 2.092(6)**
N(1)-Fe(1)-N(1) 89.31	**Fe(2)-F(2) 1.927(6)**	**Feav-X 2.113**
F(1)-Fe(1)-N(1) 96.30	**Fe(3)**	
F(3)-Fe(1)-N(1) 83.70	**Fe(3)-N(9) 2.260(3)**	**Fe(3)-F(2) 2.035(5)**
	Fe(3)-F(3) 1.953(6)	**Feav-X 2.171**

Monocrystalline X-ray diffraction in **1** to 273 K was also examined, obtaining the same structure, without changes in the angles, properties (color, magnetism) and distances, which indicates that the center of the iron (II) is in the HS state as well as 100 K. This suggests that the compound does not present SCO. This fact is in accordance with the above mentioned in the introduction of this chapter, because the compound that we obtained has a molecular formula: $\{[Fe(PM\text{-}Tria)_2(\mu_2\text{-}F)](BF_4)\}_n$, having just only four donor nitrogen ligands instead of 6.

The crystal packing of **1** along the *c*-axis shows that the polymeric one-dimensional chains are packed parallel to the c-axis with an interchain distance between iron centers of 19.94 Å. Because of the considerable distance between the two metal centers, small molecules or gases could be introduced. However, it is important to take into account that the counter ions could or could not be an impediment when introducing molecules because in this case, they are located at the central region of the cavities, partially filling them (Figure 33 a).

On the other hand, it may be observed in direction b that the **PM-Tria** ligands are tilted 35.71˚ with respect to ligand plane and the metallic chain (Figure 33 b) whereas the vast majority of the ligands have been reported to be straight[174].

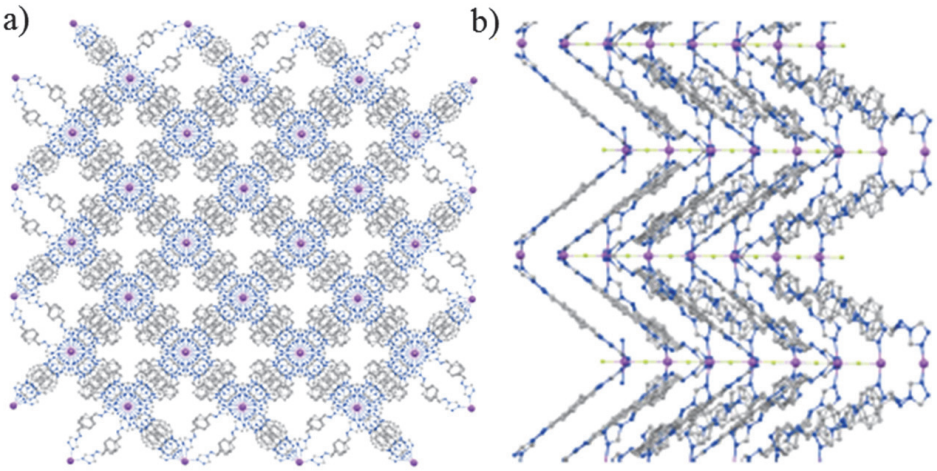

Figure 33. a) *c* axis view of **1** reveals the cavities contained by the structure and b) The representation along *b* axis evidences the collapsed character of the structure[168].

The principal interactions between ligands are π···π contacts and lone pair-π interactions. These latest interactions are less well known, only a few examples of lone pair-π interactions involving small synthetic molecules have been reported so far in literature. These consist of interactions of π-systems with electron-rich atoms. These ligands display strong supramolecular interactions between them, evidenced by short ring to ring contacts (the shortest being 3.337 Å, see Figure 34) that allow in turn building a robust extended MOF.

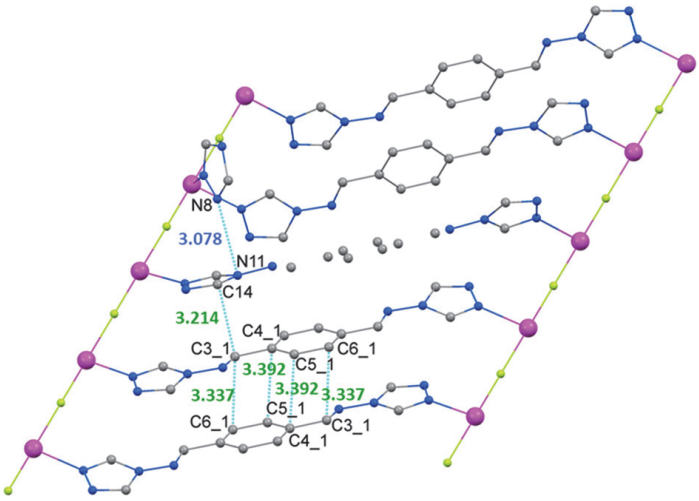

Figure 34. This Figure shows the principals π···π and lone pair π interactions between the rings of the PM-tria ligand[168].

Moreover, it is worth mentioning that the tetrafluoroborate counter ions required for a charge balance are weakly interacting with the **PM-Tria** ligands. Figure 35 shows the weak interactions between the BF_4^- counter ion and the hydrogen of the ligand. These interactions reinforce the structural stability of the crystals in the three dimensions (Figure 33 a and Table 3).

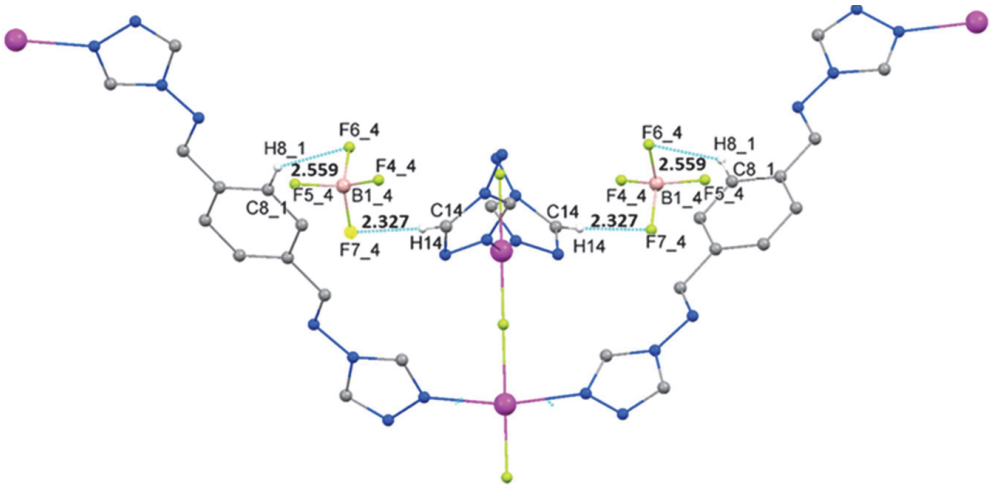

Figure 35. Representation of the weak interactions of the tetrafluoroborate counterions with the PM-Tria ligands[168].

The distances of these interactions are in concordance with the values founded in the literature[175] and are summarized in the table below.

Table 3. Principal interactions [Å] for compound **1**

π···π contacts (C···C)	
C3_1-C6_1 3.337	**C4_1-C5_1 3.392**
C3_1-C(14) 3.214	
Lone pair π interaction	
N(11)-N(8) 3.078	
Hydrogen bonds	
F6_4-H8_1 2.559	**F7_4-H(14) 2.327**
F6_4-C8_1 3.363	**F7_4-C(14) 3.258**

X-ray powder diffraction of the different crystalline samples synthetized by both strategies have been compared with the theoretically obtained from single-crystal X-ray diffraction of **1**, affording a superimposed spectrum (ANNEX A 8).

The thermogravimetric study of **1** confirms the presence of solvent molecules from the synthesis (approximately 0.5 molecules of ethanol and 1.5 of water molecules per unit cell, ANNEX A 6 is confirmed). The weights loss is produced at 50°C and 150°C, the percentage of mass corresponds to 1.909 % and 3.927 %, respectively, followed by the complete decomposition of **1**. This irreversible weight

loss corresponding to the decomposition process of the MOF is observed at around 225 °C, which implies high robustness and a high thermal stability. Thermogravimetric profile of **1** is represented in the Figure 36 showing the mass variation (green curve) and its first derivative (blue curve) upon heating at 2 ºC/min in air.

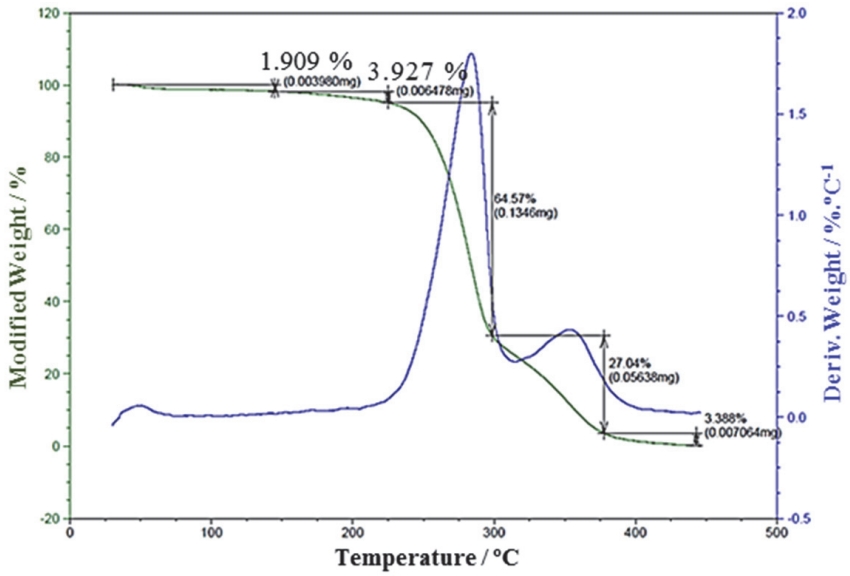

Figure 36. Thermogravimetric profile of **1** (0.3220 mg in air) showing the mass variation (green curve) and its first derivative (blue curve) upon heating of 2 ºC min^{-1} [168].

2.2.3. Magnetic study

The last technique used to characterize compound **1** was the magnetometry. This measured was carried out in the Institute of Chemical Research of Catalonia (ICIQ) in collaboration with Jose R. Galan Mascarós. The magnetic property of **1** determined in the 2–300 K temperature range under a constant field of 1 T and the data are summarized in Figure 37. The value of χMT at room temperature is 2.5 $cm^3 \cdot K \cdot mol^{-1}$, slightly lower than the spin-only value expected for a magnetically diluted S = 2 sample (of 3 $cm^3 \cdot K \cdot mol^{-1}$). This confirms the HS state of the Fe (II) centers and suggests the presence of antiferromagnetic coupling between spin carriers along Fe-F chains. Indeed, the χMT product decreases when temperature is decreased (Figure 37, square dots). The χM versus T plot (Figure 37, triangle dots) shows a maximum around 50 K which is also a signature of dominant antiferromagnetic interactions. The high temperature regime can be fitted to a Curie-Weiss law (Figure 38), with parameters C = 3.85 cm^3 K mol^{-1} (g = 2.24) and θ = –10.6 K. However, the low temperature data deviates significantly from this model, with the appearance of a Curie tail that indicates the presence of a paramagnetic contribution. Since interchain distances are one order of magnitude

longer than intrachain ones, it can be considered in a first approximation that only the fluoride bridges are effective magnetic super-exchange pathways. Thus, we modelled the magnetic data to the analytical expression for an infinite chain of classical spins, as derived by Fisher from the exchange Hamiltonian[176].

$$H = -J \sum_{i=1}^{n-1} S_i \times S_{i+1}$$

And then, incorporating a paramagnetic contribution, $\chi_P = C_P/T$

$$\chi = \frac{Ng^2\beta^2 S(S+1)}{3kT} \frac{1+u}{1-u} + \chi_P$$

with

$$u = coth\left[\frac{JS(S+1)}{kT}\right] - \left[\frac{kT}{JS(S+1)}\right]$$

This model satisfactorily reproduces the data in all the temperature range, with parameters $S = 2$, $g = 2.12$, $J = -16$ cm^{-1} and $C_P = 0.03$ cm^3 K mol^{-1} parameters (see red and blue lines in Figure 37).

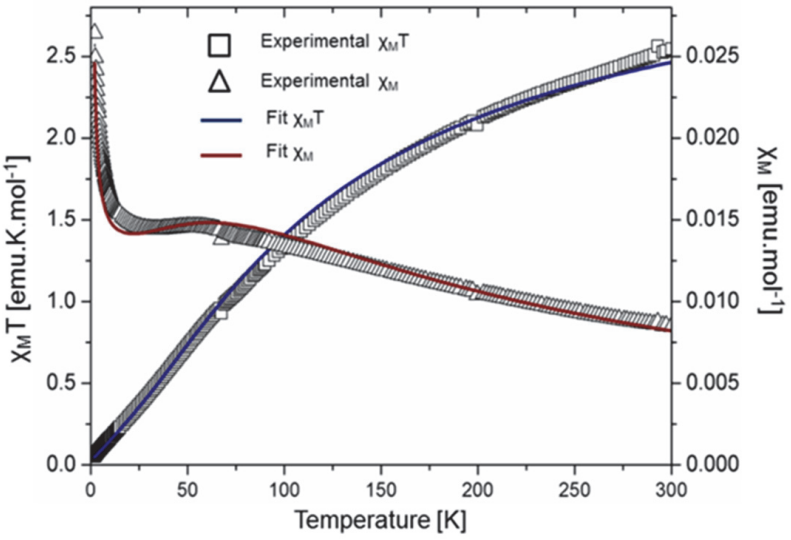

Figure 37. $\chi_M vs T$ (triangle dots for experimental data and red line for fitting curve) and $\chi_M T vs T$ (square dots and blue line) plots[168].

Such small paramagnetic contribution corresponds, approximately to 1% of the total Fe(II) content. It is probably related to the terminal metal centers, since the actual chains (and crystals) are not infinite as the model supposes. The antiferromagnetic nature of the fluoride-bridged chains is also consistent with their geometry. The Fe–F bridges of 180° favors an orbital overlap between semi-

occupied metal orbitals carrying unpaired spins, stabilizing a ground state with unparalleled spin alignment[170].

Such small paramagnetic contribution corresponds, approximately to 1% of the total Fe (II) content. It is probably related to the terminal metal centers, since the actual chains (and crystals) are not infinite as the model supposes. The antiferromagnetic nature of the fluoride-bridged chains is also consistent with their geometry. The Fe–F bridges of 180° favours an orbital overlap between semi-occupied metal orbitals carrying unpaired spins, stabilizing a ground state with unparalleled spin alignment[170].

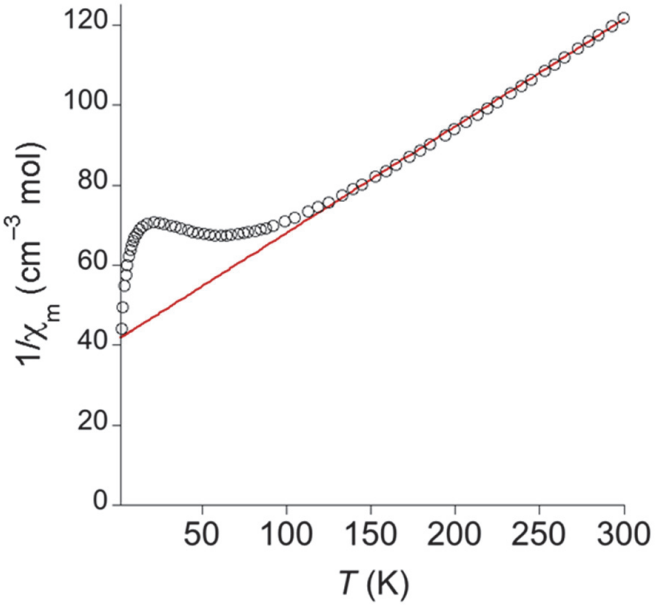

Figure 38. High temperature regime fitted to a Curie-Weiss law with parameters C = 3.85 cm^3 K mol^{-1}, g = 2.24 and θ = –10.6 K[168].

2.2.4. Porosimetry analysis

To evaluate the pore volume and surface area of this framework, gas sorption isotherm of **1** was measured via BET studies.

This representation (Figure 39) shows the amount of gas adsorbed as a function of the relative pressure at constant temperature. The sorption of nitrogen revealed a type II isotherm, which is found in macroporous and non-porous compounds[177]. Due to the hindrance of the pores by the ligands and/or the counter ions and a low surface area, 6.7 m² g^{-1}, this is a non-porous compound. Therefore, there is almost no N_2 adsorption on the surface area of the MOF. The value of the surface area according to the structural analysis represents an accessible volume with solvent of 640Å^3 and a molecular surface of 755 Å^2.

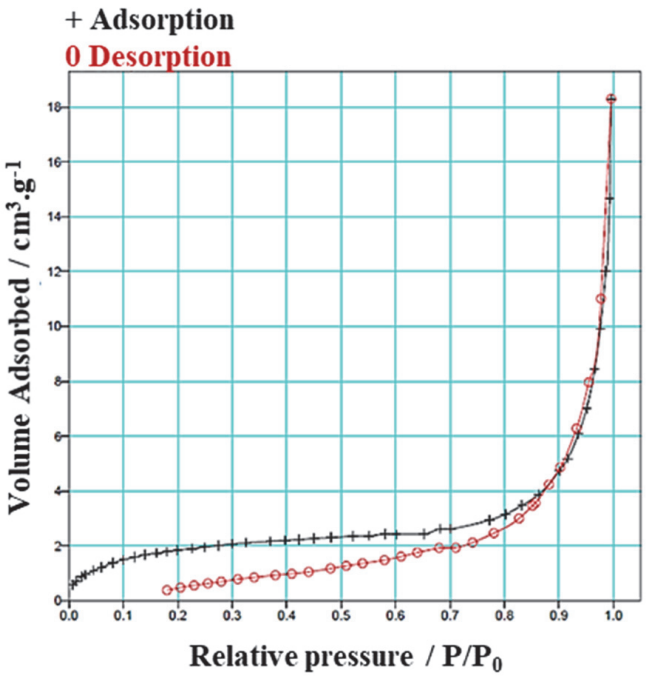

Figure 39. Nitrogen gas sorption isotherm at 78 K for compound **1** (crosses, sorption; open circles, desorption). P/P_0 is the ratio of gas pressure (P) to saturation pressure (P_0), with P_0 being 716 torr[168].

2.2.5. Sensing study; a diffusion protocol.

As previously mentioned, one of the applications of interest is chemo-sensors. The IUPAC defined chemical sensor as a "device that transforms chemical information, ranging from the concentration of a specific sample component to total composition analysis, into an analytically useful signal. The chemical information, mentioned above, may originate from a chemical reaction of the analyte or from a physical property of the system investigated"[178]. In spite of being a non-porous compound, as discussed in section 1.6.3, there are non-porous materials that can act as porous because they are capable of reorganizing their structure and host different guest molecules.

For this purpose, the sorption of molecules following a vapor diffusion protocol has been tested. In this strategy, crystalline materials were exposed to several small volatile molecules at a saturated vapor pressure in a *vial to vial* reactor at different temperatures (Figure 40).

After that, the measurable physico-chemical changes (sensing experiments) were studied by different characterization techniques, mainly: infrared spectra (FTIR), optical reflectivity, ^{1}H NMR, mass spectrometry, thermogravimetric analysis and X-ray techniques.

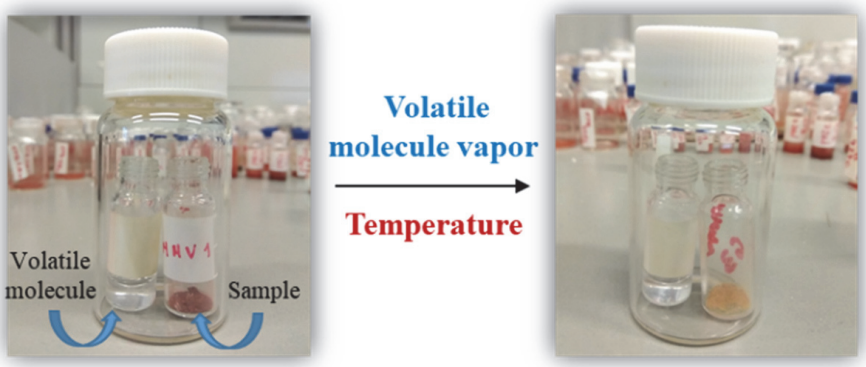

Figure 40. Exposition of single crystals of **1** to a small volatile molecule following the reported protocol.

In this particular case, crystals of **1** were exposed to different volatile compounds (mentioned below) at 50 °C and subsequently characterized by different techniques.

By observing the strong supramolecular interactions between ligands, it has been attempted to intercalate volatile molecules with aromatic rings to break these interactions, such as benzene, toluene, pyridine, pyrrole, among others. In addition, we tested other solvent molecules to be exchanged with the solvents inside the dense network of **1** (this was verified with thermogravimetric analysis), like acetic acid, formic acid, formaldehyde, acetone, acetonitrile, methanol, etc.

Following the protocol, all compounds were characterized by optical reflectivity, FTIR spectroscopy and thermogravimetric analysis after exposure to volatile compound at a saturated vapor pressure. To date, changes in material have only been identified, when **1** was exposed to a saturated atmosphere of acetic acid. Firstly, a color change from red to yellow was observed (Figure 41 a). This color change is supported by FTIR spectroscopy technique (Figure 41 b). One of the most remarkable changes that can be observed in the spectrum is the displacement and intensities of the bands as well as the appearance of a new band at 1712 cm^{-1}, this band can be assigned to the carbonyl stretch C=O of acetic acid. The acetic acid could have been exchanged for the ethanol or water molecules inside the MOF, because the OH band between (3500-3600) cm^{-1} decreases. By the thermogravimetric analysis (Figure 42), a weight loss of 15.59 % (137 g/mol) can be seen taking place at proximally 30 ºC. This loss could correspond to the release of two acetic acid molecules. Therefore, the acetic acid may have been interchanged with any of these two solvent molecules from the synthesis (ethanol and water). However, several characterization techniques will be needed to accurately define the new material's structure, including single-crystal X-ray diffraction technique. Therefore, we are working on this goal.

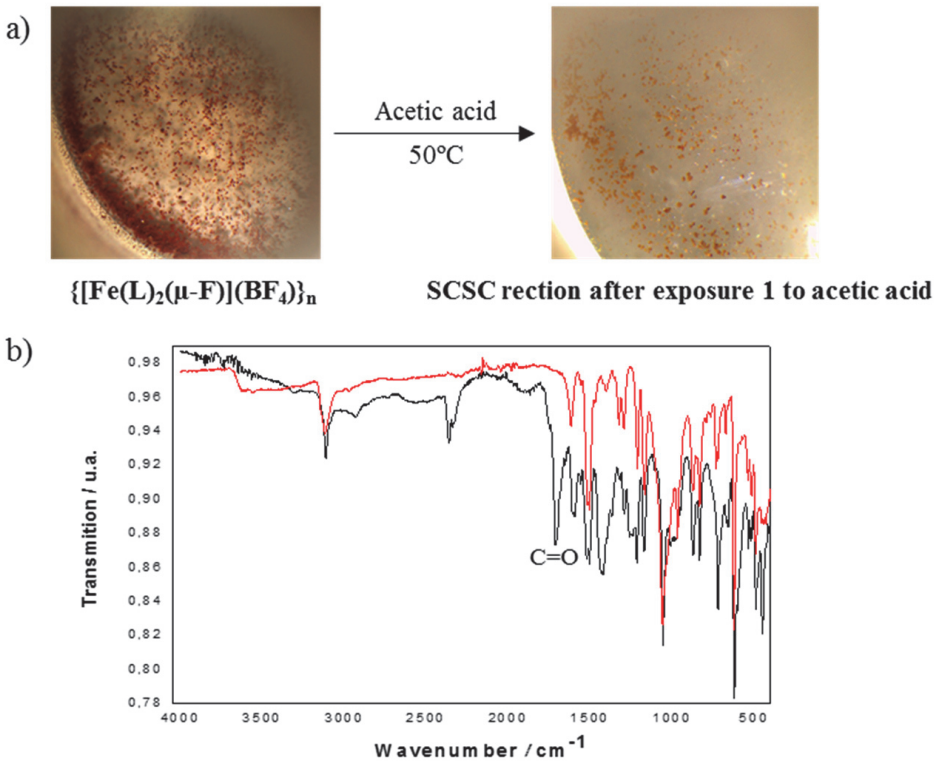

Figure 41. a) SCSC reaction, including a picture of the crystal after and before exposure to acetic acid vapors. b) Infrared superimposed spectra of starting material (**1**) (red) and the infrared spectra of SCSC reaction with acetic acid at 50 °C (black).

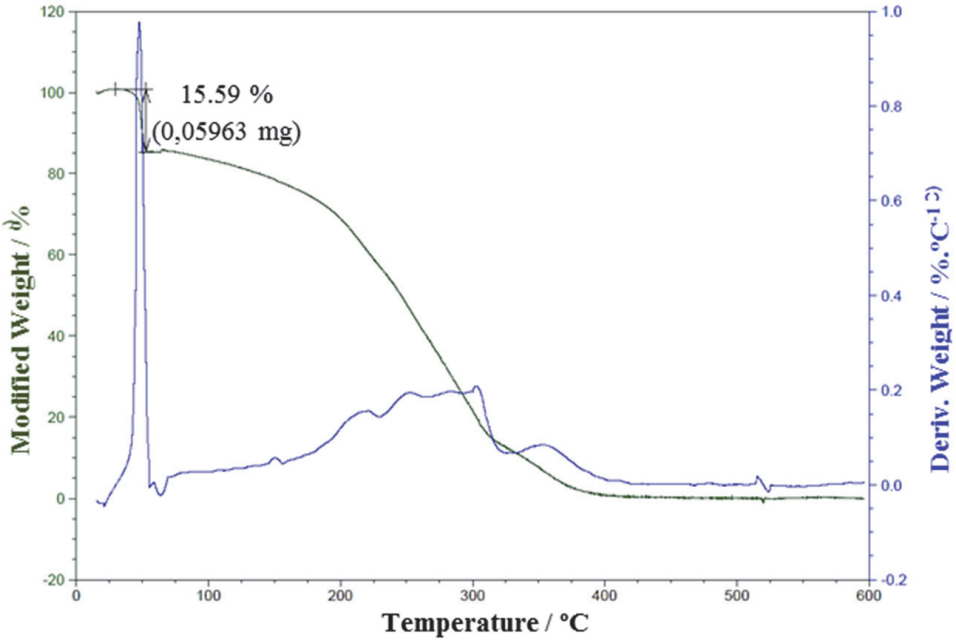

Figure 42. Thermogravimetric analysis of the SCSC reaction with acetic acid at 50 °C[168].

On the other side, a second experiment employed to evaluate changes in the overall MOF properties and use it as sensors was the interchange of counter ions. To this end, the crystals of compound **1** were introduced in saturated solutions of different iron salts, $Fe(ClO_4)_2$, $FeBr_2$ and $FeCl_2$, in order to attempt the exchange of tetrafluoroborate counter ions. After the characterization of these compounds, no change in their properties was observed.

2.2.6. Tessellation

Nature sometimes encounters geometrical shapes of great beauty such as mosaics. A mosaic is defined as a design made with small pieces of ceramic, glass, stones or other objects. These can either be organized in exact geometric shapes or created from more haphazard and broken pieces. There has been an enormous amount of research on mosaic tilings worldwide, and they are a source of many teaching subjects in mathematics and art. Probably, the Dutch M.C. Escher is one of the most recognized artists inspired by these pieces of arts.

He was greatly surprised by Islamic art after visiting the Alhambra Palace in Granada (Spain) in 1922 and in 1936. Later, in 1958, he published a book titled 'Regular Division of the Plane', in which he described the systematic build-up of mathematical bridges. Today the Escher techniques are well known to create tiles that, by applying geometric movements, may be used to produce a variety of mosaics. Despite the fact that the colossal database of novel MOFs has enabled the development of novel synthetic tools and progress of the rational design vs. the serendipitous assembly, this second method's randomness is still offering us beautiful surprises every now and then. We have found in this compound a nice surprise in its crystalline structural pattern. What we have found for **1**, is that the view generated along the *c* axis almost perfectly fits with an Islamic mosaic found at the Alhambra Palace (see Figure 43 and ANNEX A 9).

This genuine tessellation found for **1** mainly arises from an unusual rotation of the central metal equatorial coordination plane along the one-dimensional direction. In particular, the rotation from Fe(1) to Fe(2) planes is 16.03˚ and from Fe(2) to Fe(3) 9.23˚. The total rotation from Fe(1) to Fe(3) is equal to 25.26˚ (see Figure 44). Remarkably, the tetrafluoroborate counter ions are filling the space that in the mosaic is occupied by the octagram.

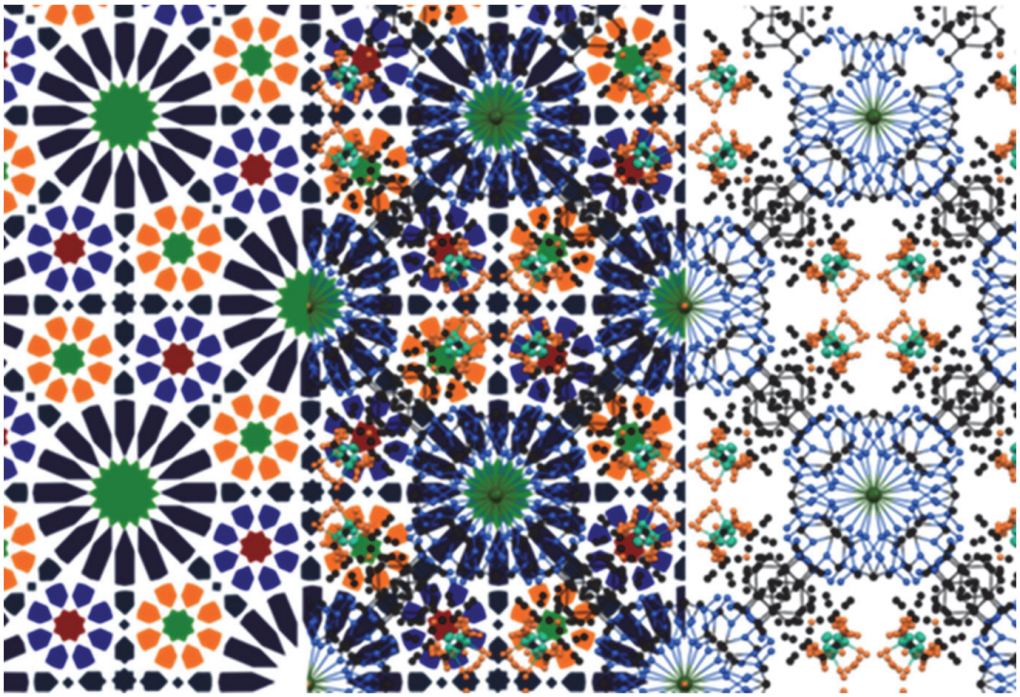

Figure 43. On the left we see the Islamic mosaic found at the Alhambra Palace of Granada. On the right an illustration of **1** along its c axis. On the middle, a superposition of the two pictures[168].

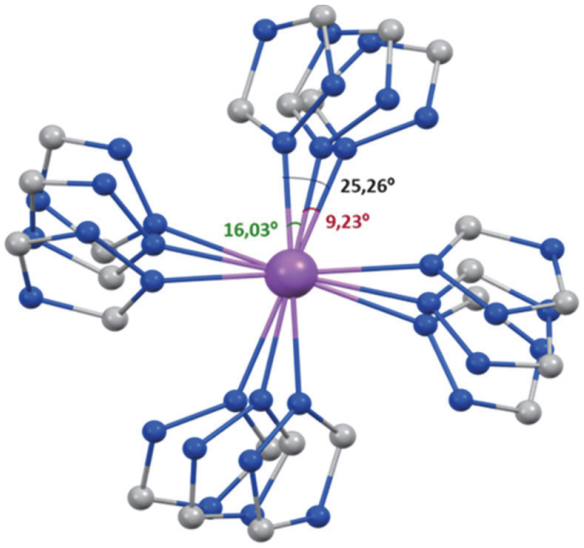

Figure 44. Illustration of the rotation of compound **1** along *c* crystallographic direction[168].

2.2.7. Modifications in the synthesis conditions

Considering the result described above, variations of the synthetic strategy have been explored in order to get other iron (II) PM-Tria based-materials, more precisely:

- The iron source, to study the effect of the counter ions.
- The solvent of the reactions, to study the polarity role.

- The ligand/metal stoichiometry, to study the role of the concentration. 2:1, 1:2 and 1.33:1 ligand/metal stoichiometry was used, in the case of only using an iron salt in the reaction and 2.67:1:1, if a combination of iron salts is employed.
- And finally, the temperature. The reactions were carried out at two temperatures: 120 ºC and 25 ºC.

Table 4 summarizes the results of the different synthetic modifications at 120 ºC. The red cross represents the reactions that have not worked, that is, the precipitated obtained after the reaction was the starting pure ligand. By contrast, the green tick represents the reactions that have worked, in other words, the reaction described in this chapter (section 1.1.2) that resulted in the formation of the crystals of compound **1**. Unfortunately, all reaction attempts at 25 ºC and with different ligand/metal stoichiometry have afforded the starting pure ligand. Thus, it did not function either, not even with $Fe(BF_4)_2 \cdot 6H_2O$ and FeF_2 salts. It is therefore concluded that the reaction of **1** only occurs under very optimal conditions.

Table 4. Reactions between PM-Tria, iron (II) salts and different solvents in a pressure tube under the same conditions of temperature and ligand/metal stoichiometry as compound **1**.

SOLVENTS / IRON SALTS	H_2O	MeOH	EtOH	H_2O+MeOH	H_2O+EtOH	DMF	Acetic acid	CH_3CN	Acetone
$Fe(BF_4)_2 \cdot 6H_2O$	✗	✗	✓	✗	✗	✗	✗	✗	✗
$Fe(BF_4)_2 \cdot 6H_2O$ + FeF_2	✗	✗	✓	✗	✗	✗	✗	✗	✗
FeF_2	✗	✗	✗	✗	✗	✗	✗	✗	✗
$Fe(ClO_4)_2 \cdot 6H_2O$	✗	✗	✗	✗	✗	✗	✗	✗	✗
$FeCl_2$	✗	✗	✗	✗	✗	✗	✗	✗	✗
$FeBr_2$	✗	✗	✗	✗	✗	✗	✗	✗	✗
$Fe(ClO_4)_2 \cdot 6H_2O$ + FeX_2, X= F^-, Cl^- and Br^-	✗	✗	✗	✗	✗	✗	✗	✗	✗
$Fe(BF_4)_2 \cdot 6H_2O$ + FeX_2, X= Cl^- and Br^-	✗	✗	✗	✗	✗	✗	✗	✗	✗

2.3. CONCLUSIONS AND FUTURES PERSPECTIVES

In summary, a novel extended triazole-based ligand (**PM-Tria**) has provided a promising entry into a MOF 3D architecture with Fe(II)-F chains which exhibits a perfect linearity on its growing-mode. The magnetic study of this material confirms an antiferromagnetic 1D behavior. Furthermore, this molecular architecture is compared with an XIV century Islamic mosaic found in the Alhambra Palace in Granada (Spain) showing a surprising and beautiful resemblance. The reaction of PSM with acetic acid could be very promising so it will be deeply characterized and the structure will be precisely determined. It has been tried to obtain this type of compound **1** with other salts of Fe (II), but there has only been success with $Fe(BF_4)_2$ salt. Finally, as future perspectives: we are going to explore reactions with tetrazoles ligands in order to obtain iron (II) porous 3D SCO structures. In addition, in order to increase the sensibility, selectivity and solubility, novel structural analogs ligands could be developed that including molecular receptors (functional groups), and thus be able to obtain new three-dimensional structures searching for the same type of coordination ($Fe(L)_2(\mu\text{-}F)$). As well as further investigations under external stimulus to activate the porous material.

3. PYRIDINE-PYRAZINE TRAPPING & RELEASE INTO AN IRON- BASED COORDINATION POLYMER: A REVERSIBLE SCSC TRANSFORMATION

Reversible Single-Crystal-to-Single-Crystal (SCSC) transformations promoted by a gas-solid reaction have recently received great attention due to their potential applications in today's science[123,179,180,181,182,183]. This development is mainly due to the advancement in X-ray diffraction techniques for both synchrotron large infrastructures and conventional X-ray diffractometers.

SCSC transformations are solid state phase transitions between different crystalline states in which the crystal integrity and the long range are retained, as mentioned in section 1.2. These transformations allow monitoring atomic processes for further expanding our knowledge in molecular systems, particularly, in the development of chemical sensors. Therefore, SCSC transformations triggered by a gas-solid reaction are a powerful tool in the development of functional materials, porous and non-porous, capable of reacting selectively with toxic gases or volatile organic compounds, VOCs[184,182,183] (see section 1.6).

VOCs are generated under normal conditions of temperature and pressure from some solids or liquids. VOCs are emitted from a wide variety of anthropogenic sources, including motor vehicles, chemical industry facilities, refineries, factories, consumer and commercial products. VOCs also are introduced in the atmosphere by natural sources, such as trees (vegetation), bacteria, volcanoes and fossil fuel deposits among others. VOCs are among the most emitted air pollutants by the chemical and petrochemical industries. Furthermore, VOCs are one of the main responsible for photochemical reaction in the atmosphere causing various environmental risks, such as the formation of tropospheric ozone[185] (Figure 45 a). The presence of VOCs in the atmosphere represents a threat to human health. According to World Health Organization (WHO), VOCs can enter the human body,

mainly by way of air or through the skin, and cause symptoms that may lead to pathologies, including asthma, atopic dermatitis and neurologic problems[186].

One important VOC, due to its health effects is the pyridine (py) (Figure 45 b). Pyridine is an organic, colorless, volatile liquid with an unpleasant odor, miscible in water and in the most common organic solvents and has a boiling point of 35 ºC, higher than benzene, 115 ºC. It is produced from coal tar, or obtained as a byproduct of coal gasification and by chemical synthesis, based on acetaldehyde, formaldehyde and ammonia[187]. It is extensively used as solvent in organic chemistry and as an intermediate in the synthesis of wide variety of industrials manufactures, such as insecticides, herbicides, pharmaceuticals, dyes, adhesives, agrochemicals, dyes and paints, rubber products, polycarbonate resins and water repellents or explosives[188,189].

Pyridine is a hazardous substance if inhaled, ingested, or absorbed through the skin or into the eyes. In humans pyridine intoxication affects the central nervous system, leading to dizziness, headache, asthmatic breathing nausea and it is also related as cause of male infertility and is considered carcinogenic as well[190].

Pyridine may be present in surface water as a result of the discharge from coking operations and oil processing and it has been also found in both subsurface and groundwater as a result of industrial activities and may, therefore, lead a risk of contamination of groundwater aquifers[191]. For these reason and due to its high water solubility, pyridine could be considered a teratogenic compound categorized as a priority pollutant by the United States Environmental Protection Agency (USEPA)[192,193]. Pyridine can also be found in the outdoor air, in areas nearby to industrial or waste-treatment facilities, and in indoor air since pyridine is a component of tobacco and marijuana smoke[191]. In addition, pyridine has been also detected in foods, because it is a byproduct of the food putrefaction processes[194], therefore its detection is very important in the food industry nowadays.

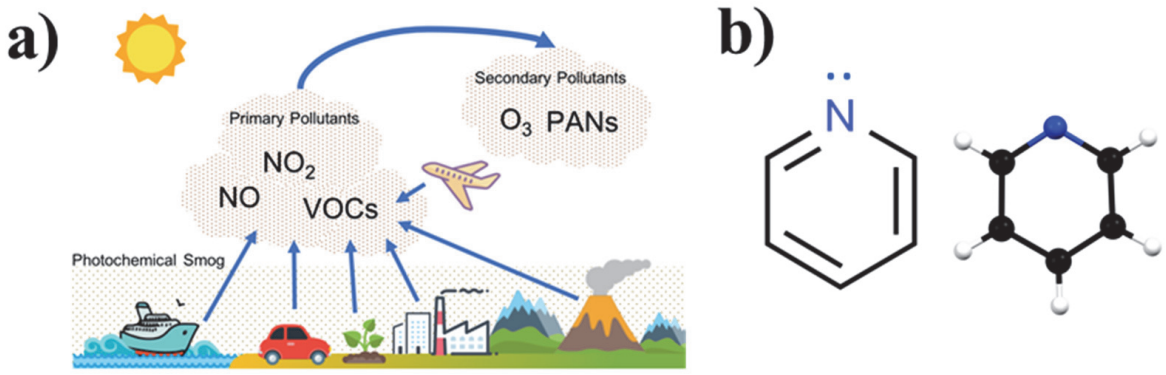

Figure 45. a) Scheme of the sources emitting VOCs[195] and b) Chemdraw illustration of a pyridine molecule.

Therefore, due to their potential damage to air/soil/water systems, monitoring and treatment of VOCs, and in particular pyridine, is a critical task in environmental management, which can have both short-term and long-term impacts on human health as well as on the natural ecosystem.

Many methods that provide specific responses such as kinetic spectrophotometry, high performance liquid chromatography (HPLC), spectrophotometry, gas chromatography fluorometric/colorimetric detection, optical fiber sensor, quartz crystal microbalance and electrical field-stimulated liquid-phase micro extraction have been used to determine this type of substance, but they are too expensive for routine measurements, non-portable and not all have high selectivity and low energy. Consequently, the detection of VOCs by simple media involving only low-cost technology is an attractive research objective due to the increasing extent of harmful waste. In an attempt to perform portable and low-cost, control and treatment techniques for VOCs, many types of materials have been developed, including activated carbon, nanoparticles, nanocomposites, graphite, zeolites, metal oxides, carbon nanotubes and coordination polymers[196]. As mentioned in previous chapters, coordination polymers can be porous or non-porous materials and they can be used in many applications such as sensors and guest exchange reactions. Both materials, porous and non-porous, can absorb molecules, producing a response easy to measure[124], such as a change in color or any other macroscopic property. Therefore, these vapochromic materials are excellent candidates for detection applications.

Here, a vapochromic 2D Fe(II) coordination polymer, $\{FeCl_2(pyz)_2\}_n$ (**1**), where *pyz* is pyrazine, is used as sensing material. This polymer undergoes reversible SCSC transformations on exposure to pyridine vapor. The uptaking process is accompanied by a color change, first from red to orange (**2**) and finally, orange to yellow, obtaining the final compound (**3**). Interestingly, the initial structure (**1**) can be regenerated once compound **3** is introduced into a concentrated solution of pyrazine, obtaining a reusable sensor.

3.1. SYNTHESIS OF COMPOUNDS 1, 2, 3, PMMA/1, PMMA/3, PDMS/1 AND PDMS/3.

3.1.1. Synthesis of $\{FeCl_2(pyz)_2\}_n$ (1)

$FeCl_2 \cdot 4H_2O$ (81.12 mg, 0.408 mmol) and ascorbic acid (approx. 3 mg) were introduced in acetonitrile (2.5 ml) and then added drop by drop to a suspension of pyrazine (96 mg, 1.19 mmol) in the same solvent (2.5 ml). The mixture was stirred for 15 minutes at room temperature. A red solid was obtained in 31% yield (57 mg)

after filtering and washing the previous suspension with acetonitrile. The red solid was recrystallized in methanol at 50 °C. Red crystals (**1**) suitable for X-ray diffraction were obtained by evaporation 3 days after.

FTIR (neat, cm^{-1}): 1667 (w), 1482 (w), 1411 (s), 1376 (m), 1154 (s), 1116 (s), 1087 (s), 1052 (s), 989 (w), 813 (s), 463 (s), 443 (m), 417 (m) (Figure 53 b). Elemental analysis calculated (%) for $FeN_4C_8H_8Cl_2$. C 33.43, H 2.81 N 19.53; found C 33.70, H 2.58 N 19.75.

3.1.2. Synthesis of $\{FeCl_2(pyz)_2(py)_2\}_n$ (2)

Single crystals of **1** were placed in a screw vial for chromatography (diameter 12 mm, height 32 mm). Afterwards, this tube was placed in a clear glass simple vial (diameter 27 mm, height 55 mm) containing a saturated atmosphere of pyridine at room temperature. The vial was sealed to allow a gas /solid phase reaction between the pyridine and **1**. One day after, orange crystals suitable for X-ray diffraction analyses were obtained (**2**).

FTIR (neat, cm^{-1}) of **2**. 1652 (w), 1602 (w), 1482 (w), 1415 (s), 1164 (m), 1117 (s), 1053 (s), 813 (m), 789 (w), 755 (s), 693 (w), 632 (w), 464 (s), 414(w) (Figure 53 b). Elemental analysis calculated (%) for $FeN_4C_8H_8Cl_2$. C 46.06, H 3.87 N 15.35; found C 46.22, H 3.68 N 15.12.

3.1.3. Synthesis of $[FeCl_2(py)_4]\cdot H_2O$ (3)

Single crystals of **2** were placed in a screw and follow to previous procedure. The vial was sealed to allow a gas /solid phase reaction between the pyridine at room temperature. After one day of exposure to pyridine vapors resulted in a complete replacement of pyrazines groups, giving rise to the final compound (**3**) in the form of yellow crystals which can be also analysed by means of SCXRD.

FTIR (neat, cm^{-1}) of **3**: 1632 (w), 1597 (m), 1571 (w), 1484 (m), 1443 (s), 1246 (m), 1151 (m), 1073 (m), 1035 (s), 1006 (m), 984 (w), 944 (w), 878 (w), 755 (s), 694 (s), 621 (m), 420 (s) (Figure 53 b). Elemental analysis calculated (%) for $FeN_4C_{20}H_{20}Cl_2.2H_2O$ C 50.13, H 5.05 N 11.69; found C 50.39, H 5.30 N 11.75.

3.1.4. Regeneration of 1 from 3

A pyrazine chloroform solution (70 mg/ml) was placed in a glass vial provided with a plastic lid. Single crystals of **3** (20 mg) were added to the pyrazine solution and the vial was closed immediately. When single crystals of **3** where left over 3 days (the solution being renewed each day) in contact with the pyrazine concentrated

$CHCl_3$ solution, the red crystals underwent a color change, first, from yellow to orange and then from orange to red, thus, single crystals of **1** were reobtained.

FTIR (neat, cm^{-1}) of regeneration of **1**: 1655 (m), 1638 (m), 1480 (w), 1410 (s), 1375 (m), 1152 (s), 1115 (s), 1050 (s), 987 (w), 812 (s), 460 (s), 443 (s), 417 (m) (Figure 54 b).

3.1.5. Synthesis of PMMA/1

The composite material was elaborated by a mix of a suspension of $\{FeCl_2(pyz)_2\}_n$ powder (20 mg, 0.067mmol) in $CHCl_3$ (0.2 ml) over a solution of PMMA (20 mg) in $CHCl_3$ (0.2 ml). This suspension was mixed with a silicon substrate (1×1 cm^2) let dry unperturbed, obtaining **PMMA/1**.

FTIR (neat, cm^{-1}) of **PMMA/1**: 3337 (w), 3108 (w), 2995 (w), 2948 (w), 1730 (s), 1683 (m), 1652 (m), 1484 (m), 1440 (m), 1415 (s), 1376 (m), 1262 (m), 1240 (m), 1193 (m), 1155 (s), 1116 (s), 1052 (s), 988 (m), 844 (m), 814 (s), 792 (s), 750 (m), 684 (m), 465 (s), 418 (s) (Figure 58 a).

3.1.6. Synthesis of PMMA/3

PMMA/1 was placed in a screw vial for chromatography (diameter 12 mm, height 32 mm). Afterwards, this tube was placed in a clear glass simple vial (diameter 27 mm, height 55 mm) containing a saturated atmosphere of pyridine at room temperature. 15 hours after a yellow film was obtained (**PMMA/3**).

FTIR (neat, cm^{-1}) of **PMMA/3**: 3319 (w), 3064 (w), 3001 (w), 2949 (w), 1726 (s), 1641 (m), 1601 (s), 1485 (s), 1445 (s), 1387 (m), 1364 (m), 1267 (w), 1239 (s), 1219 (s), 1191 (s), 1149 (s), 1081 (s), 1073 (s), 1036 (s), 1010 (m), 985 (m), 878 (w), 841 (m), 812 (w), 795 (w), 755 (s), 693 (s), 631 (s), 622(m), 468 (m), 421 (s) (Figure 58 a).

3.1.7. Synthesis of PMMA/1'

PMMA/3 was placed in contact with the pyrazine ethanol solution (70 mg/ml) for more 5 days (the solution being renewed each day), **PMMA/3** suffered a color change from yellow to yellow/orange, giving rise an intermediate composite, **PMMA/1'**.

FTIR (neat, cm^{-1}) of **PMMA/1'**: 2958 (m), 1724 (s), 1484 (m), 1448 (s), 1437 (s), 1412 (m), 1390 (m), 1260 (s), 1191 (s), 1188 (s), 1146 (s), 1667 (s), 1022 (s), 991 (s), 908 (m), 842 (s), 798 (s), 753 (s), 684 (m), 485 (s), 463 (s), 413 (s) (Figure 59).

3.1.8. Synthesis of PDMS/1

PDMS/1 film was prepared by mixing $\{FeCl_2(pyz)_2\}_n$ powder (40mg) and 20 mg of dimethylvinyl-terminated dimethylsiloxane (PMDS) to obtain a uniform mixture. Subsequently, the film was spin-coated on a Petri dish and placed in the oven at 70 ºC during one hour, to end polymerization.

FTIR (neat, cm^{-1}) of **PDMS/1**: 2962 (m), 2904 (w), 1638 (w), 1597 (m), 1484 (m), 1443 (m), 1412 (m), 1259 (s), 1215 (m), 1071 (s), 1016 (s), 864 (s), 843 (s), 794 (s), 755 (s), 694 (s), 621 (m), 601 (m), 462 (s) (Figure 58 b).

3.1.9. Synthesis of PDMS/3

PDMS/1 was inserted in a screw vial for chromatography (diameter 12 mm, height 32 mm). Afterwards, this tube was placed in a clear glass simple vial (diameter 27 mm, height 55 mm) containing a saturated atmosphere of pyridine at room temperature. After five hours a yellow film was obtained (**PDMS/3**).

FTIR (neat, cm^{-1}) of **PDMS/3**: 2962 (m), 2900 (w), 1663 (w), 1481 (w), 1448 (w), 1415 (m), 1257 (s), 1160 (m), 1066 (s), 1046 (s), 1013 (s), 861 (s), 844 (s), 792 (s), 756 (s), 692 (m), 601 (m), 509 (m), 460 (m) (Figure 58 b).

3.1.10. Regeneration of PDMS/1 from PDMS/3

PMMA/3 was immersed in an aqueous solution with pyrazine (70 mg/ml), the yellow film experienced an immediate color change from yellow to red, and **PDMS/1** was reobtained in a 100% yield

FTIR (neat, cm^{-1}) of regeneration of **PDMS/1**: 2962 (m), 2904 (w), 1638 (w), 1597 (m), 1484 (m), 1443 (m), 1411 (m), 1258 (s), 1049 (s), 1014 (s), 863 (s), 843 (s), 793 (s), 757 (s), 688 (s), 621 (m), 601 (m), 461 (s) (Figure 59).

3.2. RESULTS AND DISCUSSION

3.2.1. Synthesis and structural study of 1

Red crystalline $\{FeCl_2(pyz)_2\}_n$ complex (**1**) was obtained by reacting pyrazine with $FeCl_2 \cdot 4H_2O$ in acetonitrile. Slow evaporation of the red powder in a methanolic solution, led to red cube-shaped single crystals, suitable for Single-Crystal X-Ray Diffraction (SCXRD) (Figure 46).

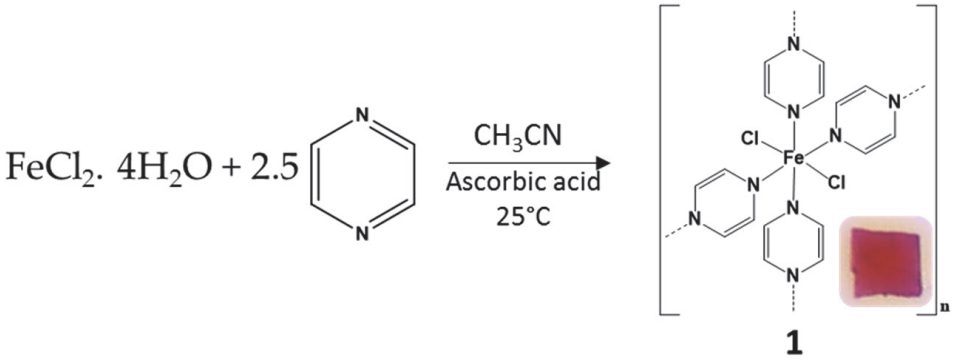

Figure 46. Schematic representation of the synthetic reaction to obtain **1** (including a picture of a single red crystal).

The structure of **1** was collected at 100 K in ALBA synchrotron. **1** crystallized in the orthorhombic crystal system (space group *Cmce*) (ANNEX B 1) and displays a structural arrangement similar to those following the general formula $\{MCl_2(pyz)_2\}_n$[197,198,199].

The lattice consists of one crystallographically independent iron (II) site in a $[Fe^{II}N_4Cl_2]$ octahedral environment. Two chloride atoms occupy the axial positions whereas the equatorial positions are filled by four pyrazines ligands (Figure 47 a).

The pyrazine rings in *trans* positions are tilted 88.36° with respect to the N-Fe-N plane. In addition, each pyrazine group acts a bidentate ligand, thus, binding adjacent Fe(II) sites resulting in the formation of $\{Fe\text{-}pyz\}_n$ layers stacking along b axis (Figure 47 b). The Fe-N and Fe-Cl distances are 2.221 and 2.399 Å respectively, in agreement with an iron(II) high-spin (HS) state[125,200,168] (ANNEX B 2).

The layers alternate so that the iron atoms in one layer lie vertically above/below the centers of the Fe-(pyz) squares defined along the a-c plane. The shortest distance between two consecutive layers, determined by Mercury program, is 5.26 Å. Hydrogen bond interactions between the Cl atoms in one sheet and the hydrogens of the pyrazines groups in the adjacent layer occur along the b axis. The average Cl-H(pyrazine) bond lengths is 2.927 Å[201] (Cl-C: 3.555 Å) (Figure 47 c, ANNEX B 2).

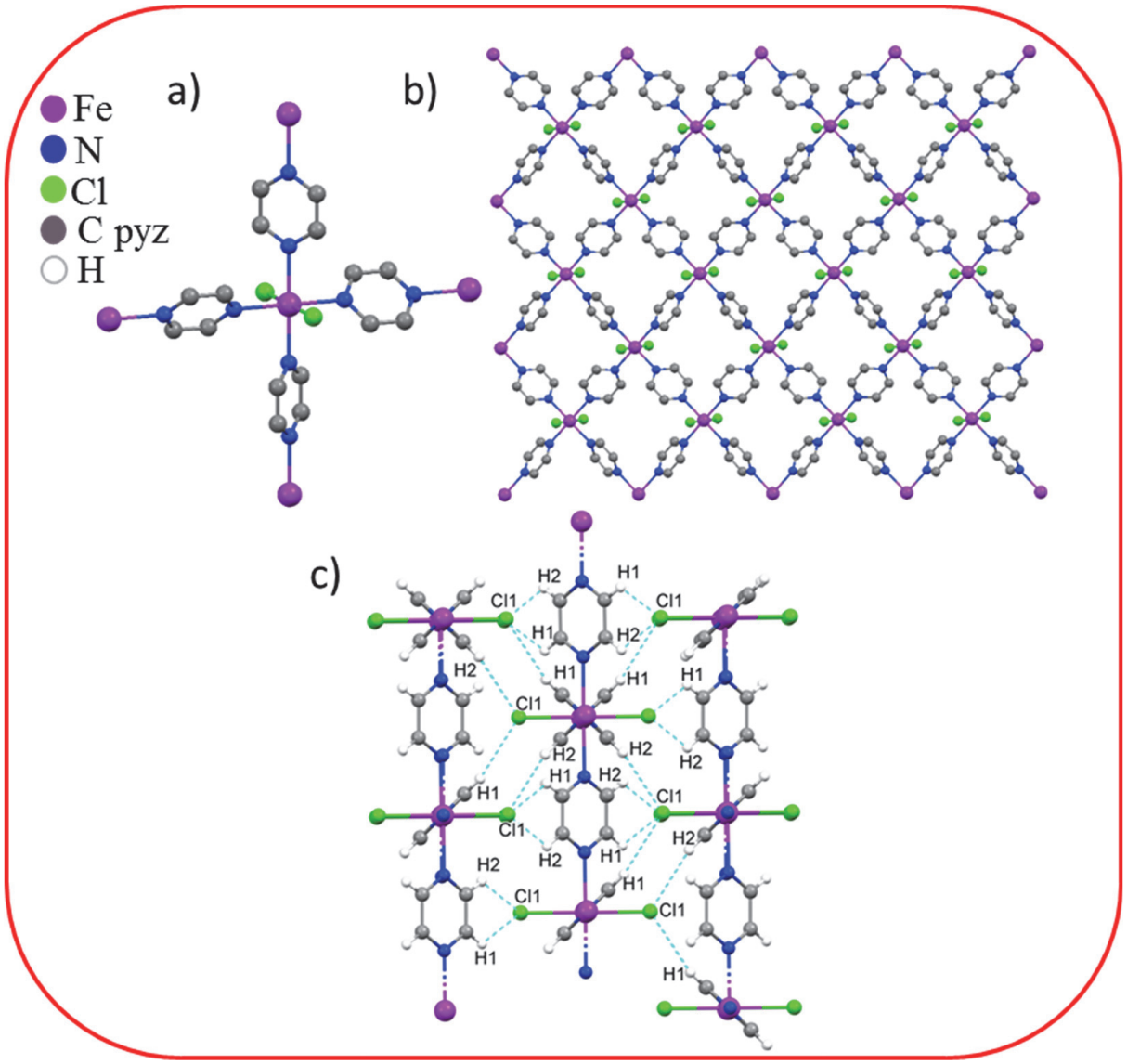

Figure 47. MERCURY representation of **1**. a) $[Fe^{II}N_4Cl_2]$ octahedral environment. b) $\{Fe\text{-}pyz\}_n$ layers stacking along b axis and c) Main hydrogen interactions.

3.2.2. Surface area study of 1

Brunauer–Emmett–Teller (BET) surface area analysis was performed to evaluate the surface area and pore size of **1**. The nitrogen sorption revealed a type II isotherm, (Figure 48) which is characteristic of non-porous and macroporous compounds[177]. The pyrazine and chorine ligands partially filled the interlayer region, thus, a low specific surface area (*i.e.* 50.73 $m^2\ g^{-1}$), was observed. Therefore, as it occurred in the compounds of the previous chapters, this compound is non-porous due to the hindrance of the pores by the ligands and the chloride atoms.

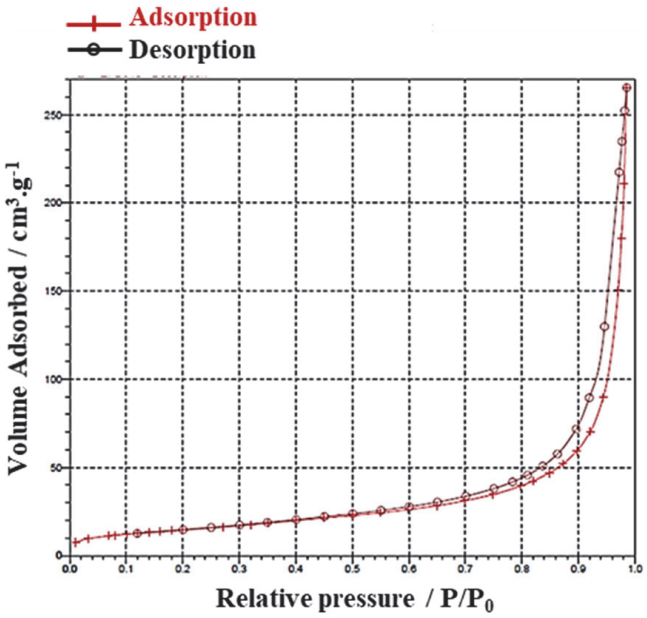

Figure 48. Nitrogen gas sorption isotherm at 78 K for compound **1** (crosses, adsorption; open circles, desorption). P/P_0 is the ratio of gas pressure (P) to saturation pressure (P_0), with P_0 being 716 torr.

3.2.3. Sensing study of 1 and SCSC transformations accomplished

In spite of the pore hindrance, the absorption of small molecules has been tested, following the reported protocol in section 2.2.5. For that purpose, single crystals of **1** have been exposed to several volatile molecules (pyridine, methylamine, pyperidine, TEA, pyrrole and dimethylformamide (DMF)). All these new attempts were characterized by different techniques (optical reflectivity, FTIR spectroscopy, X-Ray diffraction and TGA) to study the uptaking process.

Unfortunately, measureable changes have only been recorded when crystals of **1** were placed under a pyridine saturated atmosphere at room temperature for two days. The starting compound was found in the rest of the VOC expositions (methylamine, pyperidine, TEA, pyrrole and DMF). Thus, we focused on studying this process. Remarkably, the first macroscopic modification was noticed by naked-eye evidence when crystals of **1** were placed under a saturated atmosphere of pyridine. Two color changes are reported, first from red to orange (from now on, **2**) and from orange to yellow (**3**).

This color change associated with both the SCSC **1→2→3** transformation and the bulk was monitored and recorded by optical reflectivity experiments under a MOTIC SMZ-171 optical stereoscope coupled with a MOTICAM 3 (see Figure 49). In the coming sections, these new compounds (**2** and **3**) will be characterized by X-ray diffraction, FTIR spectroscopy and TGA experiments.

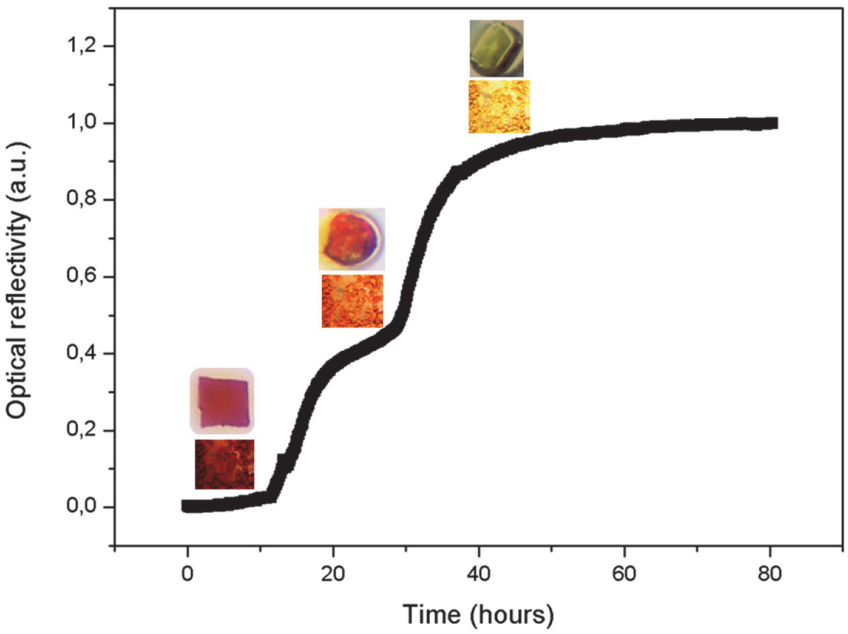

Figure 49. Optical reflectivity variation with time over pyridine exposure to **1** (powder and crystal form)**.**

Figure 49 shows the evolution of the reflectivity *versus* time. The intensity associated with the presence of red crystals of **1** remains constant for 11 hours. Afterwards, a sharp increase takes place over 8 hours. This observation is in agreement with the color evolution from red to orange, *i.e.* the **1**→**2** gas/solid phase transformation (Figure 49 and Figure 50). Then, an increasing low intensity value remains for the next 6 hours, which shows that intermediate product **2** is stable under such conditions and can be isolated.

Finally, a second drastic increase of the intensity occurs over 11 hours (Figure 49). Such change in intensity corresponds with the color change, from orange to yellow, that correlates well with an ongoing reaction where atmospheric pyridine replaces the remaining pyrazine groups in **2**, thus, leading to the final product **3** (Figure 49 and Figure 50).

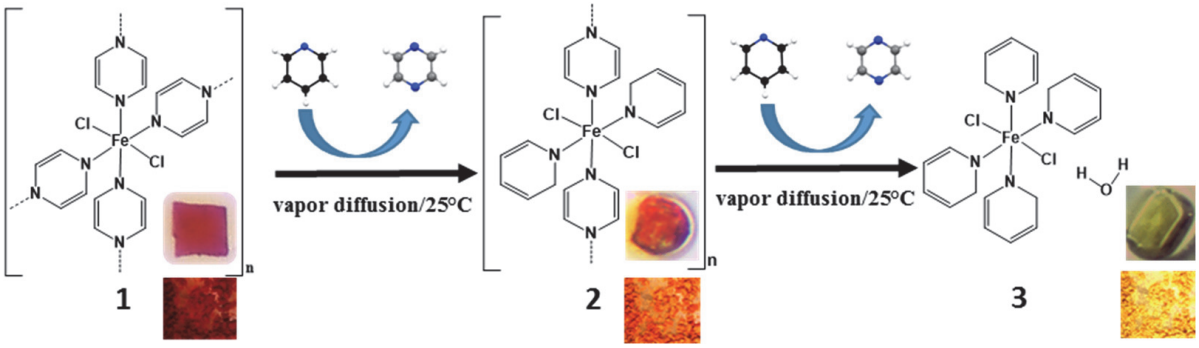

Figure 50. General scheme of the SCSC and bulk transformations of **1** after exposure to pyridine vapors, giving rise to **2** and **3**.

The color variation, which can be seen by naked-eye, is in agreement with the reflectivity curve displayed on Figure 49 and can be understood considering that the lighter the color, the higher the reflectivity, red-orange-yellow color, thus, intensity increases in the order **3**>**2**>**1**.

3.2.4. Structural study of compounds 2 and 3

Crystalline structures of **2** and **3** were also measured at 100 K by X-ray diffraction ALBA synchrotron.

2 exhibits the same crystalline system as **1** (orthorhombic) although it displays a different space group (Pbca) (ANNEX B 1). In this case, two pyrazines groups have been replaced by two pyridines, thus, the crystallographically independent iron (II) center is octahedrally coordinated to two pyrazine ligands, two chloride atoms and two pyridines, leading to the $[FeCl_2(pyz)_2(py)_2]_n$ formula (Figure 51 a). This replacement might have been assisted through the intercalation of the pyridines by π–π intermolecular interaction between pyridines and pyrazines. The average Fe-N(py), Fe-N(pz) and Fe-Cl distances are in the range (2.258-2.395 Å) of those characteristics of Fe (II) centers in the HS state[125,200,168] (see ANNEX B 2).

Just like in **1**, the pyrazine groups connect two neighboring iron atoms resulting in the formation of 1D polymeric chains that run along the b axis because the pyridine is only coordinated by the N donor atom. The chains are stacked along the crystallographic c direction, thus, defining layers spaced apart 6.702 Å (Figure 51 b). Intermolecular contacts in the form of hydrogen bonds take place along a axis between the chloride atoms from one chain and the hydrogen atoms of the pyrazine rings in an adjacent chain with Cl_1-H_7 distance of 2.947 Å. Moreover, hydrogen bonds also occur between the hydrogen atoms of the pyridines and the chloride atoms in a consecutive chain along the c axis, due to the torsion of the former ligands (Cl-H_3 distance, 2.762 Å) (Figure 51 c, see ANNEX B 2).

In **3**, the remaining pyrazine groups in **2** have been replaced by pyridine groups. The crystal structure of $[FeCl_2(py)_4]\cdot H_2O$ was reported in 1978 for the first time[202]. Herein, a remarkable structural change takes place due to the SCSC reaction and is revelled when comparing the crystal structure of **1** with that of **3**. The latter features the monoclinic crystal system (P21/n space group) instead of the orthorhombic system exhibited by both **1** and **2**. In **3** two crystallographically independent chloride atoms are axially bonded to an independent iron (II) center. The equatorial positions are occupied by non-equivalent pyridine ligands, providing the metal center with a distorted octahedral geometry (Figure 52 a). In this case, the pyridine rings are tilted 74.35° about the N-N axes to the plane of the iron; this is a little lower than compound **1**. Since pyridine can only act as a monodentate ligand, a 0D polymer is formed. The distances between Fe-N_1 (py), Fe-N_2, Fe-N_3, Fe-N_4 are 2.251 Å, 2.267 Å, 2.242 Å, 2.245 Å, respectively, and the distances between Fe-Cl_1

and Fe-Cl_2 are 2.419 Å and 2.419 Å, respectively, indicating that the Fe (II) centers are in the HS state just like **1** and **2** (ANNEX B 2).

SCXRD data also shows the presence of a molecule of water *per* iron center. The presence of this water molecule makes the Cl atoms and the four pyridine ligands crystallographically non-equivalent as it has been observed in the distances. The oxygen atom is located 3.331 Å from Cl(2). The water molecule lowers the symmetry of the unit cell until the point that both Cl atoms and the four pyridine groups become crystallographycally independent (i.e. <Fe-$N_{1,2,3,4}$> = 2.251 Å, 2.267 Å, 2.242 Å, 2.245 Å, respectively and <Fe-Cl_{12}> = 2.419 Å, 2.419 Å, respectively) (see ANNEX B 2).

The hydrogen atoms in the water molecule forms intramolecular hydrogen bonds with two chloride atoms from two different neighbouring iron centers (Figure 52 b). The bond distances Cl_1-H_{1A} and Cl_2-H_{1B} being 2.369 Å and 2.236 Å, respectively, are in the range of the expected values for hydrogen bonds[201].

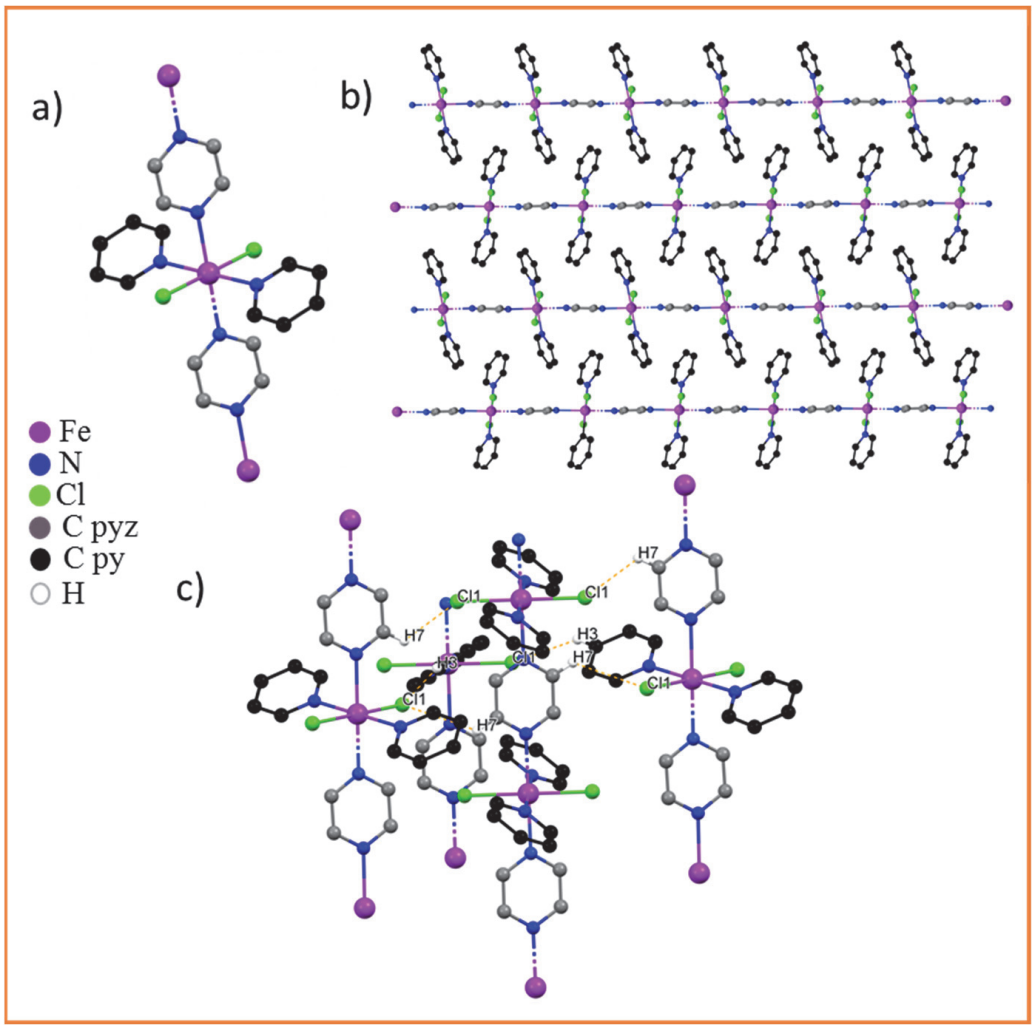

Figure 51. Crystal structure of **2**. a) [$Fe^{II}N_4Cl_2$] octahedral environment. b) [$FeCl_2(pyz)_2(py)_2]_n$ layers stacking along the c axis. c) Main hydrogen interactions.

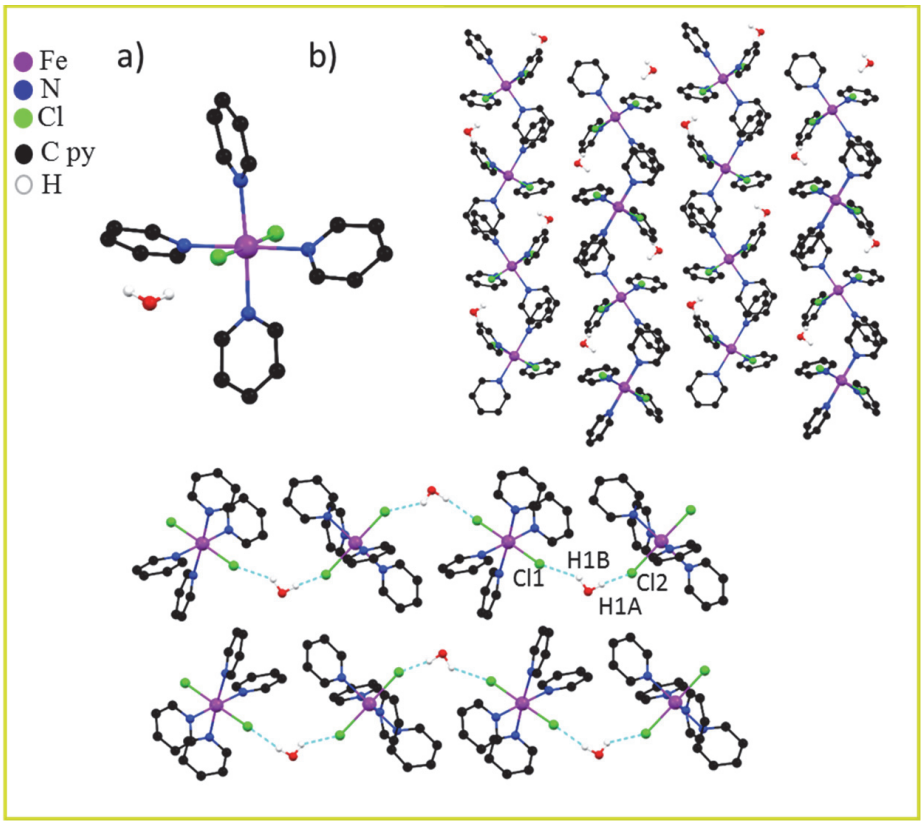

Figure 52. Crystal structure of **3**. a) $[Fe^{II}N_4Cl_2]$ octahedral environment. b) Discrete units of $[FeCl_2(py)_4]\cdot H_2O$ along a axis. c) Main hydrogen interactions of **3**.

3.2.5. X-ray Powder Diffraction (XPRD), FTIR spectroscopy and TGA studies of 1, 2 and 3.

These SCSC transformations were also monitored by X-ray powder diffraction, FTIR spectroscopy and TGA experiments. For this purpose, 10 mg crystalline samples **1**, **2** and **3**, previously isolated by optical reflectivity, were used.

Firstly, simulated X-ray diffraction patterns for **1-3** have been compared with the experimental data obtained for the synthetized crystalline samples of **1-3** (Figure 53 a). Nearly identical spectrum was obtained for **1** with simulated. In the case of **2**, the experimental spectrum is very similar to the simulated one, although there are some displaced signals and also new ones emerge, presumably due to the previous treatment of the sample, grinding, before it is measured by XPRD analysis. A similar situation occurs with **3**. By milling the sample, the guest water molecule may be released. Figure 53 a, compares the experimental spectrum of **3** with the simulated spectrum of the same compound without water, which was published by Gary J. Long[202]. It can be observed that **3** shows signals that closely resembles the spectrum without the water molecule confirming the total loss of water. As it was expected, the diffraction patterns of **1-3** do not match, thus, corroborating the

occurrence of drastic structural changes when going from **1** to **3**. In addition, the crystal symmetry lowering when going from **1** to **3** is reflected by a minor number of peaks in the latter compared to the former.

FTIR spectroscopy applied on **1-3** confirmed the occurrence of the **1→2→3** SCSC gas/solid phase reaction. The spectrum collected for **1** at room temperature shows characteristic vibrational modes corresponding to the presence of pyrazine groups (Figure 53 b). For instance, the stretching bands in pyrazine (C=C and C=N) can be seen in the frequency interval 1595-1440 cm^{-1} while the bending of the hydrogen atoms attached to the carbons in the pyrazine ring lead to four bands in the [1163-1056] cm^{-1} frequency range. Finally, the absorption band at 463 cm^{-1} correspond to γ [ring(pz)] vibration (Figure 53 b).

In the spectra collected for **3** at the same temperature, the bands associated with the skeletal vibration in pyridine occur at higher frequencies, [1595-1440] cm^{-1} range. The same upshift can be seen for CH aromatic bending in the pyridine ring taking place in the frequency interval [1216-1003] cm^{-1}. The opposite trend may occur regarding γ [ring(py)] vibration at 419 cm^{-1} (Figure 53 b). As expected, the spectra of **2**, show the presence of pyrazine rings (ν [ring pyz] = 1411 cm^{-1}, β [C-H(pyz)] = 1118; 1056 cm^{-1}, γ [ring(pyz)]= 463 cm^{-1}) and pyridine groups (β [C-H(py)] =1154; 1011; 755; 619 cm^{-1}, γ [ring(pyz)] = 463 cm^{-1}) (Figure 53 b).

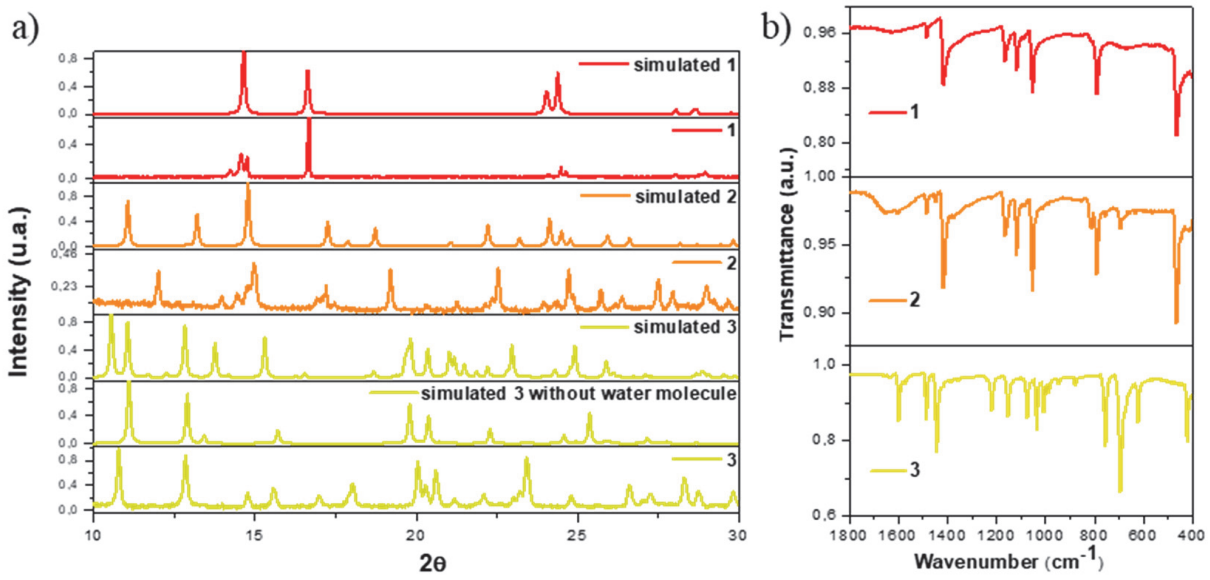

Figure 53. a) Simulated and experimental powder X-ray diffraction patterns of compounds **1, 2** and **3**. b) FTIR spectra of compounds **1**, **2** and **3**.

To provide an insight into the thermal stability of the compounds, thermogravimetric analyses were carried out for **1-3** (ANNEX B 3, ANNEX B 4 an ANNEX B 5). Apparently, the first weight loss of **1** started above 100°C (ANNEX B 3) whereas **2** began at 40°C (ANNEX B 4). In **3**, the weight loss of 3.927 % taking

place above 50 ºC, corresponds to the release of the water molecule that was observed by X-ray diffraction (ANNEX B 5).

3.2.6. Reversibility study of compound 3

Interestingly, when yellow single crystals of **3** are placed in a concentrated pyrazine $CHCl_3$ solution (70 mg/ml), an instantaneous color change from yellow to orange occurs.

The new specie will be referred to as **2'** from now. **2'** could not be determined by SCXRD. Instead, X-ray powder diffraction was collected for **2** (Figure 54 a) with a first straightforward conclusion, the pattern compared with the MERCURY simulated from **2** reveals that both are different.

Nevertheless, one can assume that this new phase **2'** should be an intermediate specie between **2** and **3** since the infrared spectrum (Figure 54 b), shows the characteristic bands of pyrazine and pyridine groups meaning that **2'** might be $[FeCl_2pyz(py)_3]$ or $[FeCl_2(pyz)_3py]$.

Moreover, whether **2'** is kept in contact with a pyrazine saturated solution for 5 days (the solution being renewed each day), the single crystals color change from orange to red (herein after labelled as **1'**). In this case, both FTIR and the comparison with simulated X-ray pattern indicate that **1'** is similar to **1**.

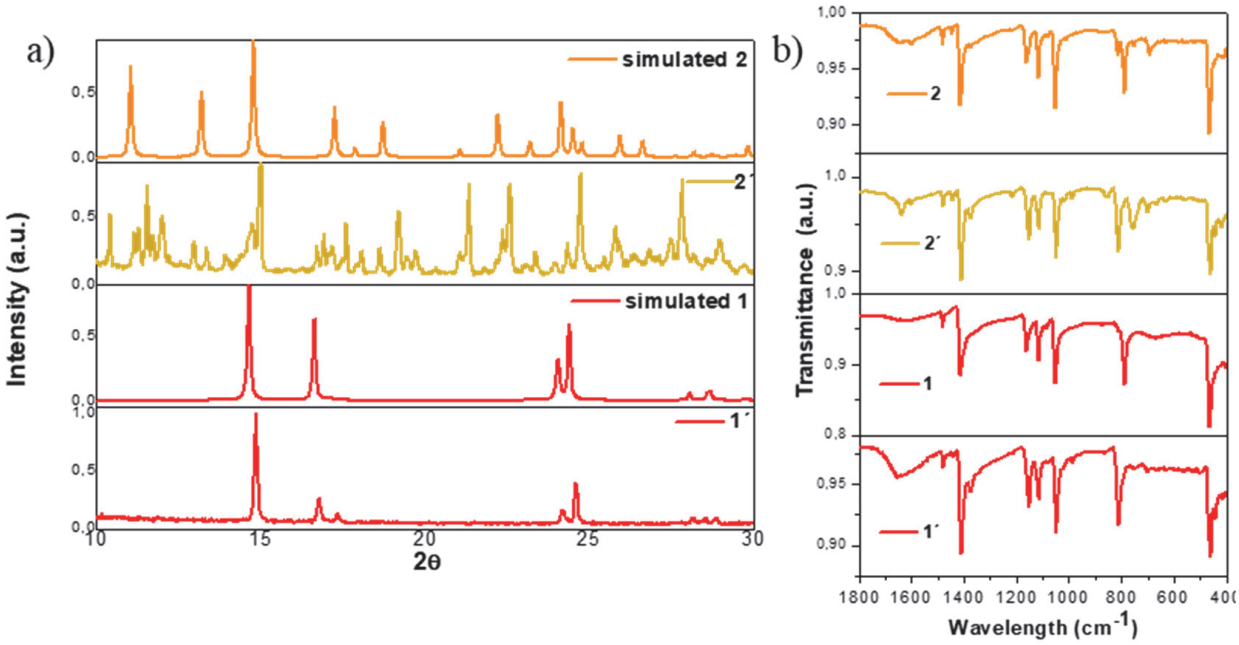

Figure 54. a) Simulated and experimental powder X-ray diffraction patterns of compounds **2**, **1** and **2'** and **1'**, respectively. b) FTIR spectra of compounds **2**, **2'**, **1** and **1'**.

Notably, XRPD measurements (Figure 54 a) together with FTIR spectra (Figure 54 b) performed on **1'** supported the occurrence of a reversible **3→intermediate→1** SCSC transformation (Figure 55). Figure 55 collects the information obtained throughout these SCSC experiments.

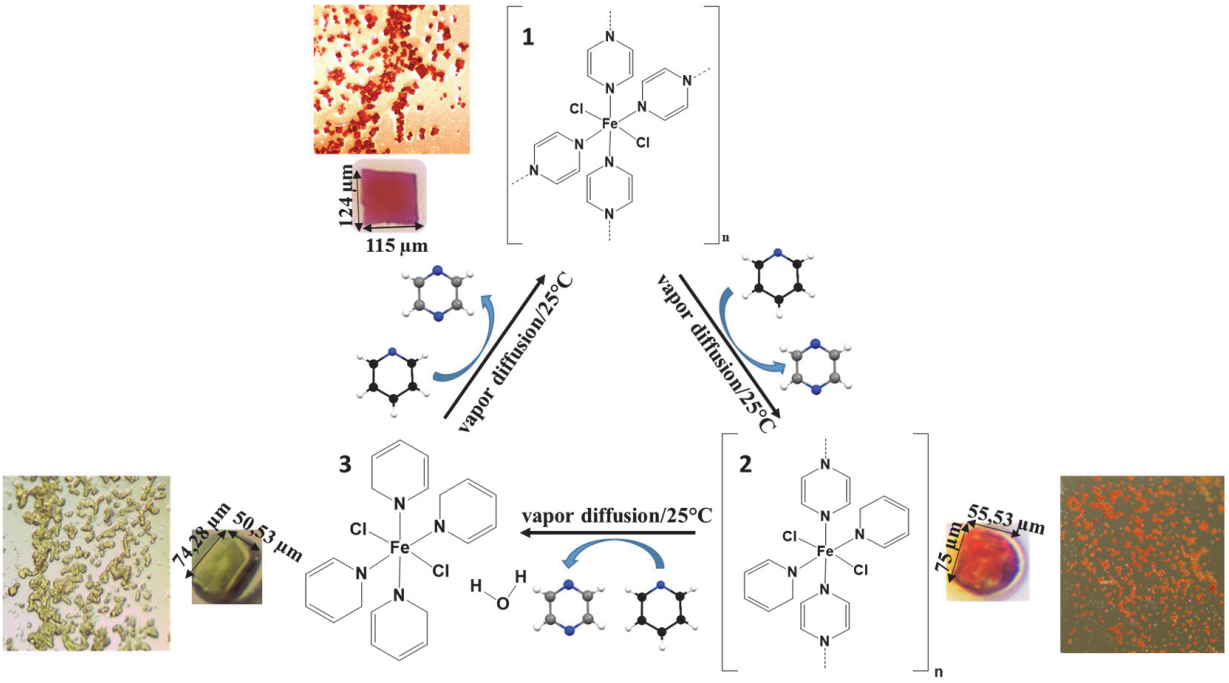

Figure 55. SCSC transformation from compound **1** to **3** in presence of pyridine vapors and the reversibility process in a saturated pyrazine solution.

3.2.7. $\{FeCl_2(pyz)_2\}_n$ complex (1) dispersed in a poly(methylmethacrylate) (PMMA) and polydimethylsiloxane (PDMS).

Nowadays, the interest in embedded coordination compound in polymers has become much more use mainly due to their integration in devices that can have potential applications in different technological fields[203].

In order to test the sensor properties of **1** in a composite, the embedding of **1** in PMMA[204] and PDMS[205] polymers was performed giving rise to **PMMA/1** and **PDMS/1**, respectively. Predictably, when **PMMA/1** (Figure 56 a) and **PDMS/1** (Figure 56 b) composites were exposed to pyridine vapors, the expected color evolution took place, first from red to orange and then, from orange to yellow, resulting in **PMMA/3** and **PDMS/3**, respectively, Figure 56.

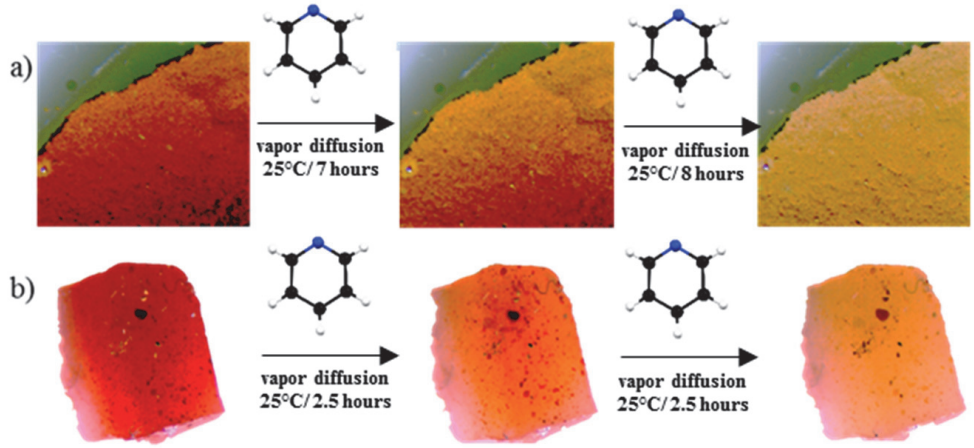

Figure 56. Color change from a) **PMMA/1** to **PMMA/3** and b) **PDMS/1** to **PDMS/3** composites in presence of pyridine vapors.

The color variation was again monitored by MOTIC SMZ-171 optical stereoscope coupled to a MOTICAM 3 (Figure 57). As it can be observed, the intensity associated with the presence of the **PDMS/1** polymer remains constant for 2.5 hours (Figure 57 a). Then, the first color change (i.e. from red to orange) takes place over 2.5 hours in **PDMS/1** composite, whereas **PMMA/1** takes 7 hours (Figure 57 b).

Secondly, a sharp increase in intensity occurs, lasting over 2.5 hours for PDMS polymer (Figure 57 a) and 8 hours for PMMA (Figure 57 b). This corresponds to a color change from orange to yellow, showing complete replacement of pyridine groups by pyrazine groups, thus leading to the final product **PDMS/3** and **PMMA/3**. The color change occurs faster with PDMS polymer due to its higher porosity and moisture absorption[204,205] with respect to PMMA.

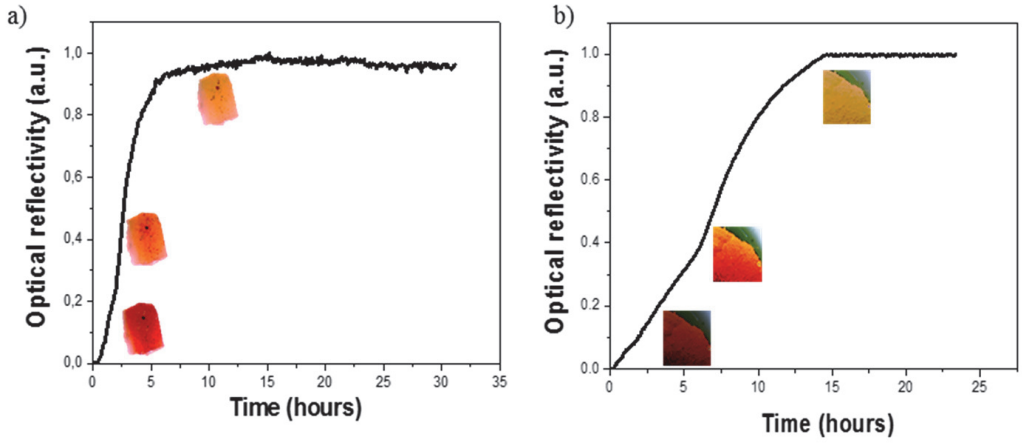

Figure 57. Optical reflectivity variation with the time of a) **PDMS/1** and b) **PMMA/1**.

The composites were also analyzed by FTIR Spectroscopy. PMMA and PMDS matrixes can be inferred by the presence of their characteristic bands. Figure 58

compares the spectra of the composites, **PMMA/1**, **PDMS/1**, **PMMA/3** and **PDMS/3**, with respect to **1** and **3**, to verify that **1** has been embedded into the polymers (PMMA and PDMS) and that the transformation has happened when these composites are exposed to pyridine. Figure 58 also shows the spectra of the polymers. As expected, the infrared spectra of both **PMMA/1** and **PMMA/3** (Figure 58 a) as well as **PDMS/1** and **PDMS/3** (Figure 58 b) display the characteristic vibrations of **1** and **3**, respectively. Minor bands are hidden by either PMMA or PDMS polymer signals (Figure 58 a and b). In view of the results achieved, it could be concluded that **1** has been embedded in both polymers and that pyrazine has been completely exchanged for pyridine, giving rise to **PMMA/3** and **PDMS/3**.

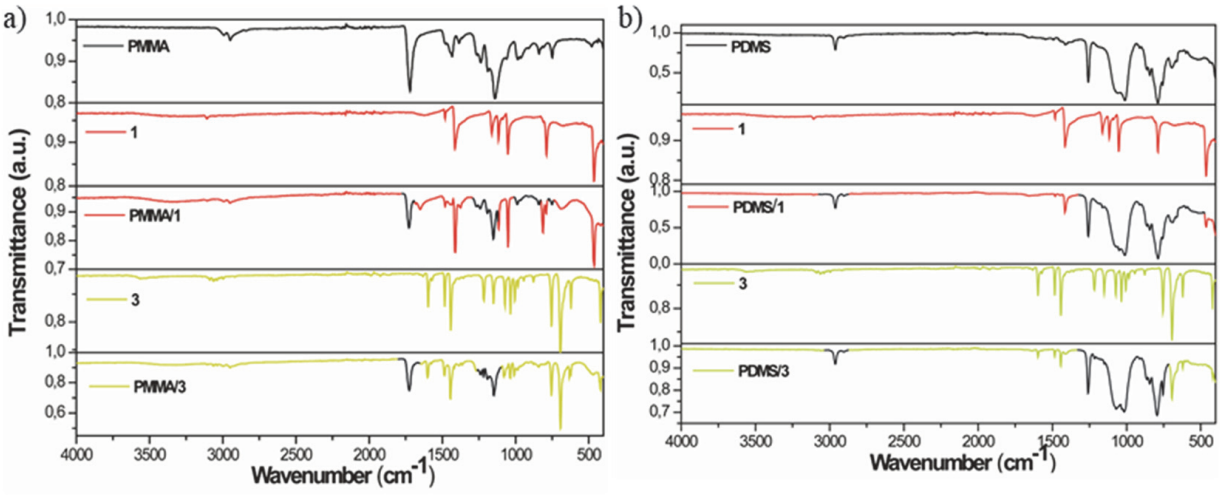

Figure 58. a) FTIR spectra of PMMA and compounds **1**, **PMMA/1**, **3** and **PMMA/3**. b) FTIR spectra of PDMS and compounds **1**, **PDMS/1**, **3** and **PDMS/3**.

As for **3**, the reversibility of both polymers was also studied. For this purpose, **PMMA/3** was placed in a pyrazine ethanol concentrated solution (70 mg/ml) for 5 days (the solution being renewed each day), and a color change from red to orange-yellow, took place leading to **PMMA/1'**. In the case of **PDMS/3** reversibility was attempted with a pyrazine water concentrated solution (70 mg/ml) giving rise to an instantaneous color change from yellow to red. The new species being **PDMS/1'**.

These novel phases defined as **PMMA/1'** and **PDMS/1'** were studied by FTIR spectroscopy (Figure 59). In Figure 59, it can be seen that an incomplete reversibility is achieved in the case of **PMMA/1'** polymer, presumably owing to its low porosity. In contrast, the FTIR spectrum of the **PDMS/1'** polymer (Figure 59) clearly matches that of the **PDMS/1** composite thus a complete reversibility is accomplished when using a much more porous polymer such as PDMS.

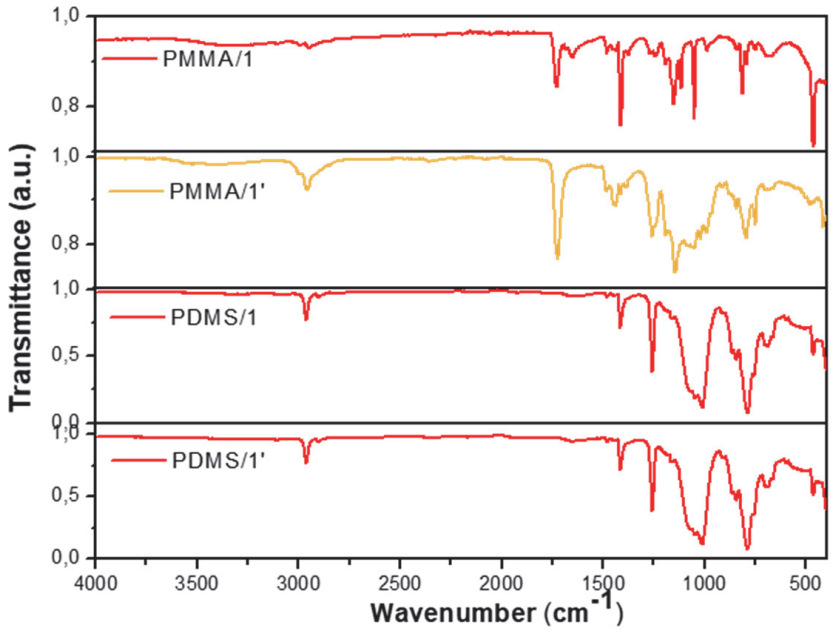

Figure 59. FTIR spectra of compounds **PMMA/1**, **PMMA/1'**, **PDMS/1** and **PDMS/1'**.

3.3. CONCLUSIONS

In summary, we have reported the synthesis and characterization of **1**, which undergoes a gas/solid phase SCSC reaction in the presence of pyridine vapors affording compound **2** where two pyrazine groups have been replaced by two pyridine rings. A vapochromic effect (i.e. color change from red to orange) indicates the **1→2** transformation. If single crystals of **2** are kept under a pyridine atmosphere for more than 6 hours, another SCSC transformation might lead to compound **3** where the remaining pyrazine groups are being replaced by pyridine ligands. A change of color from orange to yellow shows the occurrence of **2→3** reaction.

Extraordinarily, the observed ligand exchange process is fully reversible with persistence of the crystallinity, thus, obtaining a reusable sensor.

The exposure of **PMMA/1** and **PDMS/1** to pyridine vapors was also studied. In both cases the change of color from red to orange and from orange to yellow took place. Remarkably, the ligand exchange process observed is also totally reversible with the PDMS polymer, thus highlighting its potential use in reusable pyridine sensory devices. However, the low porosity of PMMA, prevented a complete reversibility of **PMMA/1'** into **PMMA/1**. In future work compound **1** will be embedded in other different polymer matrixes of technological interest.

4. DEVELOPMENT OF THE FIRST DYNAMIC CRYSTALLINE FULLERENE WITH SUPRAMOLECULAR "STICKY FINGERS" INTERACTIONS: SENSING STUDIES

Carbon-based materials have attracted tremendous scientific and industrial interest due to their wide commercial applicability over the past four decades[206,207,208]. Within this field, the fullerenes, and in particular, the fullerene [C_{60}] (the fourth allotropic form of carbon after the graphite, diamond and lonsdaleite) has considerably broadened the scope and variety of well-known carbon molecules and it is opening a completely new chapter on carbon physics and chemistry, due to its excellent redox, optical and optoelectronic properties[209,210,211,212].

The fullerene discovery took place in 1985 by H. Kroto, R. Curl and R. Smalley[213], who were awarded with the Nobel Prize in Chemistry in 1996. However, fullerenes really became manageable and chemically modifiable chemicals compounds from since 1990, when the nuclear physicists Wolfgang Krätschmer and Donald Huffman (two astrophysicists), developed a method to produce fullerenes on a multigram scale, by causing an arc between two graphite rods to burn in a helium atmosphere and extracting the carbon condensate so formed using an organic solvent. This fact opened an entirely new branch of chemistry for the chemical community with theirs famous publication in the magazine Nature entitled: "Solid C_{60}: A new form of coal"[214].

A general understanding of the term fullerene is represented as a highly symmetric cage-shaped molecule of purely carbon (with $sp^{2,3}$ hybridization) atoms positioned at the junction of a network of five-membered rings (pentagons) and six-membered rings (hexagons). In order to close into a spheroid, the C_{60} has the structure of a truncated icosahedron, constructing by exactly 12 pentagons and 20 hexagons, which are disposed in a lattice of cages and defined by single and double alternating bonds, giving it the appearance of a football ball (Figure 60). The

pentagons present are necessary to introduce the curvature, since hexagonal nets are planes. There are two kind of bonds in its structure, on one side, the [6, 6] bonds with a length of 1.37 Å, located in the fusion of two hexagonal rings; and on the other side, the [5, 6] bonds, located in the fusion of a hexagonal ring and a pentagonal ring and longer (1.45 Å).

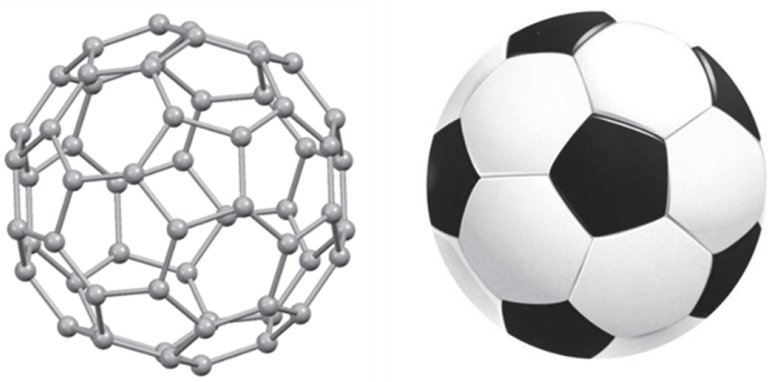

Figure 60. Representation of C_{60} fullerene and its similarity with a football ball.

Due to their spherical shape and energetically unstable double bonds within the pentagon rings, fullerenes display electron-accepting properties, meaning that fullerenes are highly electron deficient molecules. The electron deficiency creates potential reactive sites (the most reactive bonds are the double bonds [6, 6]) giving rise to new and interesting chemical transformations to be tested. Therefore, the structural uniqueness of the C_{60} molecule makes them attractive precursors for macromolecular and supramolecular chemistry.

Over the last two decades, synthetic functionalization methods[215] such as 1,3-dipolar additions[216,217], Diels-Alder reactions[218,219,220] and Bingel cyclopropanation[221] have been extensively used and optimized. In particular, the cyclopropanation reaction has undoubtedly been the most used resulting in an important number of fullerenes derivatives. This reaction is produced by the addition of 2-bromomalonate esters to C_{60} in the presence of a non-nucleophilic base (NaH or diazabicyclo [5.4.0] undec-7-ene (DBU)), which leads to the formation of a cyclopropane ring merged with the fullerene core in a union of [6,6]. Advantages of this method are: (1) exclusive addition in [6,6] double bonds position of the fullerene framework, (2) soft reaction conditions resulting in high yields and (3) the introduction of ester varieties permitting more chemical transformations. Although the Bingel protocol has been shown to be successful in the mono-functionalization [60] fullerene, the multiple functionalization of fullerenes by this method continued to be problematic because of the non-regioselectivity, which

leads to the formation of different regioisomers, due to the use of alternative malonates that contain dendritic chains or long alkylic side chains.

For this reason, Hirsch and co-workers reported in 1997 an optimized method to generate a reactive mono-halomalonate intermediate in situ, by direct treatment of the fullerene with malonates in the presence of CBr_4 and DBU[222]. Once the matter was solved by improving the synthetic method, the multiple functionalization in fullerenes could be achieved without regioselective problems. Bis-[223], tris-[224], tetrakis-[225], pentakis-[226] and hexakis-[222] functionalization C_{60} derivatives are the best known.

One of the most straight-forward approaches to obtain crystalline fullerene based advanced materials, with special electronic and structural properties, is the use of hexakis-substituted C_{60} as building blocks. The Th-symmetrical octahedral pattern owning on the hexakis-substituted C_{60} adducts (Figure 61) provides a unique and attractive spherical scaffold (cage structure) for the construction of multifunctional materials, by self-assembly, either with itself or through metal centers. The structural uniqueness combined with the awesome electronic properties makes them potentials candidates for endless applications[215].

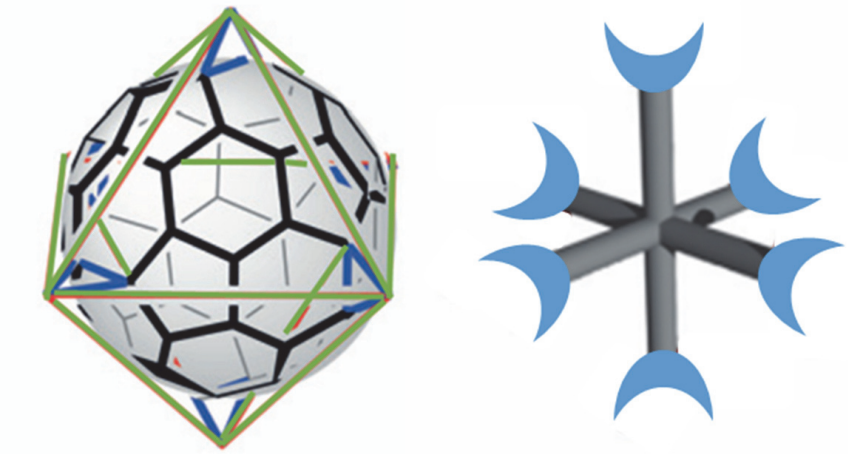

Figure 61. Schematical representation of Th symmetrical [60] fullerene hexakis.

Since the first supramolecular architecture based on hexakis-substituted C_{60} reported by Diederich and co-workers, in 1998[227], numerous efforts have been devoted to synthetize crystalline C_{60} frameworks but only few examples have been reported. In 2013 and 2014, Echegoyen and co-workers used silver[228,229] and cadmium[230] cations to synthetize 1D and 2D crystalline fullerene polymers, respectively, with the aim of carrying out future work to make 3D MOF with accessible pores to find applications in gas sorption/storage of organic molecules.

Beuerle and co-workers investigated the impact of different bonding motifs on the solid-state structure and packing. They synthetized and described different rigid

three-dimensional hexakis C_{60}-frameworks with 12 side chains. With particular emphasis on the dodecaacid adducts as the first organic scaffold to build hydrogen-bonding frameworks[231] in 2014, or in 2016 the synthesis of the first three-dimensional metal–fullerene frameworks[232], through coordination with Zinc ions. Afterwards, in 2017, they synthesized new metal-fullerene frameworks by varying the divalent metallic components, Ca^{+2}, Cu^{+2}, Cd^{+2} [233] and two new three-dimensional hydrogen-bonding frameworks based on [60]fullerene dodecaacids adducts comparing the effect on the elongation of the alkyl spacers[234].

In these works, Beuerle and co-workers tried to use these materials as supramolecular host–guest systems, but when attempting to activate the potential porous of the compounds only showed Henry behavior and no microporosity was observed resulting in low surface areas, and the activation at higher temperatures resulted in a complete collapse of the framework.

Therefore, the crystallization of stable fullerenes structures possessing porosity or showing the ability to incorporate molecules by internal structural reorganization (breathing effect) is still a challenge.

Hence, an alternative and very newfangled approach is the formation of dynamic structures (porous or non-porous acting as porous), by means of weak supramolecular interactions between molecules. Such dynamic structures can rival the porosity of conventional rigid structures while offering the ability to absorb small molecules.

In this chapter, we report for the first time how a dynamic non-porous organic molecule connected through supramolecular Van der Waals interactions, so-called "sticky fingers"[235], behaves as an excellent dynamic molecular receptor. Furthermore, the inclusion of small molecules inside this material allows an unprecedented hydrogenation reaction that occurs only in a confined crystalline space and not by traditional wet chemistry. The reaction is performed in a single-crystal-to-single-crystal (SCSC) fashion, which has allowed us to study how this material behaves upon the inclusion of these small molecules with atomic detail[125]. This study is an important breakthrough in endohedral fullerene material chemistry, which has been done in collaboration with Professor Nazario Martín and his group, who shared their knowledge in the chemistry of fullerenes.

4.1. SYNTHESIS OF COMPOUNDS 2, 3, 3A AND 4A

Materials. Chemicals and reagents were purchased from commercial suppliers and used as received.

4.1.1. Synthesis of dibutyl 2-bromomalonate (2)

To a solution of dibutyl malonate (**2**) (2 mL, 9.040 mmol) and p-toluenesulfonic acid (344 mg, 1.808 mmol) in dry DCM (120 mL) at 0 ºC, N-bromosuccinimide (1.61 g, 9.04 mmol) was added in one portion. After stirring at that same temperature for 2 h, the reaction was filtered and sequentially washed with water (3×50 mL) and brine (50 mL), dried over Na_2SO_4, filtered, and the solvent removed under reduced pressure. The resulting transparent oil (2.472 g, 8.407 mmol, 93%) was used in the next reaction step without further purification. 1H NMR (CDCl3, 400 MHz, δ): 4.83 (s, 1H), 4.23 (t, *J* = 6.6 Hz, 4H), 1.66 (m, 4H), 1.40 (m, 4H), 0.94 (t, *J* = 7.4 Hz, 6H) ppm (ANNEX C 1).

4.1.2. Synthesis of hexakisadduct fullerene (3 and 3a)

A suspension of **2** (1.63 g, 5.55 mmol) and C_{60} (200 mg, 0.278 mmol) in chlorobenzene (100 mL) is sonicated until fullerene is fully dissolved (*ca.* 15 min), the resulting solution is cooled to 0 ºC and DBU (1.66 mL, 11.11 mmol) is dropwise added. The reaction mixture is allowed to warm to room temperature and then stirred for 24 h. After quenching the reaction with water (50 mL), the organic layer is separated, dried over Na_2SO_4, filtered, and the solvent removed under reduced pressure. Resulting crude is purified by column chromatography (silica gel; CS_2/EtOAc 50:1 to remove minor adducts, then 40:1) to provide a red-orange oily solid which still contained dibutyl malonate. Addition of a few drops of MeOH followed by a small amount of hexane allowed to remove trapped starting material by sonication and decantation of the hexane, yielding an orange solid (251 mg, 0.125 mmol, 45%) (Figure 62).

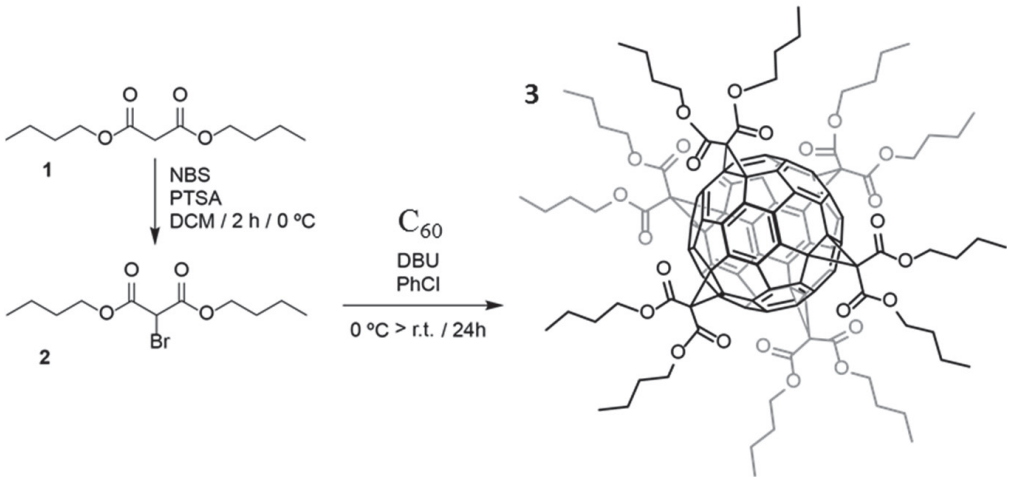

Figure 62. Synthesis of **3**; N-bromosuccinimide (NBS), p-toluenesulfonic acid (PTSA),dichloromethane (DCM), 1,8-diazabicyclo[5.4.0]undec-7- ene (DBU) [221,236].

A suspension of iron (II) tetrafluoroborate hexahydrate (8.79 mg, 0.026 mmol) and ascorbic acid (approx. 3 mg) in ethanol (4 mL) was added to a suspension of **3**, (10 mg, 0.005 mmol) in ethanol (8 mL). The orange solution was transferred into a pressure tube, sealed, and kept at 120 °C in a furnace. After 2 days, the solution was filtered and placed in a closed vial. Orange crystals (Figure 63) suitable for X-ray diffraction were formed after 4 days (80%, 8mg) (compound **3a**).^{1}H NMR (400 MHz, $(CD_3)_2CO$, δ): 4.33 (t, J = 6.4 Hz, 24H, OCH_2), 1.68 (m, 24H, CH_2), 1.41 (m, 24H, CH_2), 0.92 (t, J = 7.4 Hz, 36H, CH_3) ppm (Figure 73 and ANNEX C 2); ^{13}C NMR ($CDCl_3$, 100 MHz, δ): 164.1, 145.8, 141.3, 69.3, 66.8, 45.7, 30.5, 19.2, 13.7 ppm (Figure 75); Mass Spectrometry. (MALDI MS MS): m/z calc. for [M+1] 2006.251, found 2005.8. (ANNEX C 3); FTIR (neat, cm^{-1}): 2959 (m), 2993 (m), 2872 (w), 1740 (s), 1670 (w), 1621 (w), 1454 (w), 1385 (w), 1356 (w), 1261 (s), 1210 (s), 1118 (m), 1061 (s), 1014 (m), 964 (m), 923 (m), 806 (m), 758 (w), 726 (m), 712 (m), 669(s) 656 (m), 526(s) ANNEX C 4); elemental analysis calculated (%) for $C_{126}H_{108}O_{24}$ C 75.43, H 5.43; found C 75.12, H 5.53.

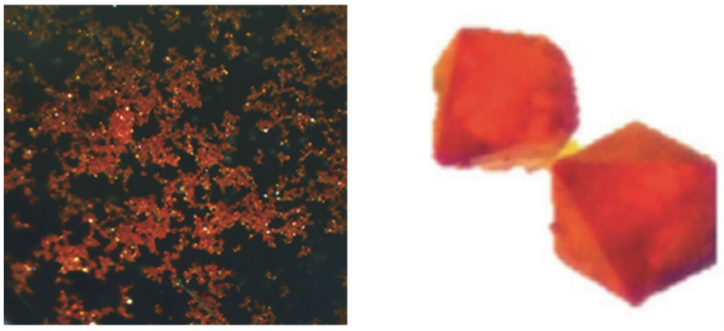

Figure 63. Orange-red single crystals of **3a**[237].

4.1.3. Synthesis of hydrogenated fullerene (4a)

Single crystals (about 5 mg) of **3** were put in a screw for chromatography (diameter 12 mm, height 32 mm). This tube was then placed in a clear glass vial (diameter 27 mm, height 55 mm) containing a saturated atmosphere of hydrazine monohydrate. The vial was sealed and kept at 67 °C for 3 days in a furnace to allow a gas phase/solid phase reaction between the organic reactant and the crystals. After this time, yellow crystals suitable for X-ray diffraction analysis, were obtained (**4a**). ^{1}H NMR ($(CD_3)_2CO$), 400 MHz, δ): 4.20 (m, 24H, OCH_2), 3.58 (s, 24H, CH) 1.66 (m, 24H, CH_2), 1.41 (m, 24H, CH_2), 0.93 (t, J = 7.4, 36H, CH_3) ppm (Figure 73, ANNEX C 5); ^{13}C NMR ($(CD_3)_2CO$), 100 MHz, δ): 167.1, 144.0, 134.3, 67.6, 66.2, 44.8, 39.8, 35.5, 31.4, 19.8, 13.9 ppm (Figure 76); Mass Spectrometry (MALDI MS MS): m/z calc. for [M-1] 2028.8, found 2030.4 (ANNEX C 6); FTIR (neat, cm^{-1}): 3334 (w), 2957 (m), 2927 (m), 2872 (w), 1725 (s), 1612 (w), 1453 (w), 1384 (w), 1307 (w), 1242 (s), 1212 (s), 1118 (m), 1078 (s), 1020 (m), 905 (m), 806 (m), 757 (m),

739 (m), 705 (w), 646 (m), 512(m) (ANNEX C 4); elemental analysis calculated (%) for $C_{126}H_{132}O_{24}$. 0.5 N_2H_4: C 73.95, N 0.68, H 6.60; found C 73.66, N 0.64, H 6.37.

4.2. RESULT AND DISCUSSION

4.2.1. Structural and physico-chemical study of compound 3a

The hexakis adduct has been synthesized by applying the well-known Bingel–Hirsch synthetic strategy[221,236] (see reaction scheme in Figure 62). The synthesis was carried out by the addition of the previously obtained bromomalonate (**2**) to a solution of C_{60} in chlorobenzene by employing DBU as a chemical base. This straightforward and reproducible method affords compound **3** in good yield (45%). Upon purification, the resulting hexaadduct was characterized by the usual analytical and spectroscopic techniques. Crystallization of **3** from ethanol was achieved using the pressure tube technique (as described in the synthesis). This method afforded large, regular, orange crystals, **3a**, that were suitable for X-ray diffraction analysis (Figure 63).

Compound **3a** crystallized in the cubic space group $Fd\bar{1}$ (Figure 64, ANNEX C 8) and it was measured at 100 K in The Advanced Light Source (ALS) Synchrotron. The unit cell is composed of eight symmetry equivalent hexaadducts placed in four unequal layers (Figure 64 b). Importantly, in contrast to the major packing driving force of pristine [60] fullerene[238], in **3a** there is no evidence of any supramolecular π–π contacts between neighboring fullerene buckyballs (Figure 64 b and c).

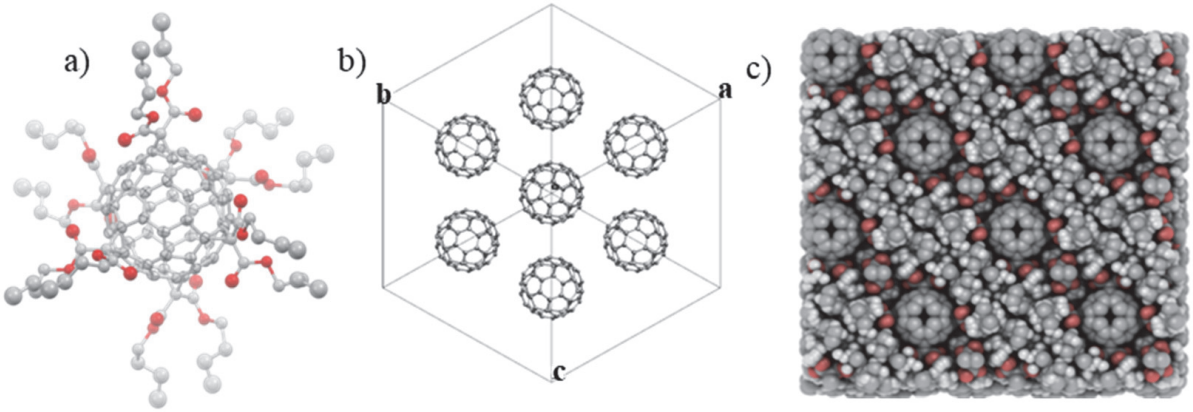

Figure 64. a) An ORTEP[239] illustration of a single hexakis adduct of [60]fullerene, including the malonate groups (only one branch of the distorted malonate structure is illustrated for clarity). b) Unit cell of **3a**. View of the 3D packing of **3a**. c) View of the packing of **3a**[237].

For **3a**, the shortest separation between two adjacent fullerenes placed in different layers is 5.2 Å, which is utterly out of the range of supramolecular π–π interactions[240]. Furthermore, the separation between fullerene entities located on the exact same position along the same axis is very long (26.879 Å) and is separated by five layers of fullerenes at different heights in the perpendicular axis; thereby, precluding any possible π–π interactions. Altogether, it is considered that the packing force must be driven by another kind of non-covalent interaction. From the single-crystal XRD structure of **3a** we can observe that six butyl malonate groups are clearly distorted.

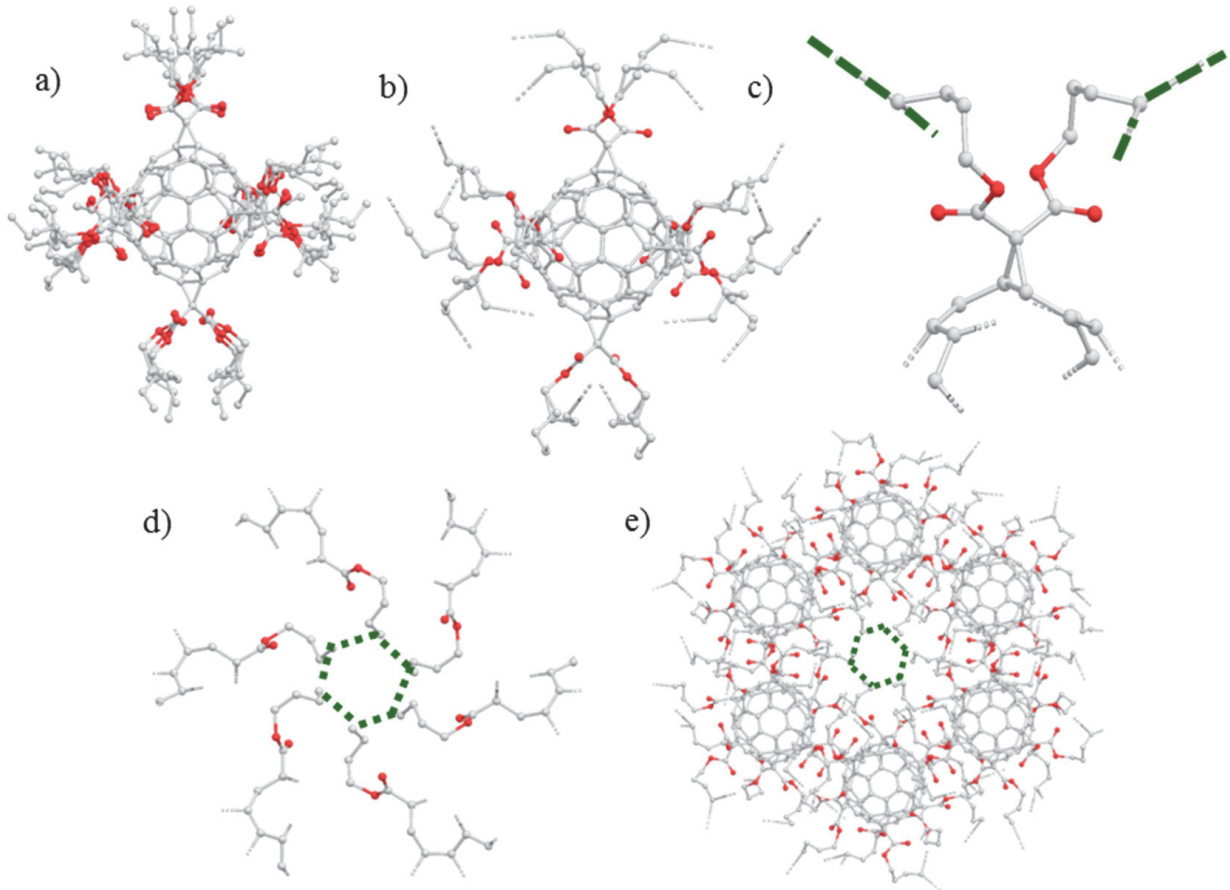

Figure 65. a) An ORTEP[239] illustration of a single hexakis adduct of [60]fullerene, including the three positions of each -COOR group, giving rise to four different butyl branches. b) A depiction of the Van der Waals connections of **3a** and c) of a single malonate group with its close neighbours (the bond direction is plotted as a deep-green dashed line). e) An expansion of the connection network illustrated in (c) with [60] fullerene units omitted for clarity. e) The same six interacting malonate groups illustrated in (d) accompanied by their corresponding C_{60} buckyballs[237].

Each -COOR group is placed over three positions, giving rise to four different butyl branches (two of the branches coming from the same C_{60}-COOR group), for 48 different positions over the whole packing (Figure 65 a). Figure 64 c and Figure

65 d and e reveal the intricacy of the hexakis–fullerene network and the interdigitated arrangement of the interacting butyl chains. Figure 65 b-e depict one of these interactions, as well as a network view of the crystal packing created by the hexaadducts through this interaction. The different occupancy factors and the contacts between carbon atoms for this interaction, and for the entire intricate network, are detailed in the ANNEX C 7 and ANNEX C 8. Thus, the main information stemming from this crystallographic study is that these branches create a densely packed 3D structure maintained by Van der Waals contacts established between the alkyl chains of neighbouring hexakis-[60] fullerenes, at an average distance of 2.2 Å. This supramolecular Van der Waals C–H···H–C interactions are called "sticky fingers"[235]. The second order Møller-Plesset (MP2) computational studies[241] of a methane dimer calculated its dissociation energy to be approximately 1.3 kJmol^{-1}. The dihydrogen contacts in alkanes therefore appear to be among the weakest intermolecular interactions as can be observed in Figure 66.

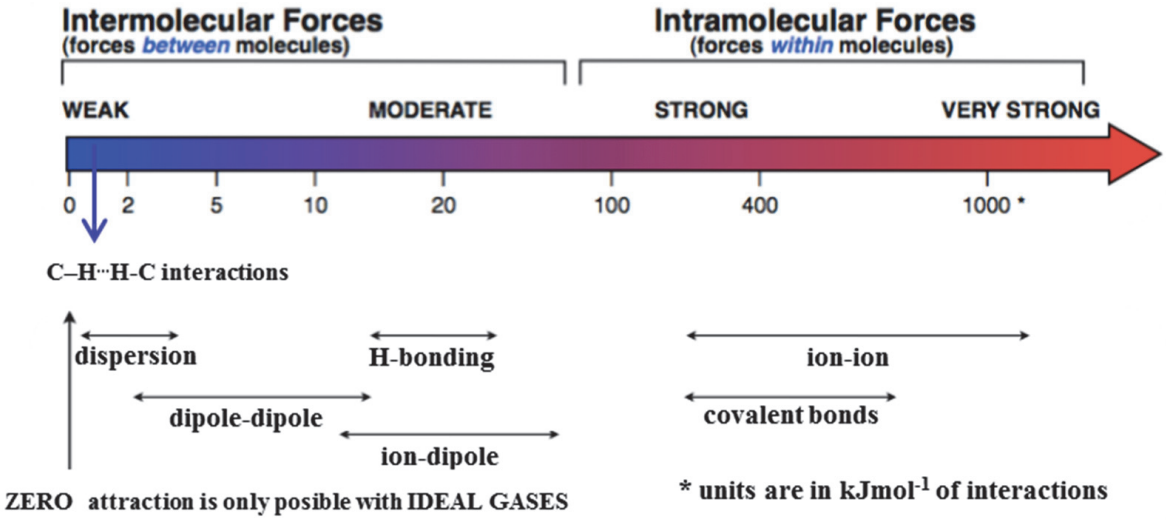

Figure 66. Principal inter- and intramolecular forces[242].

Nevertheless, these interactions are cumulative and, for longer alkanes chains, the number of lateral contacts between neighbouring molecules increases, resulting in higher dissociation energies of dimers, up to 19 kJ mol^{-1} has been found for n-hexane[243]. The increase in the number of intermolecular contacts per molecule as the length of an alkane is extended could explain the high thermal stability observed by the TGA technique, starting to decompose at temperatures above 275 ºC (Figure 67). No loss of solvent is evident; therefore, all interactions correspond only to the Van der Waals C–H···H–C interactions.

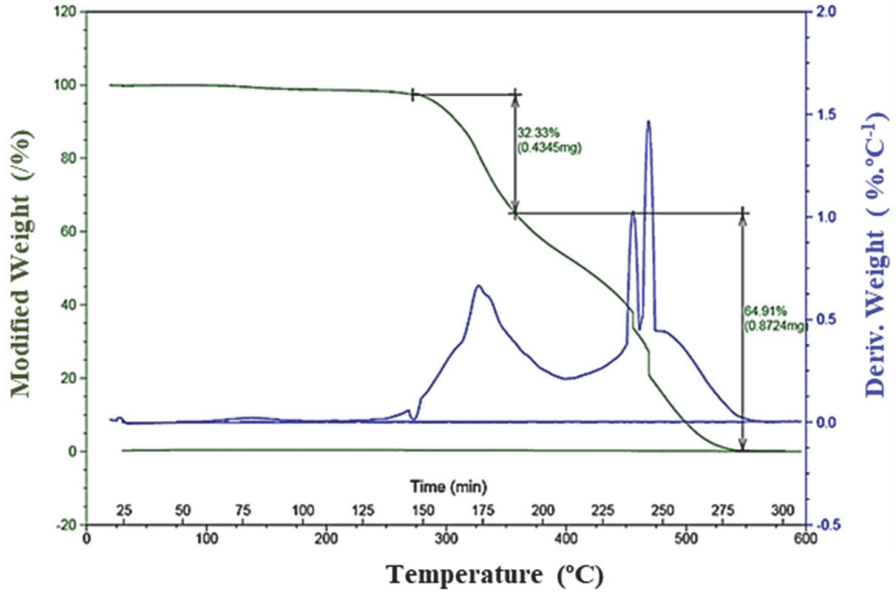

Figure 67. Thermogravimetric profile of **3a** (1.3130 mg in air) showing the mass variation (green curve) and its first derivative (blue curve) upon heating at 2 ºC/min[237].

Interestingly, a close look at the crystallographic data confirms that the densely packed 3D structure of fullerene based **3a** shows small cavities that mainly surround the buckyball (Figure 68 a). Despite the presence of small cavities within the structure of the material, the closely packed aliphatic butyl chains prevent volatile molecules from diffusing through the crystal network, as indicated by a Brunauer–Emmett–Teller (BET) surface area value close to zero (Figure 68 b).

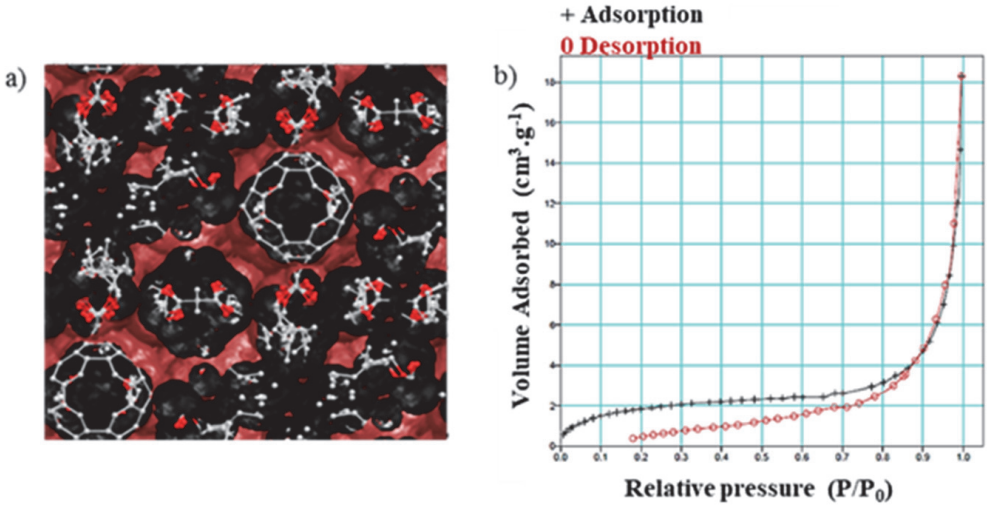

Figure 68. a) Occupancy calculated with OLEX2[244] highlighting the potential cavities surrounding the [60]fullerene in red. b) Nitrogen gas sorption isotherm at 78 K for compound **3a** (crosses, sorption; open circles, desorption). P/P_0 is the ratio of gas pressure (P) to saturation pressure (P_0), with P_0 being 716 torr[237].

4.2.2. Sensing studies using the fullerene-based molecular material.

In order to study the sensing capabilities of **3a**, the protocol was followed (section 2.2.5, Figure 40), single crystals of **3a** were exposed to a saturated atmosphere of a variety of organic and inorganic volatiles compounds (formic acid, bromine, thionil, acetic acid, $TiCl_4$, $SnCl_4$, hydrazine monohydrate, hexane, heptane, 1,8-Diazabicyclo[5.4.0]undec-7-ene (DBU), butylamine and HCl) at 67 ºC.

After the characterization of these new phases by optical reflectivity and FTIR, only changes were observed in the compounds exposed to $TiCl_4$, butylamine, 1,8-Diazabicyclo[5.4.0]undec-7-ene (DBU) and hydrazine monohydrate vapors, regarding compound **3a**. The most remarkable change was the color (Figure 69).

The resulting new phases exposed to $TiCl_4$, butylamine, 1,8-Diazabicyclo[5.4.0]undec-7-ene (DBU) show very slight changes in intensity and shifts of the bands, with hardly any noticeable modification in FTIR spectra (Figure 70). However, the change in color could indicate that a sorption (chemi- or physisorption) has taken place. The physisorption phenomenon would be more likely because only shifts and changes in intensities were observed in the bands without the apparition of any new bands. Unfortunately, these samples could not be measured by X-ray diffraction because of the quality of the crystals. Nonetheless, higher quality crystals are still to be obtained, in order to reveal the reaction and as a consequence the nature of sorption.

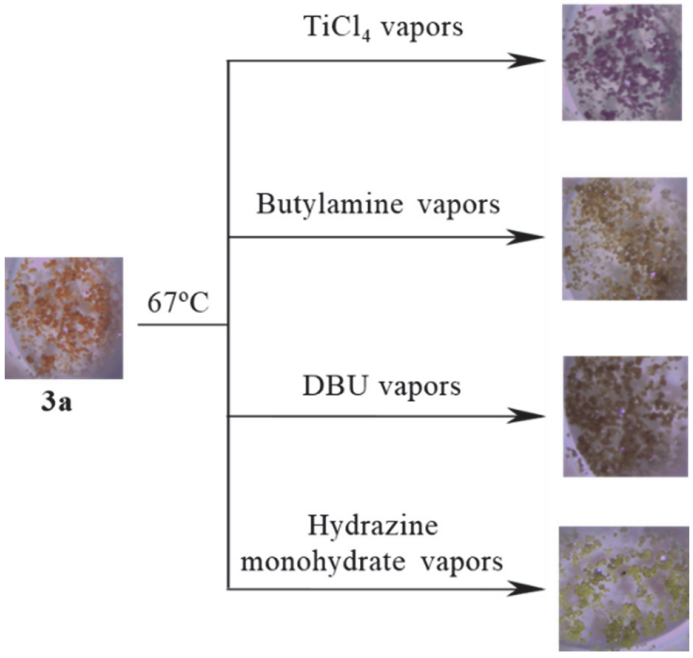

Figure 69. SCSC color changes produced by exposure **3a** to $TiCl_4$, butylamine, 1,8-Diazabicyclo[5.4.0]undec-7-ene (DBU) and hydrazine monohydrate vapors at 67 ºC.

Otherwise, when **3a** was exposed to hydrazine vapors for 3 days at 67 ºC, there were remarkable changes in the shifts and intensities, as well as the disappearance and emergence of new bands (the latter marked in black, Figure 70 b) evidenced in the FTIR spectrum.

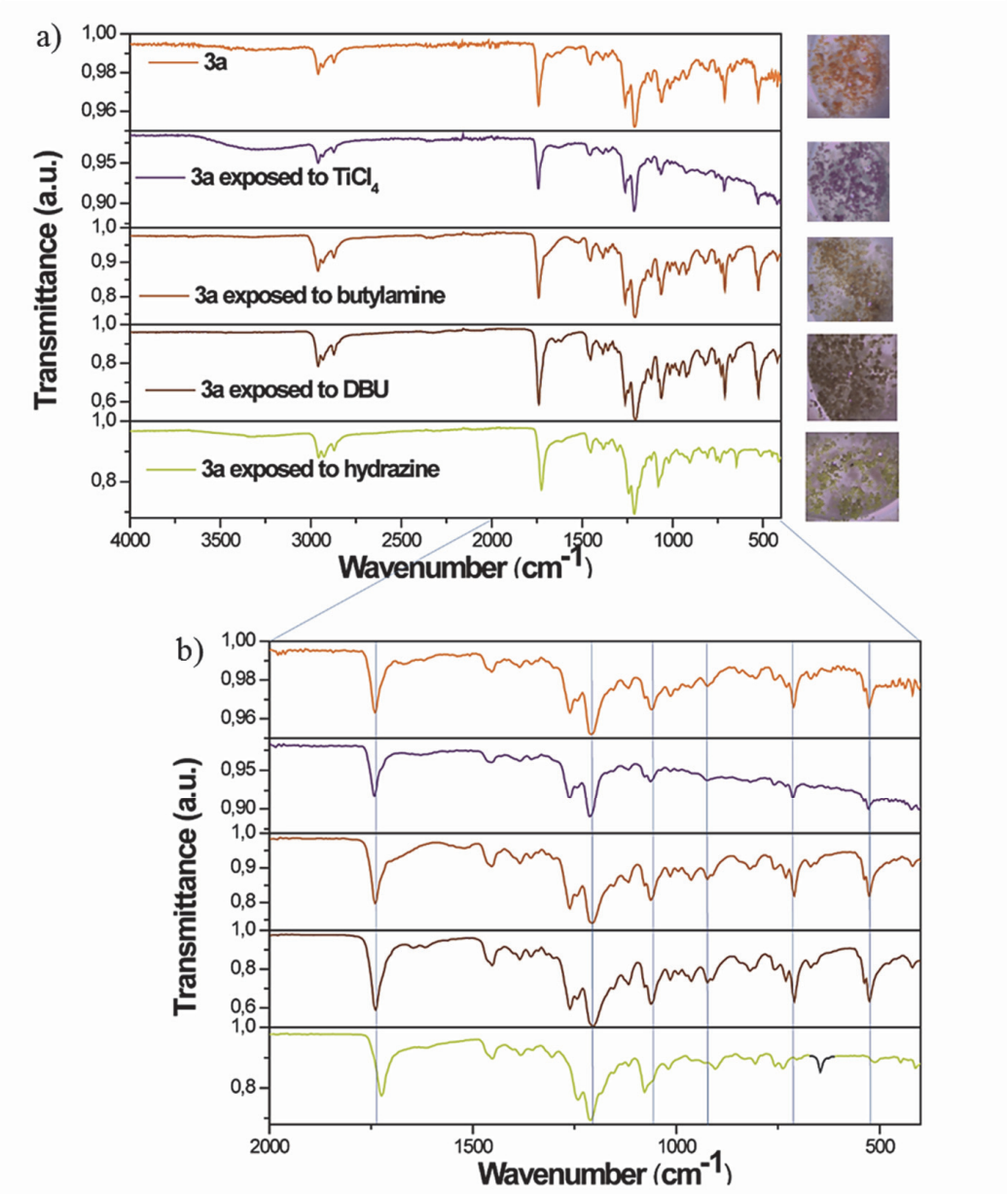

Figure 70. a) Infrared spectra of **3a**, **3a** exposed to $TiCl_4$, butylamine, DBU and hydrazine by SCSC reactions with their respective color change images on the right. b) Amplification of the IR spectrum between 2000 and 400 cm^{-1} to show the main shifts of the bands.

In addition, in this case, crystals suitable for X-ray diffraction could be obtained (Figure 71) allowing a complete characterization study and the absorption process

that takes place. Therefore, the next sections of the chapter will be focused on the study of this new compound, **4a**.

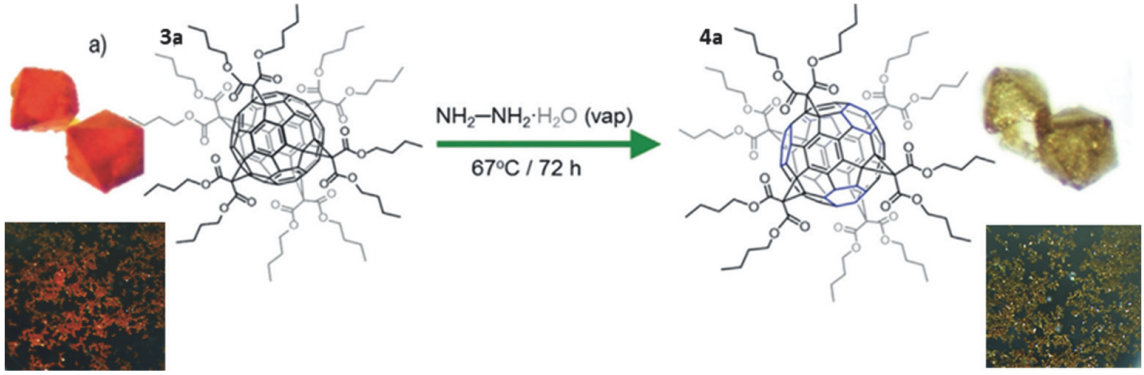

Figure 71. General scheme SCSC reaction of **3a** to **4a**, including a picture of the crystal after (left) and before (right) exposure to hydrazine vapors[237].

This color change was monitored and recorded by optical microscopy experiments (ANNEX C 12). The results indicated that the color change from orange to yellow due to the hydrogenation of **3a** occurred completely after 3 days (ANNEX C 12), confirming the above-mentioned result.

4.2.3. Structural and physico-chemical study of the hydrogenated compound.

The structure of **4a** was studied by both single-crystal (measured at 100 K in ALBA Synchrotron, ANNEX C 7 and ANNEX C 8) and crystalline powder XRD studies as well as **3a** (ANNEX C 9, ANNEX C 10). Complex **4a** retains the same space group as its precursor, although the value of the axis diminishes from 26.878(1) to 26.156(3) Å (ANNEX C 8) and there are also changes in the C-C distances between hexagon-hexagon and hexagon-pentagon (Table 5).

Table 5. Selected angles [°] for compounds **3a** and **4a**.

	Compound 3a	Compound 4a
C1-C2 (hexagon-hexagon)	1.353	1.502
C1-C2 (hexagon-pentagon)	1.432	1.467
C3-C4 (hexagon-hexagon)	1.384	1.389
C3-C4 (hexagon-pentagon)	1.442	1.383

From the X-ray crystal structure of **4a**, it is concluded that half of the six-membered rings associated with [60]fullerene in **3a** have been hydrogenated after the exposure of the crystals to the hydrazine vapors (Figure 71 and Figure 72 b-d, hydrogen atoms are denoted in black). Remarkably, under these reaction conditions only half of the accessible six membered rings are hydrogenated. As well as occurred in **3a** there is no evidence of any supramolecular π–π contacts between neighboring fullerene buckyballs (Figure 72 e) and in this case the main interactions also were the Van der Waals C–H···H–C interactions (Figure 72 c and d).

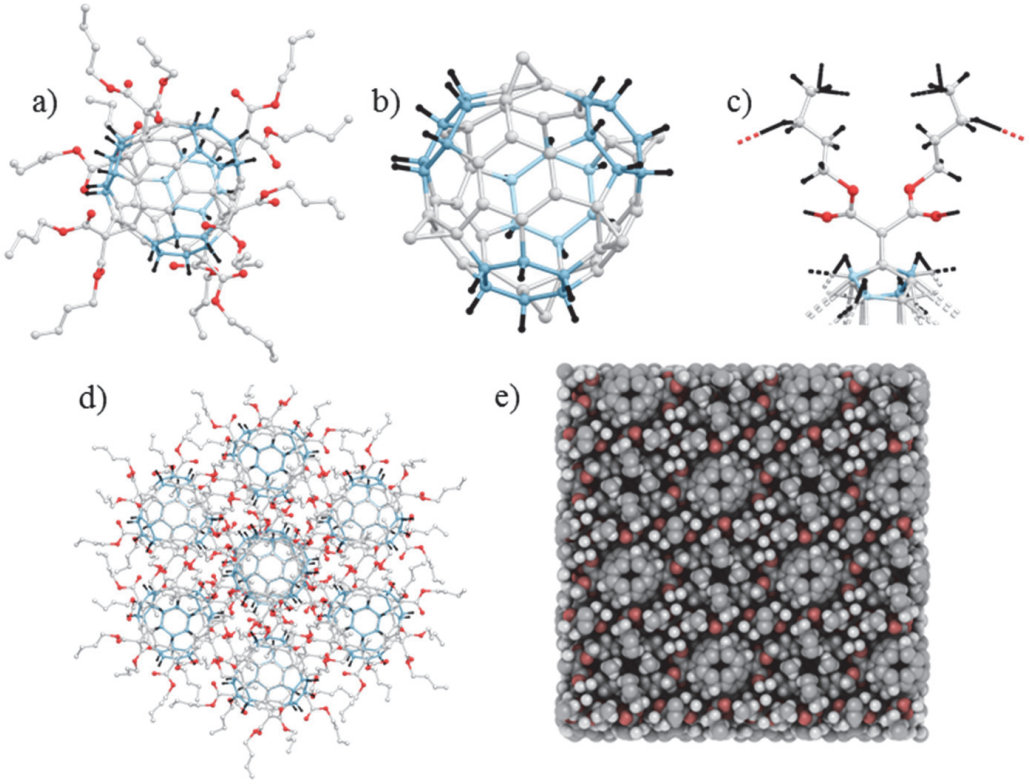

Figure 72. a) A crystal structure visualization of the hydrogenated hexaadduct including the hydrogen atoms contained within C_{60} and the malonate functional groups (only one branch of the distorted malonate is illustrated for clarity). b) A view of the C_{60} hydrogenated fullerene with the added hydrogen atoms distinguished in black. c) A depiction of the Van der Waals interactions between a single malonate group and its close neighbors. d) Expansion of the connection network including the C_{60} buckyballs. e) An iRASPA view of **4a**[237].

Interestingly, the partial hydrogenation of **3a** always takes place with preservation of the symmetry of the molecule, which is also evident in the extremely simple ^{1}H NMR pattern observed (Figure 73).

This result has been reproduced around 50 times and the same hydrogenation pattern is always obtained. Because of partial hydrogenation, the fullerene cage

experiences a strong distortion, which arises from the sp^2 to sp^3 hybridization change of the hydrogenated six-membered rings. The XRD data show an increase of the C-C bonding distances (Table 5), along with a decrease of the hybridization angle of the involved carbon atoms (Figure 72 and Figure 74). Like its parent molecule (**3a**), the hydrogenated hexakis adduct (**4a**) crystals are non-porous (Figure 72 e). Characterization of **3a** and **4a** was carried out by standard spectroscopic techniques and was greatly facilitated by the high symmetry of the complexes. The ^{1}H NMR spectra of **3a** and **4a** are shown in Figure 73, ANNEX C 2 and ANNEX C 5.

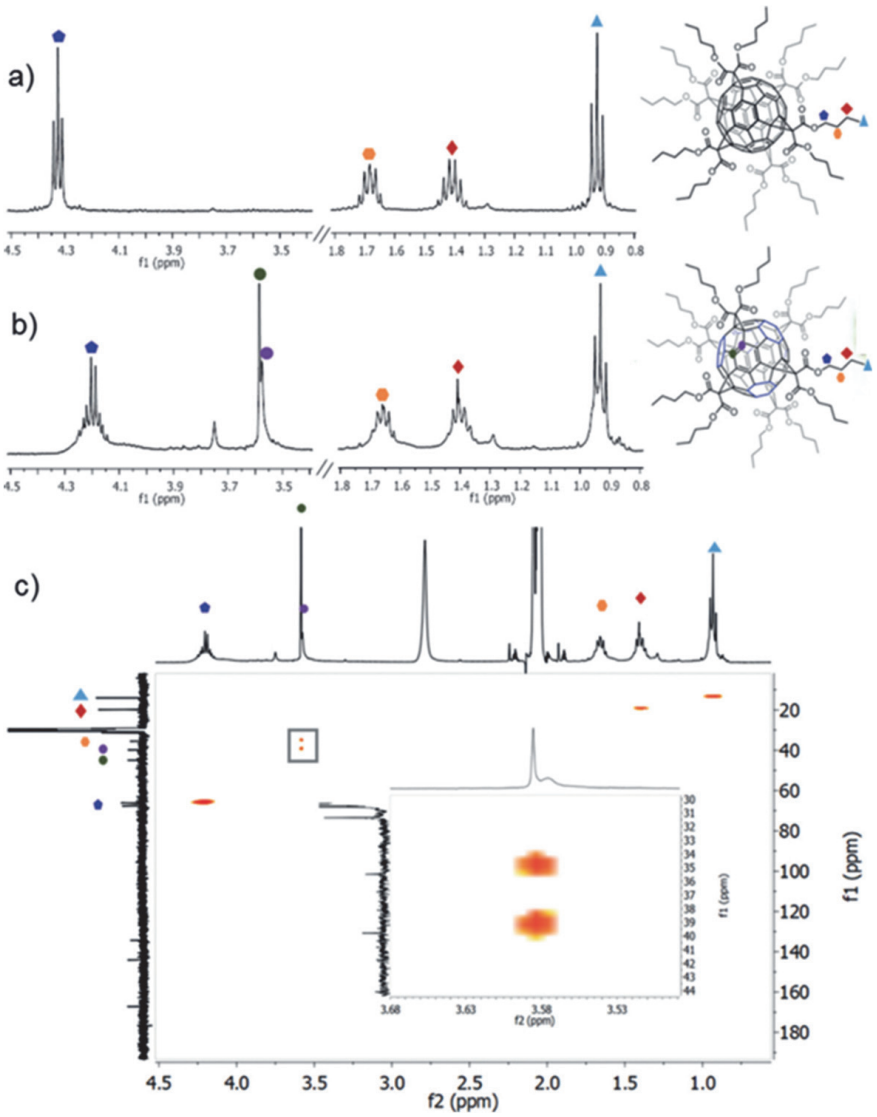

Figure 73. a) and b) ^{1}H NMR spectra of compounds **3a** and **4a**, respectively. c) HSQC NMR spectrum of compound **4a** and the amplified HSQC NMR spectrum (inset) of the novel hydrogen signals (3.58 ppm). The resonances of each spectrum have been assigned to key atoms under discussion with symbols and colors[237].

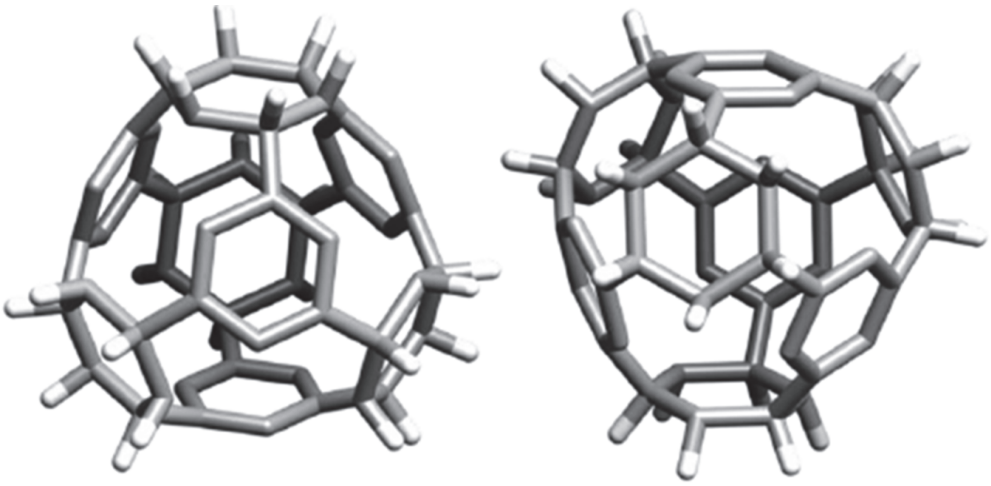

Figure 74. Tetrahedral fashion mode of **4a** after hydrogenation with hydrazine in a single-crystal to single-crystal reaction type[237].

Thus, the ^{1}H NMR spectrum of **3a** displays four signals at 4.33, 1.68, 1.41, and 0.92 ppm that are consistent with 12 butyl malonate groups, -OCH_2, -CH_2, -CH_2 and -CH_3, respectively (Figure 73 a and ANNEX C 2). The hydrogenation of **3a** is clearly evident in the ^{1}H NMR spectrum where two nearly isochronous signals emerge at 3.58 ppm that integrate to 24 protons (Figure 73 b and ANNEX C 5). This is consistent with the total hydrogenation of four of the eight six-membered rings of **3a**. Jointly with a ^{135}DEPT (distortion less enhancement by polarization transfer, ANNEX C 11) experiment, where it is showed CH/CH_3 signals with a positive phase and CH_2 signal with a negative phase, the C-H correlations found by heteronuclear single quantum coherence spectroscopy (HSQC) these new H signals to be correlated with methyne carbon atoms on the fullerene surface (Figure 73 c). The environment changes induced upon hydrogenation cause an upfield shift in the -$COOCH_2$- methylene resonances from 4.33 to 4.20 ppm. Furthermore, this signal also shows signs of splitting probably as a consequence of methylene groups lying over hydrogenated and unsaturated rings.

As for **3a**, the ^{13}C NMR spectrum of **4a** shows a fine and simple pattern derived from the high symmetry of the complex. As a consequence of this symmetry, all the sp^2 carbons belonging to the fullerene cage manifest as two signals at 144.0 and 134.3 ppm (significantly shielded compared to the parent complex **3a**, at 145.8 and 141.3 ppm, respectively). The signals of the hydrogenated sp^3 carbons appear as two peaks at 39.8 and 35.5 ppm (correlating with the protons at 3.58 ppm) (Figure 75 and Figure 76). The signal at 66 ppm approximately and the three most unscreened signals correspond to the butyl malonate groups, -OCH_2, -CH_2, -CH_2 and -CH_3, respectively.

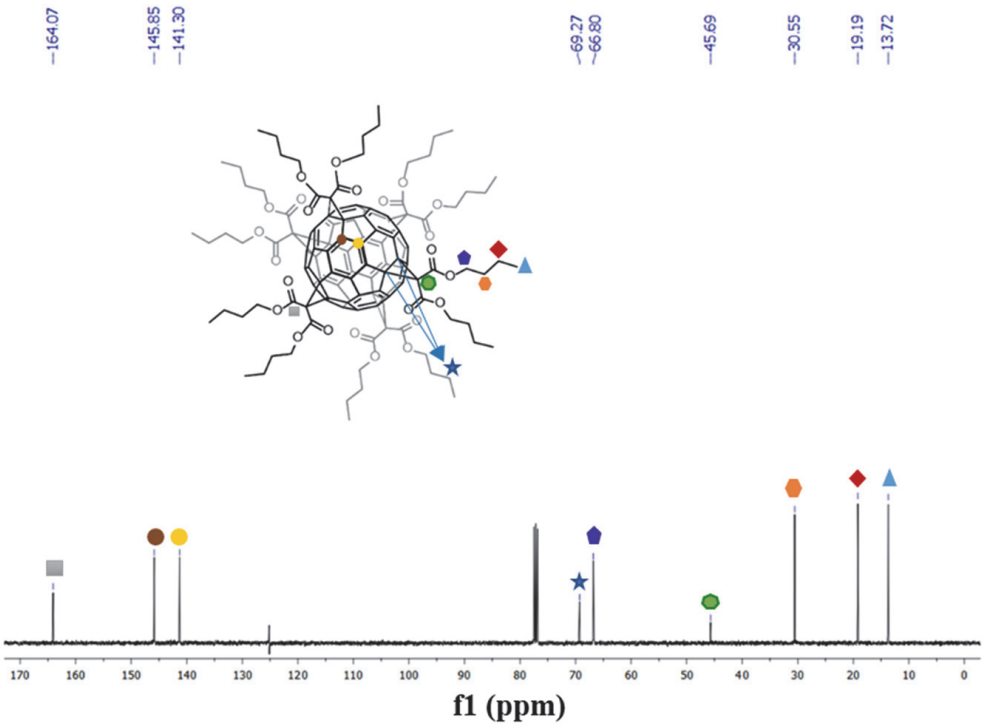

Figure 75. ^{13}C NMR spectrum (100 MHz, $CDCl_3$) of **3a**.

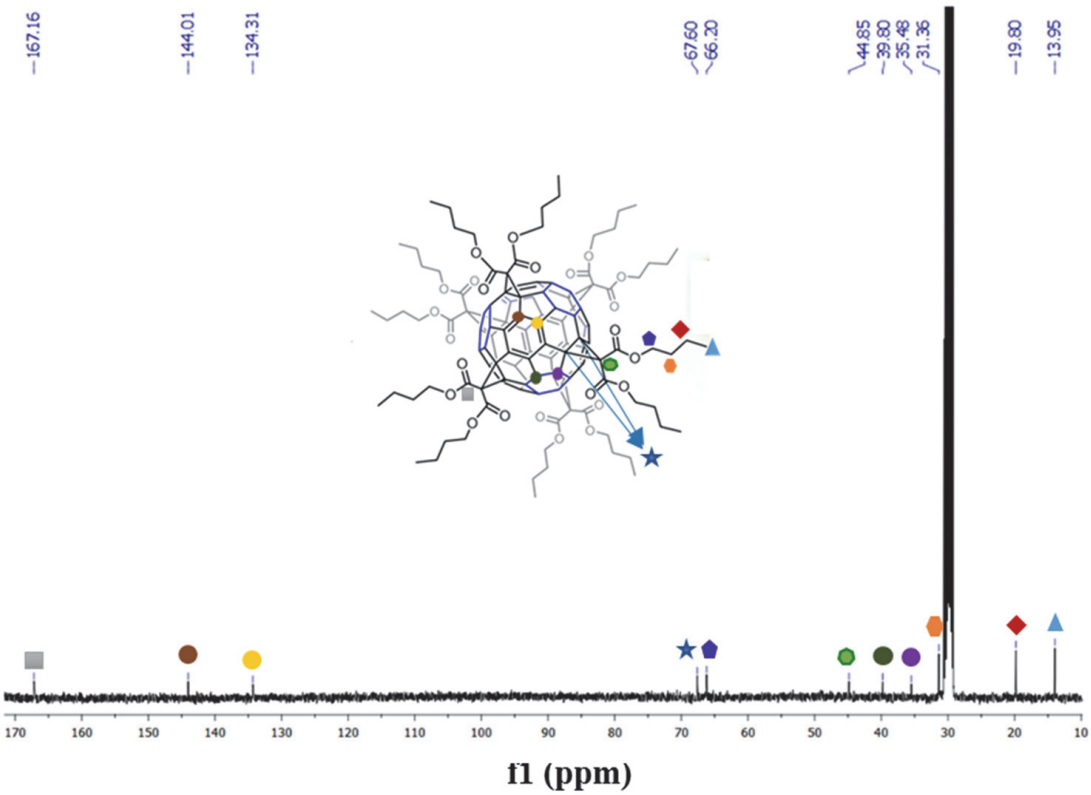

Figure 76. ^{13}C NMR spectrum (100 MHz, $(CD_3)_2CO$) of **4a**.

Thermogravimetric analysis provides an insight into the thermal stability of hydrogenated compound **4a**, which is stable up to 150 ºC when its first weight loss starts (Figure 77). In contrast, as mentioned above, non-saturated **3a** exhibits high stability and its first weight loss begins above 275 ºC (Figure 67). This stability loss is attributed to the increased strain supported by the fullerene cage upon conversion of 24 sp^2 carbon atoms into sp^3 carbon atoms. This is observed in dramatic fashion in the XRD crystal structure, where the cage appears to bulge beyond a spherical shape (Figure 74).

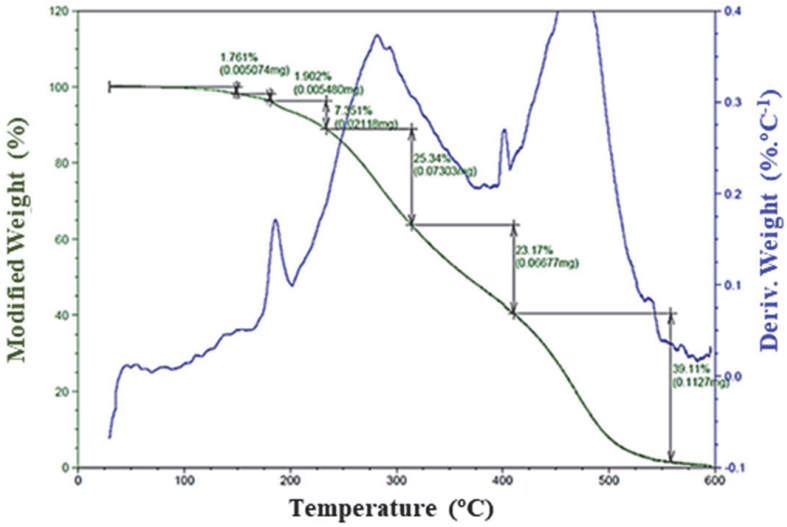

Figure 77. Thermogravimetric profile of **4a** (0.3830 mg in air showing the mass variation (green curve) and its first derivative (blue curve) upon heating at 2 ºC/min[237].

Attempts to duplicate this result in solution resulted in either no evolution of the reaction or led to a complex mixture of byproducts, none of them consistent with the chromatographic Rf of **4a** (Figure 78). Therefore, controlled and selective hydrogenation only could be obtained in solid phase.

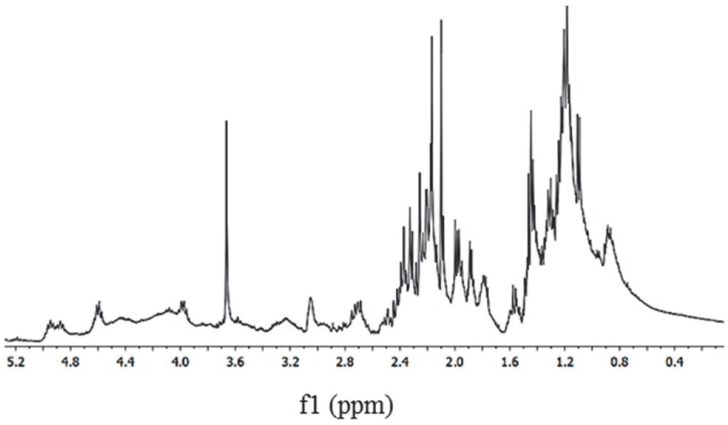

Figure 78. ^{1}H NMR spectrum (400 MHz, CDCl3) of the mixture of by-products obtained by hydrazine solution experiment[237].

4.2.4. Fullerene hydrogenation with hydrazine: A possible mechanism

The use of molecular hydrogen in the presence of a metal catalyst (commonly Pt, Pd or Rh) is the most recognized method for the hydrogenation of alkenes since the 19th century[245]. Despite widespread use of catalytic hydrogenation exceptional security measures are required for handling molecular hydrogen and the use of rather expensive catalysts. Hydrazine offers an alternative hydrogen source. Nevertheless, in order to produce hydrogenation of olefins, it is required to oxidise hydrazine to diimide[246], which is a reactive species that is capable of reducing olefins. This procedure involves a rather unstable diimide intermediate that is extremely short lived in solution. It has been thought that the diimide species (generated in situ from the oxidation of hydrazine, Figure 79) is stabilized within the network of **3a** as a consequence of confinement inside the pockets surrounding the fullerene moieties. In this environment concerted hydrogen transfer takes place from cis-diimide to half of the cyclohexatriene rings remaining on fullerene.

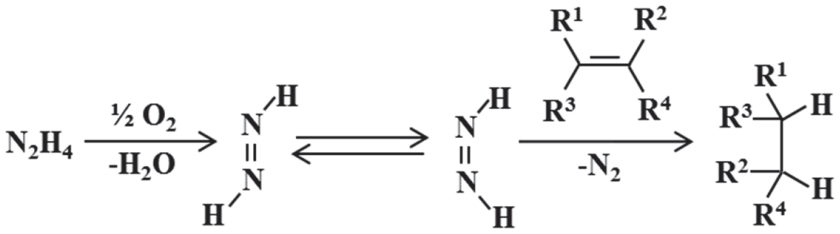

Figure 79. Oxidation of hydrazine to diimide and subsequent transfer hydrogenation.

In order to corroborate the proposed mechanism, the reaction was carried out in a pre-purged nitrogen and then saturated with hydrazine vapor atmosphere at 67 ºC (following the protocol). The reaction without oxygen yielded a new green phase (named, $\mathbf{3a_g}$) as it can be seen in the Figure 80.

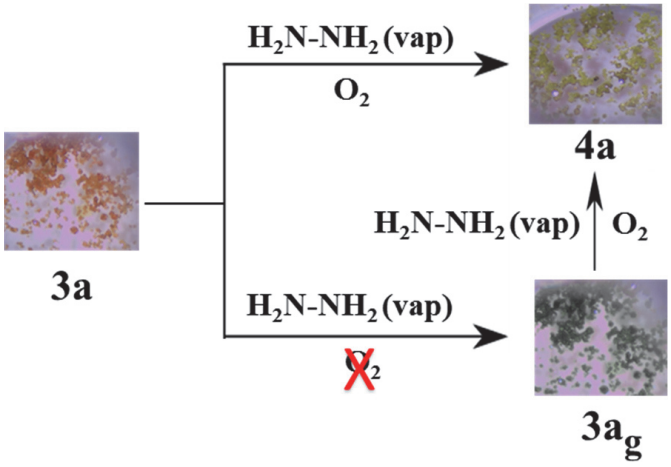

Figure 80. Principal transformations of compound **3a** upon exposure to hydrazine in the presence and absence of oxygen.

Interestingly, when compound **3a$_g$** was re-exposed to hydrazine in the presence of oxygen, a color evolution from green to yellow took place. Through the study of different techniques, FTIR and NMR, it was found that the obtained yellow phase was similar to that found for **4a**.

To find out more about the green **3a$_g$** phase, it was characterized by FTIR spectroscopy, ^{1}H NMR Spectroscopy and Mass Spectrometry. Using the FTIR spectroscopy technique, the variation on the shifts frequency values and the changes in intensities of the bands related to previous samples **3a** and **4a** let us to confirm that a new phase was isolated (see Figure 81).

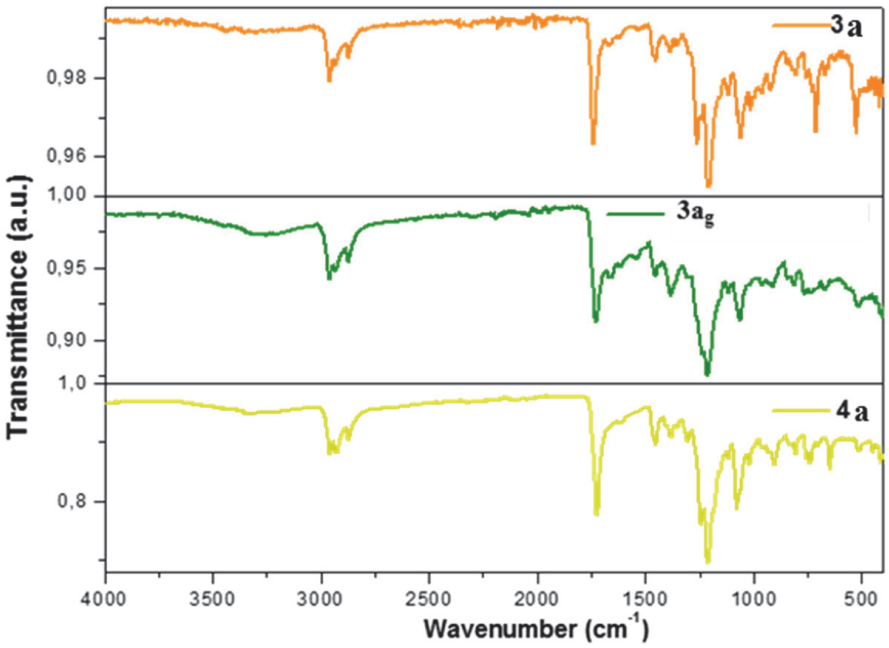

Figure 81. Infrared spectra of **3a**, **3a$_g$** and **4a**, with their respective color change images on the right.

To get more information about **3a$_g$**, it was analyzed by NMR. In Figure 82, the ^{1}H NMR spectra of compounds **3a**, **3a$_g$** and **4a** are compared. In the present case, the ^{1}H NMR spectrum has been done in chloroform, since **3a$_g$** is not soluble in acetone.

3a$_g$ exhibits 4 broadened signals. The three most shielded signals corresponding to the -CH_2, -CH_2 and -CH_3 of the butyl malonate groups have the same shifts, 1.68, 1.41, and 0.92 ppm (Figure 82 a), respectively, as compounds **3a** and **4a**, therefore there is no modification on these groups.

On the contrary, above 4 ppm two triplets appear at 4.26 and 4.20 ppm, which correspond to the -OCH_3 group signals (Figure 82 a). The most unshielded triplet signal matches the shifts of compound **3a**, by contrast, the environmental changes could induce upon a possible electronic delocalization in the aromatic rings could

cause a change in the methylene -$COOCH_2$- resonances from 4.26 to 4.20 ppm (Figure 82 a), as these methylene groups lie over these aromatic rings (as occurred in compound **4a** due to hydrogenation).

Also, unlike **4a**, the signal at 3.58 ppm, which is a signal corresponding to hydrogenation, does not appear in the **3a$_g$** spectrum. This indicates that **3a$_g$** is not hydrogenated, this is because the reaction in the absence of oxygen does not produce the formation of diimide compound (reactive species) and therefore the hydrogenation of fullerene.

Following this analysis, it can be indicated that a non-hydrogenated intermediate phase has been obtained and that the environmental changes could induce upon a possible electronic delocalization in the aromatic rings close to the OCH_3 groups.

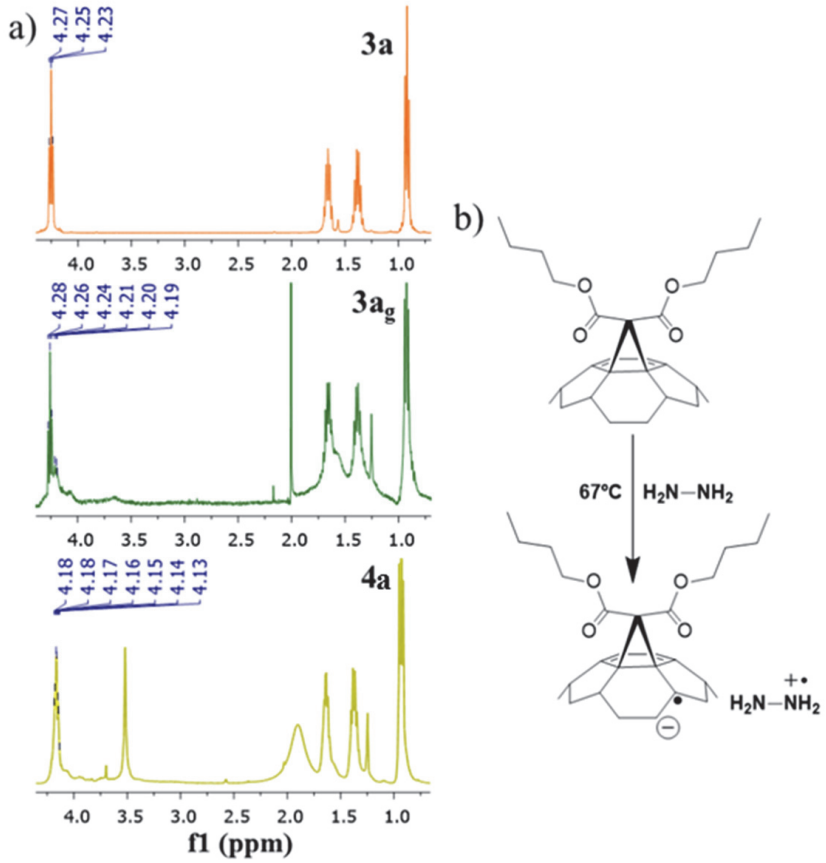

Figure 82. a) ^{1}H-NMR spectra of **3a**, **3a$_g$** and **4a**. b) Possible radical anion of the hexaadduct fullerene (**3a$_g$**).

Hydrazine has been reported to reduce fullerenes in an oxygen-free atmosphere to radical monoanion in early stages of reaction, where the fullerene would act as an oxidizing agent and hydrazine as a reducing agent[213]. Furthermore, it has been also published[247,248] that the green color is characteristics of the RC_{60}^- anion. In

view of the results obtained and those published, a radical anion could be formed (Figure 82 b).

Finally, **3a$_g$** was characterized by mass spectrometry. By this analysis broad signs (typical of anions) and a peak at 2037.7 m/z which could correspond to [Fullerene + N_2H_4]$^-$ were detected (Figure 83). This peak could agree with the reaction proposed in Figure 82 b, as mentioned above. In addition, the **3a$_g$** spectrum was compared with the simulated one and both matched in the majority of the signals. In conclusion, all the results suggest that **3a$_g$** could be a radical anion.

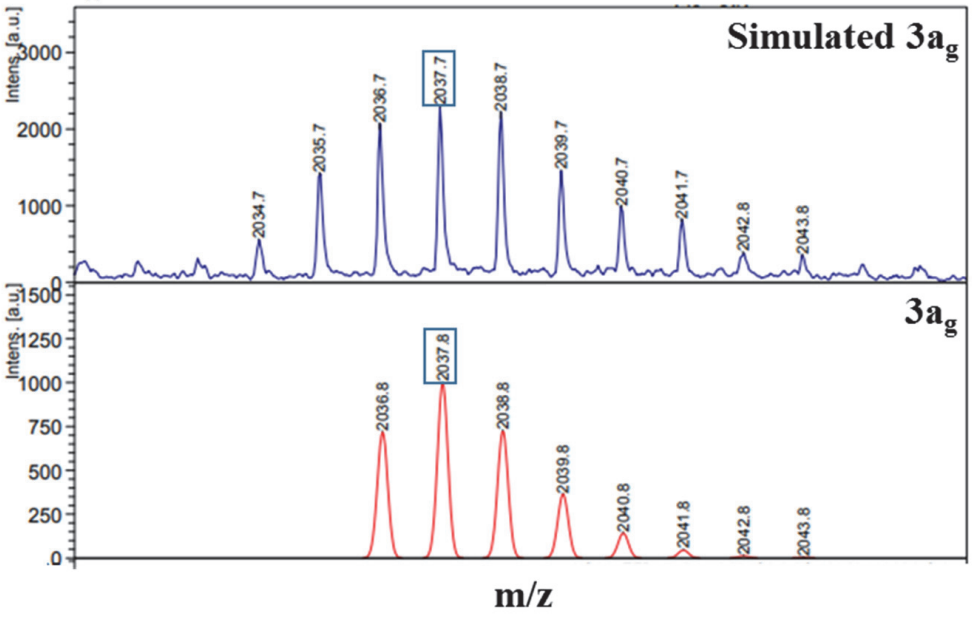

Figure 83. Mass Spectrometry spectra of simulated of the spectrum calculated from **3a$_g$** and the experimentally obtained from the synthesis. Detection of the peak at 2037.7 m/z which could correspond to [Fullerene + N_2H_4]$^-$.

4.2.5. Reversibility study of the hydrogenation process

In 2005, Guan-Wu Wang et al[249] proposed a mechanism to dehydrogenate fullerene $C_{60}H_2$ to C_{60}. In this method the hydrogenated fullerene was submerged in both organic and inorganic bases at 60 ºC, generating a fullerene anion. From this anion, peroxide anion was produced when reacting in presence of oxygen from the air. The peroxide anion was later protonated and eliminated, obtaining its complete dehydrogenation.

Inspired by this methodology, crystals of **4a** were exposed to an atmosphere saturated with different base vapors (following the vapor diffusion protocol reported previously), triethylamine, piperidine and pyridine for one day at 90 ºC. After that, these three crystalline samples were left undisturbed in air for 3 days at 67 ºC. Then, the samples obtained were characterized by ^{1}H NMR.

Unfortunately, the ^{1}H NMR spectra of those samples exposed to triethylamine and piperidine were similar to the starting **4a** spectrum, suggesting that any reaction occurs. Instead, when **4a** was exposed to pyridine, see Figure 84, not only ^{1}H NMR changes were showed but a clear color change, from yellow to orange, occurs. From now on, this new phase will be referred as **3'**. In deep regard to the NMR spectrum, in **3'**, the peak at 3.58 ppm disappears (Figure 84 b) and after exposing it again to hydrazine vapors at 67 ºC, the peak reappears and a color change is produced again, this time from orange to yellow, **4'** (Figure 84 c). In conclusion, this spectrum shows the process of dehydrogenation and rehydrogenation.

However, it is important to mention at this point that both spectra (**3'** and **4'**) are not identical to those of **3a** and **4a** reported previously. As a consequence, it cannot be assumed that the reaction is totally reversible and that further work is needed to understand either the mechanism of the reaction and the precise nature of the novel dehydrated fullerene material.

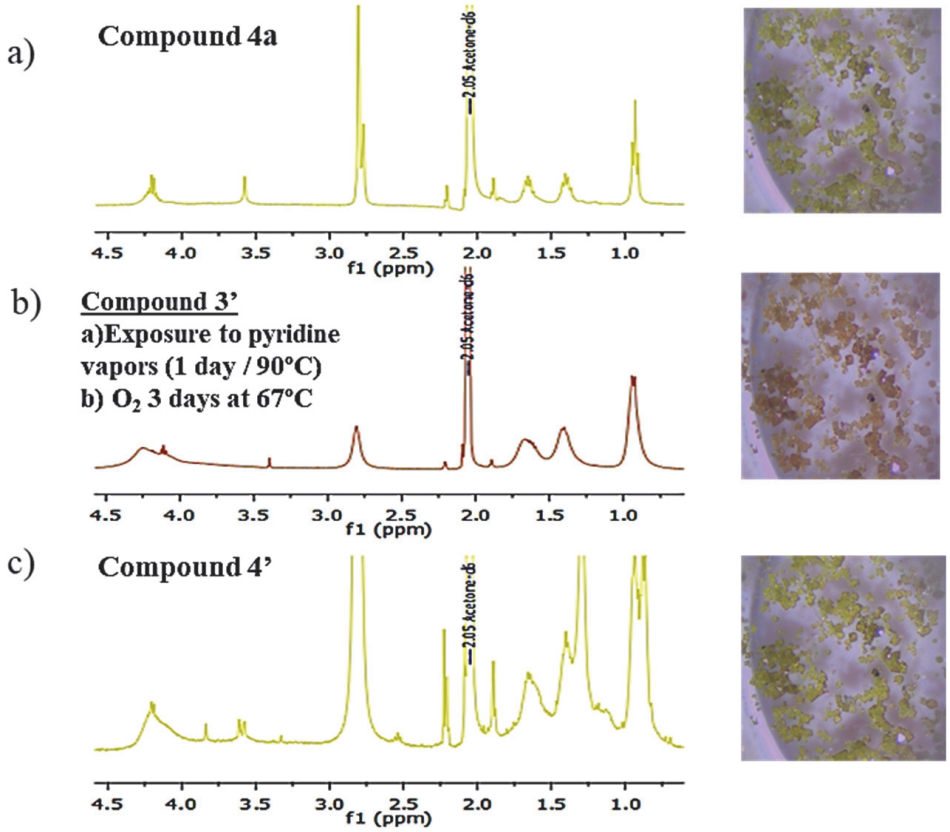

Figure 84. Dehydrogenation/re-hydrogenation of compound **4a** with their respective color change images on the right.

4.3. CONCLUSIONS

The work herein describes the first reported weak Van der Waals “sticky fingers” crystalline structure of a C_{60} fullerene hexakis adduct. These non-covalent (dispersion stabilization) interactions, also known as “sticky fingers”, are established between the non-polar butyl chains linked to the malonate functionalities. The large number of butyl branches shown in the XRD experiments indicates a dynamic interaction between interdigitating aliphatic chains. The resulting material shows small cavities at the surface of the fullerene, although the overall structure is non-porous. Despite this apparent non-porosity, the dynamic nature of the “sticky fingers” interaction allows for the diffusion of volatiles to the cavities. Interestingly, hydrazine molecules allocated inside these pockets trigger the toposelective hydrogenation of half of the remaining cyclohexatriene rings of the hexaadduct in a SCSC reaction accompanied by a color change into the visible range. We believe that further design of new suitably functionalized hexaadducts will allow materials to be obtained with customizable pockets ready for capturing different volatiles and gases. Therefore, the new and groundbreaking strategy described in this manuscript on topochemical solid-state reactions involving fullerenes will contribute to the creation of novel carbon-based advanced absorbent materials with a variety of direct technological applications, as a hydrazine deactivator and sensor, due to its known toxicity and carcinogenesis capacity of the latter. Due to the change of color with other volatile compounds ($TiCl_4$, butylamine, DBU), we are trying to obtain crystals of higher quality to unveil the nature of the adsorption.

Our study shows that the complete dehydrogenation/rehydrogenation process has occurred, but further research is needed to know the mechanism of this process and the nature of the novel phases. Finally, in future works, the retro-Bingel reactions attemps by the electrochemical method will be carried out, in order to obtain the $C_{60}H_{24}$ buckyball without malonates groups.

5. THERMAL STIMULI-RESPONSIVE AND HYDROGENATION IN DYNAMIC ORGANIC FUNCTIONALIZED FULLERENE CRYSTALS

The development and design of smart crystalline materials whose physical properties can be significantly changed and controlled at molecular level by external stimuli (i.e. temperature, light, chemical compounds or pressure), has attracted the researchers' interest because of their potential applications in diverse fields such as biochemistry and technology[250,251]. Osamu Sato calls these functional materials "dynamic molecular crystals"[252] (Figure 3) as they display different switching effects on their physical properties. For instance, a given smart crystalline material can display structural changes, which redefine its out coming properties and thus its potential functionalities. As mentioned above in the introduction, temperature, among other external stimuli[253,87], can trigger phase transition[55,56,254] in crystalline materials at molecular level.

Furthermore, these phase transition reactions can also occur in SCSC when temperature is applied. In some cases, a polymorph can be formed from these transformations. The term polymorphism comes from the Greek roots "poly" and "morph" meaning "many" and "shape", respectively. In Chemistry, this means that a solid compound can adopt different forms and/or or crystal structures[255]. The polymorphs present the same chemical composition and, present different crystalline structures, *i.e.* the arrangement of the atoms or atomic groups in a space lattice is different from one to another. Thereby they might show markedly different physical properties. According to the IUPAC, the transition of a solid crystalline phase at a certain temperature and pressure to another phase of the same chemical composition with a different crystal structure is a polymorphic transition[256].

In SCSC transformations, these polymorphic phase transitions are caused by the cooperative effect which will then propagate through the entire crystalline material via intermolecular interactions[257]. In the tight packaging of the dynamic molecular

crystals, cooperativity takes place thanks to the non-covalent bonds between the different molecules these weak intermolecular forces also play a crucial role in self-assembly strategies. Such interactions not only govern the assembly process leading to the formation of the arranged architecture, but also control the dynamic behavior and properties of the final molecule (material, the material has the property)[258].

Although there are some examples reported in the literature of polymorphic phase transition in fullerene-based materials[259,260], such phenomena remains unexplored and has become a challenge in the crystalline dynamic fullerene materials field. The study of polymorphic phase transitions taking place in functionalized crystalline dynamic fullerene materials is of major importance and will contribute to the development and creation of novel carbon-based advanced materials with the variety of direct technological applications, such as molecular machines and actuators[261], among others.

Based on the acquired experience in fullerene-based materials chemistry, the main aim in this chapter is to study the thermally induced polymorphic phase transformation of the fullerene crystalline dynamic frameworks. This has never been studied before. Throughout this chapter, the changes in the structural and physical properties arising from the occurrence of polymorphic phase transformations will be revealed.

5.1. SYNTHESIS OF COMPOUND 3B

10 mg of hexakis adduct fullerene (orange powder, synthesis available in chapter 4) were dissolved in EtOH (12 mL) in a pressure tube (diameter 27 mm, height 55 mm). The tube was sealed and kept at 120 °C for 3 days in a furnace. A week after, orange orthoedric crystals suitable for X-ray diffraction analysis, were obtained (**3b**) (5.5 mg, 50%).

^{1}H NMR (400 MHz, $(CD_3)_2CO$, δ): 4.33 (t, J = 6.4 Hz, 24H, OCH_2), 1.68 (m, 24H, CH_2), 1.41 (m, 24H, CH_2), 0.92 (t, J = 7.4 Hz, 36H, CH_3) ppm (ANNEX D 1); ^{13}C NMR ($CDCl_3$, 100 MHz, δ): 164.1, 145.8, 141.3, 69.3, 66.8, 45.7, 30.5, 19.2, 13.7 ppm (ANNEX D 3).

FTIR (neat, cm^{-1}): 2959 (m), 2933 (m), 2873 (m), 1738 (s), 1455 (m), 1433 (w), 1381 (m), 1354 (s), 1260 (s), 1202 (s), 1076 (s), 1014 (m), 966 (m), 963 (m), 925 (m), 844 (m), 814 (m), 759 (m), 730 (m), 713 (s), 699 (m), 657 (m), 621 (w), 540 (m), 527 (s), 432 (m) (Figure 93); elemental analysis calculated (%) for $C_{126}H_{132}O_{24}$: C 75.43, H 5.43; found C 75.22, H 5.49.

5.2. RESULT AND DISCUSSION

As discussed in chapter 4, the crystallization of the hexakisadduct fullerene (**3**) in an ethanolic solution, in the presence of iron salt, affords octahedral crystals of **3a**. Seeing that the iron salt was not present in the characterization of the final compound (**3a**) either in powder or in crystal form, we attempted to make in a metal-free ethanolic solution. Surprisingly, **3a** was not obtained, a new crystalline phase (orthoedrical) appears and giving rise to a new polymorph (**3b**) as shown in Figure 85. This highlights the well-known crucial role that iron salts play in the crystallization of this compound despite being absent in the chemical composition of the final compound. The presence/absence of iron salt in the same solvent and temperature conditions led to crystals of the same product with different geometries.

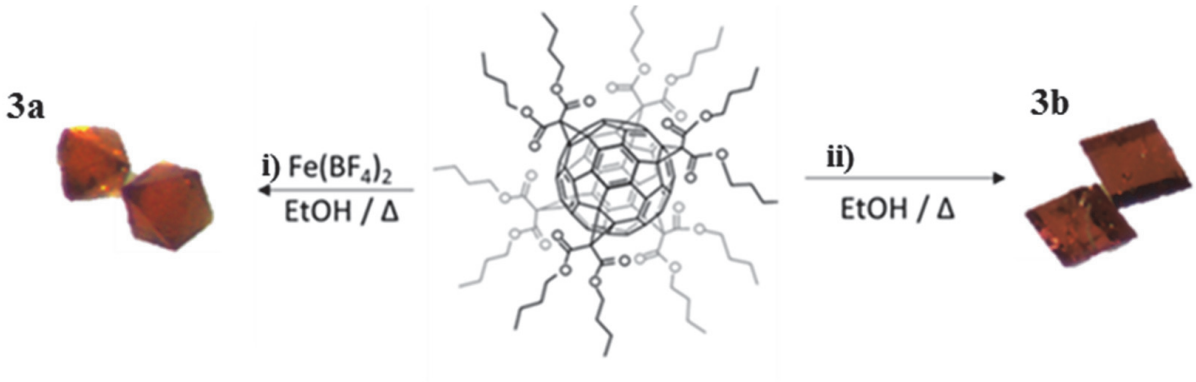

Figure 85. Scheme of the different polymorphs (**3a** and **3b**) obtained from hexakisadduct fullerene (**3**) in presence or absence of iron salt.

5.2.1. Structural study of compound 3b

3b crystallized in the triclinic space groups $P\bar{1}$ (see ANNEX D 4) and it was measured at 100 K in ALBA Synchrotron. The unit cell is composed a total of nine fullerenes. Eight hexaadducts are placed on each vertex, shared by eight other unit cells, and the ninth fullerene inside the cell, giving rise to two fullerenes per unit cell distributed in three different layers. The shortest distance between two neighbouring fullerenes of adjacent layers in **3b** (6.874 Ă) is outside of the supramolecular π-π interactions range[238]. Thus, there is no possibility of π-π interactions, and other supramolecular interactions must drive the packing structure as seen previously in **3a**.

As can be appreciated in the asymmetric unit of **3b** (Figure 86 a), there are two different fullerenes where the C_{60} buckyballs are joined by six butyl malonate groups with diverse conformations. One fullerene (placed on the vertex in the unit cell) has four butyl malonate arms closed in on itself (both pairs have a very similar conformation, red colour, Figure 86 b, the conformation b and b'), while the other

two remaining branches have a stretched conformation (Figure 86 b, the conformation a). In contrast, in the other fullerene (placed inside the unit cell) the three conformations are different (Figure 86 c). Here, two branches are completely stretched (blue, Figure 86 c, the conformation a), two butyl malonate arms are bent (red, Figure 86 c, the conformation c and the remaining are in a half-bent position thus showing a combination of the other two pairs (green, Figure 86 c, the conformation b).

Table 6 reveal the main bond lengths and C-H···H-C interactions between the branches of the close by neighbours hexaaducts and Figure 87 shows the network view of the packing structure through these interactions. The main forces that maintain the densely packed 3D structure are the supramolecular Van der Waals interactions between the alkyl chains of adjacent hexaaducts, the so-called "sticky fingers"[235] as mentioned above in compound **3a**.

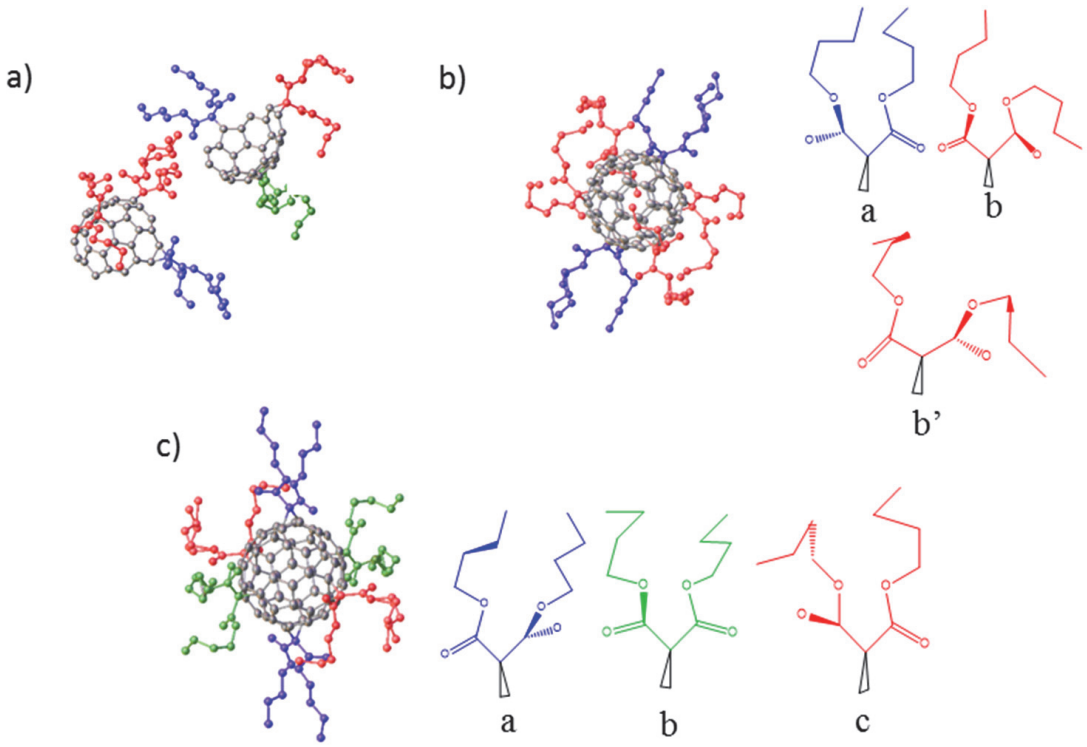

Figure 86. a) Asymmetric unit of **3b**. b) Fullerene place on the vertex of the unit cell and a, b, and b' arms conformation. c) Fullerene placed inside the unit cell and) a, b and c arms conformation.

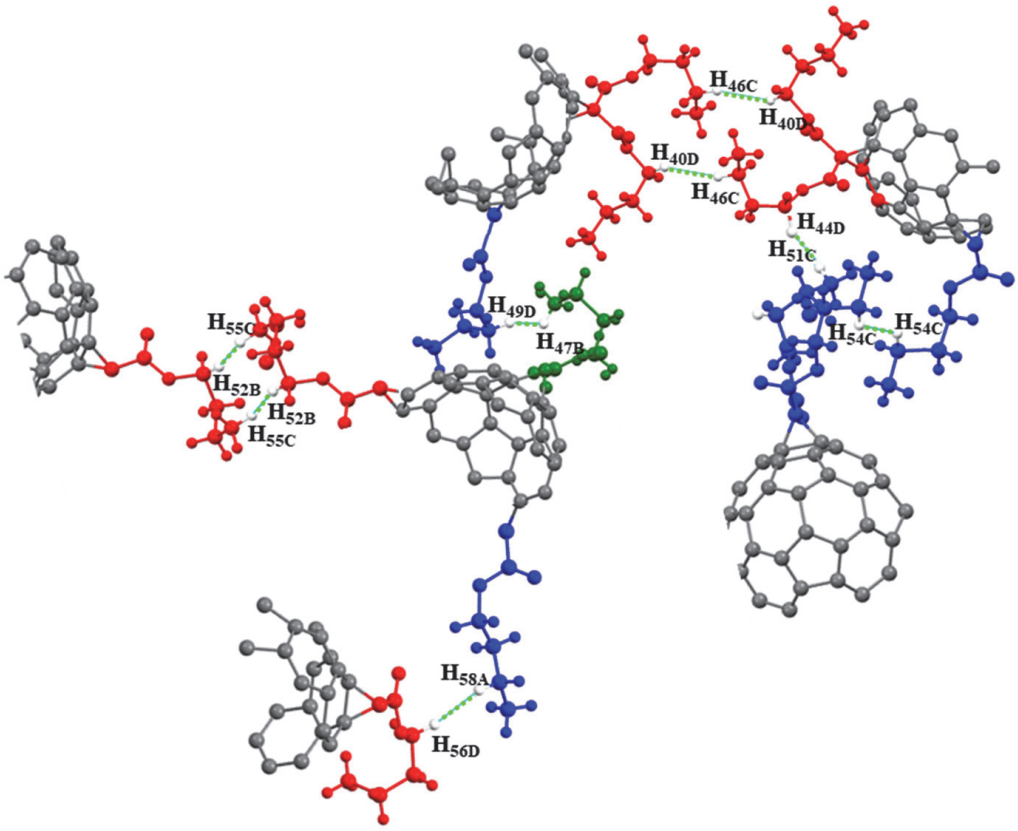

Figure 87. A depiction of the Van der Waals connections of the diverse malonate group with its close neighbors in **3b**.

Table 6. Selected bond lengths [Å] for compound **3b**.

	Selected bond lengths [Å]		Selected bond lengths [Å]
C52A(H52B)-(H55C)C55A	3.793	**H55C-H55B**	2.341
C40B(H40D)-(H46C)C56B	4.070	**H40D-H46C**	2.359
C44B(H47B)-(H49D)C51B	3.465	**H47B-H49D**	1.946
C44B(H44D)-(H51C)C51B	3.971	**H44D-H51G**	2.374
C56B(H56D)-(H58A)C58A	3.919	**H56D-H58A**	2.296
C54B(H54C)-(H54C)C54B	3.859	**H54-H54C**	2.303

5.2.2. Physico-chemical study of compound 3b

In order to study the physical properties of **3b**, this compound was characterized by differential scanning calorimetry (DSC) measurements, temperature dependent optical reflectivity and thermogravimetric analysis.

Thermal stability of **3b** has also been evaluated, by heating and cooling thermal ramps at DSC, from 523 K back to 303 K. Differential scanning calorimetry thermograms of **3b** are showed in Figure 88.

During first heating ramp (Figure 88 a and b) three endothermic peaks are recorder, which means that the crystal absorbs energy, at 387 K (7.2239 J/g), 460 K and 490 K (33.7610 J/g). The cooling thermogram display one exothermic peak, the crystal releases energy, at 388K (18.820 J/g) (Figure 88 b). Then at the second heating ramp, the endothermic peak at 387K not was detected, and only appears the other two endothermic peaks at 460 K and 490 K (32.501 J/g) (Figure 88 b). The sharp peaks indicate a first-order phase transition in **3b**.

DSC measurements are indicative that a phase transition takes place by thermal effect. In order to observe the possible physical changes in the crystal associated with a thermal-phase transition, two single crystals were monitored and recorded with a microscope coupled to a heating-and-cooling device (Figure 88).

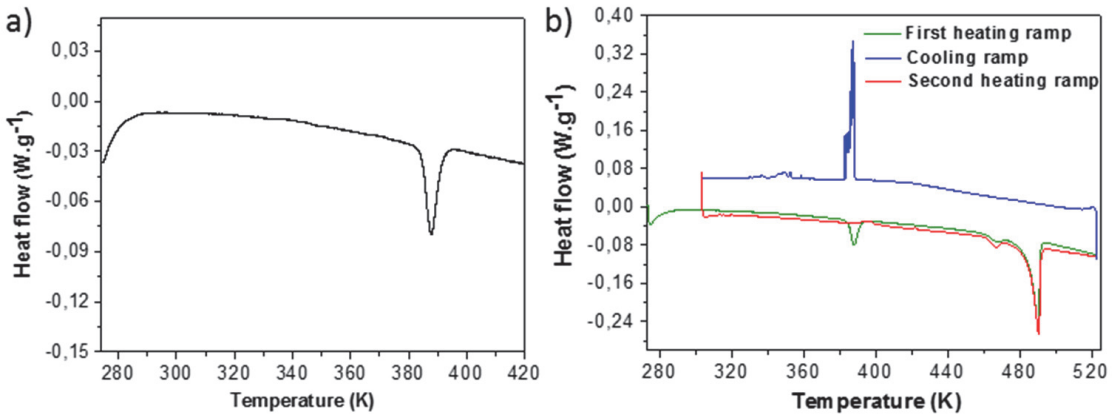

Figure 88. Temperature dependence of differential scanning calorimetry for **3b**. a) DSC curve as a function of temperature showing amplification of an endothermic peak at 387 K in the first heating ramp. b) DSC curves as a function of temperature for three consecutive heating and cooling ramps.

The resulting temperature dependent optical reflectivity spectra are shown in Figure 89. Like in the DSC experiment, three thermals ramps were measured. As it can be appreciated on the first heating ramp, Figure 89 a and b, **3b** displayed three peaks as well as DSC experiments. The first one is centered around 387 K and is consistent with the phase transition of **3b**. This thermal phase transition is also accompanied by a brightness change, due to the loss of crystallinity, and crystal

size change. The size of the crystal increased in the order of $\bar{x}$= 5.25 % (Figure 90). The second peak appeared at 460 K would represent the beginning of the rupture of supramolecular interactions before fusion and the last one, at 493 K corresponded to the fusion of **3b**.

Although, the peaks of the cooling ramp and second heating ramp are not reflected in the optical reflectivity graph versus temperature, the video recorded revealed what these peaks represent. The peak at 388 K in the cooling ramp indicated the recrystallization of the liquid form of **3b** and the peaks at 460 K and 490 K of the second heating ramp, again correspond to the starting of the rupture of supramolecular interactions before the fusion and to the fusion of the compound, respectively.

Therefore, crystals of **3b** exhibits a non-reversible first order thermal phase transition at 387 K.

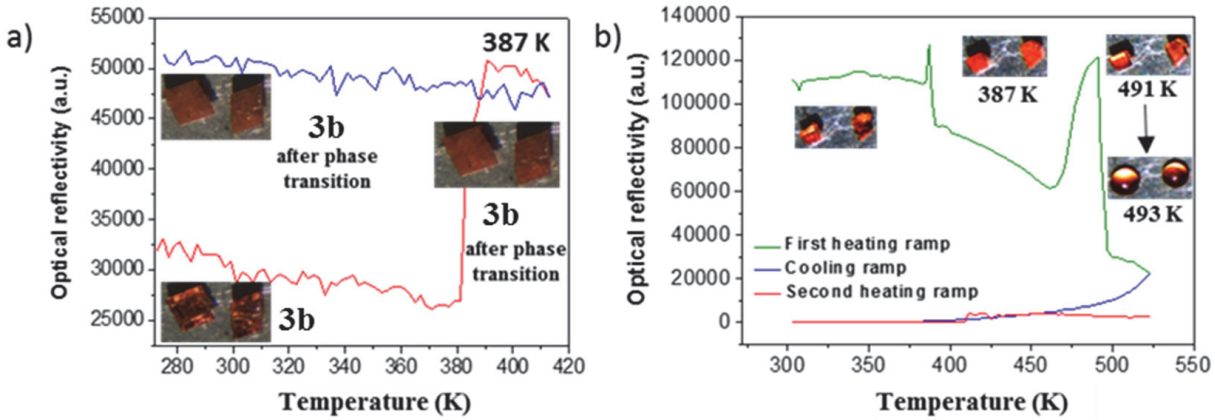

Figure 89. Optical reflectivity of **3b**. a) Optical reflectivity as a function of temperature showing the amplification of an endothermic peak at 387 K and images in the first heating ramp. b) Optical reflectivity as a function of temperature measures of three consecutives heating and cooling ramps.

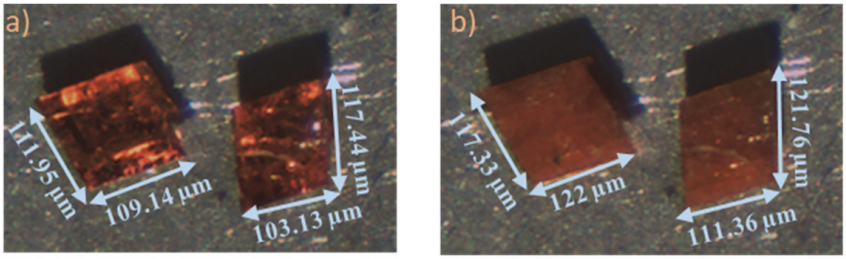

Figure 90. Crystal size and brightness change. a) Before (at 298 K) and b) after the phase transition, at 387 K.

Additionally, the thermogravimetric analysis of the samples shows no solvent weight loss, indicating that the thermal transition is not due to a release of lattice

solvent molecules. TGA measurements also reveals that **3b** is stable until reaching 275 ºC (548 K, as well as **3a**) in which the sample start to lose weight (Figure 91).

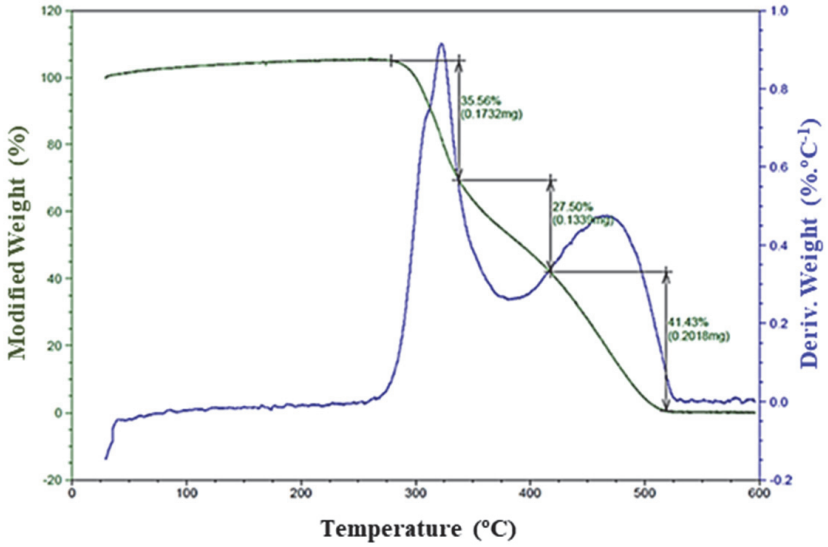

Figure 91. Thermogravimetric profile of **3b** (0.5270 mg in air) showing the mass variation (green curve) and its first derivative (blue curve) upon heating at 2 ºC/min rate.

5.2.3. Structural and Physico-chemical characterization of compound 3b after thermal treatment, 3b^{t}

In order to obtain more information about the nature of the new thermal phase, called **3b^{t}**, structural and physical studies, such as powder X-Ray diffraction, FTIR and DSC studies, have been performed.

Taking advantage of the fact that the phase transition leading to **3b^{t}** was irreversible, powder diffraction of **3b** and **3b^{t}** compounds were carried out. Here, it is important to mention that **3b** and its simulated from their crystal structure by using Mercury software are very close (Figure 92). Thus, powder present the same crystalline structure as the crystalline sample, thus milling does not affect the sample's structure and properties.

In opposite, Figure 92 shows that **3b** and **3b^{t}** spectra are different. Therefore, it can be affirmed that a phase transition occurred in **3b** by applying temperature as external perturbation. Finally, upon obtaining **3b^{t}**, its spectrum was compared with the spectrum of compound **3a**. The two spectra superimpose (Figure 92). Thereby, we can confirm that **3b^{t}** and **3a** are the same compound.

The thermal phase transition, **3b^{t}**, was also monitored by FTIR spectroscopy. When comparing **3b** and **3b^{t}** FTIR spectra, one can see that they are not alike. Major difference takes place the region of (1100-700) cm^{-1}, corresponding to the CH bands

of the fullerene branches. However, these bands are identical in both **3b**^{t} and **3a** (Figure 93), corroborating they are both the same structure.

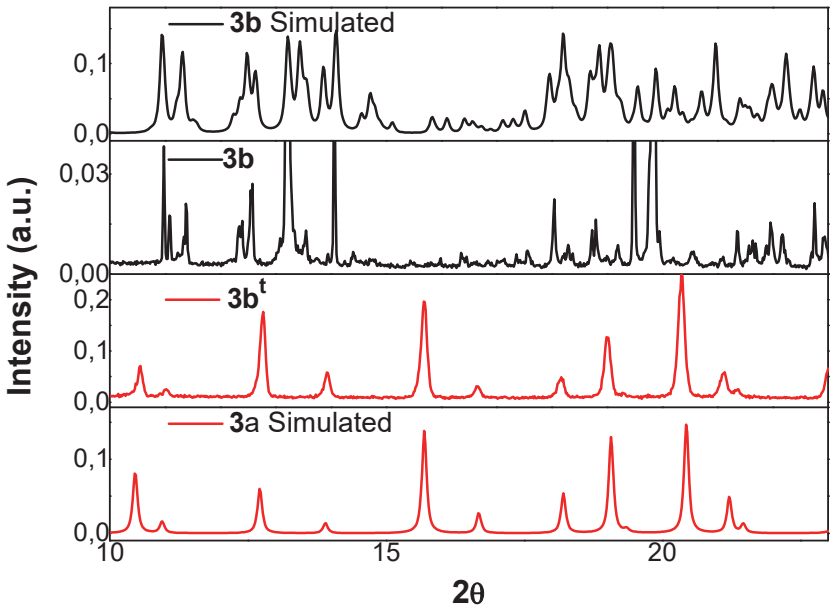

Figure 92. Simulated and experimental powder X-ray diffraction patterns of compound **3b**, phase transition compound **3b**^{t} (after the heating of crystals at 114 °C (387 K) and simulated pattern of compound **3a**.

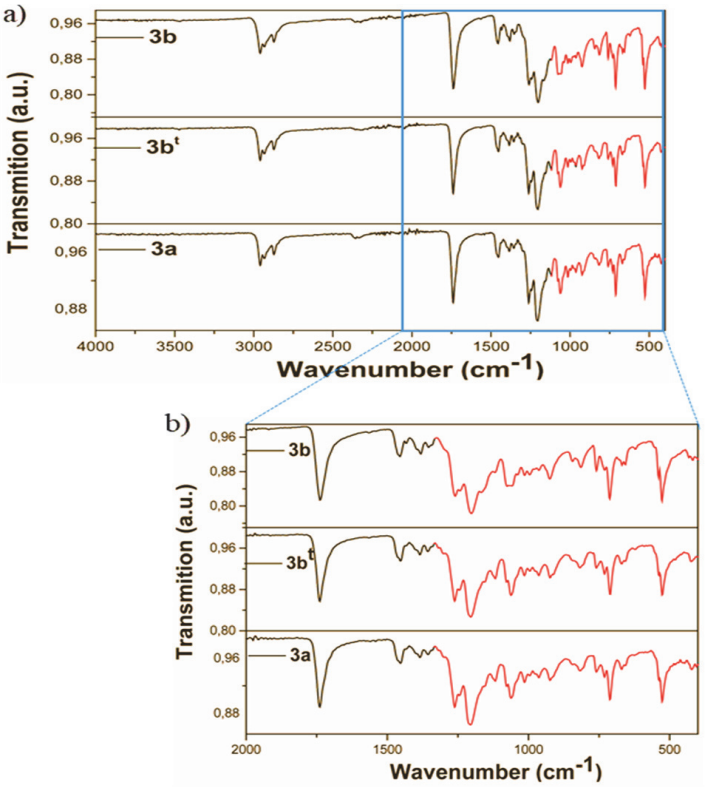

Figure 93. a) Infrared spectra of compound **3b** before and after the heating of crystals at 114 °C (387 K) and compound **3a**. b) Amplification of the IR spectrum between 2000 and 400 cm^{-1} to show the main shifts of the bands.

A freshly **3a** sample was prepared and analyzed by DSC and optical reflectivity as a function of temperature. During the first heating ramp, the endothermic peak at 387 K, that have been reported to correspond to the thermal phase transition, is not found (Figure 94). Nevertheless, above this temperature (387 K) and on the following ramps (cooling and heating), it can be appreciated that **3a** exhibits the same behavior as **3b**^{t} (Figure 94 c, d and ANNEX D 5).

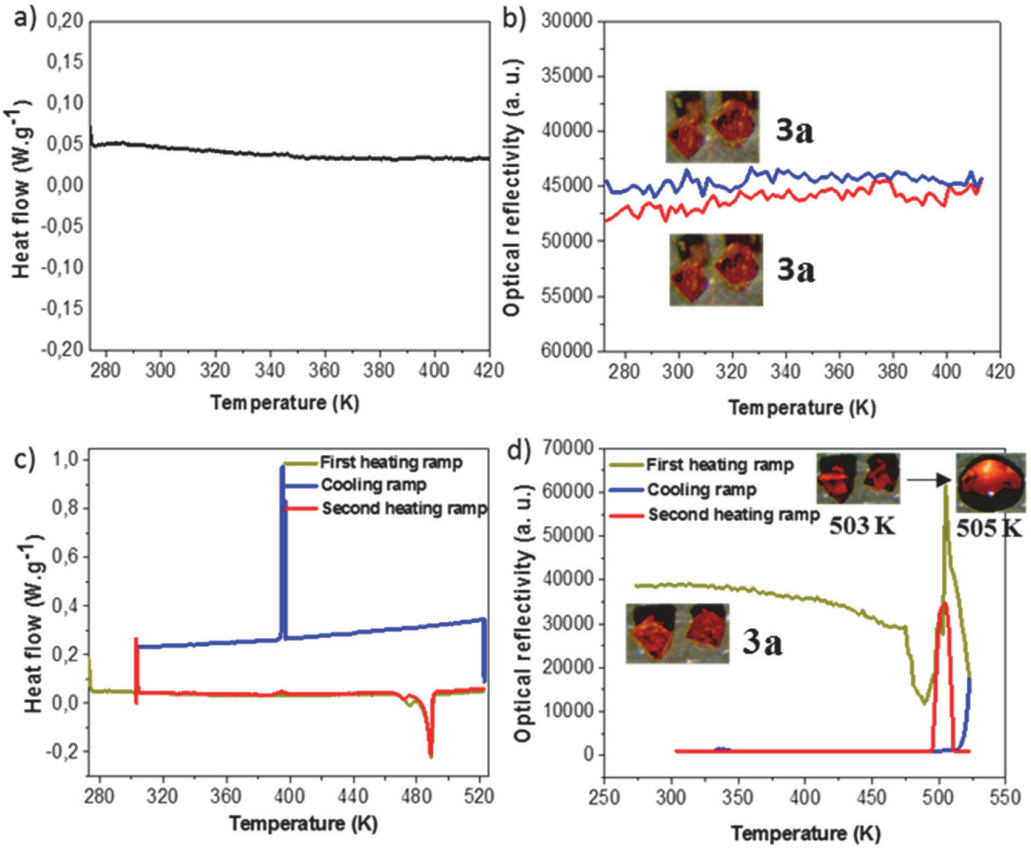

Figure 94. a) DSC curves of **3a** showing a non-detectable phase transition in the first heating ramp. b) Optical reflectivity of **3a** showing a non-detectable phase transition in the first heating ramp. c) DSC curves of **3a** of three consecutive heating and cooling ramps d) Optical reflectivity as a function of temperature measures of **3a** of three consecutive heating and cooling ramps.

Structurally the conversion from **3b** to **3a** is coherent. As it was described previously, compound **3b** presents two different conformations (Figure 86) where the arms are stretched out, bent and in an intermediate state. When applying temperature to compound **3b**, the thermal transition leads to **3b**^{t}. Structurally, this means that when temperature is applied, all butyl branches go into the same conformation, that is to say, the branches are completely stretched, just like in **3a** (Figure 95).

On the other side, in Figure 95 is observed that the transition is not reversible. However, by placing **3b** crystals in an ethanol solution at 120 °C for 3 days in a

furnace in the absence of the metallic salt, crystals of **3a** were obtained. Therefore, **3b** crystals are reusable (Figure 95). Figure 95 collects the information obtained throughout these experiments.

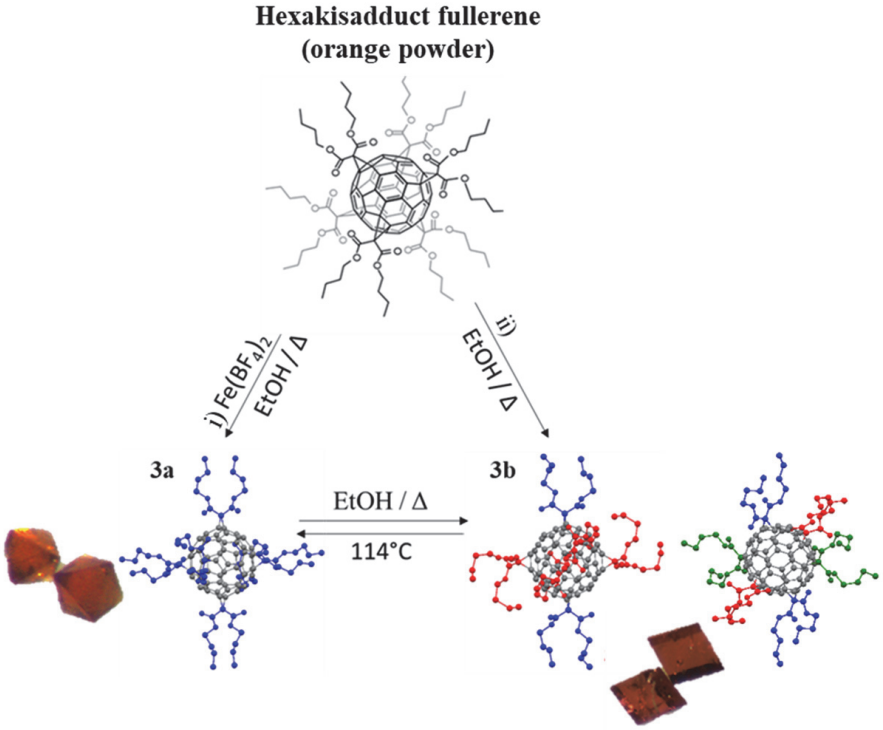

Figure 95. Scheme of the different polymorphs from hexakisadduct fullerene in presence or absence of iron salt and phase transition from **3b** to **3a**, phase transition and recrystallization of **3a**.

5.2.4. Hydrogenation of 3b

As with compound **3a**, a color change from orange to yellow was produced by exposing crystals of **3b** to an atmosphere saturated with hydrazine at 67 ºC (but in this case after 7 days), resulting in the formation of compound **4b**, by SCSC reaction. This color change is indicative of the hydrogenation of the compound by the action of the hydrazine (Figure 96).

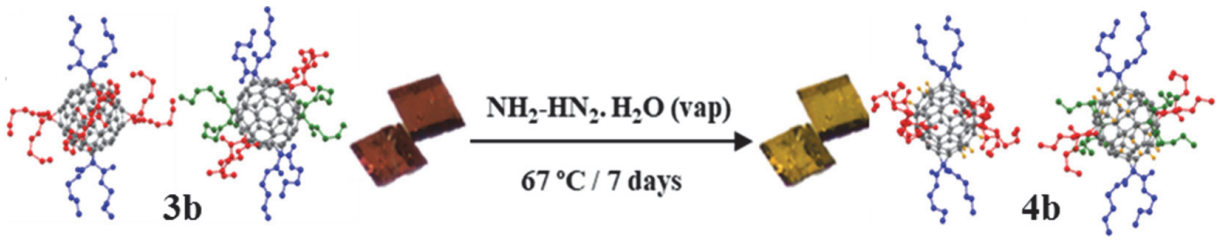

Figure 96. General scheme SCSC reaction of **3b** to **4b** by the exposition to hydrazine vapors.

4b was characterized by NMR Spectroscopy, SCXRD (measured in ALBA Synchrotron) and mass spectrometry. Figure 97 compares the ^{1}H NMR of compound **3b** and **4b**. The ^{1}H NMR spectrum of **3b** exhibits four signals at 4.33, 1.68, 1.41 and 0.92 ppm correspond to the 12 groups of butyl malonate, -OCH_2 (H_5), -CH_2 (H_3), -CH_2 (H_2) and -CH_3 (H_1), respectively (Figure 97 a).

As well as **4a**, the signal that indicates that **3b** has been hydrogenated, emerge at 3.57 ppm and integrates to 24 protons (Figure 97 b, H_4).

On the other side, the different disposition of the butyl malonate arms induced to a dissimilar hydrogenation resulting in the splitting of two triplets in the signals corresponding to methylene -$COOCH_2$- (at 4.33 and 4.20 ppm) in **4b** (Figure 97 b, H_{5a} and H_{5b}). The triplet signal at 4.33 ppm (Figure 97 b, H_{5a}) did not suffer any displacement because these groups were not located near the hydrogenated positions. In contrast, the methylene groups -$COOCH_2$- that lie over these hydrogenated positions causing an upward field change in methylene resonances from 4,33 to 4,20 ppm (Figure 97 b, H_{5b}). Therefore, the formulation of this new compound (**4b**) is the same as **4a**, $C_{126}H_{132}O_{24}$.

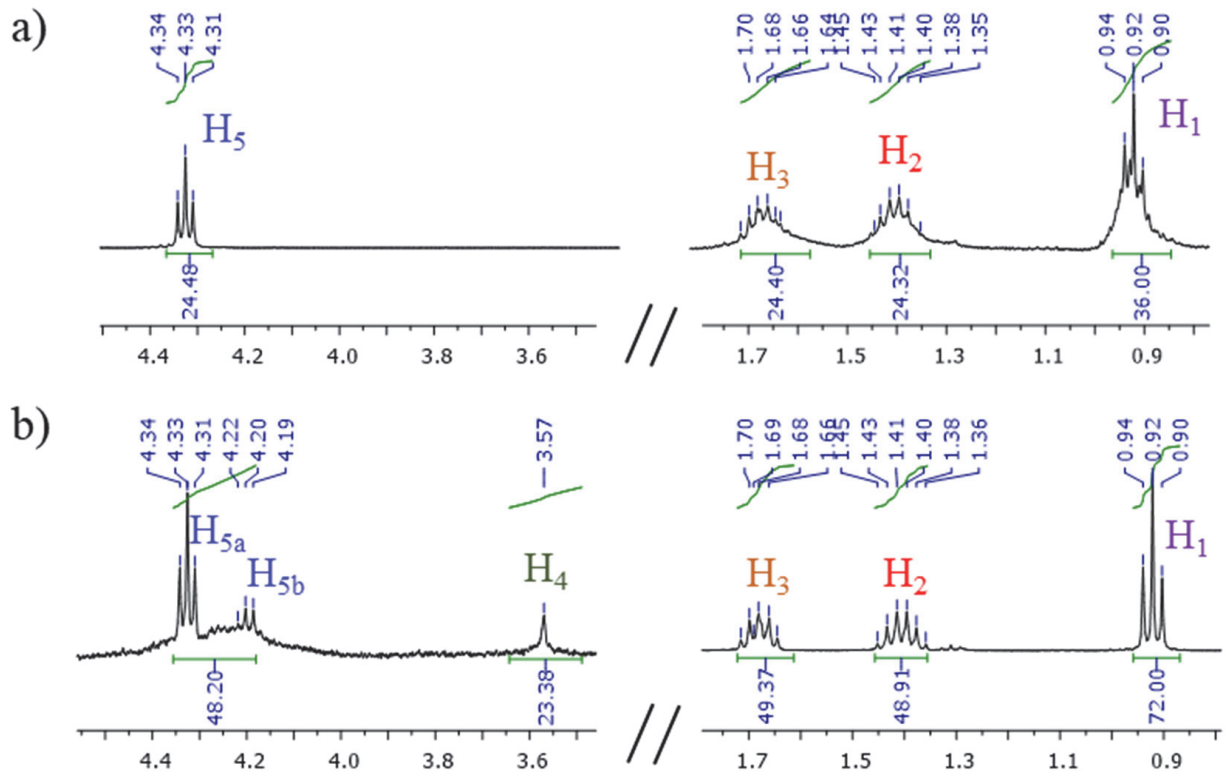

Figure 97. ^{1}H NMR spectra of compounds a) **3b** and b) **4b**.

By SCXRD is observed that compound **4b** retains the same space group and crystalline system as **3b** (ANNEX D 4). Figure 98 provides a comparative study of

the distances between the starting fullerene (**3b**) and hydrogenated fullerene (**4b**) and also the location of the hydrogenated positions in **4b**.

As discussed above, the scaffold of **3b** is composed by two fullerenes with a different disposition of the butyl malonate arms (Figure 86 b and c) and as a consequence, each fullerene has suffered a dissimilar hydrogenation which may also be owed to that different disposition of the arms (Figure 98 c and d).

The pink colored linkages are the anchored positions of the butyl malonate groups (Figure 98). Moreover, the green colored are the doubles linkages that will be hydrogenated (Figure 98 a and b) and the blue ones are the bonds where hydrogenation takes place (Figure 98 c and d). It can be seen as such distances increase when the compound is hydrogenated, resulting in a change from hybridization sp^2 to sp^3. However, the lengths are not as long as an aliphatic single bond since the rigid structure of the fullerene restricts the stretch of the bonds.

Furthermore Figure 98 c and d show the dissimilar hydrogenation that takes place in both fullerenes as mentioned above. The different spatial disposition of the arms of the most hydrogenated fullerene, are described as **a**, **b** and **c**, where **a** is completely stretched and **b** is a combination of the other two pairs (**a** and **c**) (Figure 86 c). A rational explanation for this dissimilar hydrogenation could be that spatial disposition of the butyl malonate arms facilitate the hydrazine dispersion and the diimide formation reaction around the more stretch out arms (**a** and **b**), allowing its hydrogenation in 16 positions (Figure 98 b).

In contrast, the other fullerene contains two pairs of arms, **b** and **b'**, which are bent (Figure 86 b). The steric hindrance of this bent arms obstructs the hydrazine diffusion, and consequently, in this fullerene only 8 hydrogenated positions were available for the hydrogenation reaction (Figure 98 d).

Therefore, the information obtained by ^{1}H NMR is corroborated. 24 positions are hydrogenated in **4b**.

Finally, **4b** was characterized by mass spectrometry. In the spectrum two peaks at 2013.7 and 2021.8 m/z were detected (Figure 99). These peaks corresponded to [**3b** + 8 protons] and [**3b** + 16 protons], respectively. These results confirm that it is hydrogenated in 24 different positions between the two kinds of fullerenes and in a dissimilar way, not symmetrically, unlike **4a** (Figure 72) due to the conformation of the malonate branches.

From the results obtained, it can be concluded that a toposelective control can be made on the hydrogenation of this type of fullerenes.

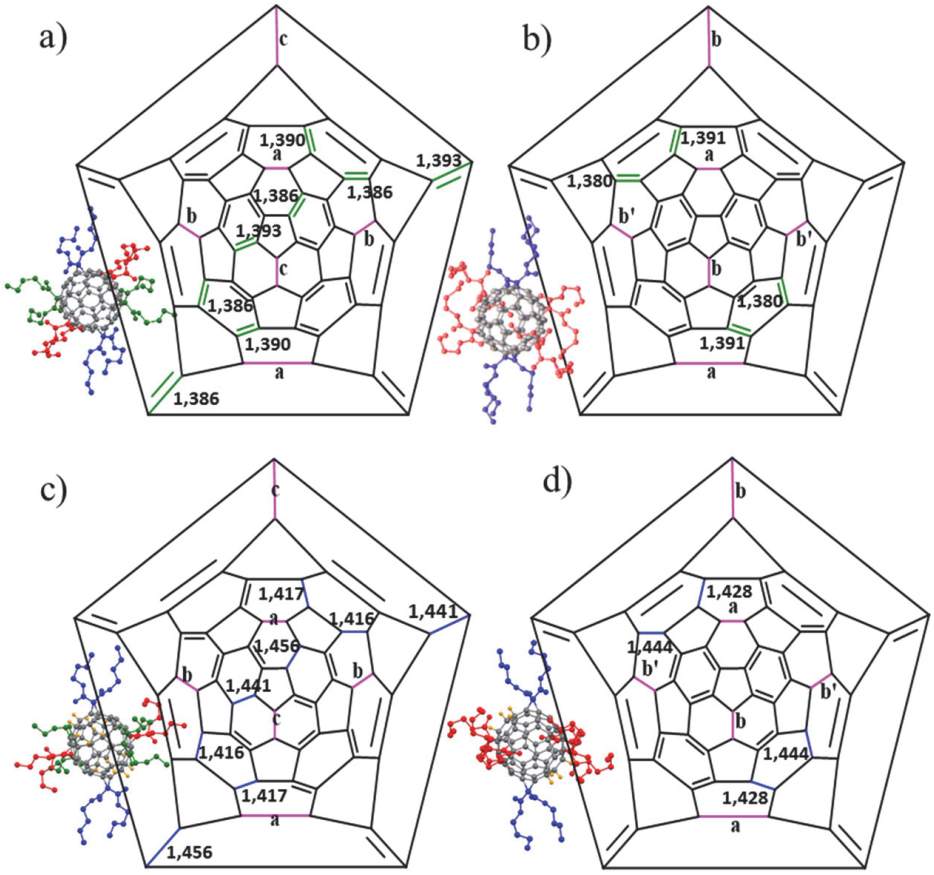

Figure 98. Comparison between the distances of a) and b) starting fullerene (**3b**) and c) and d) hydrogenated fullerene (**4b**).

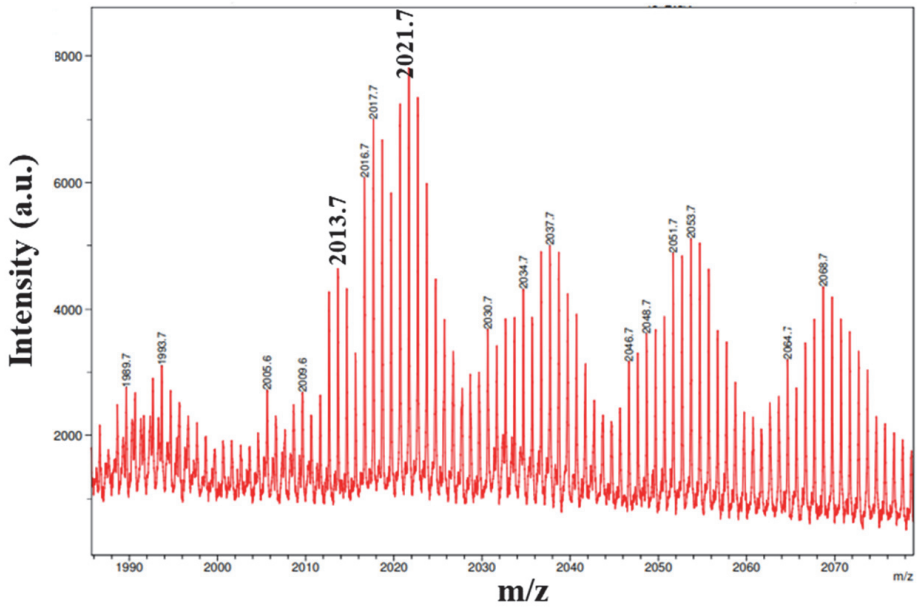

Figure 99. Mass Spectrometry of compound **4b**. Two detected peaks at **2013.7** and **2021.8 m/z** that correspond to [**3b** + 8 protons] and [**3b** + 16 protons], respectively.

5.3. CONCLUSIONS

We have reported a fullerene crystalline dynamic framework, **3b** that exhibits an abrupt and irreversible phase change transition in response to external stimuli, temperature. This phase transition led to the formation of a new polymorph, which by exhaustive characterization study was discovered to be compound **3a**, which had been obtained in chapter 4. By heating compound **3b**, a complete stretching of the butyl arms (of both types of fullerenes present in **3b**) occurs. This fact creates a densely compact 3D structure due to the reorganization of the butyl chains and their Van der Waals contacts, as observed in the crystalline structure of **3a**. In spite of not being a reversible phase transition, the crystals of compound **3b** can be obtained again by a simple reaction with ethanol as indicated in Figure 95. Finally, this phase thermal transition is also accompanied by a change of brightness and crystal size, which is increased order of $\bar{x}$= 5.25 %, hence, it could be used in applications such as molecular actuators and machines. On the other hand, when **3b** was exposed to hydrazine vapors and as in **3a**, a change in color from orange to yellow occurred due to the hydrogenation of the compound, in twenty-four positions. In this case, the hydrogenation is dissimilar in the two different fullerenes of **3b**, in a fullerene, sixteen positions are hydrogenated and in another eight positions, and this could be due to the disposition of the butyl malonate arms of the fullerene. From **3a** and **3b** we can control the hydrogenation of twenty-four positions as shown in Figure 98 and Figure 100.

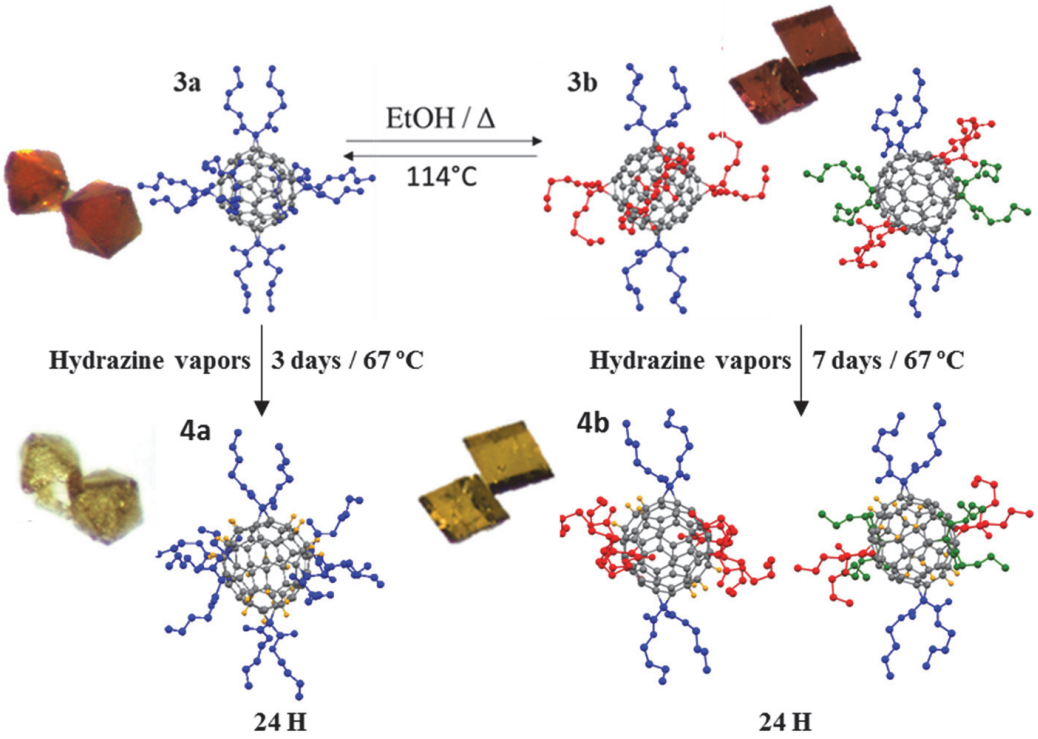

Figure 100. Controlled SCSC topo selective hydrogenation reaction under the exposition to hydrazine vapors of **3a** and **3b**.

The relative spatial disposition of the butyl malonate arms could be essential for the diimide generation reaction. This might show the importance and the catalytic function of the fullerene on the hydrazine stabilization and confined space reaction for the diimide generation[262]. These controlled topochemical solid-state reactions will contribute to the creation of novel softs and dynamics carbon-based advanced absorbent materials with a variety of direct technological applications, as chemo-sensor and environmental remediation devices.

6. CONCLUSIONS

From the results obtained in the different chapters, the following conclusions have been drawn:

In chapter 2, a novel and interesting 3D MOF crystalline structure, {[Fe(PM-Tria)$_2$(μ_2-F)](BF$_4$)}$_n$, from a new extended ligand based on triazoles (PM-Tria, N,N'E,N,N'E)-N,N'-(1,4-phenylenebis(methanylylidene))bis(4*H*-1,2,4-3) and iron salts has been synthesized using specific synthesis conditions (Fe(BF$_4$)$_2$·6H$_2$O and FeF$_2$ salts, ethanol as solvent, 120 ºC of temperature and 1.33:0.5:0.5 of stoichiometry), without which the formation of the compound would not have been possible. In addition, this interesting compound exhibits along the Fe(II)-F chain a perfect linearity in its growth mode, and an antiferromagnetic behavior along this chain. Furthermore, its attractive molecular structure is compared to a 14th century Islamic mosaic found in the Alhambra Palace in Granada (Spain) and surprisingly fits almost perfectly with that of the mosaic. SCSC reactions were also performed by exposing the compound to different vapors, obtaining a change in color, infrared and thermogravimetric analysis with acetic acid. Therefore, the reaction with acetic acid can be very promising, so it will be profoundly characterized and the structure will be precisely determined, which could be used for multiple applications, with high selectivity sensors or molecular storage. Finally, as future perspectives: new structural analogues to the PM-Tria ligand will be developed including molecular receptors (functional groups), as well as additional research to activate the material. As well as new synthetic reactions with ligands based on tetrazoles.

In chapter 3, the synthesis and characterization of a compound with formula {FeCl$_2$(pyz)$_2$}$_n$ is reported, which undergoes a reversible SCSC reaction in gaseous/solid phase in the presence of pyridine vapors which is accompanied by a color change, first from red to orange (affording the an intermediate compound, where two pyrazine groups have been replaced by two pyridine rings) and finally, orange to yellow, obtaining the final compound, [FeCl$_2$(py)$_4$].H$_2$O (where the four pyrazine groups have been totally replaced by four pyridine groups). Notably, when the final compound is introduced into a concentrated pyrazine solution, the ligand

exchange process is completely reversible without loss of crystallinity, resulting in regeneration of the initial compound and thus obtaining a reusable sensor.

In chapter 4 the first reported weak Van der Waals “sticky fingers” crystalline structure of a [60]fullerene hexakis adduct is described. This fullerene exhibits a non-porous dynamic crystalline structure capable of undergoing SCSC reactions. Concretely, under the exposure to hydrazine vapors induce a structural and chemical changes, that is to say, distorsion and change in the color is produced resulting in the topo selective and controlled hydrogenation on the fullerene surface. Therefore, the creation of novel carbon-based advanced absorbent materials with a variety of direct technological applications, as a hydrazine deactivator and sensor, due to its known toxicity and carcinogenesis capacity of the latter.

In the last chapter, a new crystalline dynamic polymorph hexakis adduct fullerene has been reported, which exhibits an irreversible thermal phase transition leading to the formation of a new polymorph, which through an extensive characterization study was identified to be the non-hidrogenated [60]fullerene hexakis adduct described in the chapter 4. The crystals of the novel dynamic fullerene could be obtained again by a simple reaction with ethanol. This phase thermal transition is also accompanied by a change in the brightness and size of glass, so that it could be used in applications such as molecular actuators. Finally, by exposing the new polymorph to hydrazine vapors, toposelective hydrogenation of this compound takes place in 24 positions. The hydrogenation is dissimilar in the two different fullerenes of the novel polymorph, in a fullerene, sixteen positions are hydrogenated and in another eight, and this could due to the different disposition of its butyl malonate arms. Therefore, this material can be controlled the hydrogenation and it could be used in applications such as chemical sensors.

In conclusion, in this thesis unprecedented crystalline materials of diverse nature have been developed, including diverse polymers of coordination and non-porous dynamic organic materials, that are very interesting and functional and that can be applied in diverse fields as sensors and stores of harmful molecules.

7. References

1 G. K. Kole and J. J. Vittal, *Chemical Society Reviews*, 2013, **42**, 1755–1775.

2 F. R. S. and C. N. R. Rao and J. Gopalakrishnan, *New Directions in Solid State Chemistry Second Edition*, 2001.

3 J. I. Urgel, D. Écija, G. Lyu, R. Zhang, C. A. Palma, W. Auwärter, N. Lin and J. V. Barth, *Nature Chemistry*, 2016, **8**, 657–662.

4 R. S. Forgan, J. P. Sauvage and J. F. Stoddart, *Chemical Reviews*, 2011, **111**, 5434-5464.

5 S. H. Petrosko, R. Johnson, H. White and C. A. Mirkin, *Journal of the American Chemical Society*, 2016, **138**, 7443−7445.

6 V. V. Boldyrev, *Journal of Thermal Analysis*, 1993, **40**, 1041–1062.

7 I. G. Georgiev and L. R. MacGillivray, *Chemical Society Reviews*, 2007, **36**, 1239–1248.

8 A. Chaudhary, A. Mohammad and S. M. Mobin, *Crystal Growth and Design*, 2017, **17**, 2893–2910.

9 G. M. J. Schmidt, *Pure and Applied Chemistry*, 1971, **27**, 647–678.

10 V. V. Boldyrev, *Reactivity of solids : past, present, and future*, Blackwell Science, 1996.

11 F. Toda, *Organic Solid-State Reactions*, Springer Netherlands, 2002.

12 G. R. (Gautam R. . Desiraju, J. J. Vittal and A. Ramanan, *Crystal engineering : a textbook*, World Scientific, 2011.

13 F. Huang and E. V. Anslyn, *Chemical Reviews*, 2015, **115**, 6999.

14 S. R. Batten, N. R. Champness, X.-M. Chen, J. Garcia-Martinez, S. Kitagawa, L. Öhrström, M. O'Keeffe, M. Paik Suh and J. Reedijk, *Pure and Applied Chemistry*, 2013, **85**, 1715–1724.

15 https://www.britannica.com/science/organic-compound (accessed 15

September 2019).

16 A. E. de Barr, *Contemporary Physics*, 1961, **2**, 409–422.

17 A. R. Prajapati and S. Rajpurohit, *Indian Journal of Scientific Research*, 2017, **17**, 53–59.

18 S. K. Chatterjee, *Crystallography and the World of Symmetry*, Springer, 2006.

19 Unit Cells States Of Matter, https://courses.lumenlearning.com/cheminter/chapter/unit-cells/ (accessed 7 June 2019).

20 F. A. Duward Shriver, Mark Weller, Tina Overton, Jonathan Rourke, *Inorganic Chemistry*, Macmillan Education (W. H. Freeman), 2014.

21 L. Dünkel, *Zeitschrift für Physikalische Chemie*, 2011, **198**, 273–274.

22 M. Cardona, P. Fulde, K. Von, K. R. Merlin, H.-J. Queisser and H. Störmer, *Springer Series in Solid-State Sciences*, Springer Series, 2017.

23 A. L. Gentile and D. F. Elwell, *Crystal Growth*, 1988, vol. 13.

24 A. R. Prajapati and S. Rajpurohit, *Indian Journal of Scientific Research*, 2017, **17**, 53-59.

25 G. M. Parkinson, J. M. Thomas, J. O. Williams, M. J. Goringe and L. W. Hobbs, *Journal of the Chemical Society, Perkin Transactions 2*, 1976, 836–838.

26 E. N. Duesler, K. E. Wiegers, D. Y. Curtin and I. C. Paul, *Molecular crystals and liquid crystals*, 1980, **59**, 289–298.

27 H. nakanishi. W. Jones and j J. M. Thomas, *Chemical Physics Letters,*1980, **71**, 44-48.

28 K. Novak and K. B. Wagener, *Journal of the American Chemical Society*, 1993, **115**, 10390–10391.

29 E. Lee, Y. Kim, J. Heo and K. M. Park, *Crystal Growth and Design*, 2015, **15**, 3556–3560.

30 J. Shen, H. Bai, X. Zhou, J. Liu, X. Hu, P. K. Chu and G. Tang, *CrystEngComm*, 2019, **21**, 1102–1106.

31 N. L. Rosi, M. Eddaoudi, J. Kim, M. O'Keeffe and O. M. Yaghi, *Angewandte Chemie International Edition*, 2002, **41**, 284.

32 J. P. Zhang, P. Q. Liao, H. L. Zhou, R. B. Lin and X. M. Chen, *Chemical Society Reviews*, 2014, **43**, 5789–5814.

33 I. Halasz, *Crystal Growth and Design*, 2010, **10**, 2817–2823.

34 J. P. Zhang, P. Q. Liao, H. L. Zhou, R. B. Lin and X. M. Chen, *Chemical Society Reviews*, 2014, **43**, 5789–5814.

35 W. W. He, S. L. Li and Y. Q. Lan, *Inorganic Chemistry Frontiers*, 2018, **5**, 279–300.

36 J. J. Vittal, *Coordination Chemistry Reviews*, 2007, **251**, 1781–1795.

37 M. Kawano and M. Fujita, *Coordination Chemistry Reviews*, 2007, **251**, 2592–2605.

38 S. B. Choi, H. Furukawa, H. J. Nam, D. Y. Jung, Y. H. Jhon, A. Walton, D. Book, M. O'Keeffe, O. M. Yaghi and J. Kim, *Angewandte Chemie International Edition*, 2012, **51**, 8791–8795.

39 E. Y. Lee and M. P. Suh, *Angewandte Chemie International Edition*, 2004, **43**, 2798–2801.

40 Santiago Reinoso, B. Artetxe and J. M. Gutirrez-Zorrilla, *Acta Crystallographica Section C: Structural Chemistry*, 2018, **74**, 1222–1242.

41 A. Michaelides and S. Skoulika, *Crystal Growth and Design*, 2005, **5**, 529–533.

42 K. Takaoka, M. Kawano, M. Tominaga and M. Fujita, *Angewandte Chemie International Edition*, 2005, **44**, 2151–2154.

43 T. Kretz, J. W. Bats, S. Losi, B. Wolf, H. W. Lerner, M. Lang, P. Zanello and M. Wagner, *Journal of the Chemical Society. Dalton Transactions*, 2006, 4914–4921.

44 J. P. Zhang, Y. Y. Lin, W. X. Zhang and X. M. Chen, *Journal of the American Chemical Society*, 2005, **127**, 14162–14163.

45 H. J. Choi and M. P. Suh, *Journal of the American Chemical Society*, 2007, **126**, 15844–15851.

46 M. P. Suh, J. W. Ko and H. J. Choi, *Journal of the American Chemical Society*, 2002, **124**, 10976–10977.

47 R. Gheorghe, M. Kalisz, R. Clérac, C. Mathonière, P. Herson, Y. Li, M. Seuleiman, R. Lescouëzec, F. Lloret and M. Julve, *Inorganic Chemistry*, 2010, **49**, 11045–11056.

48 E. Coronado, M. Giménez-Marqués and G. Mínguez Espallargas, *Inorganic Chemistry*, 2012, **51**, 4403–4410.

49 S. Kitagawa, R. Kitaura and S. I. Noro, *Angewandte Chemie International Edition*, 2004, **43**, 2334–2375.

50 V. I. Ovcharenko, S. V. Fokin, E. T. Kostina, G. V. Romanenko, A. S. Bogomyakov and E. V. Tretyakov, *Inorganic Chemistry*, 2012, **51**, 12188–12194.

51 K. Gedrich, I. Senkovska, I. A. Baburin, U. Mueller, O. Trapp and S. Kaskel, *Inorganic Chemistry*, 2010, **49**, 4440–4446.

52 J. P. Ma, S. C. Liu, C. W. Zhao, X. M. Zhang, C. Z. Sun and Y. Bin Dong, *CrystEngComm*, 2014, **16**, 304–307.

53 S. Oliver, A. Kuperman, A. Lough and G. A. Ozin, *Chemistry of Materials*, 1996, **8**, 2391–2398.

54 C. Hu and U. Englert, *Angewandte Chemie International Edition*, 2005, **44**, 2281–2283.

55 Z. S. Yao, M. Mito, T. Kamachi, Y. Shiota, K. Yoshizawa, N. Azuma, Y. Miyazaki, K. Takahashi, K. Zhang, T. Nakanishi, S. Kang, S. Kanegawa and O. Sato, *Nature Chemistry*, 2014, **6**, 1079–1083.

56 S. Q. Su, T. Kamachi, Z. S. Yao, Y. G. Huang, Y. Shiota, K. Yoshizawa, N. Azuma, Y. Miyazaki, M. Nakano, G. Maruta, S. Takeda, S. Kang, S. Kanegawa and O. Sato, *Nature Communications*, 2015, **6**, 1–7.

57 M. Kurmoo, H. Kumagai, K. W. Chapman and C. J. Kepert, *Chemical Communications*, 2005, 3012–3014.

58 M. Kondo, M. Murata, H. Nishihara, E. Nishibori, S. Aoyagi, M. Yoshida, Y. Kinoshita and M. Sakata, *Angewandte Chemie International Edition*, 2006, **45**, 5461–5464.

59 K. L. Wong, G. L. Law, Y. Y. Yang and W. T. Wong, *Advanced Materials*, 2006, **18**, 1051–1054.

60 W. L. Leong and J. J. Vittal, *Chemical Reviews*, 2011, **111**, 688–764.

61 M. Nagarathinam and J. J. Vittal, *Macromolecular Rapid Communications*, 2006, **27**, 1091–1099.

62 L. T. Ni, M. Nagarathinam and J. J. Vittal, *Angewandte Chemie International Edition*, 2005, **44**, 2237–2241.

63 H. A. Al-Mohsin, A. Almousa, S. A. Oladepo, A. S. Jalilov, M. Fettouhi and A. M. P. Peedikakkal, *Inorganic Chemistry*, 2019, **58**, 10167–10173.

64 Q. Chu, D. C. Swenson and L. R. MacGillivray, *Angewandte Chemie International Edition*, 2005, **44**, 3569–3572.

65 N.-Y. L. and J.-P. L. Dong Liu, *Dalton Transactions*, 2011, **40**, 2141–2147.

66 M. H. Mir, L. L. Koh, G. K. Tan and J. J. Vittal, *Angewandte Chemie International Edition*, 2010, **49**, 390–393.

67 W. J. Gong, Z. G. Ren, H. X. Li, J. G. Zhang and J. P. Lang, *Crystal Growth and Design*, 2017, **17**, 870–881.

68 S. Y. Yang, X. L. Deng, R. F. Jin, P. Naumov, M. K. Panda, R. Bin Huang,

L. S. Zheng and B. K. Teo, *Journal of the American Chemical Society*, 2014, **136**, 558–561.

69 S. Dutta, D. K. Bučar, E. Elacqua and L. R. MacGillivray, *Chemical Communications*, 2013, **49**, 1064–1066.

70 K. M. Hutchins, T. P. Rupasinghe, L. R. Ditzler, D. C. Swenson, J. R. G. Sander, J. Baltrusaitis, A. V. Tivanski and L. R. Macgillivray, *Journal of the American Chemical Society*, 2014, **136**, 6778–6781.

71 Y. C. Ou, D. S. Zhi, W. T. Liu, Z. P. Ni and M. L. Tong, *Chemistry - A European Journal*, 2012, **18**, 7357–7361.

72 R. Medishetty, L. L. Koh, G. K. Kole and J. J. Vittal, *Angewandte Chemie International Edition*, 2011, **50**, 10949–10952.

73 R. Medishetty, R. Tandiana, L. L. Koh and J. J. Vittal, *Chemistry - A European Journal*, 2014, **20**, 1231–1236.

74 M. H. Xie, X. L. Yang and C. De Wu, *Chemistry - A European Journal*, 2011, **17**, 11424–11427.

75 X. Gao, T. Friščić and L. R. MacGillivray, *Angewandte Chemie International Edition*, 2003, **43**, 232–236.

76 A. M. P. Peedikakkal, L. L. Koh and J. J. Vittal, *Chemical Communications*, 2002, **8**, 441–443.

77 M. Nagarathinam and J. J. Vittal, *Chemical Communications*, 2002, **8**, 438–440.

78 Y. F. Han, Y. J. Lin, W. G. Jia, G. L. Wang and G. X. Jin, *Chemical Communications*, 2008, 1807–1809.

79 A. M. P. Peedikakkal and J. J. Vittal, *Inorganic Chemistry*, 2010, **49**, 10–12.

80 G. S. Papaefstathiou, Z. Zhong, L. Geng and L. R. MacGillivray, *Journal of the American Chemical Society*, 2004, **126**, 9158–9159.

81 P. B. Chatterjee, A. Audhya, S. Bhattacharya S. T. Abtab, K. Bhattacharya and M.Chaudhury, *Journal of the American Chemical Society,* 2010, **132**, 15842–15845.

82 A. Chanthapally, W. T. Oh and J. J. Vittal, *CrystEngComm*, 2013, **15**, 9324–9327.

83 A. M. P. Peedikakkal and J. J. Vittal, *Chemistry - A European Journal*, 2008, **14**, 5329–5334.

84 J. Sun, F. Dai, W. Yuan, W. Bi, X. Zhao, W. Sun and D. Sun, *Angewandte Chemie International Edition*, 2011, **50**, 7061–7064.

85 M. Nagarathinam, A. Chanthapally, S. H. Lapidus, P. W. Stephens and J. J.

Vittal, *Chemical Communications*, 2012, **48**, 2585–2587.

86 V. Safarifard and A. Morsali, *CrystEngComm*, 2011, **13**, 4817–4819.

87 H. Ito, M. Muromoto, S. Kurenuma, S. Ishizaka, N. Kitamura, H. Sato and T. Seki, *Nature Communications*, 2013, **4**, 1–5.

88 T. Seki, K. Sakurada and H. Ito, *Angewandte Chemie International Edition*, 2013, **52**, 12828–12832.

89 G. Liu, J. Liu, Y. Liu and X. Tao, *Journal of the American Chemical Society*, 2014, **136**, 590–593.

90 R. Medishetty, D. Jung, X. Song, D. Kim, S. S. Lee, M. S. Lah and J. J. Vittal, *Inorganic Chemistry*, 2013, **52**, 2951–2957.

91 A. Chem, I. Ed, K. Biradha, Y. Hongo and M. Fujita, *Angewandte Chemie International Edition*, 2002, **41**, 3395–3398.

92 S. K. Ghosh, J. P. Zhang and S. Kitagawa, *Angewandte Chemie International Edition*, 2007, **46**, 7965–7968.

93 S. K. Ghosh, W. Kaneko, D. Kiriya, M. Ohba and S. Kitagawa, *Angewandte Chemie International Edition*, 2008, **47**, 8843–8847.

94 W. Kaneko, M. Ohba and S. Kitagawa, *Journal of the American Chemical Society*, 2007, **129**, 13706–13712.

95 A. Kondo, T. Nakagawa, H. Kajiro, A. Chinen, Y. Hattori, F. Okino, T. Ohba, K. Kaneko and H. Kanoh, *Inorganic Chemistry*, 2010, **49**, 9247–9252.

96 F. Wang, Y. X. Tan, H. Yang, Y. Kang and J. Zhang, *Chemical Communications*, 2012, **48**, 4842–4844.

97 L. Wen, P. Cheng and W. Lin, *Chemical Communications*, 2012, **48**, 2846–2848.

98 D. Bradshaw, J. E. Warren and M. J. Rosseinsky, *Science*, 2007, **315**, 977–980.

99 M. Du, C. P. Li, J. M. Wu, J. H. Guo and G. C. Wang, *Chemical Communications*, 2011, **47**, 8088–8090.

100 Q. Chen, Z. Chang, W. C. Song, H. Song, H. Bin Song, T. L. Hu and X. H. Bu, *Angewandte Chemie International Edition*, 2013, **52**, 11550–11553.

101 J. Zhang, R. Liu, P. Feng and X. Bu, *Angewandte Chemie International Edition*, 2007, **46**, 8388–8391.

102 X. N. Cheng, W. X. Zhang, Y. Y. Lin, Y. Z. Zheng and X. M. Chen, *Advanced Materials*, 2007, **19**, 1494–1498.

103 L. H. Xie, Y. Wang, X. M. Liu, J. Bin Lin, J. P. Zhang and X. M. Chen, *CrystEngComm*, 2011, **13**, 5849–5857.

104 S.S.Y. Chui, S.M.F. Lo, J.P.H. Charmant, A.G. Orpen and I.D. Williams, *Science*, 1999, **283**, 1148.

105 D. Lässig, J. Lincke, R. Gerhardt and H. Krautscheid, *Inorganic Chemistry*, 2012, **51**, 6180–6189.

106 D. D. Zhou, Z. J. Liu, C. T. He, P. Q. Liao, H. L. Zhou, Z. S. Zhong, R. B. Lin, W. X. Zhang, J. P. Zhang and X. M. Chen, *Chemical Communications*, 2015, **51**, 12665–12668.

107 E. Deiters, V. Bulach and M. W. Hosseini, *Chemical Communications*, 2005, 3906–3908.

108 S. S. Chen, Q. Liu, Y. Zhao, R. Qiao, L. Q. Sheng, Z. Di Liu, S. Yang and C. F. Song, *Crystal Growth and Design*, 2014, **14**, 3727-3741.

109 Z. S. Cai, S. S. Bao, X. Z. Wang, Z. Hu and L. M. Zheng, *Inorganic Chemistry*, 2016, **55**, 3706–3712.

110 C. J. Kepert and M. J. Rosseinsky, *Chemical Communication*, 1999, **536**, 375–376.

111 M. Nihei, L. Han and H. Oshio, *Journal of the American Chemical Society*, 2007, **129**, 5312–5313.

112 J. Seo, C. Bonneau, R. Matsuda, M. Takata and S. Kitagawa, *Journal of the American Chemical Society*, 2011, **133**, 9005–9013.

113 A. Demessence and J. R. Long, *Chemistry - A European Journal*, 2010, **16**, 5902–5908.

114 J. Xiao, Y. Wu, M. Li, B. Y. Liu, X. C. Huang and D. Li, *Chemistry - A European Journal*, 2013, **19**, 1891–1895.

115 X. M. Zhang, Z. M. Hao, W. X. Zhang and X. M. Chen, *Angewandte Chemie International Edition*, 2007, **46**, 3456–3459.

116 H. J. Choi, M. Dincă and J. R. Long, *Journal of the American Chemical Society*, 2008, **130**, 7848–7850.

117 J. P. Zhang and X. M. Chen, *Journal of the American Chemical Society*, 2008, **130**, 6010–6017.

118 M.-H. Zeng, X.-L. Feng and X.-M. Chen, *Dalton Transactions*, 2004, 2217.

119 Y. Takashima, V. M. Martínez, S. Furukawa, M. Kondo, S. Shimomura, H. Uehara, M. Nakahama, K. Sugimoto and S. Kitagawa, *Nature Communications*, 2011, **2**, 168.

120 S. Yang, X. Lin, W. Lewis, M. Suyetin, E. Bichoutskaia, J. E. Parker, C. C. Tang, D. R. Allan, P. J. Rizkallah, P. Hubberstey, N. R. Champness, K. Mark Thomas, A. J. Blake and M. Schröder, *Nature Materials*, 2012, **11**, 710–716.

121 J. P. Zhang, S. Horike and S. Kitagawa, *Angewandte Chemie International Edition*, 2007, **46**, 889–892.

122 S. Libri, M. Mahler, G. Mínguez Espallargas, D. C. N. G. Singh, J. Soleimannejad, H. Adams, M. D. Burgard, N. P. Rath, M. Brunelli and L. Brammer, *Angewandte Chemie International Edition*, 2008, **47**, 1693–1697.

123 S. Supriya and S. K. Das, *Journal of the American Chemical Society*, 2007, **129**, 3464–3465.

124 S. Rodríguez-Jiménez, H. L. C. Feltham and S. Brooker, *Angewandte Chemie International Edition*, 2016, **55**, 15067–15071.

125 J. S. Costa, S. Rodríguez-Jiménez, G. A. Craig, B. Barth, C. M. Beavers, S. J. Teat and G. Aromí, *Journal of the American Chemical Society*, 2014, **136**, 3869–3874.

126 E. Resines-Urien, E. Burzurí, E. Fernandez-Bartolome, M. Á. García García-Tuñón, P. de la Presa, R. Poloni, S. J. Teat and J. S. Costa, *Chemical Science*, ,2019, **10**, 6612-6616.

127 J. L. Atwood, L. J. Barbour, A. Jerga and B. L. Schottel, *Science*, 2002, **298**, 1000–1002.

128 O. S. Wenger, *Chemical Reviews*, 2013, **113**, 3686–3733.

129 D. A. Miessler, Gary L., Paul J. Fischer, Tarr, *Inorganic Chemistry*, Fifth Edit., 2014.

130 E. Takahashi, H. Takaya and T. Naota, *Chemistry - A European Journal*, 2010, **16**, 4793–4802.

131 K. Fujii, A. Sakon, A. Sekine and H. Uekusa, *Growth (Lakeland)*, 2011, 4305–4308.

132 H. Iida, S. Iwahana, T. Mizoguchi and E. Yashima, *Journal of the American Chemical Society*, 2012, **134**, 15103–15113.

133 A. G. Slater and A. I. Cooper, *Science*, 2015, **348**, aaa8075-10.

134 G. G. E. Galli, *Minerals and Rocks 18*, 1985.

135 Y. Zheng, X. Li and P. K. Dutta, *Sensors*, 2012, **12**, 5170–5194.

136 H. de St. Claire-Deville, *Comptes Rendus Chimie*, 1862, **54**, 324.

137 R. M. Barrer, *Journal of the Chemical Society*, 1948, **435**, 2158–2163.

138 C. Martínez and A. Corma, *Coordination Chemistry Reviews*, 2011, **255**, 1558–1580.

139 P. Eliášová, M. Opanasenko, P. S. Wheatley, M. Shamzhy, M. Mazur, P. Nachtigall, W. J. Roth, R. E. Morris and J. Čejka, *Chemical Society Reviews*, 2015, **44**, 7177–7206.

140 O. M. Yaghi, M. O'Keeffe, M. Eddaoudi and H. Li, *Nature*, 1999, **402**, 276–279.

141 O. M. Yaghi and H. Li, *Journal of the American Chemical Society*, 1995, **117**, 10401–10402.

142 The Cambridge Crystallographic Data Centre (CCDC), https://www.ccdc.cam.ac.uk/ (accessed 10 June 2019).

143 O. M. Y. Hexiang Deng, S. Grunder, Kyle E. Cordova, C. Valente, H. Furukawa, M. Hmadeh, F. Gándara, A. C. Whalley, Z. Liu, S.Asahina, H.Kazumori, M.O'Keeffe, O.Terasaki, J. Fraser, *Science*, 2013, **336**, 225–240.

144 M. Zhao, K. Deng, L. He, Y. Liu, G. Li, H. Zhao and Z. Tang, *Journal of the American Chemical Society*, 2014, **136**, 1738–1741.

145 S. Qiu, M. Xue and G. Zhu, *Chemical Society Reviews*, 2014, **43**, 6116–6140.

146 J. Huang, C. Li, L. Tao, H. Zhu and G. Hu, *Journal of Molecular Structure*, 2017, **1146**, 853–860.

147 T. C. Wang, N. A. Vermeulen, I. S. Kim, A. B. F. Martinson, J. Fraser Stoddart, J. T. Hupp and O. K. Farha, *Nature Protocols*, 2016, **11**, 149–162.

148 D. J. Tranchemontagne, J. L. Mendoza-Cortés, M. O'Keeffe and O. M. Yaghi, *Chemical Society Reviews*, 2009, **38**, 1257–1283.

149 J. A. Mason, J. Oktawiec, M. K. Taylor, M. R. Hudson, J. Rodriguez, J. E. Bachman, M. I. Gonzalez, A. Cervellino, A. Guagliardi, C. M. Brown, P. L. Llewellyn, N. Masciocchi and J. R. Long, *Nature*, 2015, **527**, 357–361.

150 E. D. Bloch, W. L. Queen, R. Krishna, J. M. Zadrozny, C. M. Brown and J. R. Long, *Science*, 2012, **335**, 1606–1610.

151 L. E. Kreno, K. Leong, O. K. Farha, M. Allendorf, R. P. Van Duyne and J. T. Hupp, *Chemical Reviews*, 2012, **112**, 1105–1125.

152 K. Tan, S. Zuluaga, Q. Gong, Y. Gao, N. Nijem, J. Li, T. Thonhauser and Y. J. Chabal, *Chemistry of Materials*, 2015, **27**, 2203–2217.

153 N. S. Bobbitt, M. L. Mendonca, A. J. Howarth, T. Islamoglu, J. T. Hupp, O. K. Farha and R. Q. Snurr, *Chemical Society Reviews*, 2017, **46**, 3357–3385.

154 A. Schoedel, Z. Ji and O. M. Yaghi, *Nature Energy*, 2016, **1**, 1–13.

155 C. W. Rogers and M. O. Wolf, *Coordination Chemistry Reviews*, 2002, **233**–**234**, 341–350.

156 J. A. Real, A. B. Gaspar and M. C. Muñoz, *Dalton Transactions*, 2005, 2062.

157 S. Roy, A. Chakraborty and T. K. Maji, *Coordination Chemistry Reviews*, 2014, **273**–**274**, 139–164.

158 O. Kahn, *Current Opinion in Solid State and Materials Science*, 1996, **1**, 547–554.

159 J. Sanchez Costa, *Comptes Rendus Chimie*, 2018, **21**, 1121–1132.

160 P. Gütlich, A. B. Gaspar and Y. Garcia, *Beilstein Journal of Organic Chemistry*, 2013, **9**, 342–391.

161 P. Gütlich and H. A. Goodwin, 2012, **1**, 1–47.

162 Y. Liu, J. Z. Huo, Y. Y. Liu, X. Su, J. H. Guo, B. Ding, X. G. Wang and J. Xia, *Zeitschrift fur Anorganische und Allgemeine Chemie*, 2015, **641**, 2422–2428.

163 O. Roubeau, *Chemistry - A European Journal*, 2012, **18**, 15230–15244.

164 Z. R. Herm, B. M. Wiers, J. A. Mason, J. M. Van Baten, M. R. Hudson, P. Zajdel, C. M. Brown, N. Masciocchi, R. Krishna and J. R. Long, *Science*, 2013, **340**, 960–964.

165 J. A. Mason, J. Oktawiec, M. K. Taylor, M. R. Hudson, J. Rodriguez, J. E. Bachman, M. I. Gonzalez, A. Cervellino, A. Guagliardi, C. M. Brown, P. L. Llewellyn, N. Masciocchi and J. R. Long, *Nature*, 2015, **527**, 357–361.

166 W. T. Liu, J. Y. Li, Z. P. Ni, X. Bao, Y. C. Ou, J. D. Leng, J. L. Liu and M. L. Tong, *Crystal Growth and Design*, 2012, **12**, 1482–1488.

167 Z. Yan, M. Li, H. L. Gao, X. C. Huang and D. Li, *Chemical Communications*, 2012, **48**, 3960–3962.

168 E. Fernandez-Bartolome, J. Santos, S. Khodabakhshi, L. J. Mcormick, S. J. Teat, C. S. De Pipaon, J. R. Galan-Mascarós, N. Martín and J. Sanchez Costa, *Chemical Communications*, 2018, **54**, 5526–5529.

169 S. Dammers, T. P. Zimmermann, S. Walleck, A. Stammler, H. Bögge, E. Bill and T. Glaser, *Inorganic Chemistry*, 2017, **56**, 1779–1782.

170 K. S. Pedersen, M. A. Sørensen and J. Bendix, *Coordination Chemistry Reviews*, 2015, **299**, 1–21.

171 D. L. Reger, R. P. Watson, J. R. Gardinier, M. D. Smith and P. J. Pellechia, *Inorganic Chemistry*, 2006, **45**, 10088–10097.

172 G. A. Craig, J. S. Costa, O. Roubeau, S. J. Teat and G. Aromí, *Chemistry - A European Journal*, 2012, **18**, 11703–11715.

173 Y. Garcia, V. Niel, M. C. Muñoz and J. A. Real, *Current Chemistry*, 2004, **233**, 229–257.

174 Y. C. Chuang, C. T. Liu, C. F. Sheu, W. L. Ho, G. H. Lee, C. C. Wang and Y. Wang, *Inorganic Chemistry*, 2012, **51**, 4663–4671.

175 A. V. Mudring and F. Rieger, *Inorganic Chemistry*, 2005, **44**, 6240–6243.

176 O. Kahn, *Ber. Bunsengrs. The Journal of Physical Chemistry*, 1994, **98**, 1208.

177 K. A. Cychosz, R. Guillet-Nicolas, J. García-Martínez and M. Thommes, *Chemical Society Reviews*, 2017, **46**, 389–414.

178 A. Hulanicki, S. Glab and F. Ingman, *Pure and Applied Chemistry*, 1991, **63**, 1247–1250.

179 G. van Koten, M. Albrecht, M. Lutz and A. L. Spek, *Nature*, 2000, **406**, 970–974.

180 L. Maini, F. Grepioni, D. Emiliani, D. Braga and G. Cojazzi, *Organometallics*, 2002, **21**, 1315–1318.

181 L. H. Van Poppel, S. G. Bott and A. R. Barron, *Journal of the American Chemical Society*, 2003, **125**, 11006–11017.

182 D. Braga, G. Cojazzi, D. Emiliani, L. Maini and F. Grepioni, *Chemical Communication*, 2001, **1**, 10–11.

183 J. Zhou, J. Cai, L. Wang and S. Ng, *Dalton Transactions*, 2004, **2**, 1493–1497.

184 S. Supriya and S. K. Das, *Journal of the American Chemical Society*, 2007, **129**, 3464–3465.

185 W. Ait-Helal, A. Borbon, S. Sauvage, J. A. De Gouw, A. Colomb, V. Gros, F. Freutel, M. Crippa, C. Afif, U. Baltensperger, M. Beekmann, J. F. Doussin, R. Durand-Jolibois, I. Fronval, N. Grand, T. Leonardis, M. Lopez, V. Michoud, K. Miet, S. Perrier, A. S. H. Prévôt, J. Schneider, G. Siour, P. Zapf and N. Locoge, *Atmospheric Chemistry and Physics*, 2014, **14**, 10439–10464.

186 *Indoor air quality : organic pollutants : report on a WHO meeting, Berlin, West, 23-27 August 1987.*, Copenhagen : World Health Organization, Regional Office for Europe, 1989.

187 H. I. Shinkichi Shimizu, N. Watanabe, T. Kataoka, T. Shoji, N. Abe, S. Morishita, *Ullmann's Encyclopedia of Industrial Chemistry*, 2012, **30**, 557–586.

188 D. Mohan, K. P. Singh, S. Sinha and D. Gosh, *Carbon Journal*, 2004, **42**, 2409–2421.

189 C. Elosua, C. Bariain, I. R. Matias, A. Rodriguez, E. Colacio, A. Salinas-Castillo, A. Segura-Carretero and A. Fernandez-Gutiérrez, *Sensors*, 2008, **8**, 847–859.

190 International Chemical Safety Cards; Nº CAS 110-86-1 (accessed 29 July 2019).

191 N. Chem, D. C. A. S. Reg and I. S. Name, *Chemical Abstract Service. Reg.*

No.: 110-86-1, 1996.

192 A. H. Kamel, M. E. Khalifa, S. A. Abd El-Maksoud and F. A. Elgendy, *International Journal of Electrochemical Science*, 2014, **9**, 1663–1677.

193 Raymond E. Millemann, Wesley J. Birge, Jeffrey A. Black, P. J. F. Robert M. Cushman, Karen L. Daniels, Jeffrey, M. Giddings, A. A. John F. Mccarthy and F. Stewar, *Transactions of the American Fisheries Society*, 2014, **113**, 37–41.

194 G. A. Gross, R. J. Turesky, L. B. Fay, W. G. Stillwell, P. L. Skipper and S. R. Tannenbaum, *Carcinogenesis*, 1993, **14**, 2313–2318.

195 https://chem.libretexts.org/Bookshelves/Introductory_Chemistry/Map%3A_Chemistry_for_Changing_Times_(Hill_and_McCreary)/13%3A_Air/13.5%3A_Photochemical_Smog%3A_Making_Haze_While_the_Sun_Shines (accessed 28 August 2019).

196 K. Vellingiri, P. Kumar and K. H. Kim, *Nano Research*, 2016, **9**, 3181–3208.

197 K. S. Pedersen, P. Perlepe, M. L. Aubrey, D. N. Woodruff, S. E. Reyes-Lillo, A. Reinholdt, L. Voigt, Z. Li, K. Borup, M. Rouzières, D. Samohvalov, F. Wilhelm, A. Rogalev, J. B. Neaton, J. R. Long and R. Clérac, *Nature Chemistry,* 2018, **10**, 10–15.

198 G. Bhosekar, I. Jess and C. Näther, *Inorganic Chemistry*, 2006, **45**, 6508–6515.

199 B. P. W. Carreck, E. Mary, T. Polytechnic, H. Road and N. London, *Chemical Communication*, 1971, 1634-1635.

200 G. A. Craig, J. Sánchezcosta, O. Roubeau, S. J. Teat and G. Aromí, *Chemistry - A European Journal*, 2011, **17**, 3120-3127.

201 A. Evans and K. R. Seddon, *New Journal of Chemistry*, 1999, **3**, 145–152.

202 G. J. Long and P. J. Clarke, *Inorganic Chemistry*, 1978, **17**, 1394–1401.

203 J. Roales, F. G. Moscoso, F. Gámez, T. Lopes-Costa, A. Sousaraei, S. Casado, J. R. Castro-Smirnov, J. Cabanillas-Gonzalez, J. Almeida, C. Queirós, L. Cunha-Silva, A. M. G. Silva and J. M. Pedrosa, *Materials*, 2017, **10**, 992.

204 U. Ali, K. J. B. A. Karim and N. A. Buang, *Polymer Reviews*, 2015, **55**, 678–705.

205 A. Sousaraei, C. Queiros, F. G. Moscoso, T. Lopes-Costa, J. M. Pedrosa, A. M. G. Silva, L. Cunha-Silva and J. Cabanillas-Gonzalez, *Analytical Chemistry*, 2019, **91**, 15853−15859.

206 C. Thilgen and F. Diederich, *Chemical Reviews*, 2006, **106**, 5049−5135.

207 O. Vostrowsky and A. Hirsch, *Chemical Reviews,* 2006, **106**, 5191−5207.

208 F. Giacalone and N. Martín, *Chemical Reviews*, 2006, **106**, 5136–5190.

209 G. S. Kumar, R. G. Shrestha, Q. Ji, J. P. Hill, K. Ariga, S. Acharya and L. K. Shrestha, *Physical Chemistry Chemical Physics*, 2018, **20**, 18873–18878.

210 P. Bairi, R. G. Shrestha, J. P. Hill, T. Nishimura, K. Ariga and L. K. Shrestha, *Journal of Materials Chemistry A*, 2016, **4**, 13899–13906.

211 S. Zheng, H. Ju and X. Lu, *A Advanced Energy Materials*, 2015, **5**, 1–9.

212 R. G. Shrestha, L. K. Shrestha, A. H. Khan, G. S. Kumar, S. Acharya and K. Ariga, *ACS Applied Materials and Interfaces*, 2014, **6**, 15597–15603.

213 W. E. Billups, W. Luo, A. Gonzalez, D. Arguello, L. B. Alemany, T. Marriott, M. Saunders, H. A. Jiménez-Vázquez and A. Khong, *Tetrahedron Letters*, 1997, **38**, 171–174.

214 J. Burroughs, D. Bradley and A. Brown, *Nature*, 1990, **347**, 354–358.

215 W. Yan, S. M. Seifermann, P. Pierrat and S. Bräse, *Organic and Biomolecular Chemistry*, 2015, **13**, 25–54.

216 M. Prato, T. Suzuki, H. Foroudian, Q. Li, K. Khemani, F. Wudl, J. Leonetti, R. D. Little, T. White, B. Rickborn, S. Yamago and E. Nakamura, *Journal of the American Chemical Society*, 1993, **115**, 1594–1595.

217 M. Prate, Q. C. Li and F. Wudl, *Journal of the American Chemical Society*, 1993, **115**, 1992–1994.

218 P. Belik, M. Walter, A. Kraus, E. Harth, M. Wagner, J. Spickermann and K. Mtillen, *Tetrahedron Letters*, 1996, **52**, 5007–5014.

219 F. Diederich, U. Jonas, V. Gramlich, A. Herrmann, H. Ringsdorf and C. Thilgen, *Helvetica Chimica Acta*, 1993, **76**, 2445–2453.

220 B. Krautler and M. Puchberger, *Helvetica Chimica Acta*, 1993, **76**, 1626–1631.

221 C. Bingel, *Chemische Berichte*, 1993, **126**, 1957–1959.

222 X. C. and A. Hirsch, *Perkin Communication*, 1997, **8**, 1595–1596.

223 T. M. Figueira-Duarte, J. Clifford, V. Amendola, A. Gégout, J. Olivier, F. Cardinali, M. Meneghetti, N. Armaroli and J. F. Nierengarten, *Chemical Communications*, 2006, 2054–2056.

224 S. Guerra, F. Schillinger, D. Sigwalt, M. Holler and J. F. Nierengarten, *Chemical Communications*, 2013, **49**, 4752–4754.

225 A. Hirsch, I. Lamparth, T. Grösser and H. R. Karfunkel, *Journal of the American Chemical Society,* 1994, **116**, 9385–9386.

226 F. Hörmann, W. Donaubauer, F. Hampel and A. Hirsch, *Chemistry - A European Journal*, 2012, **18**, 3329–3337.

227 T. Habicher, J. F. Nierengarten, V. Gramlich and F. Diederich, *Angewandte Chemie International Edition*, 1998, **37**, 1916–1919.

228 P. Peng, F. F. Li, F. L. Bowles, V. S. P. K. Neti, A. J. Metta-Magana, M. M. Olmstead, A. L. Balch and L. Echegoyen, *Chemical Communications*, 2013, **49**, 3209–3211.

229 C. H. Chen, A. Aghabali, A. J. Metta-Magana, M. M. Olmstead, A. L. Balch and L. Echegoyen, *Dalton Transactions*, 2015, **44**, 18487–18491.

230 P. Peng, F. F. Li, V. S. P. K. Neti, A. J. Metta-Magana and L. Echegoyen, *Angewandte Chemie International Edition*, 2014, **53**, 160–163.

231 A. Kraft, M. Gsänger and F. Beuerle, *European Journal of Organic Chemistry,* 2014, **2014**, 523–528.

232 A. Kraft, P. Roth, D. Schmidt, J. Stangl, K. Müller-Buschbaum and F. Beuerle, *Chemistry - A European Journal*, 2016, **22**, 5982–5987.

233 A. Kraft, C. Roger, D. Schmidt, J. Stangl, K. Müller-Buschbaum and F. Beuerle, *Chemistry - A European Journal*, 2017, **23**, 15864–15868.

234 A. Kraft, J. Stangl, A. M. Krause, K. Müller-Buschbaum and F. Beuerle, *Beilstein Journal of Organic Chemistry*, 2017, **13**, 1–9.

235 J. Echeverría, G. Aullón, D. Danovich, S. Shaik and S. Alvarez, *Nature Chemistry*, 2011, **3**, 323–330.

236 I. Lamparth, C. Maichle–Mössmer and A. Hirsch, *Angewandte Chemie International Edition*, 1995, **34**, 1607–1609.

237 E. Fernandez-Bartolome, J. Santos, A. Gamonal, S. Khodabakhshi, L. J. McCormick, S. J. Teat, E. C. Sañudo, J. S. Costa and N. Martín, *Angewandte Chemie International Edition*, 2019, 28–31.

238 R. D. Kennedy, M. Halim, S. I. Khan, B. J. Schwartz, S. H. Tolbert and Y. Rubin, *Chemistry - A European Journal*, 2012, **18**, 7418–7433.

239 Y. Li, J. Yu and R. Xu, *Journal of Applied Crystallography*, 2012, **45**, 855–861.

240 A. O'Neil, C. Wilson, J. M. Webster, F. J. Allison, J. A. K. Howard and M. Poliakoff, *Angewandte Chemie International Edition,* 2002, **41**, 3796–3799.

241 J. J. Novoa, M. H. Whangbo and J. M. Williams, *The Journal of Chemical Physics*, 1991, **94**, 4835–4841.

242 http://mccord.cm.utexas.edu/courses/fall2012/ch301/unit3-mccord.php (accessed 8 March 2020).

243 S. Tsuzuki, K. Honda, T. Uchimaru and M. Mikami, *Journal of Physical Chemistry A*, 2004, **108**, 10311–10316.

244 O. V. Dolomanov, L. J. Bourhis, R. J. Gildea, J. A. K. Howard and H. Puschmann, *Journal of Applied Crystallography*, 2009, **42**, 339–341.

245 B. Mattson, W. Foster, J. Greimann, T. Hoette, N. Le, A. Mirich, S. Wankum, A. Cabri, C. Reichenbacher and E. Schwanke, *Journal of Chemical Education*, 2013, **90**, 613–619.

246 B. Pieber, S. T. Martinez, D. Cantillo and C. O. Kappe, *Angewandte Chemie International Edition*, 2013, **52**, 10241–10244.

247 I. P. Romanova, V. F. Mironov, O. A. Larionova, V. I. Morozov, V. V. Zverev and O. G. Sinyashin, *Russian Chemical Bulletin*, 2008, **57**, 209–211.

248 M. S. Meier, R. G. Bergosh, M. E. Gallagher, H. P. Spielmann and Z. Wang, *Journal of Organic Chemistry*, 2002, **67**, 5946–5952.

249 G.- Wang, Y.- Li, F.- Li and Y.- Liu, *Letters in Organic Chemistry*, 2005, **2**, 595-598.

250 S. Kobatake, S. Takami, H. Muto, T. Ishikawa and M. Irie, *Nature*, 2007, **446**, 778–781.

251 S. Kobatake, S. Takami, H. Muto, T. Ishikawa, M. Irie, T. A. V. Khuong, J. E. Nunez, C. E. Godinez, M. A. Garcia-Garibay, A. Dhotel, Z. Chen, L. Delbreilh, B. Youssef, J. M. Saiter, L. Tan, D. Das, T. Jacobs and L. J. Barbour, *Nature Materials,* 2006, **39**, 778–781.

252 O. Sato, *Nature Materials*, 2016, **8**, 644–656.

253 K. Jacobson and D. Papahadjopoulos, *Biochemistry*, 1975, **14**, 152–161.

254 D. Das, T. Jacobs and L. J. Barbour, *Nature Materials*, 2010, **9**, 36–39.

255 J. P. Brog, C. L. Chanez, A. Crochet and K. M. Fromm, *RSC Advances*, 2013, **3**, 16905–16931.

256 I S. J. Chalk. IUPAC. Compendium of Chemical Terminology, 2nd ed. (the 'Gold Book'). Compiled by A. D. McNaught and A. Wilkinson. Blackwell Scientific Publications, Oxford (1997). Online version (2019).

257 H. Chung, D. Dudenko, F. Zhang, G. D'Avino, C. Ruzié, A. Richard, G. Schweicher, J. Cornil, D. Beljonne, Y. Geerts and Y. Diao, *Nature Communications*, 2018, **9**, 1-12.

258 A. Dhotel, Z. Chen, L. Delbreilh, B. Youssef, J. M. Saiter and L. Tan, *International Journal of Molecular Sciences*, 2013, **14**, 2303–2333.

259 M. Álvarez-Murga and J. L. Hodeau, *Carbon-Journal*, 2015, **82**, 381–407.

260 S. Pekker, É. Kováts, G. Oszlányi, G. Bényei, G. Klupp, G. Bortel, I. Jalsovszky, E. Jakab, F. Borondics, K. Kamarás, M. Bokor, G. Kriza, K. Tompa and G. Faigel, *Nature Materials*, 2005, **4**, 764–767.

261 Z. S. Yao, M. Mito, T. Kamachi, Y. Shiota, K. Yoshizawa, N. Azuma, Y. Miyazaki, K. Takahashi, K. Zhang, T. Nakanishi, S. Kang, S. Kanegawa and O. Sato, *Nature Chemistry*, 2014, **6**, 1079–1083.

262 A. Dhakshinamoorthy, J. He, A. Franconetti, A. M. Asiri, A. Primo and H. Garcia, *Catalysis Science and Technology*, 2018, **8**, 1589–1598.

ANNEX A

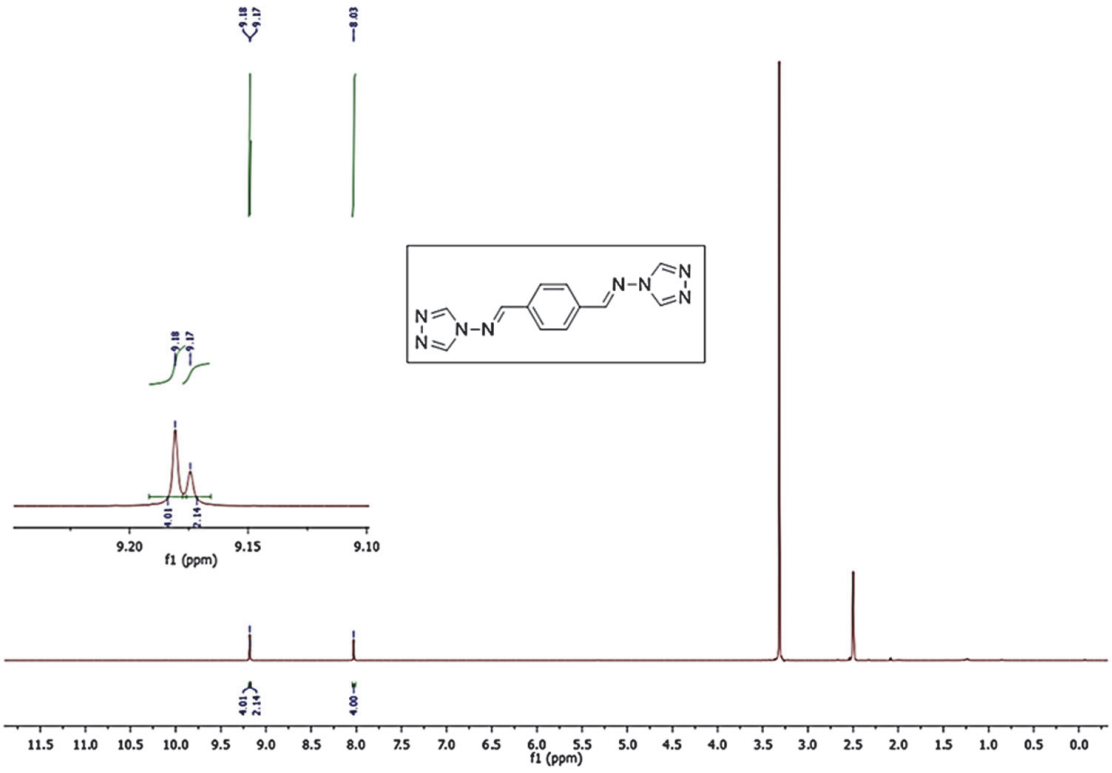

ANNEX A 1. ^{1}H NMR (400 MHz, DMSO-d^{6}, 298 K) of the PM-Tria[168]

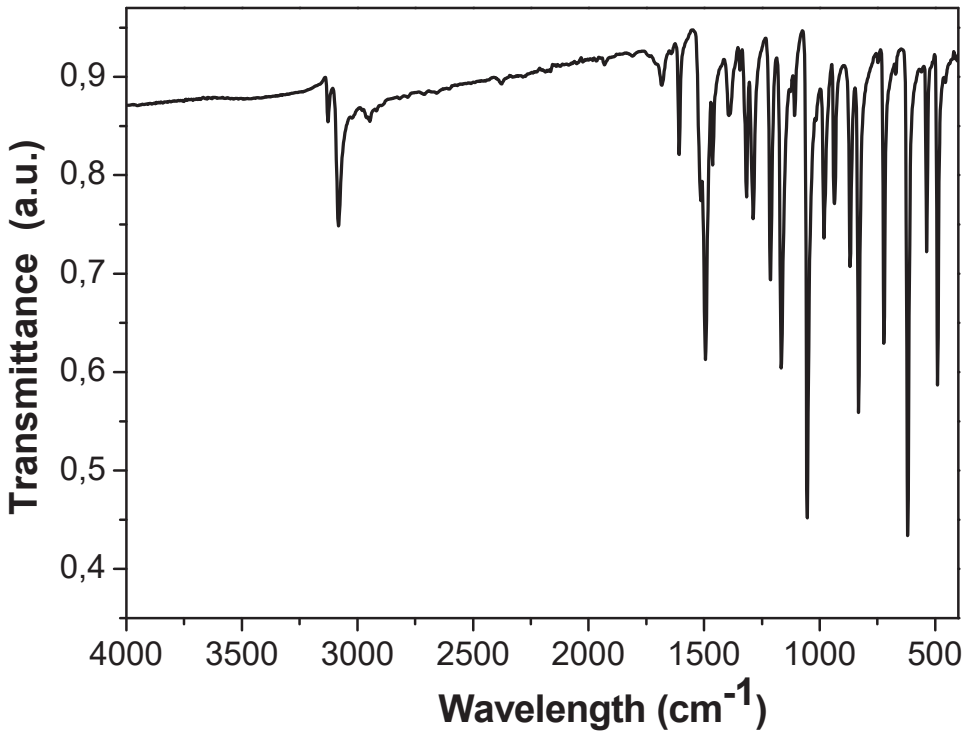

ANNEX A 2. Infrared spectrum of ligand PM-Tria[168].

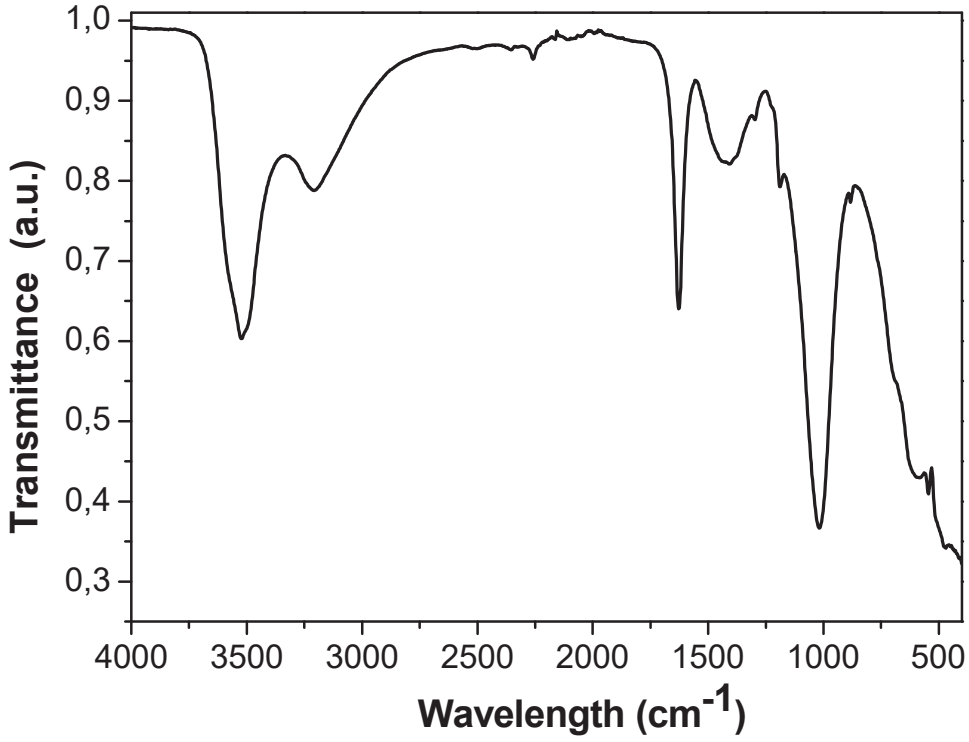

ANNEX A 3. Infrared Spectrum of $Fe(BF_4)_2$[168].

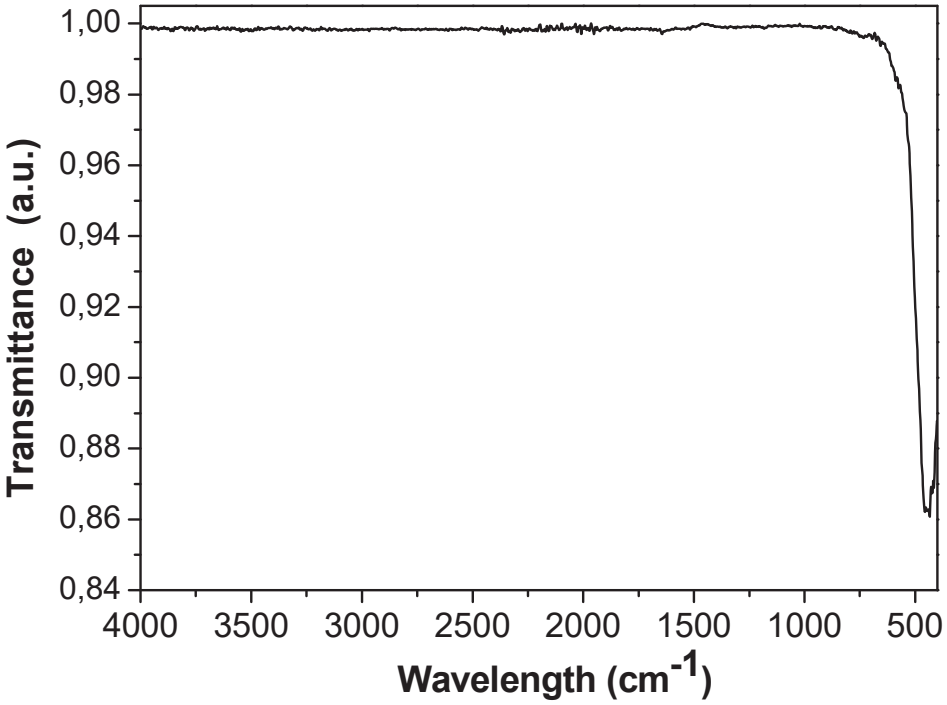

ANNEX A 4. Infrared Spectrum of FeF_2[168].

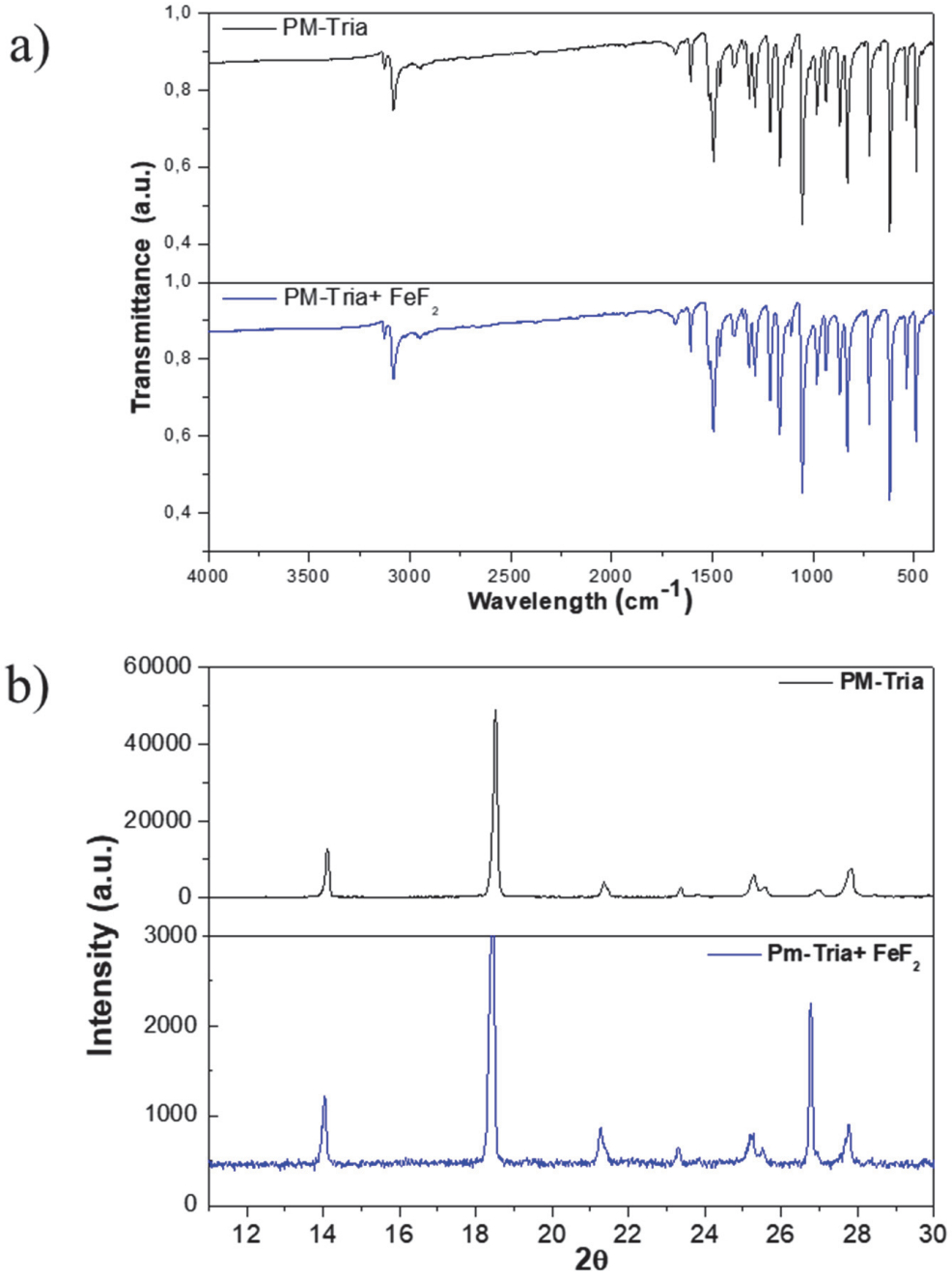

ANNEX A 5. a) and b) Comparing infrared spectra and experimental powder X-ray diffraction patterns of PM-Tria and the reaction between PM-Tria and FeF_2, respectively.

ANNEX A 6. Structural Refinement for compound **1**.

An initial data collection revealed that the crystal contained a supercell. The second data collection involved two complete datasets, one at a collection tome of 1 s, the second at a collection time of 5 s. Both datasets were integrated together, and the

full first dataset was treated as a fast scan in sadabs. This was done so that any overloaded reflections corresponding to the smaller cell could be scaled in. A solution was obtained in four space groups: *P*4/*ncc*, *P*4*cc*, $P4_12$, and $P\text{-}42_1c$. The initial R1 values were as follows:

R1	Rweak	Alpha	Orientation	Space group	Flack_x
0.315	0.002	0.067	as input	*P*4/*ncc*	
0.224	0.002	0.017	as input	*P*4*cc*	0.50
0.283	0.001	0.062	as input	$P4_12$	0.50
0.270	0.002	0.071	as input	$P\text{-}42_1c$	0.49

A complete refinement was conducted in *P*4/*ncc*, which showed that one of the two unique ligands was positionally disordered, while the other had some rotational disorder of the central aromatic ring. The positional disorder was modelled over two sites of complementary occupancy, with pairs of equivalent atoms constrained to have equal Uij values and SAME and SADI commands were used to ensure that the bond lengths and angles were equivalent for both orientations. The rotational disorder was modelled by generating remainder of the central -CH-C_6H_4-CH- from symmetry equivalent atoms and refining the entire unit with occupancy of 50%. SADI commands were used to constrain equivalent bonds to have the same length. Before modelling the BF_4 anions, a SQUEEZE analysis was performed. This showed the following:

```
loop_
    _platon_squeeze_void_nr
    _platon_squeeze_void_average_x
    _platon_squeeze_void_average_y
    _platon_squeeze_void_average_z
    _platon_squeeze_void_volume
    _platon_squeeze_void_count_electrons
    _platon_squeeze_void_content
     1  0.250  0.750  0.217      903      379 ' '
     2  0.250  0.750  0.250        7        0 ' '
     3  0.250  0.750  0.750        7        0 ' '
     4  0.750  0.250  0.781      903      379 ' '
     5  0.750  0.250  0.750        7        0 ' '
     6  0.750  0.250  0.250        7        0 ' '
_platon_squeeze_void_probe_radius              1.20
```

_platon_squeeze_details ?

As there were still anions needing to be modelled, no refinement was performed using SQUEEZE data, this was done for an estimate of residual electron density only. The above corresponds to 758 electrons per unit cell, or 63 electrons per Fe centre unaccounted for. One BF_4 contributes 42 electrons, so this leaves 21 electrons, or approximately 0.8 ethanol molecules unaccounted for. The bulk of the solvent used in the synthesis was ethanol, however, as there is a possibility that there may be small amounts of water present, these solvent molecules have not been included in the final molecular formula.

One BF_4 anion was modelled, and successive positions of the disordered BF_4 were added as more peaks of electron density appeared in the region. The BF_4 anions were refined with a common B-F bond length, which was refined as a free variable, and an F...F separation that was fixed at 1.633 times this value. Each BF_4 site was given a variable occupancy, with these constrained to sum to 0.75. Equivalent atoms were constrained to have equal Uij values.

As there were multiple potential space groups, one of which (*P*4*cc*) had a significantly lower initial *R*1 than the current model, the framework atoms were modelled for each of the other three potential solutions. The resulting *R*1 values, Flack parameters and BASF values are as follows:

*P*4*cc*	0.1502	0.52(10)	0.52085
$P42_11$	0.1482	0.52(13)	0.51576
P-42_1c	0.1513	0.51(12)	0.50817

In all cases, the R1 values are comparable to the current solution, and the Flack and BASF parameters indicate that the crystal is either centrosymmetric or a racemic twin. None of these lower symmetry space groups resulted in the ordering of the disordered ligands. As such, the space group *P*4/*ncc* was selected as the correct space group.

ANNEX A 7. Crystal data for compound **1**[168].

Compound	(1)
CCDC	1825247
Chemical formula	C_{72} H_{60} B_3 F_{15} Fe_3 N_{48}
Formula mass	2082.66
Temperature (K)	100(2) K
Crystal system	Tetragonal
Space group	*P* 4/*n c c*
***a*/Å**	19.9412(9)
***b*/Å**	19.9412(9)
***c*/Å**	24.1342(15)
α/°	90
β/°	90
γ/°	90
***V*(Å^3)**	9597.0(11)
Z	4
Radiation type	Synchrotron
Density (calculated mg/m^3)	1.441
Absorption coefficient (mm^{-1})	0.683
***F*(000)**	4224
Crystal size (mm^3)	0.130 x 0.120 x 0.080
Goodness of fit on F^2	2.717
***R*1, *wR*2 [*I*>2σ(*I*)]**	0.1301, 0.4997
***R*1, *wR*2 (all data)**	0.1508, 0.0576

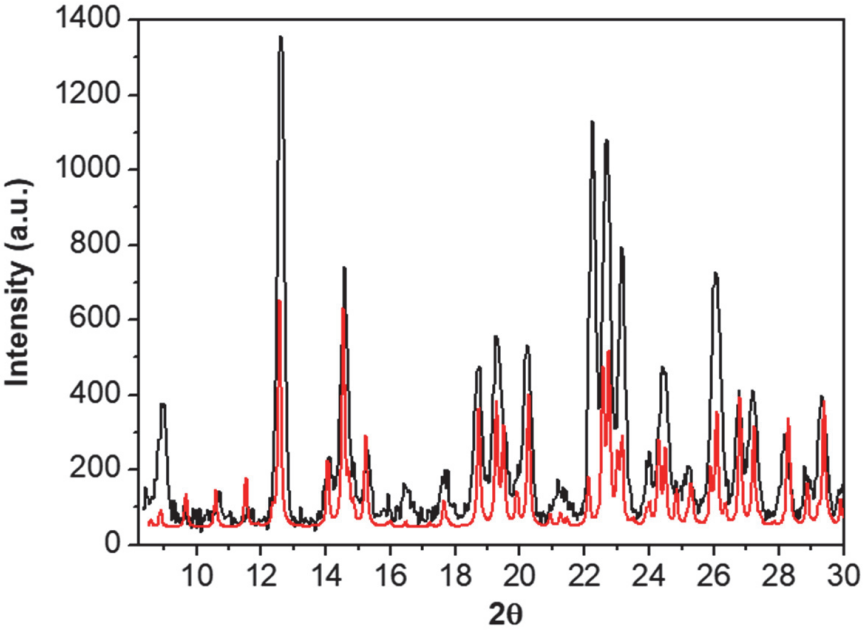

ANNEX A 8. PXRD superimposed spectra of **1** of the spectra calculated from single crystal diffraction using MERCURY software (red) and the PXRD experimentally obtained from the synthesis (black)[168].

ANNEX A 9. Picture of the original mosaic found in the Alhambra Palace[168].

ANNEX B

ANNEX B 1. Crystal data for compounds **1**, **2** and **3**.

Compound	(1)	(2)	(3)
Chemical formula	$C_8H_8Cl_2FeN_4$	$C_{14}H_{14}Cl_2FeN_4$	$C_{20}H_{22}Cl_2FeN_4O$
Formula mass	286.93	365.04	461.16
Temperature (K)	100 K	100 K	100 K
Crystal system	Orthorhombic	Orthorhombic	Monoclinic
Space group	Ccce	Pbca	P1 21/n 1
***a*/Å**	10.212(2)	13.403(3)	9.38662(4)
***b*/Å**	10.527(2)	7.3710(15)	16.76565(6)
***c*/Å**	10.256(2)	15.995(3)	13.95424(6)
α/◦	90	90	90
β/◦	90	90	93.4342(4)
γ/◦	90	90	90
***V*(Å^3)**	1102.5(4)	1580.2(5)	2192.075(15)
Z	4	4	4
Radiation type	Synchrotron	Synchrotron	Synchrotron
Density (calculated g/cm^3)	1.729	1.534	1.397
Absorption coefficient (mm^{-1})	1.822	1.289	1.011
***F*(000)**	576	744	952
Crystal size (mm^3)	0.124 x 0.115 x 0.005	0.075 x 0.055 x 0.015	0.074 x 0.050 x 0.020
Goodness of fit on F^2	1.093	1.081	1.123
***R*1, *wR*2 [$I>2\sigma(I)$]**	0.0412, 0.1112	0.0404, 0.1137	0.0705, 0.2123
***R*1, *wR*2 (all data)**	0.0414, 0.1118	0.0410,0.1149	0.0722, 0.2163

ANNEX B 2. Selected bond lengths [Å] for compounds **1**, **2** and **3**.

Selected bond lengths [Å]	
(1)	
Fe(1)-N(1) 2.221	**Fe(1)-Cl(1) 2.399**
Hydrogen interactions	
Cl(1)-C(1)(H(1)) 3.555	**Cl(1)-C(1)(H(2)) 3.555**
(2)	
Fe(1)-N(1) 2.258	**Fe(1)-Cl(1) 2.395**
Fe(1)-N(2) 2.279	
Hydrogen interactions	
Cl(1)-C(3)(H(3)) 3.549	**Cl(1)-C(7)(H(7)) 3.581**
(3)	
Fe(1)-N(1) 2.251	**Fe(1)-N(4) 2.245**
Fe(1)-N(2) 2.267	**Fe(1)-Cl(1) 2.395**
Fe(1)-N(3) 2.242	**Fe(1)-Cl(2) 2.439**
Hydrogen interactions	
Cl(2)-O(1)(H(1A)) 3.112	**Cl(1)-O(1)(H(1B)) 3.145**

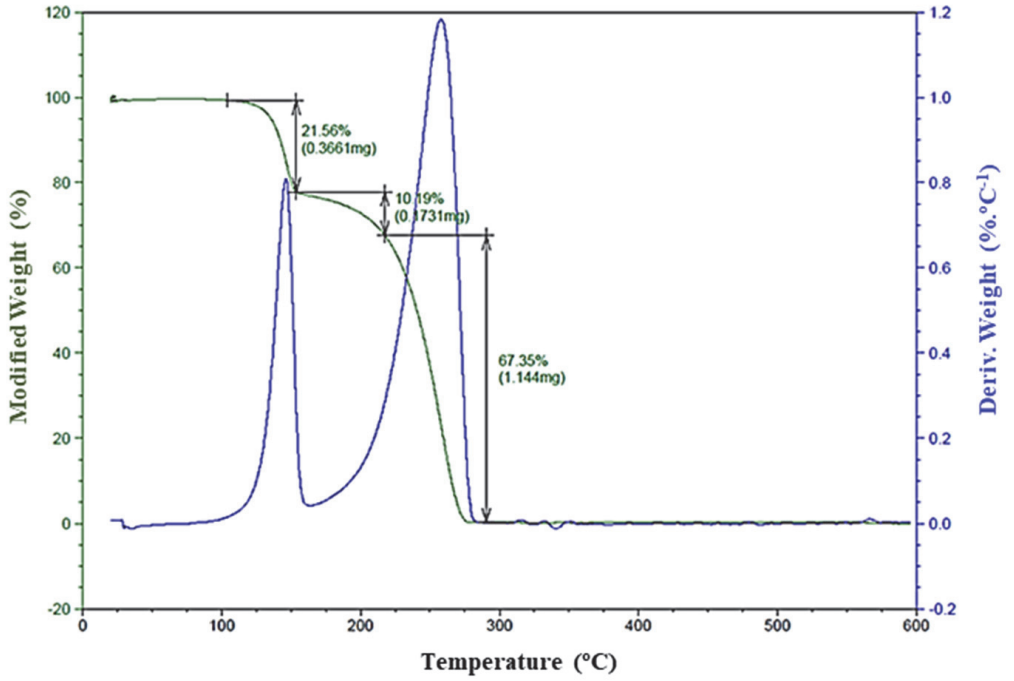

ANNEX B 3. Thermogravimetric profile of **1** (1.2820 mg in air showing the mass variation (green curve) and its first derivative (blue curve) upon heating at 2 ºC/min.

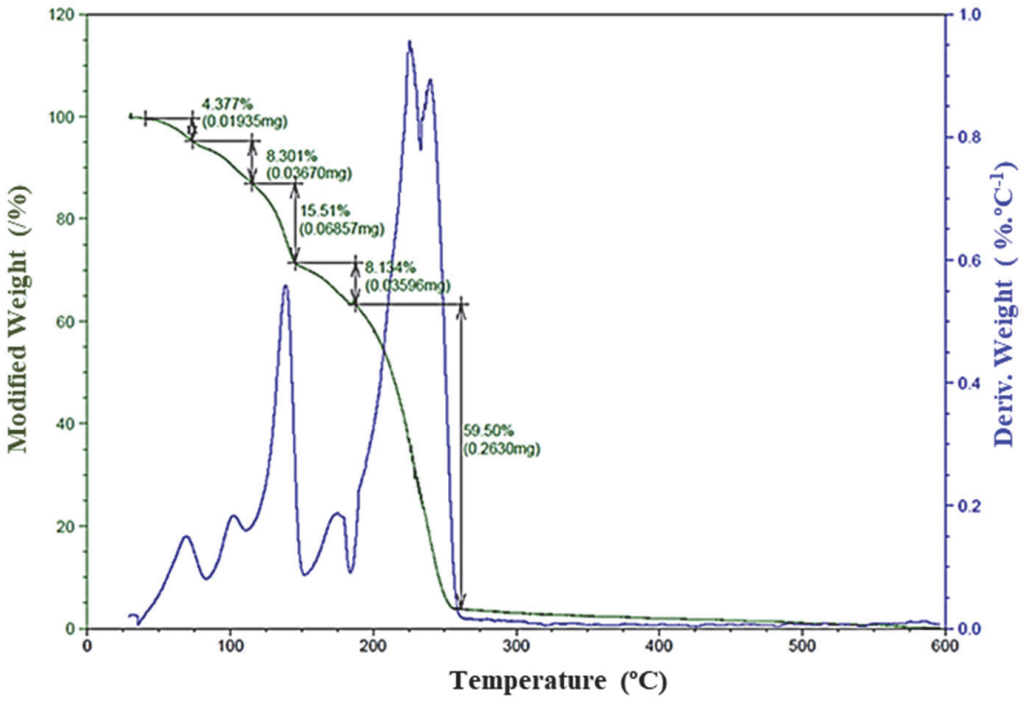

ANNEX B 4. Thermogravimetric profile of **2** (0.6560 mg in air showing the mass variation (green curve) and its first derivative (blue curve) upon heating at 2 ºC/min.

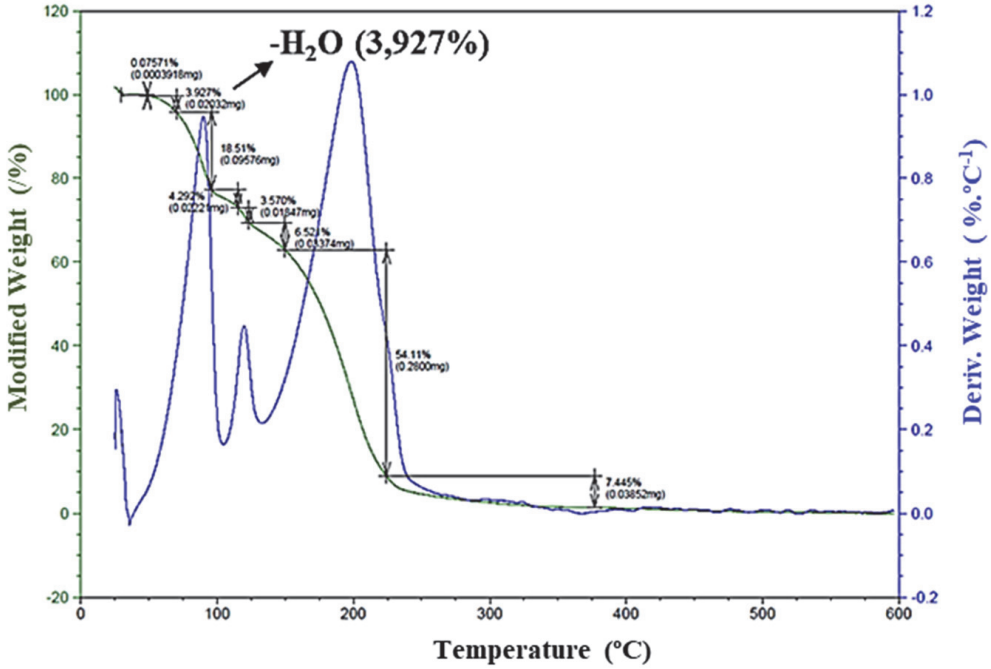

ANNEX B 5. Thermogravimetric profile of **3** (0.8650 mg in air showing the mass variation (green curve) and its first derivative (blue curve) upon heating at 2 ºC/min.

ANNEX C

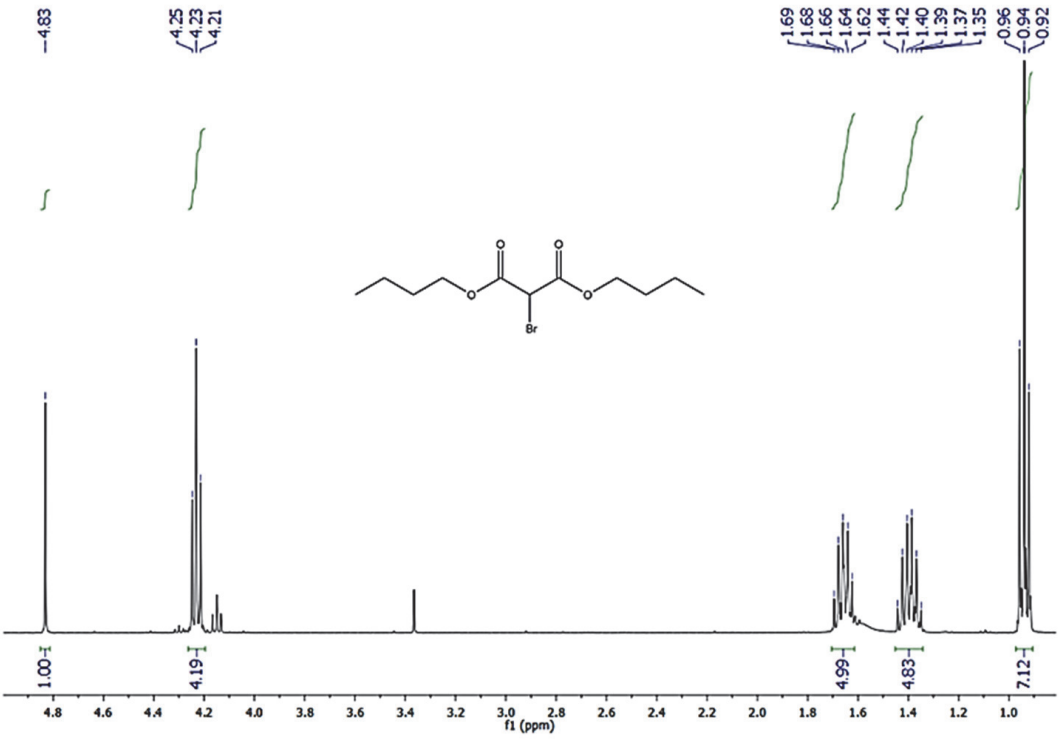

ANNEX C 1. ^{1}H NMR spectrum (400 MHz, $CDCl_3$) of **2**[237].

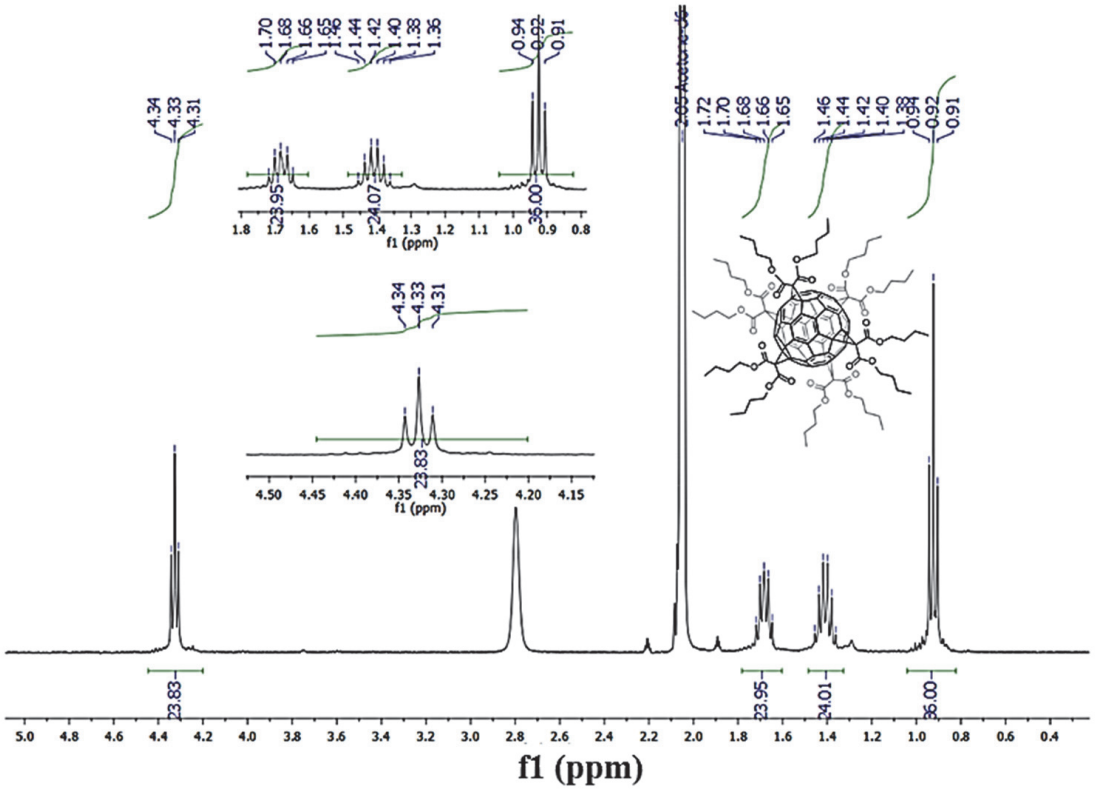

ANNEX C 2. ^{1}H NMR spectrum (400 MHz, $(CD_3)_2CO$) of **3a**[237].

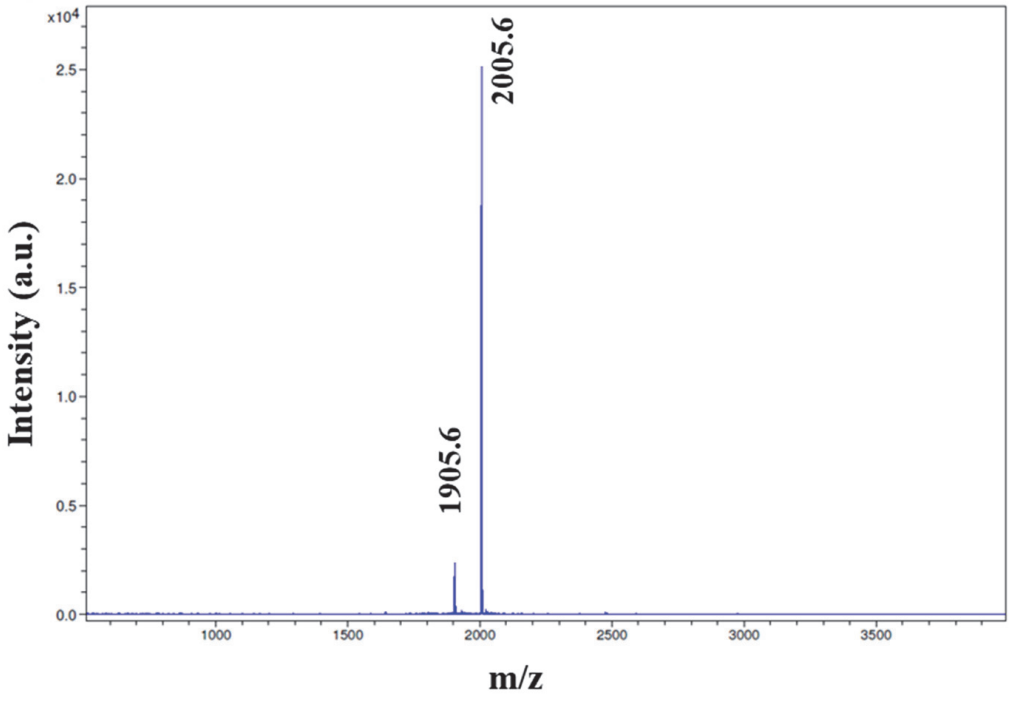

ANNEX C 3. Mass Spectrometry of compound **3a**[237].

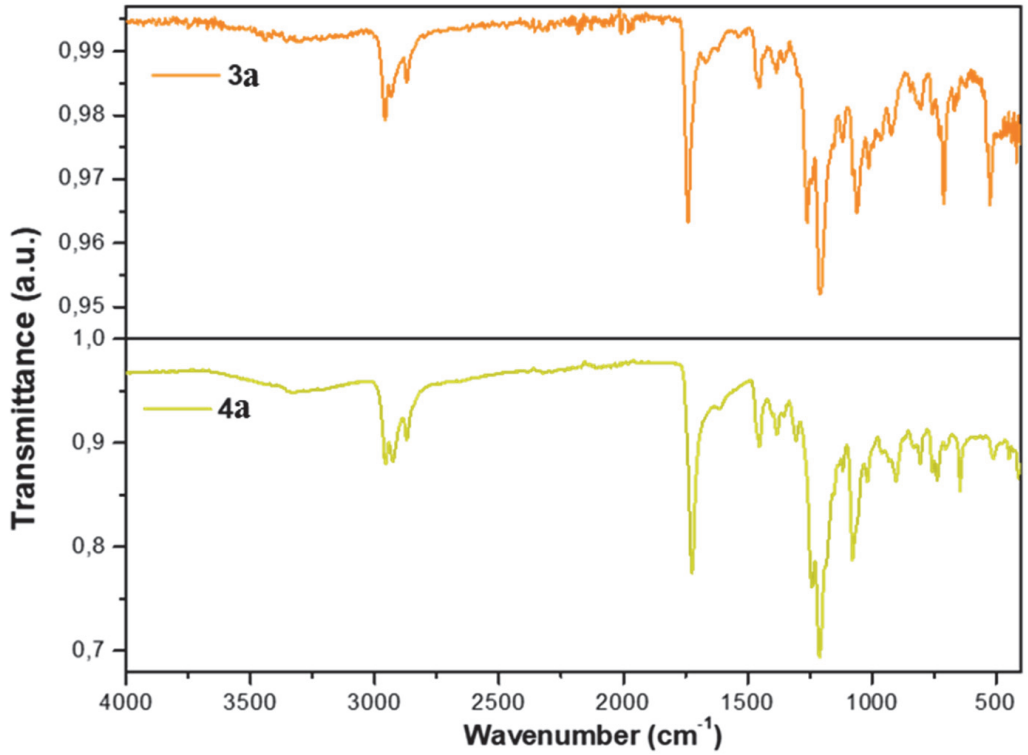

ANNEX C 4. Infrared superimposed spectra of starting material **(3a)** (orange) and the infrared spectra of final compound **(4a)** (yellow).

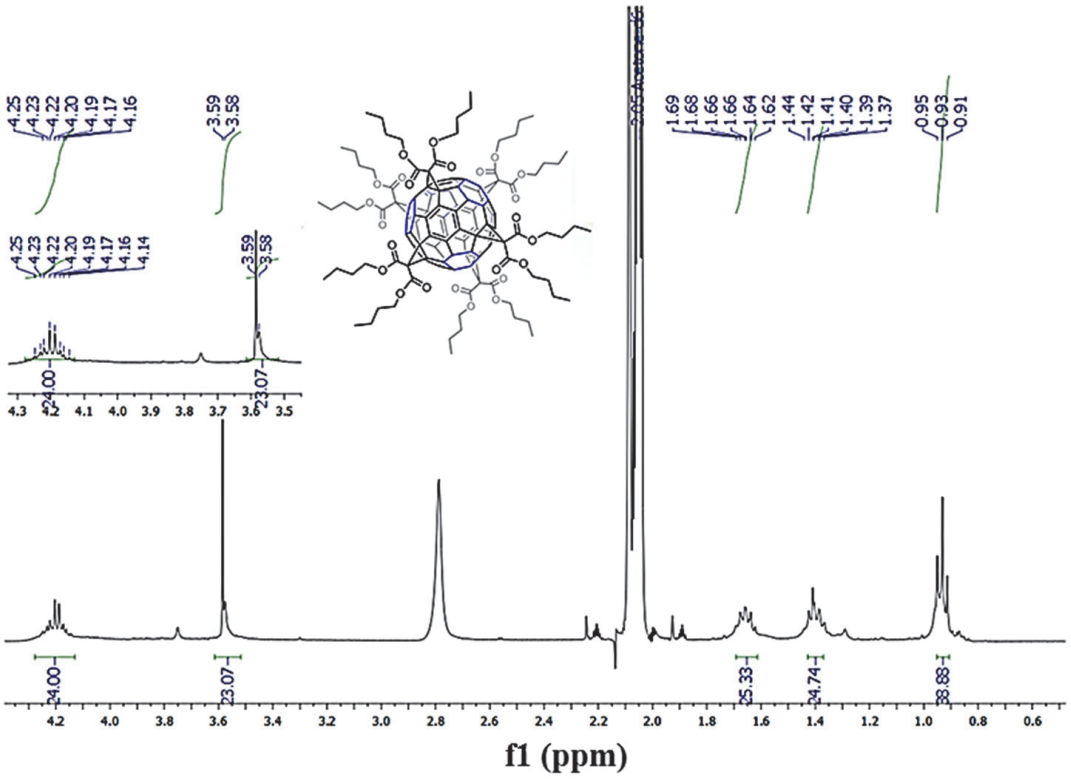

ANNEX C 5. ^{1}H NMR spectrum (400 MHz, $(CD_3)_2CO$) of **4a**[237].

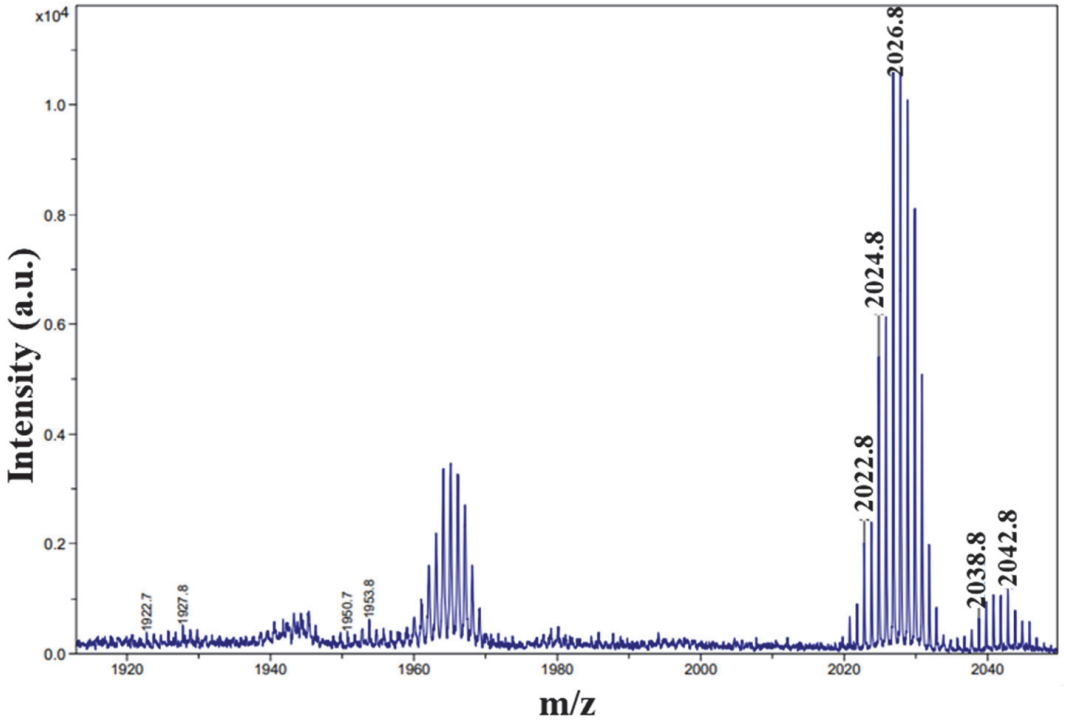

ANNEX C 6. Mass Spectrometry of compound **4a**[237].

ANNEX C 7. Structural Refinement for compounds **3a** and **4a**.

Crystallographic details of 3a.

_shelx_space_group_comment
The symmetry employed for this shelxl refinement is uniquely defined by the following loop, which should always be used as a source of symmetry information in preference to the above space-group names. They are only intended as comments.

_reflns_special_details
Reflections were merged by SHELXL according to the crystal class for the calculation of statistics and refinement.

_reflns_Friedel_fraction is defined as the number of unique
Friedel pairs measured divided by the number that would be possible theoretically, ignoring centric
projections and systematic absences.

_publ_section_acknowledgements
This research used resources of the Advanced Light Source, which is a DOE Office of Science User
Facility under contract no. DE-AC02-05CH11231.

_vrf_REFNR01_jsc01_a

PROBLEM: Ratio of reflections to parameters is < 6 for a
RESPONSE: This is correct. The crystals have a weakly diffracting nature, due to the large spaces between fullerene molecules, which has resulted in a comparatively low number of data points. All atoms belonging to the pendant ester groups appended to the fullerene have been refined with isotropic thermal
displacement parameters, however, the carbon atoms of the fullerene have been refined with anisotropic thermal displacement parameters to show that there is little evidence that the fullerene itself is disordered.

_vrf_THETM01_jsc01_a;
PROBLEM: The value of sine(theta_max)/wavelength is less than 0.550
RESPONSE: This is correct, the large spaces between the fullerene units cause the crystal to be very weakly diffracting. Visual inspection of the diffraction pattern showed a sharp decline in observed spots at resolutions greater than 1 A.

_vrf_PLAT084_jsc01_a
PROBLEM: High wR2 Value (i.e. > 0.25) ..... 0.55 Report
RESPONSE: This is correct, the crystals were very small and weakly diffracting, and the heaviest atom in
them was oxygen. The fullerene units are not closely packed, and disordered n butyl groups project into the voids between them. This combination of factors gives elevated R1 and wR2 values. SQUEEZE analysis did not show any significant electron density that is unaccounted for by the current model.

_vrf_PLAT088_jsc01_a
PROBLEM: Poor Data / Parameter Ratio ..... 5.89 Note
RESPONSE: This is correct. The crystals have a weakly diffracting nature, due to the large spaces between fullerene molecules, which has resulted in a comparatively low number of data points. All atoms belonging to the pendant ester groups appended to the fullerene have been refined with isotropic thermal
displacement parameters, however, the carbon atoms of the fullerene have been refined with anisotropic thermal displacement parameters to show that there is little evidence that the fullerene itself is disordered.

_vrf_PLAT082_jsc01_a
PROBLEM: High R1 Value ..... 0.17 Report
RESPONSE: This is correct, the crystals were very small and weakly diffracting, and the heaviest atom in them was oxygen. The fullerene units are not closely packed, and disordered n-butyl groups project into the voids between them. This combination of factors gives elevated R1 and wR2 values. SQUEEZE analysis did not show any significant electron density that is unaccounted for by the current model.

_vrf_PLAT097_jsc01_a
PROBLEM: Large Reported Max. (Positive) Residual Density 0.99 eA-3
RESPONSE: This peak of electron density lies very close to the carbonyl oxygen atoms of the n-butyl ester groups and suggests that there may be additional

rotational disorder of the butyl ester group. Given that the ester has already been modelled over two positions, with the n-butyl group having been modelled over four positions, efforts to further model this disorder would only result in making an already low data to parameter ratio even lower without a corresponding increase in the chemical understanding of the system.

_vrf_PLAT201_jsc01_a
PROBLEM: Isotropic non-H Atoms in Main Residue(s) ..... 1 Report RESPONSE: This is correct. Given the low data to parameter ratio, only the carbon atoms of the fullerene unit have been refined with anisotropic thermal displacement parameters, the atoms belonging to the pendant C(CO2nBu)2 groups have been refined isotropically.

_vrf_PLAT326_jsc01_a
PROBLEM: Possible Missing H on sp3? Carbon ..... C6 Check RESPONSE: This is not the case, C6 is indeed an sp3 hybridised carbon atom, however it binds to two symmetry-related n-butyl ester groups and two carbon atoms beloning to the fullerene unit.

_vrf_PLAT340_jsc01_a
PROBLEM: Low Bond Precision on C-C Bonds ..... 0.01478 Ang.
RESPONSE: This is due to the weakly diffracting nature of the crystal and the large amounts of disorder of the terminal n-butyl groups. _refine_special_details
The crystals are very weakly diffracting, and significant diffraction was not observed beyond 1 A. The carbon atoms belonging to the fullerene unit itself were located and refined anisotropically. The pendant C(CO2nBu)2 groups were originally modelled over only one orientation, however, elongated thermal ellipsoids of and large residual atoms indicated that the carboxylate section of the ester was rotationally disordered and the n-butyl was also disordered over multiple sites. These atoms were modelled over four different locations with site occupancies that were restrained to sum to 1. EADP commands were used to constrain the thermal parameters of the different sites of the same atom, e.g. O2_1, O2_2, O2_3 and O2_4, and a combination of SAME commands and free variables were used to restrain the C-O and C-C bond lengths, respectively, to be the same length for each of the four orientations of the n-butyl ester. Visual inspection of the extended structure showed potential voids between the fullerene units, however, SQUEEZE analysis showed that there is little residual electron density in these 'voids'. Due to the low resolution of the data, the data to parameter ratio is very low. Refining all atoms isotropically only raises the data to parameter ratio to 7.3.

_geom_special_details
All esds (except the esd in the dihedral angle between two l.s. planes) are estimated using the full covariance matrix. The cell esds are taken into account individually in the estimation of esds in distances, angles and torsion angles; correlations between esds in cell parameters are only used when they are defined by crystal symmetry. An approximate (isotropic) treatment of cell esds is used for estimating esds involving l.s. planes.

Crystallographic details of 4a.

_shelx_space_group_comment The symmetry employed for this shelxl refinement is uniquely defined by the following loop, which should always be used as a source of symmetry information in preference to the above space-group names. They are only intended as comments.

_reflns_special_details Reflections were merged by SHELXL according to the crystal class for the calculation of statistics and refinement.

_reflns_Friedel_fraction is defined as the number of unique Friedel pairs measured divided by the number that would be possible theoretically, ignoring centric projections and systematic absences.

_vrf_THETM01_EFBrun4_a PROBLEM: The value of sine(theta_max)/wavelength is less than 0.550.

RESPONSE: This is correct, the large spaces between the fullerene units cause the crystal to be very weakly diffracting. Visual inspection of the diffraction pattern showed a sharp decline in observed spots at resolutions greater than 1 A.

_vrf_REFNR01_EFBrun4_a PROBLEM: Ratio of reflections to parameters is < 8 for a RESPONSE: This is correct. The crystals have a weakly diffracting nature, due to the large spaces between fullerene molecules, which has resulted in a comparatively low number of data points. The carbon atoms of the fullerene have been refined with anisotropic thermal displacement parameters to show that there is little evidence that the fullerene itself is disordered.

_vrf_PLAT241_EFBrun4_a PROBLEM: High 'MainMol' Ueq as Compared to Neighbours of C10 Report RESPONSE: This is correct. The butyl groups are heavily disordered resulting in large anisotropic thermal displacement parameters.

_vrf_PLAT242_EFBrun4_a PROBLEM: Low 'MainMol' Ueq as Compared to Neighbors of C9 Report RESPONSE:C9 part of the and disordered n-butyl groups.

_vrf_PLAT413__EFBrun4_a PROBLEM: Short Inter XH3 .. XHn H11..H11B 1.69 Ang Report RESPONSE: This is correct. The hydrogen atoms belong to the disordered methyl from the hanging butyl groups and have been calculated.

_vrf_PLAT084_EFBrun4_a ;PROBLEM: High wR2 Value (i.e. > 0.25) ..... 0.42 Report RESPONSE: This is correct, the crystals were very small and weakly diffracting, and the heaviest atom in them was oxygen. The fullerene units are not closely packed, and disordered n-butyl groups project into the voids between them. This combination of factors gives elevated R1 and wR2 values.

ANNEX C 8. Crystal data for compounds **3a** and **4a**[237].

Compound	(3a)	(4a)
CCDC	1870483	1870484
Chemical formula	$C_{126}\ H_{108}\ O_{24}$	$C_{126}\ H_{132}\ O_{24}$
Formula mass	2006.12	2030.31
Temperature (K)	100(2) K	100 K
Crystal system	Cubic	Cubic
Space group	F d -3	F d -3
***a*/Å**	26.8785(6)	26.156(3)
***b*/Å**	26.8785(6)	26.156(3)
***c*/Å**	26.8785(6)	26.156(3)
α/°	90	90
β/°	90	90
γ/°	90	90
***V*(Å^3)**	19418.5(13)	17894(6)
Z	8	8
Radiation type	Synchrotron	Synchrotron
Density (calculated g/cm^3)	1.372	1.507
Absorption coefficient (mm^{-1})	0.113	0.144
***F*(000)**	8448	8640
Crystal size (mm^3)	0.010 x 0.010 x 0.005	0.145 x 0.145 x 0.145
Goodness of fit on F^2	2.863	2.173
***R*1, *wR*2 [$I>2\sigma(I)$]**	0.1663, 0.4945	0.1226, 0.3980
***R*1, *wR*2 (all data)**	0.1922, 0.5451	0.1289, 0.4237

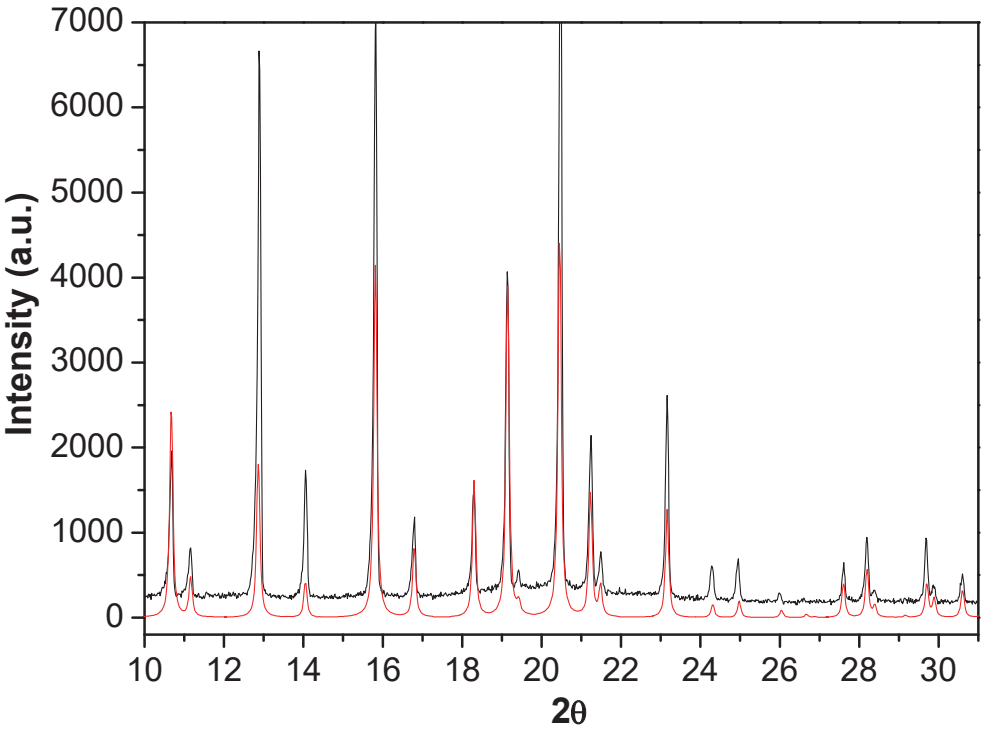

ANNEX C 9. PXRD superimposed spectra of **3a** of the spectrum calculated from single crystal diffraction using MERCURY software (black) and the PXRD experimentally obtained from the synthesis (red).

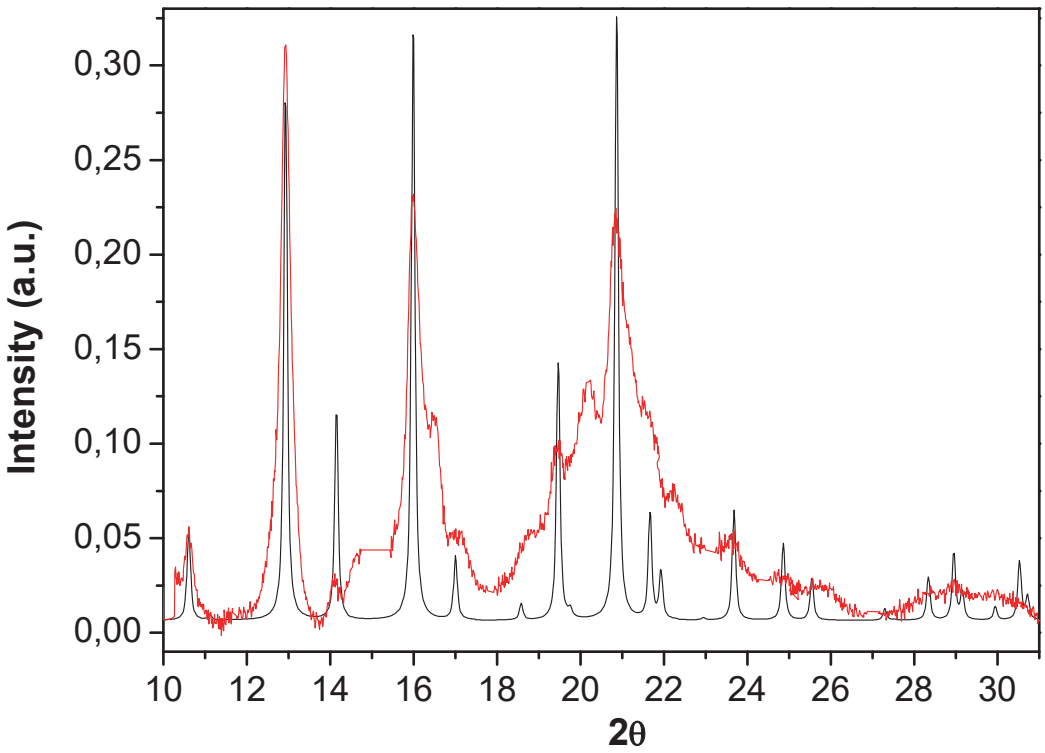

ANNEX C 10. PXRD superimposed spectra of **4a** of the spectrum calculated from single crystal diffraction using MERCURY software (black) and the PXRD experimentally obtained from the synthesis (red) [237].

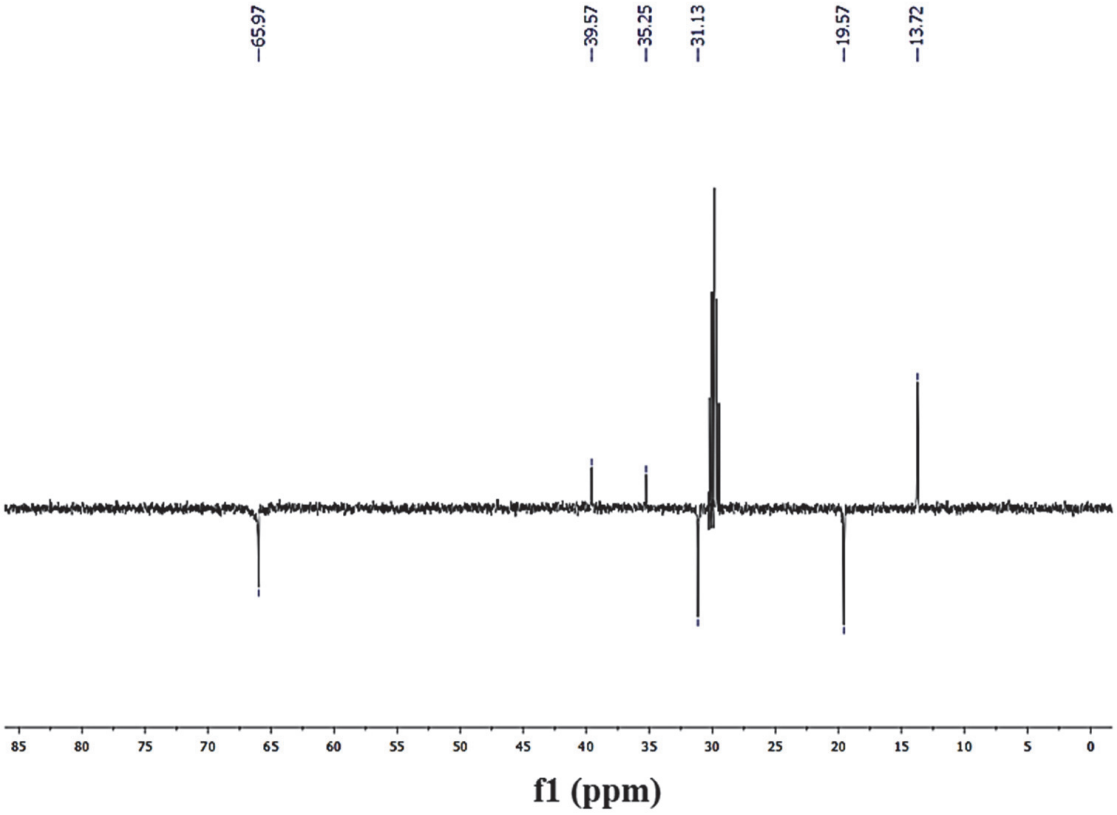

ANNEX C 11. ^{135}DEPT NMR spectrum (100MHz, $(CD_3)_2CO$) of **4a**[237].

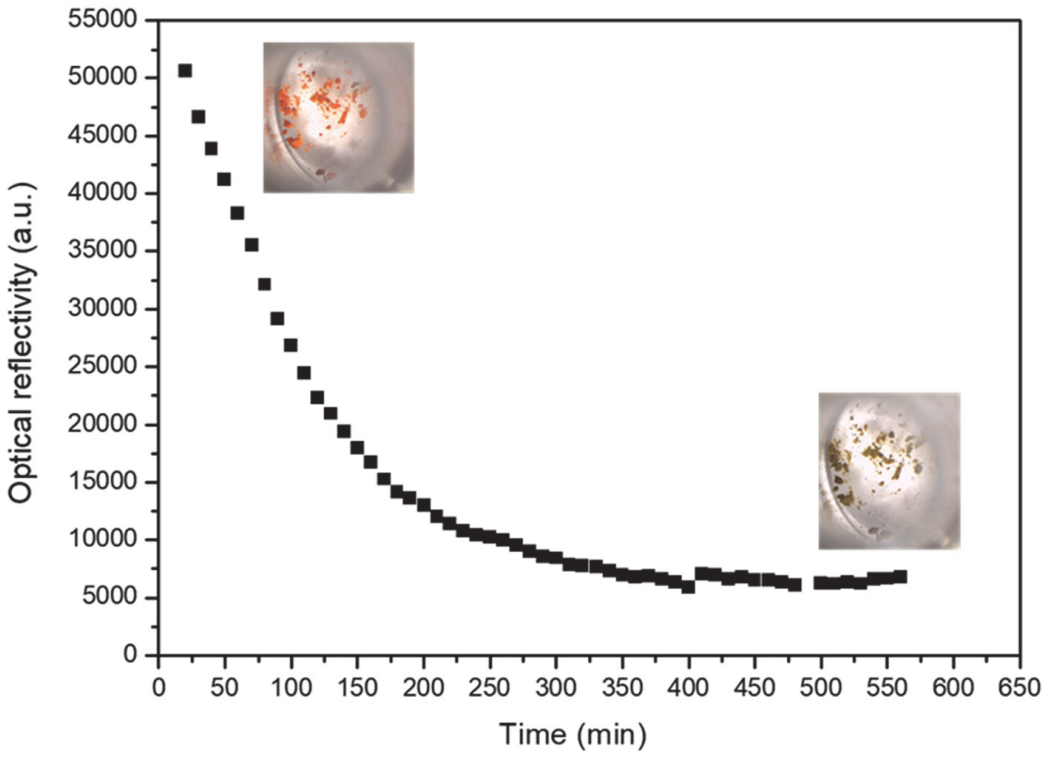

ANNEX C 12. Optical reflectivity variation with time over hydrazine exposure to **3a**[237].

ANNEX D

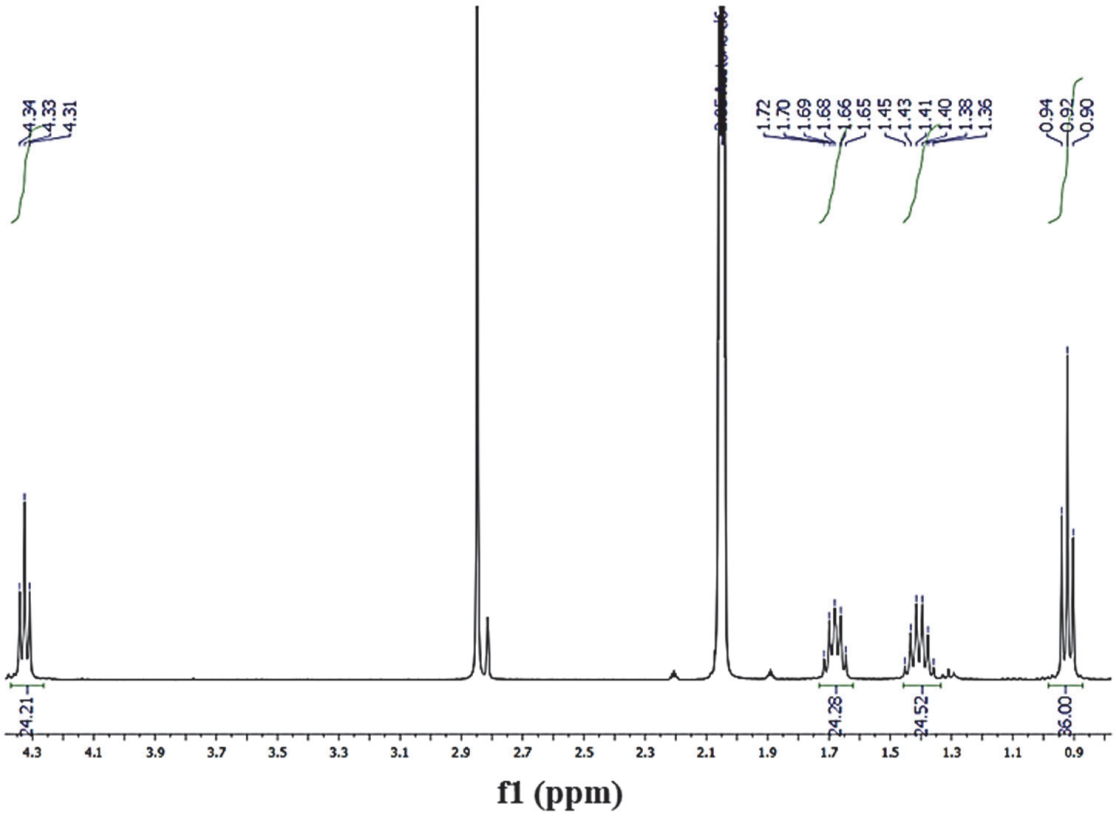

ANNEX D 1. ^{1}H NMR spectrum (400 MHz, $(CD_3)_2CO$) of **3b**.

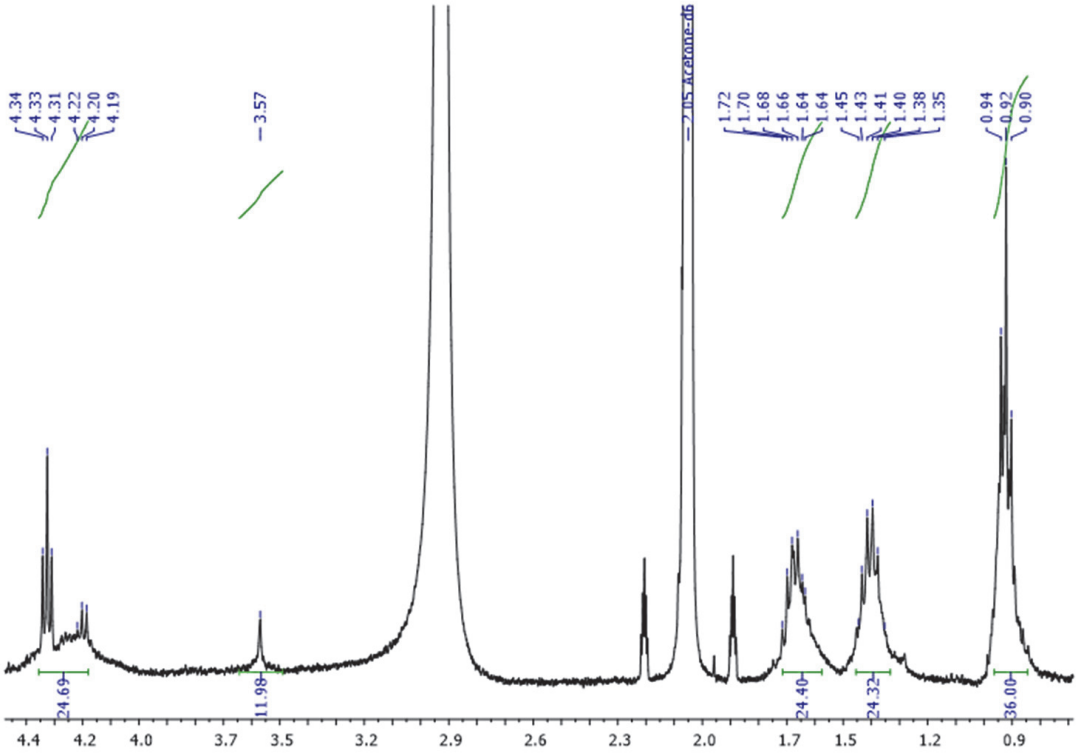

ANNEX D 2. ^{1}H NMR spectrum (400 MHz, $(CD_3)_2CO$) of **4b**.

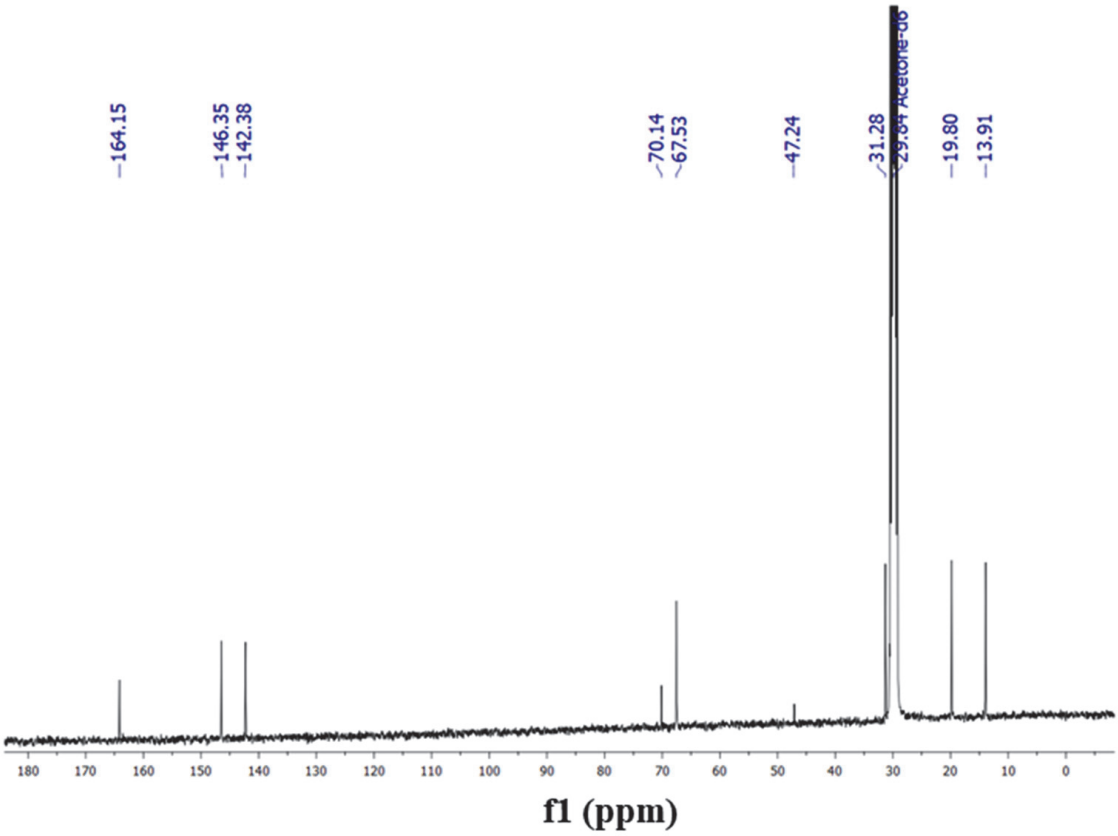

ANNEX D 3. ^{13}C NMR spectrum (100 MHz, $(CD_3)_2CO$) of **3b**.

ANNEX D 4. Crystal data for compounds **3b** and **4b**.

Compound	(3b)	(4b)
Chemical formula	$C_{126}H_{108}O_{24}$	$C_{126}H_{120}O_{24}$
Formula mass	2006.25	2018.25
Temperature (K)	100(2) K	100(2) K
Crystal system	Triclinic	Triclinic
Space group	P -1	P -1
***a*/Å**	15.460	15.480
***b*/Å**	17.120	17.080
***c*/Å**	20.310	20.480
α/°	76.74	76.88
β/°	69.11	69.85
γ/°	72.20	71.46
***V*(Å^3)**	4737.81	4777.5
Z	2	2
Radiation type	Synchrotron	Synchrotron
c(calculated g/cm^3)	1.406	1.401
Absorption coefficient (mm^{-1})	0.101	0.101
***F*(000)**	2112	2136
Crystal size (mm^3)	0.111x0.109x0.1	0.117x0.12x0.1
Goodness of fit on F^2	1.036	1.613
***R*1, *wR*2 [$I>2\sigma(I)$]**	0.0795, 0.2243	0.1976, 0.4732
***R*1, *wR*2 (all data)**	0.0765, 0.2197	0.1385, 0.4191

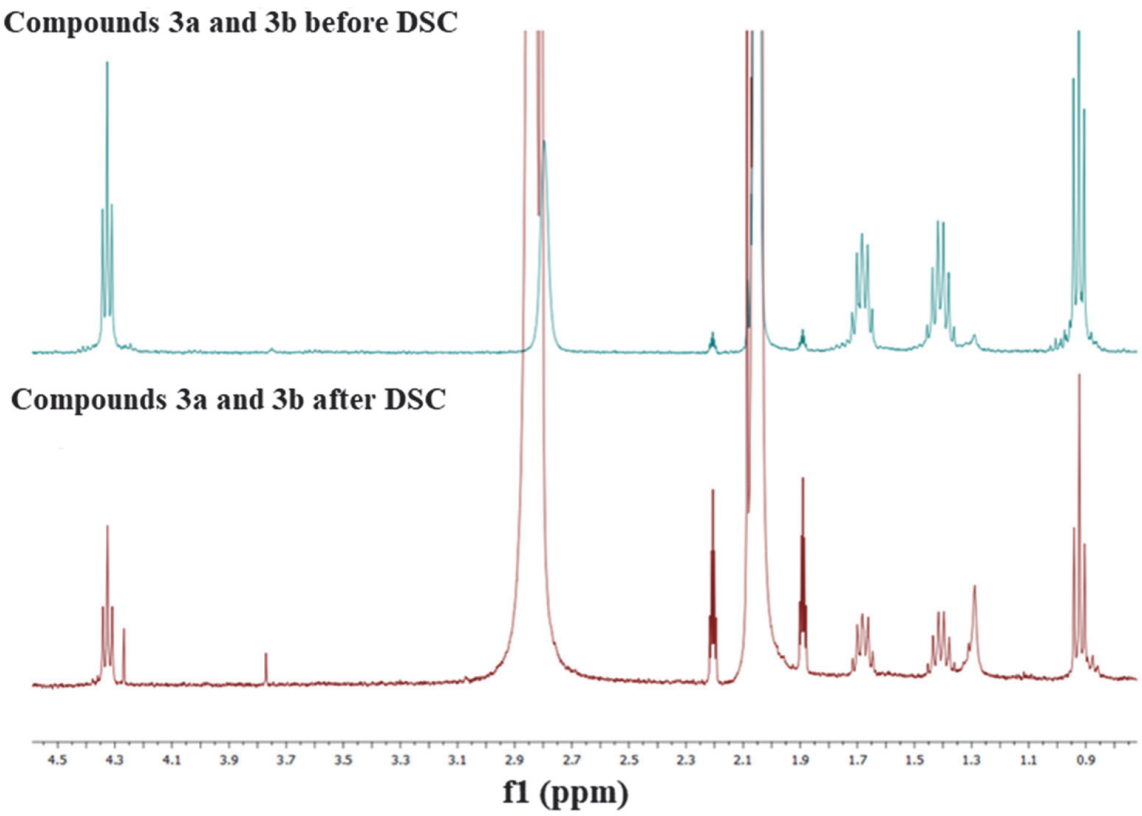

ANNEX D 5. ^{1}H NMR spectra of compounds **3a** and **3b** before and after DSC experiments.

ANNEX E. PHYSICAL TECHNIQUES

- NMR spectra were recorded on a Bruker Advance 300 (1H: 400 MHz) spectrometer at 298 K using partially deuterated solvents as internal standards. Coupling constants (J) are denoted in Hz and chemical shifts (δ) in ppm. Multiplicities are denoted as follows: s = singlet, d = doublet, t = triplet, m = multiplet.
- Mass spectra Matrix assisted Laser desorption ionization (coupled to a Time-of-Flight analyzer) experiments (MALDI-TOF) were recorded on a MAT 95 thermo spectrometer and a Bruker REFLEX spectrometer respectively.
- FT-IR spectra were recorded as neat samples in the range 400-4000 cm^{-1} on a Bruker Tensor 27 (ATR device) Spectrometer.
- TGA was performed using a TA Instrument TGAQ500 with a ramp of 2 ºC/min under air and nitrogen from 30 to 500 ºC.
- Elemental analyses (C, H and N) were performed on a LECO CHNS-932 Analyzer.
- Gas isotherm measurement was carried out on a Micromeritics Flowsorb 2300 and it was performed at 77 K, with the temperature held constant using liquid N_2 bath.
- Powder X-ray diffractograms were obtained by using a Panalytical X'Pert PRO diffractometer (Cu-Kα1 X-radiation, λ1=1.5406 Å) with parallel-beam collimator, graphite secondary monochromator and Xenon detector. Theta / 2 theta sweep has been carried out from 5º to 90º range with an angular increase of 0,04º. Diffraction patterns were recorded at room temperature.
- Magnetic susceptibility measurements between 2 K and 300 K were carried out in a Quantum Design MPMS-XL SQUID magnetometer under a 1000 Oe field. Each sample was secured inside a gel capsule with glass wool, and the capsule was pinched (0.5 mm diameter hole) on the top to allow convenient purging of the interior of the capsule. Pascal constants were used to correct for the diamagnetic contribution.
- Crystal Structure Determination has been carried out in two synchrotrons, Lawrence Berkeley National Laboratory and ALBA Synchrotron: In the first one the data were collected with a Bruker APEX II CCD diffractometer at the Advanced Light Source beamline 11.3.1 from a silicon (111) monochromator (T = 100, K, λ = 0.7749 Å). The crystal was taken directly from its solution, mounted with a drop of Paratone-N oil and

immediately put into the cold stream of dry N_2 on the goniometer. The structure was solved by direct methods and the refinement on F_2 and all further calculations were carried out with the SHELX-TL suite. In the second one, the data were collected with a MD2M–Maatel diffractometer at the XALOC beamline (BL13) with the collaboration of ALBA staff, from a Silicon (111) monochromator (T = 100 K, λ = 0.82656 Å). The crystal was taken directly from its solution, mounted with a drop of Paratone-N oil and immediately put into the cold stream of dry N_2 on the goniometer. The structure was solved by direct methods and the refinement on F_2 and all further calculations were carried out with the SHELX-TL suite and OLEX2 program.

- Optical reflectivity measurements between 288 and 373 K were performed using a MOTIC SMZ-171 optical stereoscope coupled with a MOTICAM 3. Images were collected in BMP format without any filter using the Motic Images Plus 3.0 software, with the mean value from each region of interest (ROI) analyzed under the ImageJ program. The temperature was controlled using a Linkam T95 system controller and a LNP 95 Liquid Nitrogen Cooling System.
- Differential Scanning Calorimetry (DSC) measurements were performed in a TA Instruments Discovery MDSC 25 between 273 K and 393 K under a N_2 atmosphere with a ramp of 1°C min^{-1}. The sample was secured in a hermetically sealed aluminum sample pan.